Spatially Resolved Star Formation in Cosmological Zoom-in Simulations: Understanding the Role of Feedback in Scaling Relations

Thesis by
Matthew Edward Orr

In Partial Fulfillment of the Requirements for the
Degree of
Doctor of Philosophy

Caltech

CALIFORNIA INSTITUTE OF TECHNOLOGY
Pasadena, California

2019
Defended May 28, 2019

ACKNOWLEDGEMENTS

I have no doubts that I will look back fondly on graduate school as a formative period in becoming a scientist, mentor, some degree of leader, and, in steps, a better person. I think that it would be laughable to consider any of that happening on its own without the host of family, friends, mentors, and advisors I have had supporting me over the past five years in graduate school, and for the twenty-two years before that.

First, I want to thank my late father, Steven Robert Orr, for all his encouragement and council over the years. When I was torn over whether to pursue astrophysics or "something more practical", his wisdom was my guide. When I think about the man I have become, and the man that I want to be, I will always think of my Dad. I have missed him in my time at Caltech. And yet, I am sure I could not have finished a doctorate without him.

I could not say *thank you* enough to my advisor, Phil Hopkins. Between his patience, guidance, in matters both scientific and not, and, of course, funding, I could not have become the astrophysicist I am today. I am indebted to him for shepherding me through my graduate years. In a similar vein, I am not sure any of my work would be half as good without Chris Hayward. Through both being a great mentor and his help in keeping my manuscripts from being unreadable messes, Chris kept me from becoming a mess an uncountable number of times during my doctorate.

Needless to say that my time at Caltech would have been very different without the early guidance of Jorge Pineda & Paul Goldsmith. They both showed me how fascinating and fun astrophysics is, and helped me find my way back to astrophysics in a time of doubt and uncertainty. I am forever grateful for all their help and guidance over the years, and am glad to call them friends.

I am grateful for my friends, and all that time spent not in my office in Cahill, who kept me sane over the years. In particular, the great sports dynasties of *the Fightin' Pinecones* and *the Coors Party Train Disaster*, the perfectly adequate athleticism of which were always an inspiration. My once-roommate and always-great travel companion, Vatsal Jhalani, and the men of Glen Arbor and Layton St., John Rodli, Phil Montoya, Kyle Mickelson, Connor McCann, and Kirk Nilsson, all are owed particular thanks, for putting up with my odd schedule and hobbies, and for being great guys to spend my twenties in the company of.

ABSTRACT

To understand the night sky is to understand how galaxies form their stars. Cosmological zoom-in simulations, which self-consistently evolve a small number of galaxies at very high resolution by embedding them within a fully cosmological box, have evolved over the last 25 years to a level of realism where they can begin to tackle questions of spatially resolved star formation within galaxies. Whereas a decade ago simulations faced difficulty in matching even global properties of observed galaxies (e.g., the ratio of stellar mass to total halo mass), the state of the art is now able to meaningfully recover resolved quantities in galaxies that were not put into the simulations by hand (e.g., the Kennicutt-Schmidt star formation scaling relation).

The research presented in this thesis seeks to understand how the physics of star formation and stellar feedback from massive stars shape and regulate the interstellar medium (ISM) *within* galaxies. Particularly, the focus lies on the scale of the largest coherent structures in galaxies–the disk scale height. To explore these physics, the cosmological zoom-in simulations of the Feedback in Realistic Environments (FIRE) project (Hopkins, Kereš, et al., 2014; Hopkins, Wetzel, et al., 2018) are used.

The chapters of this thesis explore various topics in spatially resolved star formation, including: the Kennicutt-Schmidt relation (Schmidt, 1959; Kennicutt, 1998), an empirical relation between gas surface density and star formation rates, in the FIRE-1 simulations (Orr, Hayward, Hopkins, et al., 2018), including an examination what set the extent of the star-forming disks in the simulations (i.e., what causes star formation to *fire* up in the outskirts); an examination of the observational method of analyzing stacks of galaxy observations, finding that temporal variations in spatially resolved star formation rates *within* individual galaxies were more than enough to bias stacking analysis of star formation rate profiles; a semi-analytic model of non-equilibrium star formation rates, relating to the competition between the feedback timescale associated with star formation and local dynamical times (Orr, Hayward, and Hopkins, 2019), which explores this as a source of scatter in the Kennicutt-Schmidt relation; and finally, investigating how gas velocity dispersions and star formation rates relate in FIRE-2 Milky Way-mass disk galaxies, exploring whether or not feedback is primarily driving the velocity dispersions in galaxies, and how quickly local patches can self-regulate with star formation (Orr et al. *in prep.*).

PUBLISHED CONTENT AND CONTRIBUTIONS

Orr, M. E., Hayward, C. C., & Hopkins, P. F. (2019) Monthly Notices of the Royal Astronomical Society 486, 4724
DOI:10.1093/mnras/sty1241
MEO conceived the project, conducted the science analysis and wrote the manuscript.

Orr, M. E., Hayward, C. C., Hopkins, P. F., et al. (2018) Monthly Notices of the Royal Astronomical Society 478, 3653
DOI:10.1093/mnras/sty1241
PFH and MEO conceived the project. MEO conducted the science analysis and wrote the manuscript.

Orr, M. E., Hayward, C. C., Nelson, E. J., et al. (2017) Astrophysical Journal 849, L2
DOI:10.3847/2041-8213/aa8f93
MEO and CCH conceived the project, coordinating with EJN. MEO conducted the science analysis, and wrote the manuscript.

Orr, M. E., Pineda, J. L., & Goldsmith, P. F. (2014) Astrophysical Journal 795, 26
DOI:10.1088/0004-637X/795/1/26
PFG and JLP took and reduced the HERSCHEL data. MEO conducted the science analysis, and wrote the manuscript.

TABLE OF CONTENTS

LIST OF ILLUSTRATIONS

LIST OF TABLES

FORWARD

At the end of graduate school, I have found that it was a rather circuitous route to get here. It was not a given that I would become a theoretical astrophysicist in the least. Had I been asked what I was going to be in the Fall of 2010, my response would be been, without hesitation, a "Rocket Scientist". Over the ensuing decade, I kept the scientist part, but moved in half-steps from the practical, albeit highly esoteric, work of astronautical engineering towards astrophysics. This thesis represents the culmination of that journey from engineer to scientist. I think, however, that the reader would enjoy knowing the fall from grace, required to make a theorist, that took place.

Arriving at the University of Southern California (USC) for college, a whole twenty-five-minute drive away from home in leafy La Cañada Flintridge, California, I was excited to study astronautical engineering. There was not a tremendous amount of thought that had gone into the decision. I feel now that I had inexorably fell into it- after all, I had grown up with countless friends whose parents had calculated launch windows for Mars probes or designed high-gain antennas for deep space missions, visited Caltech's NASA Jet Propulsions Laboratory (JPL) on what were effectively annual school-sponsored scientific pilgrimages, and somehow had gotten to building air-pressurized water rockets from parts cobbled together from soda bottles and OSH/Harbor Freight tools. Rockets were cool, space was captivating, and of course I was going to major in astronautics.

I was not a great student in high school. But I did enjoy my science and math classes. My chemistry and physics classes were the most interesting. I had taken well to learning that the world had rules, and by following them you could build neat things. Reflecting back on it, I am surprised that I did not fall in with the kids in the robotics club, jumpstarting my whole arc through engineering. I was more interested in hanging out with my friends, playing videogames, hosting frequent LAN parties, and generally just being a teenager. It was probably better for me.

In college, however, I was a great student, at least by my standards. I just *loved* my first couple of courses, especially ASTE101 with Dr. Anthony Pancotti. I was calculating orbits for imaginary missions to Ganymede, learning about rocket staging and the different kinds of rocket motors. That class lit a fire under me that had not been there before. I got my first job with Dr. Pancotti, working for the

Air Force Research Labs' Collaborative High Altitude Flow Facility (CHAFF) on campus in the Rapp Research Building (RRB). It would be my first experience with research, and arguably the most important. I spent three years there, with (the future Dr.) Matthew Gilpin, trying to melt Boron with the Sun and develop far-out in-space propulsion concepts. I do not think any other person, or experience, went so far to convince me that research was what I wanted to do in life.

During this time, I fell into the USC Rocket Propulsion Lab (RPL)[1] also housed in RRB. Though CHAFF may have shaped me into a researcher, "rocket lab" gave me a family at college in people like Julia Levy and Turner Topping, and taught me that I could build anything I wanted, provided that there was some scrap material lying around, and the lathe and mill were powered. Under Bill Murray (III) and Alec Leverette, the first two years of USC were a whirlwind of trips to the deserts near and far, late nights getting things unstuck or laid-up, and seeing some incredible flight vehicles go up[2]. Though I would leave rocket lab in my junior year, the friends I made and the things I learned would stick with me for the rest of college, and my life.

Sophomore and junior years, I had decided that my technical electives for astro-nautical engineering would be astronomy courses. I had taken the honors series of freshman physics courses with Dr. Gene Bickers, who had really opened my eyes to how enjoyable and varied the topics of physics could be. So, going through a course on the solar system, and one on astrophysics, I was hooked. I got mixed up doing helioseismology work with Dr. Ed Rhodes at the Mt. Wilson Observatory (the 60' solar tower), and that was really the first astronomy work that I did. I spent the summer between my sophomore and junior years variously in CHAFF and up Mt. Wilson. On the mountain, I was learning Bash, running the dome and its instruments, and taking long naps.

Around this time, I had begun to lose faith in the idea that I wanted a job in aerospace. My friends from rocket lab were graduating, and the jobs they got terrified me. My friends had to know their stuff day in and day out, and not fly by the seat of their pants from one project to the next like I had been doing in CHAFF and at Mt. Wilson. But I was not quite ready to abandon engineering altogether. I had it in my mind that I needed a "practical degree". And so, instead of going for astronomy, I took the half-step to physics (with an astronomy minor).

---

[1]This name was indeed a joke on NASA's JPL, since the founding students had thought that the "Jet" part was a bit disingenuous.

[2]A few even came down on parachutes.

Late in my junior year at USC, I realized that it was rather hard to get a degree in both engineering and physics at the same time in four years. After much agonizing, but with my father's encouragement, I dropped my astronautics degree[3]: I was committed. I wanted to go to graduate school in physics, or maybe astronomy.

The next summer, I got an internship at JPL, with Drs. Paul Goldsmith and Jorge Pineda studying the Taurus molecular cloud. I learned more physics of the interstellar medium that summer than I ever have since. It also required me to actually learn how to code, and write a scientific paper[4]. I got to walk the lab in thought, and watch second-string rovers practice on dusty mounds of rock in the Arroyo Seco. It was just great for someone dipping their toes into theory research.

Returning to campus in my last year of undergrad, I somehow convinced myself that though I loved physics, especially astrophysics, I needed to do something "practical". So I threw myself at nanophotonics. Sure that this was what I was going to do in graduate school, I took an EE course on the subject, wrote up an NSF graduate fellowship proposal on it, and applied to every graduate school as an applied physicist. I had never set foot in a nanophotonics lab, much less an optics lab. Much to my surprise, I got into Caltech's Applied Physics graduate program amongst other schools.

All the prospective graduate school visits during my senior spring term excited me to no end. Though I look back increasingly fondly on my time at USC now, in the moment I was very happy to be 'called up to the majors' in terms of the schools I was considering for my Ph.D. After much debate with my partner at the time, we settled on going to Caltech together for our Ph.Ds.

Graduating USC that May, with an NSF Graduate Research Fellowship in hand (for a proposed nanophotonics project), and headed up the 110 to Pasadena in the fall, I was on top of the world. After graduation, we headed off on a family trip, which would then become a trip with friends, across Northern and Central Europe. Two weeks into the adventure, I said farewell to my family in Copenhagen. I also said goodbye to my father for the last time, but I did not know it then. As we landed in Boston for the last leg of the trip, a weeklong visit in Rhode Island, I learned that my father had unexpectedly passed away during the night while I was in the air.

---

[3]With all my newfound time, I took a table tennis course, and a ballroom dance class with my college girlfriend.

[4]Though it took the rest of my senior year, and a bit into the beginning of graduate school, a paper did eventually come of it: Orr, Pineda, et al. (2014).

The fallout would cover much of the first two years of graduate school. Arriving at Caltech that fall, I found myself in misery. The light that I had from undergrad was snuffed out, and I struggled through courses. My relationship fell apart. On top of all this, I realized that I truly hated cleanrooms. They are cold, inhospitably dry, without Wi-Fi or cell service several floors underground, and have the most awful spectrum of yellow lights. This meant, amongst other things, that nanophotonics was not for me. I was adrift in the sea of graduate school.

With some encouragement, I reached out to my old mentors at JPL, inquiring if they knew anyone down on campus that was doing astronomy. It just so happened that Dr. Pineda was co-leading a Keck Institute for Space Sciences (KISS) workshop on "Bridging the Gap: Observations and Theory of Star Formation Meet on Large and Small Scales" the next month. Jorge invited me to come to the whiskey hour at the workshop, and meet the people attending. There, I first met my Ph.D. advisor, Dr. Philip F. Hopkins, whom I later reached out to so as to arrange a chat about his research; and of course, whether or not I could do a small project with him.

In the coming weeks and months, that small project became my study of the spatially resolved Kennicutt-Schmidt relation in the FIRE (Feedback in Realistic Environments) simulations, which would take up a large fraction of the early years of graduate school (Orr, Hayward, et al., 2018). Slowly, I dragged my way back to a healthy mindset. In fits and starts[5], I learned more about the simulations, how to work with them, and how to run them. I even switched from applied physics to physics, mostly symbolically, but with the (false) hope that it would save me taking a few courses. I embraced being a theorist, with only small fits of rebellion: I got certified in the machine shop, which I maintain makes me the first theorist in physics in a very long time to do so, and took up fine woodworking.

The rest of this thesis tells the story from there of the burgeoning theorist, who was once an engineer and still a bit of one at heart.

Matthew Orr   May 2019
                                                                                              Caltech, Pasadena, CA

---

[5]One of the first times that I brought a plot to Phil, he just asked, "what did you make this with?" I had made it using Matlab, and it was just so ugly that he could not focus on anything remotely scientific about the figure. He implored me to try using Python to plot things.

C h a p t e r   1

INTRODUCTION

The Big Picture: Galaxies and Their Cosmological Context

Across the vast majority of the history of the Universe, gravity has been the dominant force. That hegemony began during the Dark Age of the Universe, between decoupling approximately 400,000 years after the Big Bang, which gave us the Cosmic Microwave Background, and the time of the first stars, around 400 Myr into the history of the Universe (Abel et al., 1998; Bromm et al., 1999). Recent observations suggest that we may indeed be living through interesting times (Riess, Filippenko, et al., 1998): the presumed largest energy component of the Universe, the source of which remains a theoretical mystery, Dark Energy, is now taking the mantle from gravity, causing the expansion of the Universe to accelerate, rather than continue to slow. Gravity held the crown for about 13.3 Gyr.

In this time, gravity worked towards a singular purpose: collapsing structures on scales large and small, amplifying the initial density perturbations of the Universe handed down shortly after the Big Bang. This is a hierarchical process, where the largest structures begin to collapse first, with structures within them beginning to condense thereafter in a nested fashion. And so, a knotted web of (dark and baryonic[1]) matter begins to collapse initially (Abel et al., 1998). From those cosmological scales, gas and dark matter is drawn into the densest regions. These are the seeds of galaxies, that grow through cosmic time as gas and dark matter fall into them, and gas is processed into stars (Silk, 1983; Bromm et al., 1999; Schaye et al., 2015). Figure 1.1 shows a slice of a large-box simulation, in which galaxies have formed and evolved in the filamentary matter overdensities in line with this framework of hierarchical structure formation. Through the 1970s, much of our understanding of galaxy evolution and populations stopped with the formation of structure in the Universe, with a failure to understand why the galaxy mass function today failed to match the self-similar solution of hierarchical collapse (Press et al., 1974).

The fields of galaxy formation and evolution have experienced a renaissance in

---

[1]In astronomical contexts, baryonic matter encompasses not only the High Energy physicist's baryons (composite particles, e.g., protons and neutrons) but also all the other particles of the Standard Model including leptons, cf., the astronomer's definition of "metals".
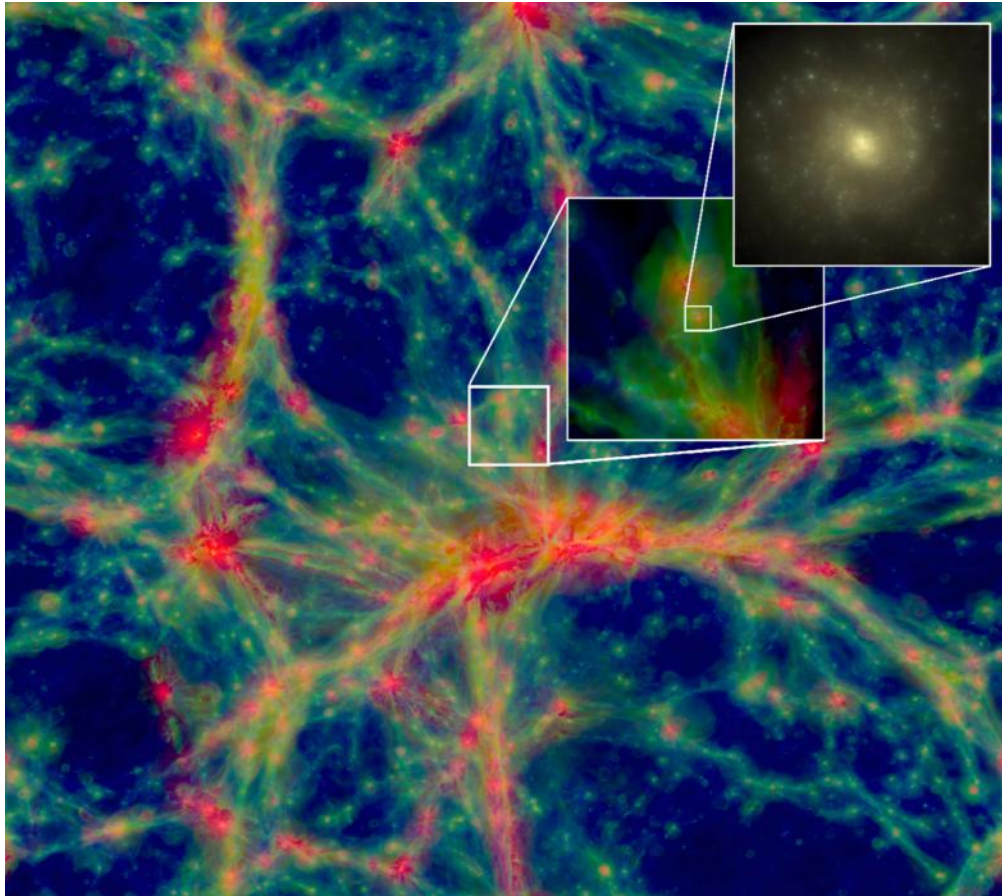
Figure 1.1: A $100\,\mathrm{Mpc} \times 100\,\mathrm{Mpc} \times 20\,\mathrm{Mpc}$ slice of a large-box simulation, showing the filamentary structure of the Universe at $z = 0$. Color hues and intensities encode gas temperature and density (red–hotter, blue–cooler). Insets show a 10 Mpc region, and a nested 60 kpc region, in which a $10^{10}\,\mathrm{M}_\odot$ stellar mass galaxy has formed. Overdensities in the volume are the sites of galaxies, with gas inflows and mergers growing them in time. Figure taken from Schaye et al. (2015, their Figure 1). Reproduced with permission of MNRAS.

the last two decades, as cosmologists pinned down the geometry and relative composition of the Universe following the careful work of the *Wilkinson Microwave Anisotropy Probe* and *Planck* satellite missions, combined with work on the distance-redshift relation from Type Ia SNe, abundances and clustering of galaxies (e.g., baryon acoustic oscillations), and constraints on the present expansion rate of the Universe (Hubble parameter H_0) (Hinshaw et al., 2013; Planck Collaboration et al., 2016; Riess, Macri, et al., 2016). The remaining uncertainties in the fundamental cosmological parameters, for the purposes of understanding galaxy formation and evolution, are largely inconsequential.

Baryons Don't Just Sit There: Physics in Galaxies

Considering the whole volume of the Universe, gravity has ruled supreme on-average. There are and have always been, however, pockets of resistance. Baryonic matter fought back, and as in the cases of supernovae, sometimes quite vigorously.

So, in order to understand the process of galaxy evolution on smaller scales than the cosmological web, we need to follow the hierarchical collapse of dark matter and baryons down to scales within galaxies. Here, gravity is not the only force involved, and baryonic processes can greatly affect the dynamics of matter. Within galaxies, physical mechanisms like photoionizing radiation, winds, and supernovae (together broadly known as feedback), the majority of which are associated with recently formed, massive stars, fight gravitational collapse on length-scales of kiloparsecs, e.g., spiral arm scales, down to less than a parsec, e.g., clumps within molecular cloud complexes (Silk, 1997; Matzner, 2002; Shetty and Ostriker, 2008; Faucher-Giguère et al., 2013; Stinson et al., 2013; Hopkins, Kereš, et al., 2014). This involves a tremendous bridging of scales, from the largest coherent structures inside of galaxies down to the photospheres massive stars providing the feedback, and poses challenges to even the most imaginative theorist or competent numericist in addressing with theory or simulations (Somerville et al., 2015).

Fundamentally, understanding how galaxies evolve in our Universe, beyond the hierarchical collapse out of the cosmic web, reduces to the questions: How does star formation proceed *in* galaxies, and what are the effects of star formation *on* galaxies?

Sweating the Small Stuff: Grid-Scale Baryonic Physics in Simulations

Large-volume cosmological galaxy simulations, like Illustris or EAGLE (Vogelsberger et al., 2014; Schaye et al., 2015; Pillepich et al., 2018), whose primary goal

is to match population statistics of galaxies and cosmological structure on 100 Mpc scales, necessarily treat the complex baryonic physics of galaxies at the grid scale, in their cases, a few kiloparsecs. For dwarf galaxies, and galaxies at high redshift, in which all of the star formation essentially occurs in a single star-forming region, treating star formation as a single kpc-scale black/closed box is fairly successful at predicting star formation histories and chemical abundances (Romano et al., 2013, Escala et al. *in prep.*). All simulations ultimately require there to be rules applied at the resolution scale, that account for the physics being simulated. These rules either parameterize our ignorance through fudge factors, or use fits to the results of simulations conducted on yet smaller scales. In these simulations, they tune their galaxy physics to match galaxy-scale observations of things like Kennicutt-Schmidt or the stellar mass–halo mass relations. The fudge factors in the large-box simulations treat galaxies as black boxes that take in cosmological gas inflows, and appropriately process it into a mass of stars and outflows. They can say very little about the internal structure of galaxies themselves below a few kiloparsecs, or anything about the process of star formation in molecular clouds.

Cosmological zoom-in simulations are situated between the large-box simulations that attempt to model a non-negligible fraction of a Hubble volume, and ultra-high-resolution simulations of individual star-forming clouds or single stars. In a real sense, they were a missing link between the scales at which much of the consequential physics in the interstellar medium (ISM) occurs and cosmological scales. Zoom-in simulations take a mid-sized cosmological volume (a few dozen Mpc) that is run with only dark matter (so called DMO, Dark Matter Only, simulations), in which a desired dark matter halo forms, e.g., a 10^{12} M$_\odot$-massed halo in which a Milky Way-like galaxy is likely to form. Once such a halo is found, the simulation is then reset to an early time in the Universe (say, $z \approx 30$), and populated with baryonic matter at high resolution in the region (with a little breathing room) that will collapse into that galaxy by $z = 0$. And so, these simulations are able to implant highly resolved galaxies in their cosmological contexts to produce realistic artificial galaxies (Hopkins, Kereš, et al., 2014; Wetzel et al., 2016; Hopkins, Wetzel, et al., 2018). Zoom-in simulations are thus able to take the results of yet-more-highly resolved simulations as rules at the resolution scale. For the FIRE-2 Milky Way mass simulations, this scale is adaptive with the local gas density, but the minimum force softening is now sub-parsec (Hopkins, Wetzel, et al., 2018). And their results on kiloparsec-scales, can be taken to inform and calibrate the large-box simulations.

Questions That Keep You (Me) Up at Night About Star Formation

My research, during the course of my graduate studies, has focused on aspects of star formation processes and their effects *within* galaxies, on kiloparsec (kpc) scales. Several questions have arisen repeatedly in each of my published, and in progress, works. In one form or another, they have been:

1. How does the local rate of star formation scale with the local properties of the ISM within galaxies?

2. To what extent is star formation an active process versus a passive one, i.e., does star formation drive or regulate itself, and the ISM writ large, or is it primarily subject to the whims of galaxy structure and ISM dynamics.

3. On what length- and timescales is it appropriate to ask these questions? On kiloparsec-scales the ISM has turbulent momentum and an average density which may inform, be affected by, or drive star formation on the timescale of galactic dynamical times, but down at the parsec scale things are different. Stellar evolution and the properties of the ISM matter only in the direct vicinity of individual (or a few) stars. Scaling relations like Kennicutt-Schmidt are simply not well defined on that spatial scale, or over timescales much shorter than a galactic dynamical time.

These questions rake at the mystery of star formation in galaxies from several directions: the empirical question of simply, what does star formation scale with; questions of causality, what can or ought to be considered driving the evolution of galaxies; and semantic arguments relating to what meaning star formation scaling relations can be held to have under which circumstances (e.g., what is the *efficiency* of star formation?).

This last question is particularly vexing, as observers rarely, perhaps only in the star-forming regions in the nearest dwarf companions to the Milky Way, count up young stellar objects to get star formation rates (SFRs). They measure fluxes in different wavelength bands. These fluxes are then connected, through a chain of reasoning with a sturdy physical basis, to the properties of the unresolved stellar populations within spatially resolved regions of galaxies. And from this, an estimate for the mass of young stars present (which, owing to their short lifetimes, must have formed recently). So there is an inference of what UV flux (or Hα, 24 μm, radio flux, etc.) in a kpc-sized pixel corresponds to what mass of young stars and thus star

formation rates. But again, the issue often at hand is the fact that observers measure something that is *correlated* with star formation, but not star formation itself; and so, the door is open to ask when do those fluxes not mean what an astronomer thinks they mean.

The issue of connecting what is observable, fluxes from the far reaches of the Universe, with the "ground truths" of the conditions within galaxies, is not reserved solely to star formation rates. The issues calibrating star formation rate tracers are nearly one and the same with those calibrating tracers of dense[2] gas in galaxies.

A theorist, however, has a perfect model universe. Galaxies are well defined. Star formation rates are the rate at which stars form. And dense gas masses are the amount of gas of at least some density in a galaxy. We have no Humean[3] uncertainty in our knowledge of our models or simulations. Moreover, simultaneous 'observations' of both the gaseous and stellar components of galaxies are easy[4].

The Kennicutt-Schmidt (or is it Schmidt-Kennicutt?) Relation

At least since the work of Schmidt (1959), but definitely since that of Kennicutt (1989), astronomers and astrophysicists have framed much of the star formation process *in galaxies*, i.e., on scales > 100 pc, as having something to do with the Kennicutt-Schmidt (KS, or Schmidt-Kennicutt, SK) relation (Bigiel et al., 2008; Leroy, Walter, Brinks, et al., 2008; Dib, 2011; Ostriker et al., 2011; Faucher-Giguère et al., 2013; Leroy, Walter, Sandstrom, et al., 2013; Shetty, Kelly, et al., 2014; Orr, Hayward, Hopkins, et al., 2018, among others). The Kennicutt-Schmidt relation is just the relationship between the surface density in dust and gas in a galaxy, and the surface density of star formation. Canonically, it was found by Kennicutt (1998) to have a scaling of $\dot{\Sigma}_\star \propto \Sigma_{\mathrm{gas}}^{1.4}$ (see Figure 1.2). The exponent of this power law, and any other dependencies on galaxy quantities like metallicity, gas fraction, etc., depend to varying extents on the tracers compared between the gas surface densities, e.g., only molecular vs. atomic hydrogen, and star formation rates, e.g., Hα vs. UV fluxes, each having different averaging timescales (Bigiel et al., 2008; Leroy, Walter, Sandstrom, et al., 2013; Dib, Hony, et al., 2017; Orr, Hayward, Hopkins, et al., 2018).

---

[2]Dense, here, is quite diffuse in human terms. Throughout this thesis, dense gas is taken often to encompass any gas denser than $n_{\mathrm{H}} = 1$ cm^{-3} (atoms of Hydrogen per cubic centimeter).

[3]David Hume (1711–1776), Scottish philosopher, economist, and historian. *A Treatise of Human Nature (1739–1740).*

[4]As long as you have included both in your model or simulation.
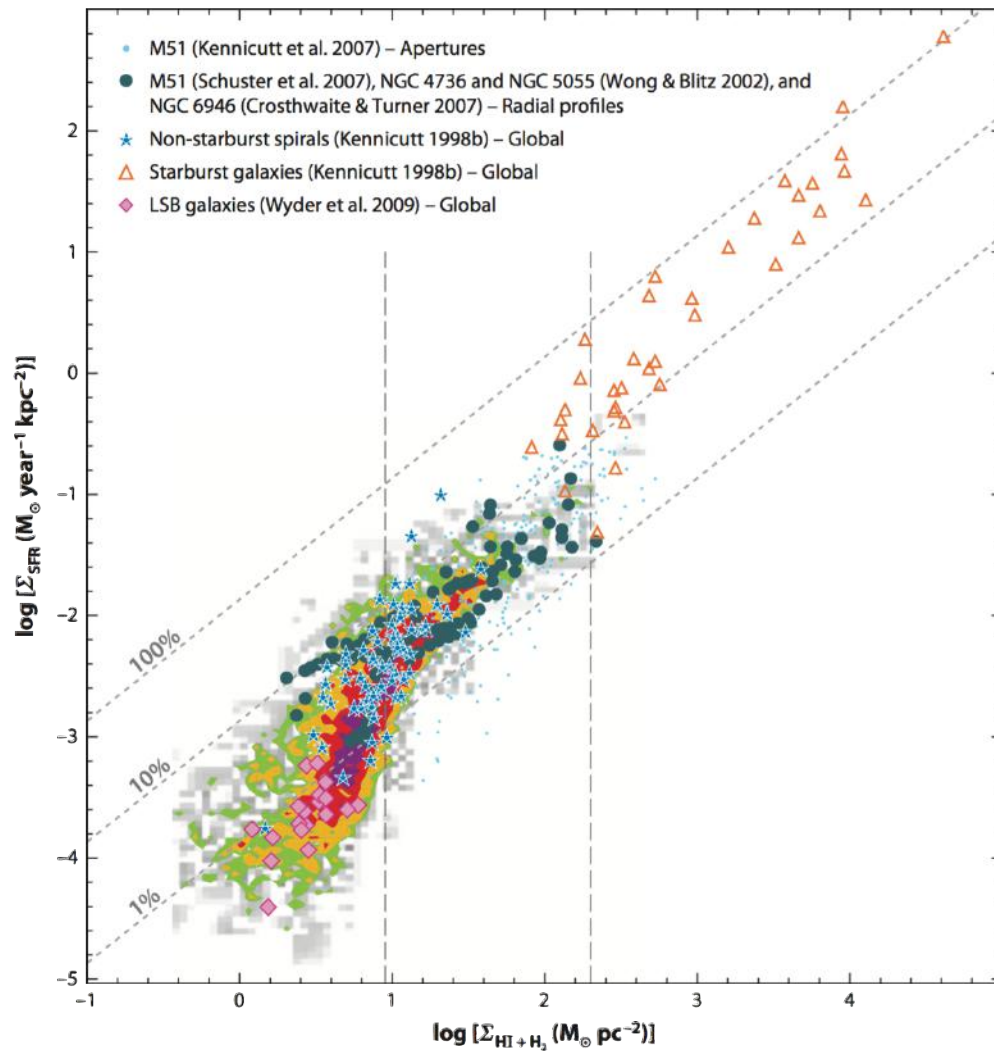
Figure 1.2: Kennicutt-Schmidt relation between star-formation-rate (SFR) surface densities and total (atomic and molecular) gas surface densities for various sets of measurements (from Bigiel et al. 2008). Regions colored gray, green, yellow, and red show the distribution of values from measurements of subregions of SINGS galaxies. Other points represent a variety of star formation profiles and integrated galaxy observations from the labelled references. The three dotted gray diagonal lines extending from lower left to upper right reflect a constant global star formation efficiency. Figure taken from Kennicutt and Evans (2012). Reproduced with permission of Annual Reviews.
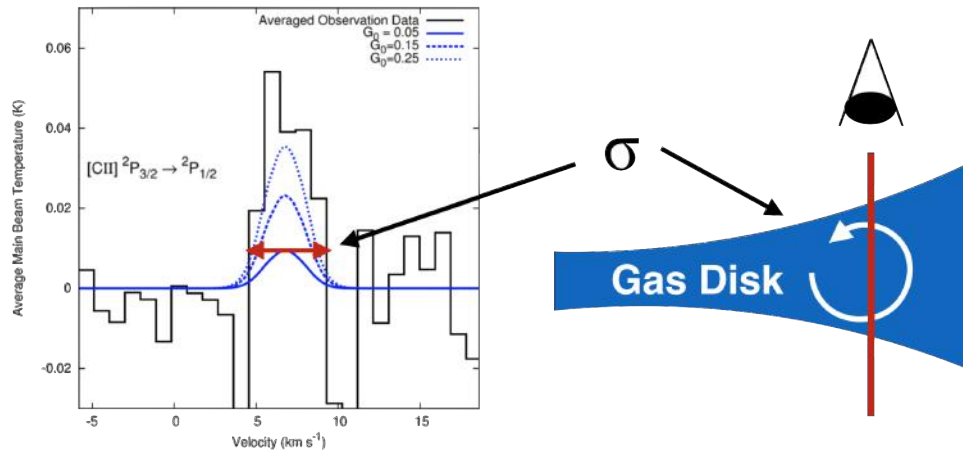
Figure 1.3: Observers and theorists often refer to different things when discussing velocity dispersions. Observers (left panel) talk of linewidths in gas emission or absorption lines, then connected to conditions in the gas, whereas theorists (right panel) think of Gaussian velocity dispersions and gas scale heights in galaxies or clouds directly. Left panel figure taken from Orr, Pineda, et al. (2014). Reproduced with permission.

As a scaffold for understanding, and defining, star formation processes in galaxies, the Kennicutt-Schmidt relation has helped astronomers address many aspects of star formation in galaxies and continues to be an intense area of research, though these days primarily beyond the first order, comparing the subdominant dependences of, e.g., metallicity, gas fraction, etc., on the star formation rate (Leroy, Walter, Sandstrom, et al., 2013; Orr, Hayward, Hopkins, et al., 2018; Gallagher et al., 2018). Understandably, all of the proceeding chapters of this thesis relate to the Kennicutt-Schmidt relation in some way or another.

Linewidths, Velocity Dispersions, and Turbulence, Oh My!

Observers and theorists often run in different circles. Unsurprisingly, their vocabularies can be slightly different. When discussing velocity dispersions, observers are often speaking in terms of linewidths of gas emission or absorption lines like, e.g., the CO $J = 1 \rightarrow 0$ or the CII $^2P_{3/2} \rightarrow^2 P_{1/2}$ transitions (e.g., Combes et al., 1997; Bolatto, Leroy, et al., 2008; Goldsmith et al., 2008; Pineda et al., 2010; Wilson et al., 2011). In this case, line broadening effects, beyond intrinsic linewidths, arise from thermal or dynamical properties of the gas along the line of sight that is emitting or absorbing light from that atomic or molecular transition. From this, observers infer the properties of the gas components of interest. The caveat here is that observations

are only on solid ground when talking about the thermal or dynamical state of *that particular component of the ISM*, which corresponds to that emission/absorption line. Theorists, on the other hand, often think directly of the dynamical structure of the gas, i.e., the true velocity dispersions of particles in a 1-D or 3-D sense (e.g., Toomre, 1964; Dib, Bell, et al., 2006; Krumholz et al., 2016; Orr, Hayward, and Hopkins, 2019). And often, careful modeling of which components would be emitting or absorbing at particular transitions is not done.

This is leaving out entirely the difficulties of translating integrated intensities to total gas masses, etc. For example, as of the time of writing this thesis, there continues to exist a lively debate in the fields studying galaxy formation and evolution, star formation, and the ISM about how to convert integrated line intensities of CO to molecular gas masses in galaxies (see Bolatto, Wolfire, et al., 2013, for a recent review).

So, there is a gulf between observations and theory, which one must be careful to navigate when interpreting either observations, or forecasting observables from simulations and models. Throughout this thesis, unless otherwise noted, I take the velocity dispersions (σ) to mean true dispersions in velocity of gas in the pixels discussed, and not as linewidths, as I have not published any linewidth predictions from the FIRE simulations. Conveniently, this means that those velocity dispersions can, in the context of galaxy disks and supersonic turbulence, to be directly related to the gas disk scale heights (though $H \approx \sigma/\Omega$, where Ω is the orbital dynamical time) and the local Mach number ($\mathcal{M} = \sigma/c_s$, where c_s is the local sound speed).

1.1 Thesis Outline

The chapters in this thesis assault the questions posed, from how does star formation scale with environment to what its roles in galaxies are. All of these investigations, using both the FIRE simulations and semi-analytic models, ask to what extent, and on what scales, can we consider the scalings of star formation meaningful in some sense. The thesis is organized as follows:

- **Chapter 2**: Adapted from Orr, Hayward, Hopkins, et al. (2018), this chapter explores the Kennicutt-Schmidt relation in the original FIRE simulations (Hopkins, Kereš, et al., 2014). At the time, these simulations were among the most highly resolved (both spatially and by particle mass) cosmological zoom-in simulations. This allowed us to investigate in great detail how star formation scaled on kpc-scales in the simulations, and the connections

with observations. The chapter explores how well various scalings predict the star formation in the simulations, and touches lightly on the question of star formation's role in galaxies more broadly. The work of this chapter, particularly in understanding what *fires* up star formation in the simulations, resulted in a collaboration with the MaNGA survey, studying star formation thresholds in galaxies using their spatially resolved data (Stark et al., 2018).

- **Chapter 3**: This chapter is taken from Orr, Hayward, Nelson, et al. (2017), and is primarily a fairly specific critique of an oft-used observational technique, stacking many similar images of different galaxies at high redshift, in order to push down on signal-to-noise limits and be able to say something about galaxy properties or outskirts at $z \gtrsim 1$. It investigates stacked star formation rate profiles in the FIRE galaxies at $z \sim 1$, and follows the observational techniques of Nelson et al. (2016). Specifically, this letter addresses the resulting physical interpretations for galaxies at high redshift, and how one must be careful to not bias their interpretations when taking cuts of galaxy populations from scaling relations like the star formation main sequence.

- **Chapter 4**: Unlike the other chapters of this thesis, this entry is not a direct application of the FIRE simulations, but rather a semi-analytic toy model of time-dependent star formation in galaxy disks, borrowing from Orr, Hayward, and Hopkins (2019). It, being an excursion from simulations into semi-analytic models, investigates the *dynamical* evolution of a feedback-regulation model, closely related to the frameworks of both Ostriker et al. (2011) and Faucher-Giguère et al. (2013). This chapter takes a more substantive stab at the second question posed: what is the role of star formation in galaxy disks? In an evasive answer, star formation is both a passive respondent to the ambient conditions, and an active driver of the state of the gas in galaxies. It responds to the local state of the ISM (set by, e.g., past star formation, cosmological inflows, or galactic structure), and then moves to bend its surroundings to its will through processes of stellar feedback. Like the phoenix, star-forming regions rise from the ashes of their predecessors, and die in a combustion of their own making (feedback, both as supernovae and radiation pressure/winds), existing in galaxies in a continual cycle of death and renewal. In a related fashion, this chapter addresses the question of on what timescales does it make sense to consider something like the Kennicutt-Schmidt relation within galaxies.

- **Chapter 5**: This chapter consists of as-of-yet unpublished work using the FIRE-2 simulations. These simulations are the successor to the FIRE simulations, improving upon the numerics, mass resolution, and feedback physics implemented in the original suite. Here, we explore the relationship between the gas velocity dispersions, in both the neutral and cold and dense gas, and the star formation rates on ~kpc-scales within the FIRE Milky Way mass spiral galaxies at late times $z \lesssim 0.1$. This work stabs at the first two questions posed: scalings for and the role of star formation with respect to the structure of the ISM within galaxy disks. Only briefly does it become philosophical about timescales of meaningfulness for star formation scalings. Particularly interesting for observers, perhaps, is that the erstwhile flat distribution of velocity dispersions in gas, for a ~ 3 dex range in star formation rates, belies a consistent structure of gas properties scaling with star formation rates. Self-regulation appears to rule galaxy disks, their gas component demanding marginal stability against gravitational fragmentation and collapse. Though the gaseous disks of these disk galaxies remembers past star formation and feedback, that memory becomes quite hazy when searching more than a single galactic dynamical time back.

Together, this opus of work constitutes both the culmination of a little more than four years of work with Phil Hopkins and the broader FIRE collaboration, and a coherent effort in understanding star formation processes within galaxies on kiloparsec-scales, from the perspective of cosmological zoom-in simulations and semi-analytic models.

References

Abel, T., Anninos, P., Norman, M. L., & Zhang, Y. (1998) ApJ 508, 518

Bigiel, F., Leroy, A., Walter, F., Brinks, E., de Blok, W. J. G., Madore, B., & Thornley, M. D. (2008) AJ 136, 2846

Bolatto, A. D., Leroy, A. K., Rosolowsky, E., Walter, F., & Blitz, L. (2008) ApJ 686, 948

Bolatto, A. D., Wolfire, M., & Leroy, A. K. (2013) ARA&A 51, 207

Bromm, V., Coppi, P. S., & Larson, R. B. (1999) ApJ 527, L5

Combes, F. & Becquaert, J.-F. (1997) A&A 326, 554

Dib, S. (2011) ApJ 737, L20, L20

Dib, S., Bell, E., & Burkert, A. (2006) ApJ 638, 797

Dib, S., Hony, S., & Blanc, G. (2017) MNRAS 469, 1521

Faucher-Giguère, C.-A., Quataert, E., & Hopkins, P. F. (2013) MNRAS 433, 1970

Gallagher, M. J. et al. (2018) ApJ 858, 90, 90

Goldsmith, P. F., Heyer, M., Narayanan, G., Snell, R., Li, D., & Brunt, C. (2008) ApJ 680, 428

Hinshaw, G. et al. (2013) ApJS 208, 19, 19

Hopkins, P. F., Kereš, D., Oñorbe, J., Faucher-Giguère, C.-A., Quataert, E., Murray, N., & Bullock, J. S. (2014) MNRAS 445, 581

Hopkins, P. F., Wetzel, A., et al. (2018) MNRAS 480, 800

Kennicutt Jr., R. C. (1989) ApJ 344, 685

– (1998) ApJ 498, 541

Kennicutt, R. C. & Evans, N. J. (2012) ARA&A 50, 531

Krumholz, M. R. & Burkhart, B. (2016) MNRAS 458, 1671

Leroy, A. K., Walter, F., Brinks, E., Bigiel, F., de Blok, W. J. G., Madore, B., & Thornley, M. D. (2008) AJ 136, 2782

Leroy, A. K., Walter, F., Sandstrom, K., et al. (2013) AJ 146, 19, 19

Matzner, C. D. (2002) ApJ 566, 302

Nelson, E. J. et al. (2016) ApJ 828, 27, 27

Orr, M. E., Hayward, C. C., & Hopkins, P. F. (2019) MNRAS 486, 4724

Orr, M. E., Hayward, C. C., Hopkins, P. F., et al. (2018) MNRAS 478, 3653

Orr, M. E., Hayward, C. C., Nelson, E. J., et al. (2017) ApJ 849, L2

Orr, M. E., Pineda, J. L., & Goldsmith, P. F. (2014) ApJ 795, 26

Ostriker, E. C. & Shetty, R. (2011) ApJ 731, 41, 41

Pillepich, A. et al. (2018) MNRAS 473, 4077

Pineda, J. L., Goldsmith, P. F., Chapman, N., Snell, R. L., Li, D., Cambrésy, L., & Brunt, C. (2010) ApJ 721, 686

Planck Collaboration et al. (2016) A&A 594, A13, A13

Press, W. H. & Schechter, P. (1974) ApJ 187, 425

Riess, A. G., Filippenko, A. V., et al. (1998) AJ 116, 1009

Riess, A. G., Macri, L. M., et al. (2016) ApJ 826, 56, 56

Romano, D. & Starkenburg, E. (2013) MNRAS 434, 471

Schaye, J. et al. (2015) MNRAS 446, 521

Schmidt, M. (1959) ApJ 129, 243

Shetty, R., Kelly, B. C., et al. (2014) MNRAS 437, L61

Shetty, R. & Ostriker, E. C. (2008) ApJ 684, 978

Silk, J. (1983) MNRAS 205, 705

– (1997) ApJ 481, 703

Somerville, R. S. & Davé, R. (2015) ARA&A 53, 51

Stark, D. V. et al. (2018) MNRAS 474, 2323

Stinson, G. S., Brook, C., Macciò, A. V., Wadsley, J., Quinn, T. R., & Couchman, H. M. P. (2013) MNRAS 428, 129

Toomre, A. (1964) ApJ 139, 1217

Vogelsberger, M. et al. (2014) MNRAS 444, 1518

Wetzel, A. R., Hopkins, P. F., Kim, J.-h., Faucher-Giguère, C.-A., Kereš, D., & Quataert, E. (2016) ApJ 827, L23, L23

Wilson, C. D. et al. (2011) MNRAS 410, 1409

Chapter 2

WHAT *FIRES* UP STAR FORMATION: THE EMERGENCE OF THE KENNICUTT-SCHMIDT LAW FROM FEEDBACK

Orr, M. E. et al. (2018) MNRAS 478, 3653

ABSTRACT

We present an analysis of the global and spatially resolved Kennicutt-Schmidt (KS) star formation relation in the FIRE (Feedback In Realistic Environments) suite of cosmological simulations, including halos with $z = 0$ masses ranging from 10^{10}–10^{13} $M_\odot$. We show that the KS relation emerges and is robustly maintained due to the effects of feedback on local scales regulating star-forming gas, independent of the particular small-scale star formation prescriptions employed. We demonstrate that the time-averaged KS relation is relatively independent of redshift and spatial averaging scale, and that the star formation rate surface density is weakly dependent on metallicity and inversely dependent on orbital dynamical time. At constant star formation rate surface density, the 'Cold & Dense' gas surface density (gas with $T < 300$ K and $n > 10$ cm^{-3}, used as a proxy for the molecular gas surface density) of the simulated galaxies is ~0.5 dex less than observed at ~kpc-scales. This discrepancy may arise from underestimates of the local column density at the particle scale for the purposes of shielding in the simulations. Finally, we show that on scales larger than individual giant molecular clouds, the primary condition that determines whether star formation occurs is whether a patch of the galactic disk is thermally Toomre-unstable (not whether it is self-shielding): once a patch can no longer be thermally stabilized against fragmentation, it collapses, becomes self-shielding, cools, and forms stars, regardless of epoch or environment.

2.1 Introduction

Understanding star formation and its effects on galactic scales has been integral to assembling the story of the growth and subsequent evolution of the baryonic components of galaxies. Observationally, the rate at which gas is converted into stars is characterized by the Kennicutt-Schmidt (KS) relation, which is a power law correlation between the star formation and gas surface densities in galaxies that holds over several orders of magnitude (Schmidt 1959; Kennicutt 1998; see Kennicutt and Evans 2012 for a recent review).

Numerous studies of the KS relation have shown that star formation is inefficient on galactic scales, with only a few per cent of a galaxy's gas mass being converted to stars per galactic free-fall time (Kennicutt, 1998; Kennicutt, Calzetti, et al., 2007; Daddi et al., 2010; Genzel et al., 2010). Understanding what regulates the efficiency of star formation and results in the observed KS relation is therefore key to understanding the formation and dynamics of galaxies. Some authors (e.g., Thompson et al., 2005; Murray et al., 2010; Murray, 2011; Ostriker and Shetty, 2011; Faucher-Giguère et al., 2013; Semenov et al., 2016; Hayward and Hopkins, 2017; Grudić et al., 2018) argue that star formation is *locally* efficient, in the sense that tens of per cent of the mass of a gravitationally bound gas clump within a giant molecular cloud (GMC) can be converted into stars on the local free-fall time, and that local stellar feedback processes–including supernovae (SNe), radiation pressure, photo-heating, and stellar winds–must stabilize gas discs against catastrophic gravitational collapse, thereby resulting in the low global star formation efficiencies that are observed. However, others claim on both theoretical and observational grounds that star formation is locally inefficient, with only of order a few per cent of the mass of clumps being converted into stars on a free-fall time independent of their density (Padoan, 1995; Krumholz and Tan, 2007; Lee et al., 2016).

In either scenario, the KS law is considered to be an emergent relation that holds on galactic scales and results from a complex interplay of the physical processes that trigger star formation and those that regulate it. It has also been argued and observed that the KS relation breaks down below some length- and timescales (Onodera et al., 2010; Schruba et al., 2010; Feldmann and Gnedin, 2011; Calzetti et al., 2012; Kruijssen et al., 2014). Calzetti et al. (2012) found that the KS relation breaks down due to incomplete sampling of star-forming molecular clouds' mass function on length-scales of less than ~ 1 kpc. Feldmann et al. (2012) claim that this breakdown on sub-kpc-scales occurs due to the stochastic nature of star formation

itself. Furthermore, Kruijssen et al. (2014) argue that the various tracers of gas column density and star formation rate surface density require averaging over some spatial and temporal scales; consequently, when sufficiently small length-scales are probed, a tight correlation between the star formation rate surface density and the gas column density should not be observed. Understanding the scales where the KS law holds therefore informs our theories of star formation as well.

On the length-scales where the KS relation does hold, the canonical power law of the total gas relation is $\Sigma_{\mathrm{SFR}} \propto \Sigma_{\mathrm{gas}}^{1.4}$ with Σ_{SFR} being the star formation rate surface density and Σ_{gas} being the total gas surface density (Kennicutt, 1998). However, there has been much debate regarding the power-law index of the relation and its physical origin; the previous literature has found KS relations ranging from highly sublinear to quadratic (Bigiel, Leroy, Walter, Brinks, et al., 2008; Daddi et al., 2010; Genzel et al., 2010; Feldmann et al., 2011; Feldmann et al., 2012; Narayanan et al., 2012; Shetty, Kelly, and Bigiel, 2013; Shetty, Kelly, Rahman, et al., 2014; Shetty, Clark, et al., 2014; Becerra et al., 2014). Some of the disagreement owes to the particular formulation of the KS relation considered, such as whether $\Sigma_{\mathrm{HI+H_2}}$ (total atomic + molecular hydrogen column) or $\Sigma_{\mathrm{H_2}}$ (molecular column alone) is employed (e.g., Rownd et al., 1999; Wong et al., 2002; Krumholz and Thompson, 2007), with the $\Sigma_{\mathrm{H_2}}$ relation typically having slope ~ 1. The relation may in principle also depend on the star formation tracer used (e.g. Hα, far infrared, or ultraviolet). Furthermore, there are questions as to whether the index depends on spatial resolution–even on scales larger than the length scale below which the relation fails altogether–or if there are multiple tracks to the KS relation, each with different slopes across several decades in gas surface density (Ostriker, McKee, et al., 2010; Liu et al., 2011; Ostriker and Shetty, 2011; Feldmann et al., 2011; Feldmann et al., 2012; Faucher-Giguère et al., 2013).

It has also been suggested that the KS relation may evolve with redshift or have a metallicity dependence (Schaye, 2004; Bouché et al., 2007; Papadopoulos et al., 2010; Dib, 2011; Gnedin and Kravtsov, 2011; Scoville et al., 2016). These are not entirely independent quantities, as metallicity generally increases as galaxies process their gas through generations of stars over cosmic timescales. Because the presence of metals results in more efficient gas cooling, and can thus aid in the transition from diffuse ionized and atomic species to dense molecular gas (Hollenbach et al., 1999), Schaye (2004) and Krumholz et al. (2009b) have argued that there is a metallicity-dependent gas surface density cutoff below which the KS relation becomes steeper.
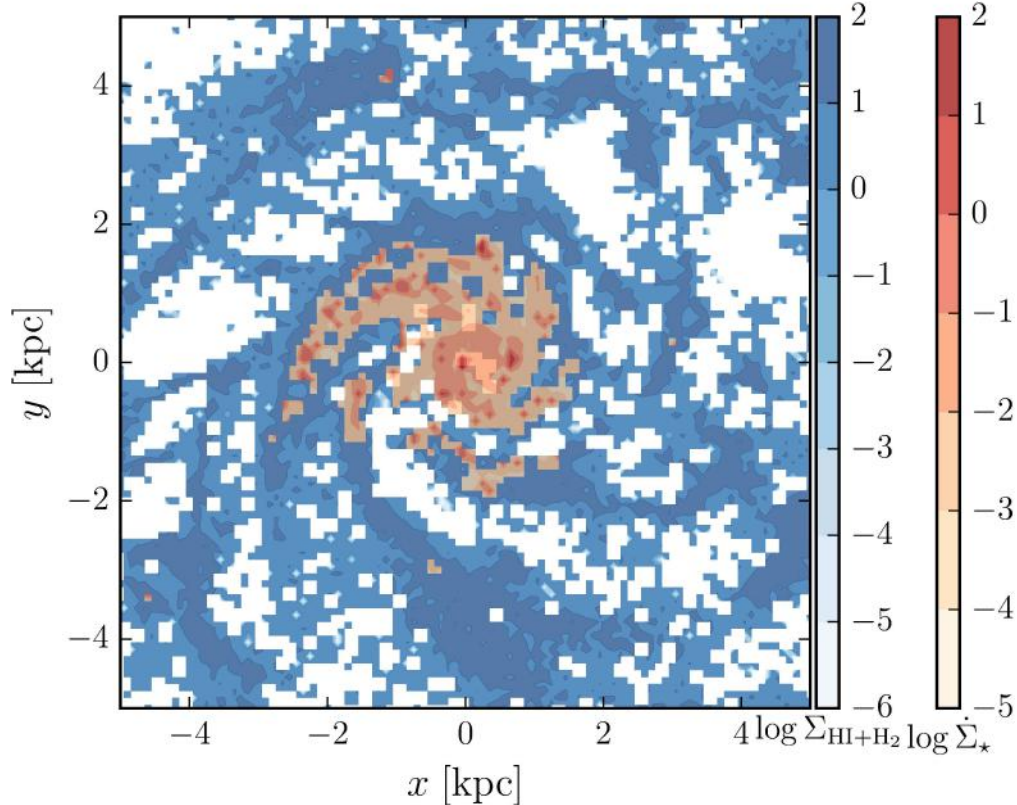
Figure 2.1: Example of one of our maps, made from a Milky Way-mass simulated galaxy at $z \approx 0$ (galaxy **m12i** from Hopkins, Kereš, Oñorbe, et al., 2014), with 100 pc pixels. Neutral hydrogen surface density, Σ_{HI+H_2} [$M_\odot$ pc^{-2}] and instantaneous gas star formation rate $\dot{\Sigma}_\star$ [$M_\odot$ yr^{-1} kpc^{-2}] are colored in blues and reds, respectively. Spiral arms and increasing density towards the galactic core are clearly visible, and the instantaneous star formation rate is seen to closely trace the densest gas structures.

Krumholz et al. (2009b) attribute the dependence to the gas column needed to self-shield molecular gas for a given metallicity. As well gas metallicity has been argued to weakly modulate the specific strength of stellar feedback, as SNe couple slightly less momentum into their immediate stellar surroundings since more of their energy is able to radiate away quickly (Cioffi et al., 1988; Martizzi, Faucher-Giguère, et al., 2015; Richings et al., 2016). Scoville et al. (2016) found evidence of shorter depletion timescales for molecular gas at higher redshifts for galaxies both on and above the star formation main sequence, perhaps due to the rapid accretion required to replenish the gas reservoirs.

Large-volume cosmological simulations often use the KS law as a sub-grid prescription for star formation, both because of the prohibitive computational complexity

of including all of the physics relevant on the scales of star-forming regions, and their inability to resolve even the most massive giant molecular clouds $\sim 10^6$ M$_\odot$ (e.g., Mihos et al., 1994; Springel et al., 2003). Even idealized disk simulations that have resolution on the order of 100 pc, but are unable to resolve a multiphase ISM, employ star formation prescriptions that assume low star formation efficiencies *a priori* or implement KS laws indirectly (Li et al., 2006; Wada et al., 2007; Schaye and Dalla Vecchia, 2008; Richings et al., 2016). It has been shown that assuming a power-law star formation relation on the resolution scale can imprint a power-law relation of identical slope on the galactic scale (Gnedin, Tasker, et al., 2014), demonstrating the importance of employing physically motivated sub-grid star formation prescriptions that produce kpc-scale relations with the 'correct' slope if the relevant physical processes cannot be treated directly. With advances in computing power, and the ability to execute increasingly complex simulations with more physics at higher mass resolution, cosmological simulations have only recently been able to *predict* the KS relation generically as a result of the physics incorporated in the simulations at the scales of molecular clouds (e.g., Hopkins et al., 2011; Hopkins, Cox, et al., 2013; Hopkins, Kereš, Oñorbe, et al., 2014; Agertz and Kravtsov, 2015).

Including realistic feedback physics in simulations that resolve GMC scales is critical to understanding the KS relation due to the multitude of competing physical effects spanning a wide range of scales. While some simulations have argued that the KS relation can be obtained without explicit feedback (e.g., Li et al., 2005; Li et al., 2006; Wada et al., 2007), these generally depend on either (a) transient and short-lived initial conditions (e.g. simulations starting from strong initial turbulence or a smooth disk, where once turbulence decays and fragmentation runs away, some additional source of "driving" or "GMC disruption" must be invoked), or (b) suppressing runaway fragmentation numerically (e.g., "by hand" setting very slow star formation efficiencies at the grid scale, or inserting explicit sub-grid models for star formation calibrated to the KS relation on GMC or galaxy scales, or adopting artificial/numerical pressure or temperature floors or fixed gravitational softening in the gas that prevent densities from increasing arbitrarily). Many of these authors do acknowledge that feedback is likely necessary to provide either the initial conditions or grid-scale terms in their simulations, even if not explicitly included (similarly, see e.g., Robertson et al. 2008; Colin et al. 2010; Kuhlen et al. 2012; Kraljic et al. 2014). Indeed, a large number of subsequent, higher-resolution numerical experiments (on scales ranging from kpc-scale "boxes" to cosmological simulations) which run for multiple dynamical times and allow fragmentation to proceed without limit have

consistently shown that absent feedback, the galaxy-scale KS law has a factor ~ 100 higher normalization than observed (see e.g., Hopkins et al., 2011; Kim, Kim, et al., 2011; Ostriker and Shetty, 2011; Shetty and Ostriker, 2012; Kim, Ostriker, and Kim, 2013; Kim and Ostriker, 2015; Dobbs, 2015; Benincasa et al., 2016; Forbes et al., 2016; Hu et al., 2017; Iffrig et al., 2017).

In this chapter, we explore the properties and emergence of the KS relation in the FIRE[1] (Feedback In Realistic Environments) simulations (Hopkins, Kereš, Oñorbe, et al., 2014). Specifically, by producing mock observational maps of the spatially resolved KS law, we investigate the form of the relation when considering several different tracers of the star formation rate and gas surface densities, and we characterize its dependence on redshift, metallicity, and pixel size. The FIRE simulations are well suited for understanding the physical drivers of the KS relation as they sample a variety of galactic environments and a large dynamic range in physical quantities (chiefly, gas and star formation rate surface densities), and they directly (albeit approximately) incorporate stellar feedback processes that may be crucial for the emergence, and maintenance of the KS relation over cosmological timescales. In the past, they have been used to investigate the effects of various microphysics prescriptions on galaxy evolution, the formation of giant gas clumps at high redshift, and the formation of galaxy discs, among other topics (Oklopčić et al., 2017; Ma et al., 2017; Su et al., 2017).

2.2 Simulations & Analysis Methods

In the present analysis, we investigate the star formation properties of the FIRE galaxy simulations originally presented in Hopkins, Kereš, Oñorbe, et al. (2014), Chan et al. (2015), and Feldmann, Hopkins, et al. (2016), which used the Lagrangian gravity + hydrodynamics solver GIZMO (Hopkins, 2013) in its pressure-energy smoothed particle hydrodynamics (P-SPH) mode (Hopkins, 2013). All of the simulations employ a standard flat ΛCDM cosmology with $h \approx 0.7$, $\Omega_M = 1 - \Omega_\Lambda \approx 0.27$, and $\Omega_b \approx 0.046$. The galaxies in the simulations analyzed in this chapter range in $z \approx 0$ halo masses from 9.5×10^9 to 1.4×10^{13} $M_\odot$, and minimum baryonic particles masses m_b of 2.6×10^2 to 3.7×10^5 $M_\odot$. For all of the simulations, the mass resolution is scaled with the total mass such that the characteristic turbulent Jeans mass is resolved. As well, the force softening is fully adaptive, scaling with the

---

[1]http://fire.northwestern.edu

particle density and mass as

$$\delta h \approx 1.6 \text{ pc} \left(\frac{n}{\text{cm}^{-3}}\right)^{-1/3} \left(\frac{m}{10^3 \, \text{M}_\odot}\right)^{1/3}, \quad (2.1)$$

where n is the number density of the particles, and m is the particle mass. Consequently, the simulations are able to resolve a multiphase ISM, allowing for meaningful ISM feedback physics. This is crucial because the vast majority of star formation occurs in the most massive GMCs due to the shape of the GMC mass function (Williams et al., 1997).

The stellar feedback physics implemented in these simulations include approximate treatments of multiple channels of stellar feedback: radiation pressure on dust grains, supernovae (SNe), stellar winds, and photoheating; a detailed description of the stellar feedback model can be found in Hopkins, Kereš, Oñorbe, et al. (2014). Star particles in the simulations each represent individual stellar populations, with known ages, metallicities, and masses. Their spectral energy distributions, supernovae rates, stellar wind mechanical luminosities, metal yields, etc., are calculated directly as a function of time using the STARBURST99 (Leitherer et al., 1999) stellar population synthesis models, assuming a Kroupa (2002) initial mass function (IMF).

In these simulations, the galaxy- and kpc-scale star formation efficiencies are *not* set 'by hand'. Star formation is restricted to dense, molecular, self-gravitating regions according to several criteria:

- The gas density must be above a critical threshold, $n_{\text{crit}} \sim 50$ cm^{-3} in most runs (and 5 cm^{-3} in those from Feldmann, Hopkins, et al., 2016).

- The molecular fraction f_{H_2} is calculated as a function of the local column density and metallicity using the prescription of Krumholz and Gnedin (2011), and the molecular gas density is used to calculate the instantaneous SFR (see below).

- Finally, we identify self-gravitating regions using a sink particle criterion at the resolution scale, specifically requiring $\alpha \equiv \delta v^2 \delta h / G m_{\text{gas}}(< \delta r) < 1$ on the smallest resolved scale around each gas particle (δh being the force softening or smoothing length).

Regions that satisfy all of the above criteria are assumed to have an instantaneous star formation rate of

$$\dot{\rho}_* = \rho_{\text{mol}}/t_{\text{ff}}, \quad (2.2)$$

i.e. 100 percent efficiency per free-fall time. As a large fraction of the dense ($n > n_{\mathrm{crit}}$), molecular ($f_{\mathrm{H_2}} \sim 1$) gas is not gravitationally bound ($\alpha > 1$) at any given time, the *global* star formation efficiency ϵ is less than 100 percent ($\epsilon < 1$) despite the assumed *local, instantaneous* star formation efficiency per free-fall time being 100 percent. We will show below that the KS relation, with its much lower *global, time-averaged* star formation efficiency ($\epsilon \lesssim 0.1$), emerges as a result of stellar feedback preventing dense gas from quickly becoming self-bound, forming stars, and disrupting gravitationally bound star-forming clumps on a timescale less than the local free-fall time. We stress here that the emergent KS relation is *not* a consequence of the star formation prescription employed in the simulations.

In Appendix 2.5 we demonstrate this explicitly. We ran several tests restarting one of the standard FIRE simulations with varying physics and star formation prescriptions. For any reasonable set of physics, only variation in the strength of the feedback affected the galactic star formation rates, because the simulated galaxies self-regulate their star formation rates via feedback. A number of independent studies have also shown that once feedback is treated explicitly, the predicted KS law becomes independent of the resolution-scale star formation criterion (Saitoh et al., 2008; Federrath et al., 2012; Hopkins et al., 2012a; Hopkins, Kereš, Murray, et al., 2013; Hopkins, Cox, et al., 2013; Hopkins, Narayanan, et al., 2013; Hopkins, Torrey, et al., 2016; Agertz, Kravtsov, et al., 2013).

To quantify the spatially resolved KS relation in the simulations, we analyze data from snapshots spanning redshifts $z = 0 - 6$. The standard FIRE snapshots from Hopkins, Kereš, Oñorbe, et al. 2014 and the dwarf runs in Chan et al. (2015) are roughly equipartitioned among redshift bins $z \sim 3 - 6$, $2.5 - 1.5$, $1.5 - 0.5$, and < 0.5, whereas the snapshots of halos from Feldmann, Hopkins, et al. (2016) have redshifts evenly spaced between $2 < z < 6$ (these were run to only $z \sim 2$). To compare the snapshots with observational constraints of the KS relation, we made star formation rate and gas surface density maps of each snapshot's central galaxy. We summed the angular momentum vectors of the star particles in the main halo of each snapshot to determine the galaxy rotation axis and projected along this axis to generate face-on galaxy maps. The projected maps were then binned into square pixels of varying size, ranging from 100 pc to 5 kpc on a side. Only particles within 20 kpc above or below the galaxy along the line of sight were included in the maps (this captures all of the star-forming gas, but excludes distant galaxies projected by chance along the same line of sight in the cosmological box). An example of the

resulting maps can be found in Figure 2.1, which shows maps of the neutral gas surface density and the instantaneous star formation rate surface density in the **m12i** simulation from Hopkins, Kereš, Oñorbe, et al. (2014), at redshift $z \approx 0$ with 100 pc pixels.

Using the star particle ages, we calculated star formation rates averaged over the previous 10 and 100 Myr, correcting for mass loss from stellar winds and other evolutionary effects as predicted by STARBURST99 (Leitherer et al., 1999). We also considered the instantaneous star formation rate of the gas particles (defined above). A time-averaging interval of 10 Myr was chosen because this approximately corresponds to the timescale traced by recombination lines such as $H\alpha$, whereas UV and FIR emission traces star formation over roughly the past 100 Myr (e.g., Kennicutt and Evans, 2012).[2] The instantaneous star formation rate of the gas particles covers a larger range of star formation rates because it is not constrained at the low end directly by the mass resolution of our simulations; it is a continuous quantity intrinsic to the gas particles themselves, which is sampled at each time-step to determine if the gas particles form stars. This quantity best demonstrates the direct consequences of feedback on the gas *in situ* by locally tracing the star formation rate, whereas the other two SFR tracers are more analogous to observables.

The gas surface density tracers were also chosen on the basis of observable analogues, including all gas, neutral hydrogen gas (total HI + H_2 column, accounting for metallicity and He corrected), and "Cold & Dense" gas which we specifically define here and throughout this chapter as gas with $T < 300$ K and $n_H > 10$ cm^{-3}. These roughly correspond to the total gas (including the ionized component), atomic + molecular gas (HI + H_2), and cold molecular gas reservoirs observed in galaxies. We have opted to use the aforementioned approximation for the molecular gas component rather than reconstruct the f_{H_2} predicted by the Krumholz and Gnedin (2011) model (which is not output in the snapshots) as the f_{H_2} model assumes a simplified geometry at the resolution scale, that can get the local optical depth quite wrong[3]. We explore the differences between the Cold & Dense gas tracer and the

---

[2]Directly computing SFR indicators from the simulations (e.g., Hayward, Lanz, et al., 2014; Sparre et al., 2015) rather than computing the SFR averaged over the past 10 or 100 Myr would provide a more accurate comparison with the observed KS relation, but doing so would considerably expand the scope of this work, so we leave it to a future study.

[3]For the purposes of our star formation criteria, however, this is not an issue for the vast majority of cases. Due to the steepness of the exponential attenuation of the local UV field, we care only whether, strictly speaking, the gas is optically thin or thick, but the exact value of τ is not especially important, as any optical depth $\tau \gg 1$ effectively yields $\exp(-\tau) \ll 1$, and $\tau \ll 1$ similarly yields $\exp(-\tau) \approx 1$.
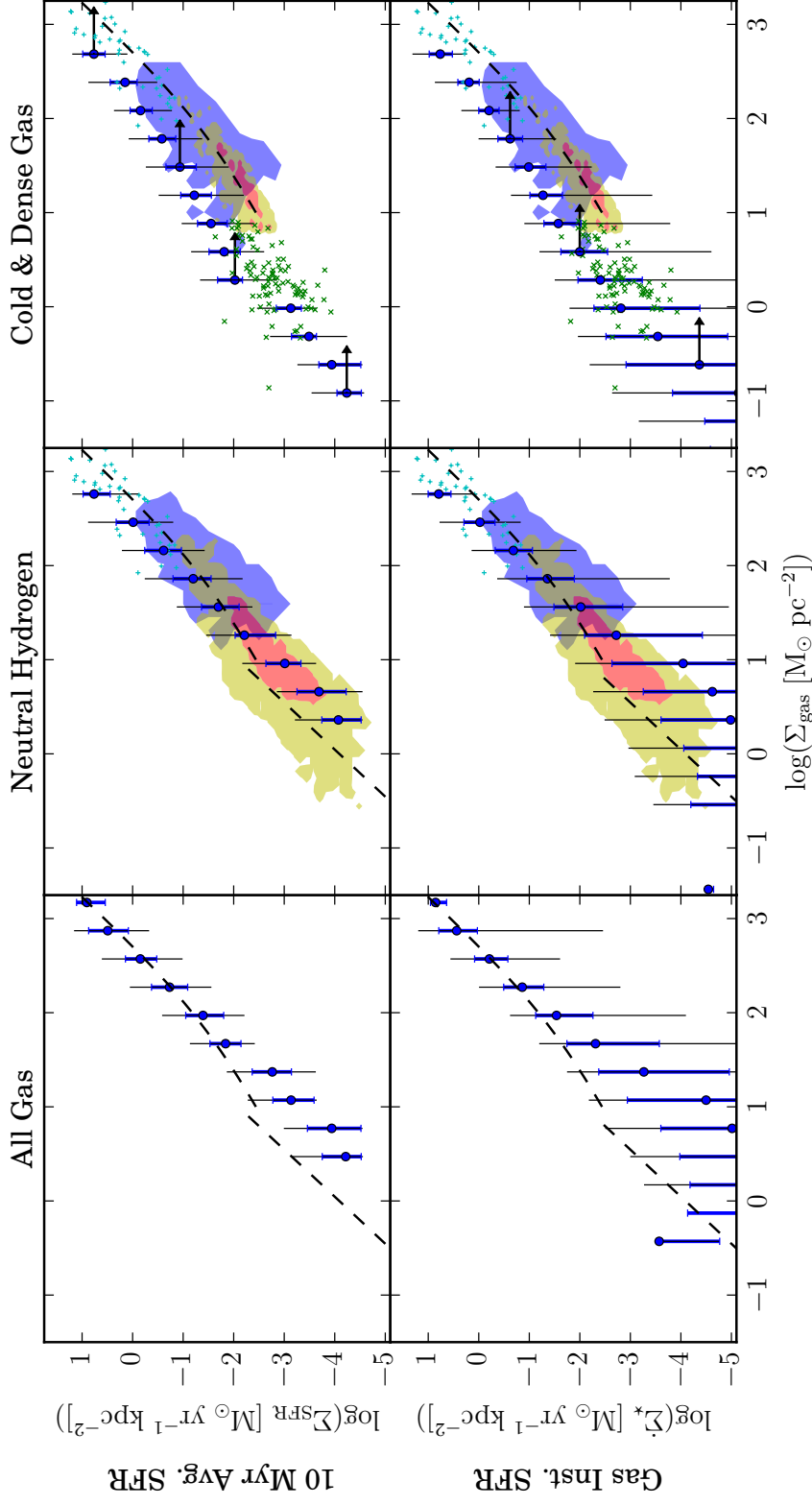
Figure 2.2: KS relation in the FIRE runs in 1 kpc^2 pixels for several gas and star formation tracers. Neutral hydrogen is $\sim \Sigma_{HI+H_2}$, and Cold & Dense gas includes particles with T < 300 K and n_H > 10 cm^{-3} ($\sim \Sigma_{H_2}$). The gas instantaneous star formation rate is calculated directly from the gas particles in each pixel, whereas the 10 Myr average star formation rate is calculated from the young star particles in each pixel. Median values of the pixel distribution are plotted, with thick (thin) error bars denoting the 25–75% (5–95%) range of resolved star formation in the Σ_{gas} bin. The yellow and red shaded regions, the blue shaded regions, cyan +'s and green x's denote observational data (from Bigiel, Leroy, Walter, Brinks, et al., 2008; Kennicutt, Calzetti, et al., 2007; Genzel et al., 2010; Verley et al., 2010, respectively). All observations have been re-calibrated with the Narayanan et al. (2012) variable X_{CO}. Theoretical star formation relations from Sections 2.4.1 and 2.4.2 are plotted with dashed black lines, assuming $\Sigma_\star = 10^2$ M$_\odot$ pc^{-2}. The FIRE neutral gas KS relation is consistent with observational constraints. The FIRE Cold & Dense gas KS relation is systematically offset from the observed molecular gas relation; this may be due to the Cold & Dense tracer underestimating the molecular fraction (see text and Appendix 2.5). The lower limit error bars in the Cold & Dense gas panels indicate the 0.5 dex uncertainty in our conservative estimator of molecular gas.

Krumholz et al. (2009b) f_{H_2} (which was the basis for Krumholz and Gnedin 2011) in a small number of snapshots, as well as with other empirical estimators such as those adopted in Leroy, Walter, Brinks, et al. (2008), in Appendix 2.5. A more detailed analysis of the true molecular fraction of the gas would require a careful radiative transfer post-processing, which we leave to a later work. Furthermore, as GIZMO lacks a detailed implementation of any chemical network, important to determining low-temperature cooling, and instead uses approximate cooling tables, we may get the temperature wrong by a factor of a few below ~ 1000 K (this error should have no *dynamical* effect in the simulations as this cool gas already effectively has no pressure compared to the bulk of the gas at higher, more reliable temperatures). Past work by Richings et al. (2016) has indeed shown that metallicity and radiation field on large scales have far larger effects on star formation rates than including detailed low-temperature chemical networks.

We acknowledge that because of the rather strict density and temperature criteria, the lack of any additional considerations, e.g., to the local UV field or the geometry of the gas, and our "low" star formation gas density threshold of $50 \, \mathrm{cm}^{-3}$, we appear to underestimate the molecular gas column as measured by the Cold & Dense gas tracer (and other estimators calculated at the particle scale) by up to a factor of a dex, which is incidentally on the order of the uncertainty in the observational CO-to-H_2 conversion factor X_{CO} (Bolatto, Wolfire, et al., 2013). This likely results in a corresponding underestimation of the local gas depletion time and overestimation of star formation efficiency. In Appendix 2.5, we show explicitly that the "molecular" fraction based on the "Cold & Dense" criteria is significantly less than the molecular gas fraction computed using two other relations for f_{H_2} versus total neutral gas surface density: that from Leroy, Walter, Brinks, et al. (2008) (which is based on Blitz et al. 2006) and the relation from Krumholz et al. (2009b) applied at the kpc-scale for total gas surface densities above their atomic-to-molecular transition thresholds. Notably, applying Krumholz et al. (2009b), with updates from Krumholz and Gnedin 2011, at the particle scale produces a similar underestimation of the molecular gas column of ~0.5 dex like the Cold & Dense gas tracer. The difficulty of estimating local (at the particle scale) column depths for shielding likely contributes to the discrepancy for both the Cold & Dense gas tracer and Krumholz et al. (2009b) fit applied at the few-pc scale.

These empirical fits for f_{H_2}, based in part on the stellar surface densities and scale heights and gas metallicity, suggest that the FIRE simulations are producing correct

star formation rates for large-scale properties of the ISM, e.g., mid-plane pressure, implying that the discrepancy in the Cold & Dense gas tracer lies with the dense end of the gas phase structure at the particle scale, and not with kpc-scale properties of the galaxies. However, we believe that the scaling relations based on the Cold & Dense' tracer are robust, since this discrepancy results in a *consistent* bias in the normalization of 'cold' gas. Again, a more accurate calculation would involve radiative transfer post-processing including a chemical network, which would allow us to directly predict the molecular hydrogen fraction and X_{CO}, which we intend to pursue in future work.

Other quantities are calculated as the mass-weighted average in each pixel, including the gas metallicity[4] Z, the Keplerian velocity v_c, and the dynamical angular velocity Ω, defined here as

$$\Omega = \frac{v_c}{R} = \frac{(GM(< R))^{1/2}}{R^{3/2}}, \tag{2.3}$$

where R is the galactocentric radius of the pixel and $M(< R)$ is the total mass enclosed within that radius (and G is the gravitational constant). These quantities allow us to investigate the dependence of star formation on gas phase metallicity, approximate the optical depth of star-forming regions, and relate galactic dynamical times to star-forming regions.

In our analysis we treat pixels from all simulations and all times equally, unless otherwise stated. However, we wish to examine only ensembles of pixels with well-resolved SFR distributions. Recalling that each of our simulations has a fixed baryonic particle mass, m_b, we discard pixels which contain <3 gas particles; for a pixel size l, this means only gas surface densities $\Sigma_{gas} > 3 \times 10^{-3} \, M_\odot \, pc^{-2} \, (m_b/1000 \, M_\odot) \, (l/kpc)^{-2}$ will be considered. However, in the example above ($m_b \sim 1000 \, M_\odot$, $l \sim kpc$), the observed Kennicutt (1998) relation gives a typical star formation surface density $\Sigma_{SFR} \sim 10^{-7} \, M_\odot \, yr^{-1} \, kpc^{-2}$ at this minimum Σ_{gas}, so in $\sim 10 \, Myr$, the expected number of $m_b \sim 1000 \, M_\odot$ star particles formed will be just 0.001. Obviously, the distribution of star formation rates will not, then, be resolved (even if the simulations capture the mean star formation rate correctly, the discrete nature of star formation means only 1 in 1000 pixels will have a star particle, while 999 have none). Thus, to ensure that the pixels we examine from each simulation at a given gas surface density have a well-resolved SFR distribution, we adopt the following criteria: (1) we first calculate the *mean* Σ_{SFR} per pixel from

---

[4]In this chapter, we take solar metallicity to be $Z_\odot \approx 0.0142$ when scaling metallicities (Asplund et al., 2009).

each simulation, for all their pixels with a given number of gas particles (fixed Σ_{gas}); (2) we estimate the average number $\langle N_\star(\Delta t)\rangle$ of star particles this would produce in the time Δt (10 or 100 Myr, as appropriate); (3) if this is $< 1(= N_{\min,\star})$, we discard all pixels which contain this number or fewer gas particles. For the example above, for $\Delta t = 10$ Myr (100 Myr), this requires > 500 (> 50) gas particles per pixel for a "resolved" star formation rate. We have repeated this exercise using instead the observed KS relation (instead of the predicted one), to estimate the resolved thresholds, and find it gives nearly identical results. We have also verified that changing the threshold $N_{\min,\star}$ by an order of magnitude in either direction does not change any of our conclusions here; we note too that the *average* star formation rates from low-resolution simulations continue to agree well with our higher-resolution simulations down to $\langle N_\star(\Delta t)\rangle$ as low as ~ 0.001.

We believe it important to reassert that **pixels with no star formation contribute to all of the plotted points in our KS relation**. We are discarding sets of pixels (those with and without star formation) that do not have at least one young star particle on average at a given gas surface density, to ensure that all of our plotted data points are drawn from well-resolved distributions of star formation (including zero star formation) at a given gas surface density.

We are careful that this prescription does not introduce bias into our star formation distributions at a given gas surface density. If we were to consider the distribution of depletion time ($\Sigma_{gas}/\dot{\Sigma}_\star$) across all gas surface densities, this method *would* bias us towards shorter depletion time by discarding all the pixels below the gas surface density that definitely produces at least one new star particle in the past 10 (or 100) Myr. However, we are investigating the distribution of SFRs in bins of gas surface density for ensembles of pixels from a number of individual galaxy simulations. To do so, we examine many snapshots from each individual simulation and consider whether the SFR distribution is well sampled by the ensemble of pixels from all of those snapshots at a given gas surface density. If at that gas surface density in the whole ensemble of pixels from that single simulation, there are at least $N_\star$ (we have chosen one here[5]) new star particles produced *on average*, then we believe we are able to say something meaningful about the distribution of star formation rates in that bin of gas surface density for that ensemble of pixels. In combining only the

---

[5]We have confirmed that this approach does not bias the average SFR surface density values by repeating the analysis requiring only an average of $N_\star = 0.001$ star particles per pixel. In this case, however, the distribution of SFR surface density at a given gas surface density is poorly sampled because of Poisson noise.

sets of pixels from individual simulations with resolved SFR distributions at a given gas surface density, we thus avoid biasing our aggregated SFR (and by extension, depletion time) *distributions* in each bin of gas surface density.

2.2.1 Observational Data

Comparing with observations, we compiled resolved KS observations from a large number of papers at various resolution scales commensurate with our mock observational maps. For our 1 kpc "fiducial" scale maps of the KS relation, we compare our neutral gas surface density results with a combination data from Kennicutt, Calzetti, et al. (2007), Bigiel, Leroy, Walter, Brinks, et al. (2008), Genzel et al. (2010); we compare our 1 kpc "Cold & Dense" gas surface density results with the appropriate H_2 results from these studies, as well as those from Verley et al. (2010). For exploring the effects of pixel size, we also used these molecular gas data to compare with our 500-pc maps, as these observations had varying resolution scales ranging from 500 pc to slightly larger than 1 kpc. For our galaxy-averaged 5 kpc maps, we used data from Kennicutt (1998), Kennicutt, Calzetti, et al. (2007), Genzel et al. (2010), Shapiro et al. (2010), Wei et al. (2010), Freundlich et al. (2013), Tacconi et al. (2013) and Amorin et al. (2016). Finally, for our highest-resolution investigations at 100 pc, we compared with high-resolution observations from Blanc et al. (2009), and Onodera et al. (2010). For exploring the star formation efficiency in this work, in the form of the Elmegreen-Silk relation, we compare our 1 kpc-scale maps with observations from Kennicutt (1998) and Daddi et al. (2010).

No distinction is made between the many estimators of SFR used in the aforementioned papers; they are simply taken at face value. However, we re-calibrate X_{CO} in the observationally inferred Σ_{H_2} data points across all the aforementioned resolved KS studies with an interpolation function taken from Narayanan et al. (2012), of the form $X_{CO} = \min[4, 6.75 \times W_{CO}^{-0.32}] \times 10^{20}$ cm^{-2}/(K km s^{-1}), independent of metallicity[6]. To correct the quoted Σ_{HI+H_2} measurements, we decomposed the total column into atomic and molecular components (the latter then being corrected in the manner of the Σ_{H_2}'s) using data in the references themselves, where available, and assuming a molecular fraction fit from Leroy, Walter, Brinks, et al. (2008) where necessary. We explore the effects of variations of the assumed X_{CO} on the (dis)agreement with our simulations in Appendix 2.5, finding ~ 0.5 dex uncertainty due to the uncertainty in X_{CO}. In the case of the Elmegreen-Silk relation observations from

---

[6]Though their full interpolation function included a metallicity dependence, we assume solar metallicity for simplicity.

Kennicutt (1998) and Daddi et al. (2010), being unable to separate out the dynamical times, we recalibrate Kennicutt (1998) only to a constant $X_{CO} = 2 \times 10^{20}$ cm^{-2}/(K km s^{-1}), consistent with Bigiel, Leroy, Walter, Brinks, et al. (2008). Data from Daddi et al. (2010) have not been altered due to the extensive efforts made therein to calibrate X_{CO} across their dataset.

2.3 KS Relation in the Simulations

2.3.1 Dependence of the KS Relation on Star Formation and Gas Tracers

Figure 2.2 demonstrates how a KS-like power-law relation self-consistently emerges (recall that the assumed instantaneous star formation efficiency of dense, gravitationally bound 'molecular' gas is 100 per cent per local free-fall time) in the FIRE simulations irrespective of specific choice of star formation or gas tracer. Two of our star formation rate tracers, the 10 Myr-averaged and gas instantaneous star formation rates, yield very similar KS relations. The points denote the median value of the star formation rate distribution in that gas surface density bin. The thick (thin) error bars in Figure 2.2 denote the 25–75% (5–95%) inclusion interval in the distribution of the star formation rates of pixels in that bin of gas surface density, effectively the $\pm 1\sigma$ ($\pm 2\sigma$) scatter. The 1σ scatter of our 10 Myr-averaged SFR, neutral gas, KS relation is ~0.4 dex, in line with quoted scatters from Bigiel, Leroy, Walter, Brinks, et al. (2008) and Leroy, Walter, Sandstrom, et al. (2013).

More restrictive gas tracers (e.g., taking gas with $T < 300$ K and $n_H > 10$ cm^{-3}, instead of all atomic + molecular gas) yield shallower power-law slopes. This is intuitive because by placing more restrictions on the gas column, we are taking pixels at a given star formation rate and moving them to lower gas surface densities (to the left) by reducing what gas contributes to the overall gas column density. The restrictions are non-linear: at high surface densities, the gas is predominately molecular, and added restrictions do little to change the participating gas column, whereas at low surface densities, relatively little of the gas column may remain after making these additional cuts. Little difference is seen between the star formation distributions in $\Sigma_{SFR} - \Sigma_{gas}$ space when considering the surface densities of all gas (including the ionized component) versus neutral gas (first and second columns of Figure 2.2) because the contribution of ionized gas to the total gas column is small in regions where significant star formation is occurring. In contrast, there is a marked change in slope of the KS relation when moving from the surface density of neutral hydrogen gas to that of Cold & Dense gas ($T < 300$ K, $n_H > 10$ cm^{-3}), with the slope shifting from ~ 1.7 to ~ 1.2 for the gas instantaneous star formation rate. This

is due to the fact that significant amounts of star formation can occur in "small" pockets of molecular gas, relative to the overall gas column, yielding a shallower slope than when considering neutral gas.

The neutral gas surface density KS relation in the FIRE simulations is consistent with the corresponding spatially resolved observational data, as represented by the shaded regions and points in the panels of Figure 2.2. No observational range has been included for "All Gas" observations as this is not typically observed; nevertheless, our data suggest that little change would be evident, as again, ionized gas does not usually contribute significantly to the column of star forming gas. There is significant, though consistent, disagreement between the simulations and observations for our Cold & Dense gas surface density because our "Cold & Dense" appears to underestimate the expected molecular gas surface density by $\sim 0.5 - 1$ dex. In Appendix 2.5, we explore the uncertainty in the molecular gas mass estimate by comparing the Cold & Dense gas tracer with other empirical estimators for the molecular fraction of our pixels, such as the dependence on the mid-plane gas pressure used in Leroy, Walter, Brinks, et al. (2008), adapted from earlier work (Blitz et al., 2006), and the self-shielding-based method from Krumholz et al. (2009b). There, we see that the Cold & Dense gas tracer (which is calculated on a per-particle basis) appears to under-predict molecular gas fractions by $\sim 0.5-0.7$ dex across surface densities of 1–100 $M_\odot$ pc^{-2} compared to the kpc-averaged empirical estimators. This suggests that although our star formation rates are appropriate given the large-scale properties of the ISM (e.g., mid-plane pressure and dust opacity), we are under-predicting the mass of gas at the highest densities, either by converting it into stars too quickly as it crosses our star formation density threshold or by incorrectly approximating the cooling and shielding properties of the densest gas. However, as this under-prediction appears to be *consistent* across the range of gas surface densities explored, we believe the *form* of the KS relation to be robust and have added arrows indicating this ~ 0.5 dex underestimate whenever results based on the Cold & Dense gas tracer are presented. Exploring this further is beyond the scope of this work and is the subject of a forthcoming study forward modeling dense gas tracers in FIRE-2.

Interestingly, the distribution of star formation rates in the FIRE simulations overlaps with that of damped Lyα systems (DLAs) observed at high redshift by Rafelski et al. (2016). Though we appear to see analogues to these systems at 1 kpc^2 pixel sizes, we leave it to a future work to investigate the detailed physical properties of these

systems.

Elmegreen-Silk Relation (Alternative KS Law)

Alternatively, in Figure 2.3, we probe the global efficiency of gas turning into stars in a dynamical time according to

$$\dot{\Sigma}_\star = \epsilon \Sigma_{\text{gas}} \Omega, \tag{2.4}$$

where ϵ represents the "star formation efficiency" on kpc scales; this relation is known as the Elmegreen-Silk relation (Elmegreen, 1997; Silk, 1997). We see systematic agreement with the neutral hydrogen gas surface density Elmegreen-Silk relation in the FIRE simulations compared to observations where ϵ ranges between $10^{-3} - 1$. We find kpc-averaged star formation efficiencies of $\epsilon \sim 0.01 - 0.1$ consistently for our entire range of star formation rate surface density. Dashed black lines indicate constant efficiencies between 0.01 and 1. Without feedback, one would expect to see $\epsilon \sim 1$.

Our efficiencies for the molecular gas formulation of the Elmegreen-Silk relation are likely over-estimated by as much as 1 dex, at efficiencies between a few and a few tens of percent, because of our systematic underestimation of the mass of "Cold & Dense" gas (see also the discussion at the end of Section 2.3.1 and in Appendix 2.5). However, since this is likely consistent across gas surface densities, we believe that the relative constancy of global star formation efficiency ϵ across Σ_{gas} is robust. Error bars of 0.5 dex (which are likely conservative) indicate this underestimation in the Cold & Dense gas panels. Even so, we find consistency at the high end of the observed efficiencies using the molecular gas formation of the Elmegreen-Silk relation, where our molecular fraction finally converges to near unity.

100 Myr-Averaged Star Formation Rate

In Figure 2.4, we see a clear flattening of the 100 Myr-averaged star formation rate surface density relative to the 10 Myr average, for neutral hydrogen columns at low gas surface densities, $\Sigma_{\text{gas}} \lesssim 1 \ \text{M}_\odot \ \text{pc}^{-2}$. This is ascribable to effects discussed in Sections 2.3.2 and 2.3.4, where individual or small numbers of young star particles are scattered into regions of very low gas surface density that are not actually forming stars. Moreover, dynamical changes in star-forming regions over the averaging period (100 Myr) cause gas complexes to dissipate and produce small numbers of star particles left in now-diffuse galactic environments. At high
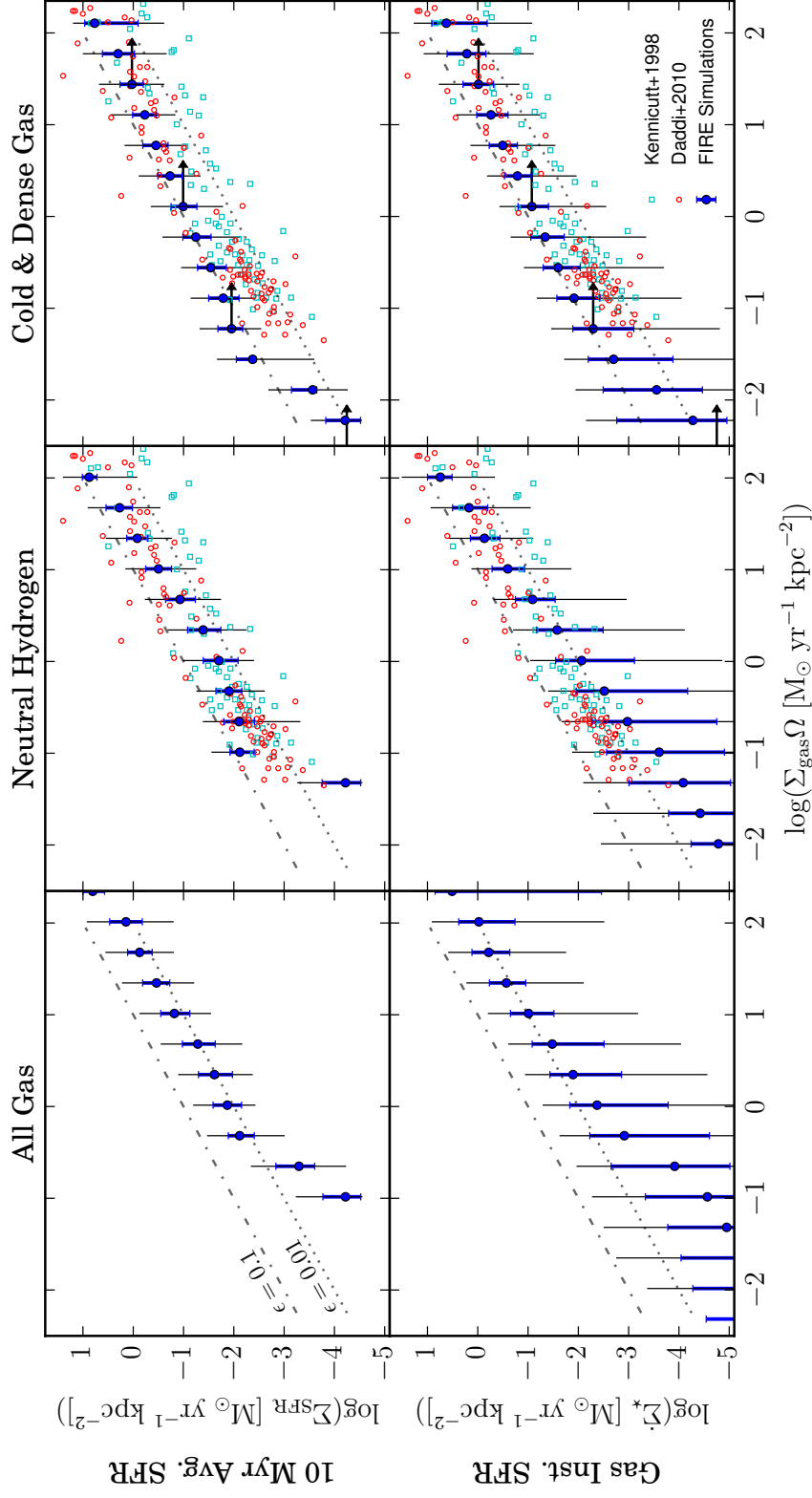
Figure 2.3: Elmegreen-Silk relation in the FIRE runs in 1 kpc^2 pixels, in the style of Figure 2.2. Lines of constant star-forming efficiency are plotted, with $\epsilon = (0.01, 0.1)$. Unfilled cyan squares and red circles are observational data from Kennicutt (1998) and Daddi et al. (2010), respectively. The data from Kennicutt (1998) have been recalibrated to an X_{CO} value consistent with Bigiel, Leroy, Walter, Brinks, et al. (2008), but those of Daddi et al. (2010) are unaltered. The simulated galaxies have kpc-scale star formation efficiencies increasing from $\sim 1\%$ (all gas) to $\sim 10\%$ (Cold & Dense gas) as denser gas tracers are selected.
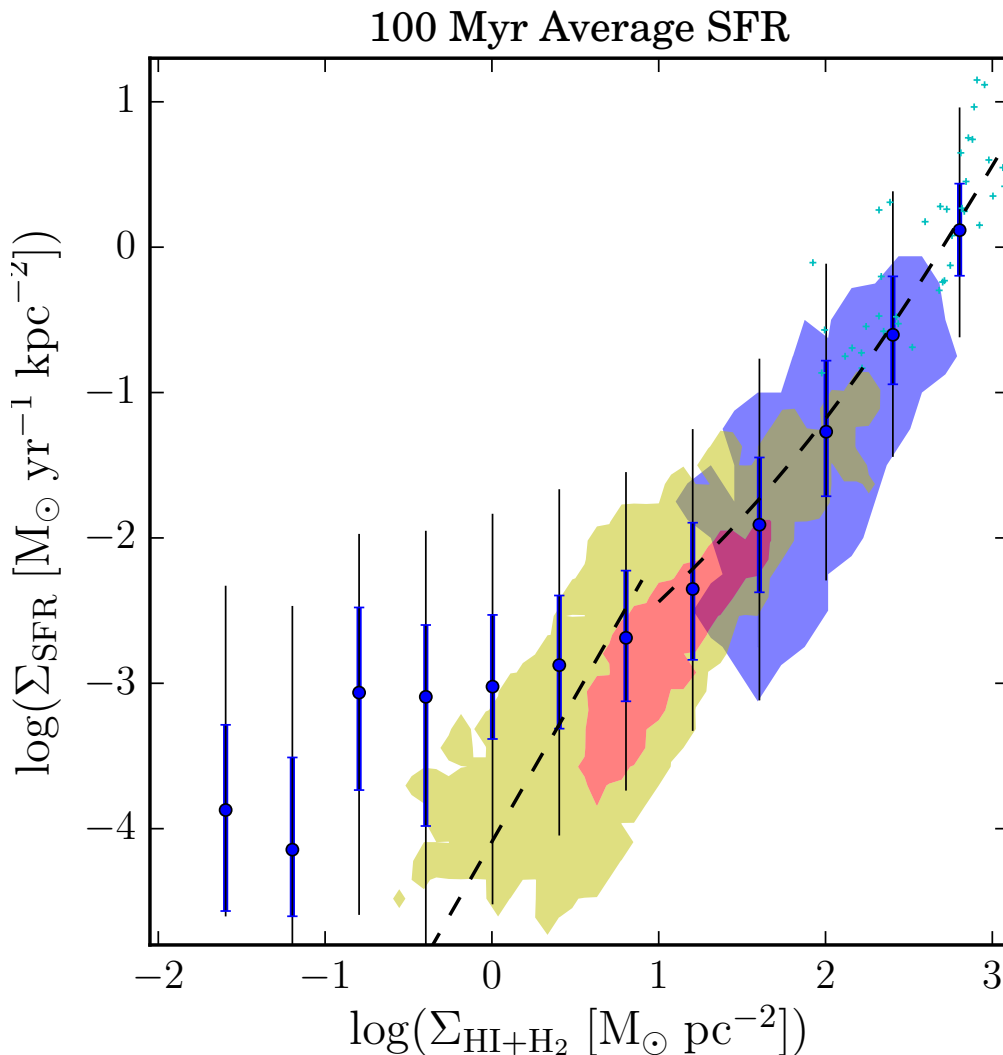
Figure 2.4: KS relation in the FIRE simulations for the 100 Myr-averaged star formation rate in 1 kpc² pixels, as Figure 2.2. The observational data shaded regions and points for the neutral (atomic + molecular) gas are those from Kennicutt, Calzetti, et al. (2007), Bigiel, Leroy, Walter, Brinks, et al. (2008), and Genzel et al. (2010) as described in Figure 2.2, measured with ~ 10 Myr tracers. At high Σ_{gas}, the ~ 100 Myr average SFRs agree well with the ~ 10 Myr observations (and by extension our ~ 10 Myr-averaged SFRs). At low Σ_{gas}, the Σ_{SFR} from the ~ 100 Myr tracer flattens. This appears to stem from a breakdown in the correlation between 100 Myr-old stars and the observed gas tracers, either from migration or other dynamical effects (e.g., mergers or strong outflow events).

gas surface densities, $\Sigma_{\text{gas}} > 10$ M$_\odot$ pc^{-2}, the 100 Myr average star formation rate surface densities agree well with the shorter timescale estimators.

2.3.2 Pixel Size Dependence

The KS relation that we find in the FIRE simulations does not appear to have a significant dependence on pixel size (i.e., map resolution) for pixels with sufficiently resolved gas and star formation rate tracers ($\gtrsim$ few gas/star particles per pixel), as shown in Figure 2.5. Over the range of pixel sizes we investigate, 100 pc - 5 kpc (0.01 - 25 kpc^2), the slope of the power law varies only weakly between ~ 1 and $\sim 4/3$. At the low end of the relation in Σ_{gas}, we expect the scatter to grow as Poisson statistics become important when only a few star particles are present in the pixels on average. However, because we exclude poorly sampled pixels, this simply manifests as a lower limit to the plotted Σ_{gas} for smaller pixels sizes (see Section 2.2).

In terms of slope, our simulated relations agree with the observed relations for the various pixel sizes considered, but again, the simulated and observed relations are systematically offset, likely because the "Cold & Dense" gas tracer systematically underestimates the column density of molecular gas (by $\sim 0.5 - 1$ dex) relative to that computed using the fits of Leroy, Walter, Brinks, et al. (2008) and Krumholz et al. (2009b), as already discussed above. In addition to the shaded regions shown in previous plots, we also compare directly with the results of Schruba et al. (2010) and Bolatto, Leroy, et al. (2011). Schruba et al. (2010) compare the KS relation found for varying aperture scales in M33, centered either on Hα or CO peaks.[7] Their results vary weakly with pixel size, except at their smallest aperture scale ~ 75 pc. Similarly, Bolatto, Leroy, et al. (2011) observed the KS relation in the Small Magellanic Cloud (SMC), and averaged their results with 200 pc and 1 kpc apertures to investigate its dependence on averaging scale. Their results are also consistent with our simulations, considering that the "Cold & Dense" tracer underestimates the molecular fraction by as much as a dex for surface densities above 10 M$_\odot$ pc^{-2}. We see, however, a slightly steeper KS relation at pixel sizes of 100 and 500 pc (their data at 200 pc lie between these scales) and a slightly shallower relation at kpc scales than Bolatto, Leroy, et al. (2011).

To compare with the global KS relation observed by a number of studies (see Section 2.2.1 for references), we summed the total 10 Myr star formation rate and

---

[7]Schruba et al. (2010) do not tile M33 with their apertures, but this does not appear to matter except at their smallest aperture scales.
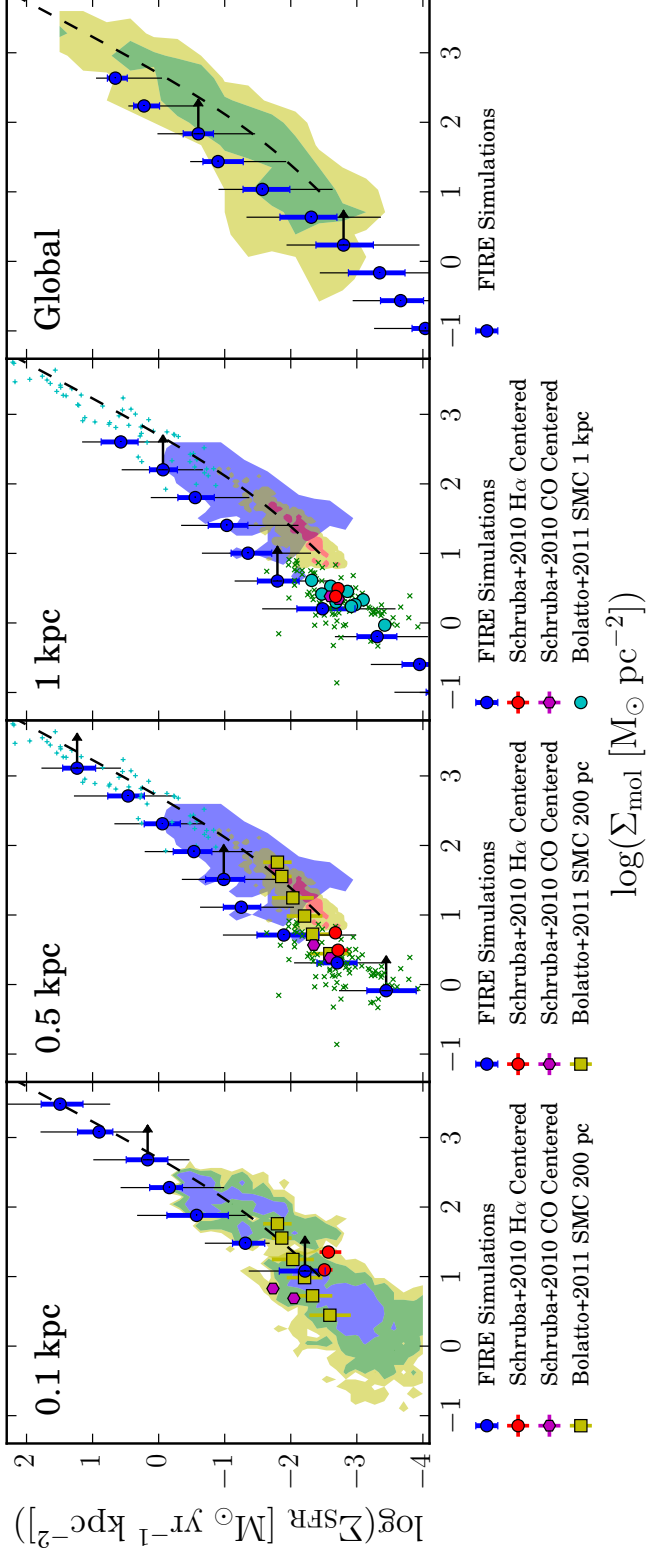
Figure 2.5: Pixel size dependence of the molecular-KS relation in the FIRE simulations, compared with selected observations. Σ_{mol} is the surface density of Cold & Dense gas; Σ_{SFR} is the 10 Myr-averaged SFR. Plotted points and error bars and styles are as in Figure 2.2. Shaded regions and points (small green x's and cyan +'s) for both 500 pc and 1 kpc are the H$_2$ data used in Figure 2.2, as a number of the source observations lie between those two spatial resolutions. For 0.1 kpc data, shaded regions are inclusion contours (100, 90, 50%) from Blanc et al. (2009) and Onodera et al. (2010). In the global KS relation panel, the shaded areas are the 70% and 50% inclusion regions for global molecular-KS observations compiled in §2.2.1. For our global KS relation, we sum the SFR and Cold & Dense gas in the map and divide by the area circumscribed by the stellar half-mass radius. Various points explicitly enumerated below the panels correspond M33 and SMC data (from Schruba et al. 2010; Bolatto, Leroy, et al., 2011; Bolatto, Leroy et al., 2010; Bolatto et al., 2010), testing the scale dependence of the KS relation. The FIRE 'molecular' KS relation exhibits no systematic trend with pixel size despite dynamical processes that might be expected to break down the correlations between young stars and gas on small scales (prominent at small pixels sizes).
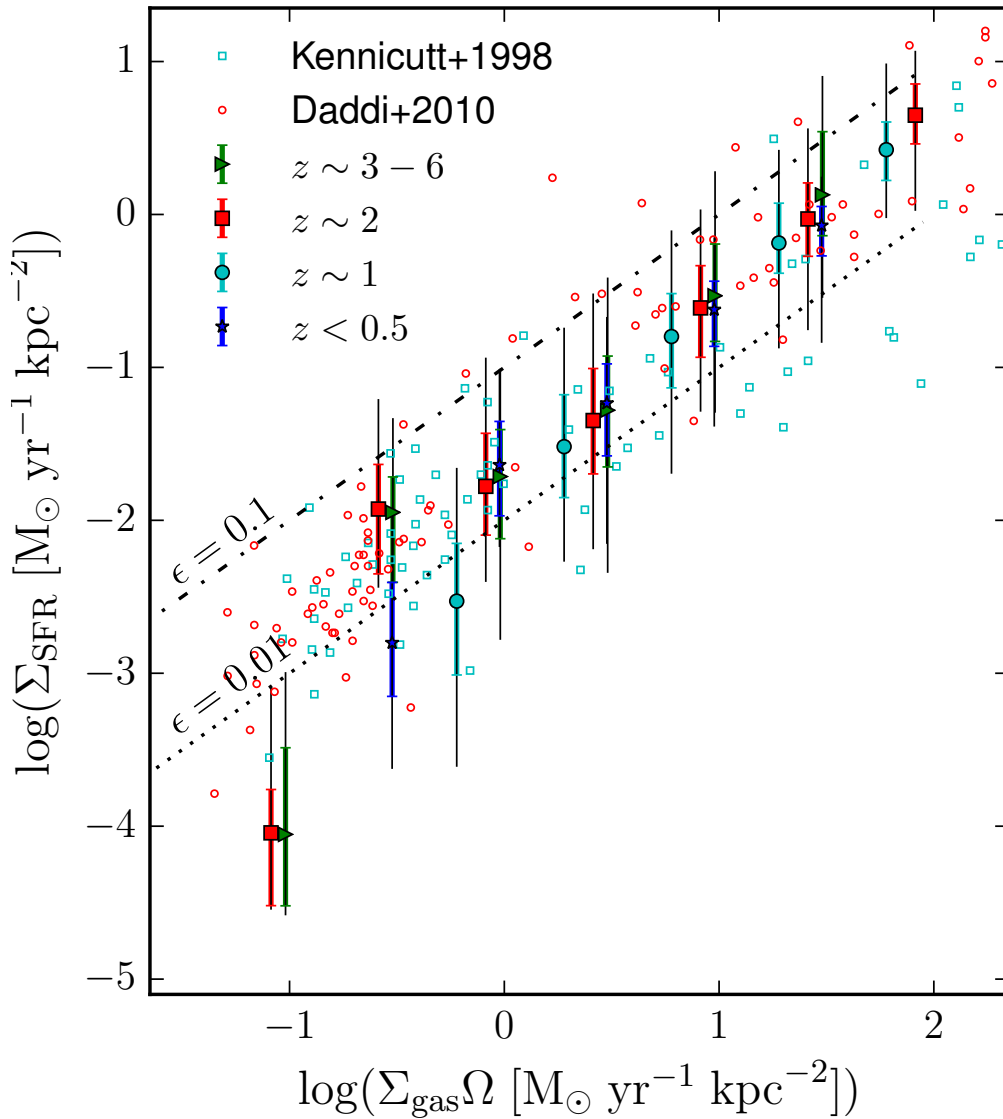
Figure 2.6: Elmegreen-Silk relation binned in redshift at 1 kpc^2 pixel size. Median values of the 10 Myr average Σ_{SFR} are plotted in bins of $\Sigma_{\text{HI}+\text{H}_2}\Omega$, in the style of Figure 2.2. Observations from Kennicutt (1998) (unfilled cyan squares) and Daddi et al. (2010) (unfilled red circles), in addition to dotted lines representing constant star formation efficiencies ϵ, are included. No significant dependence on redshift is seen: the range of data in each bin is greater than any systematic difference between bins.
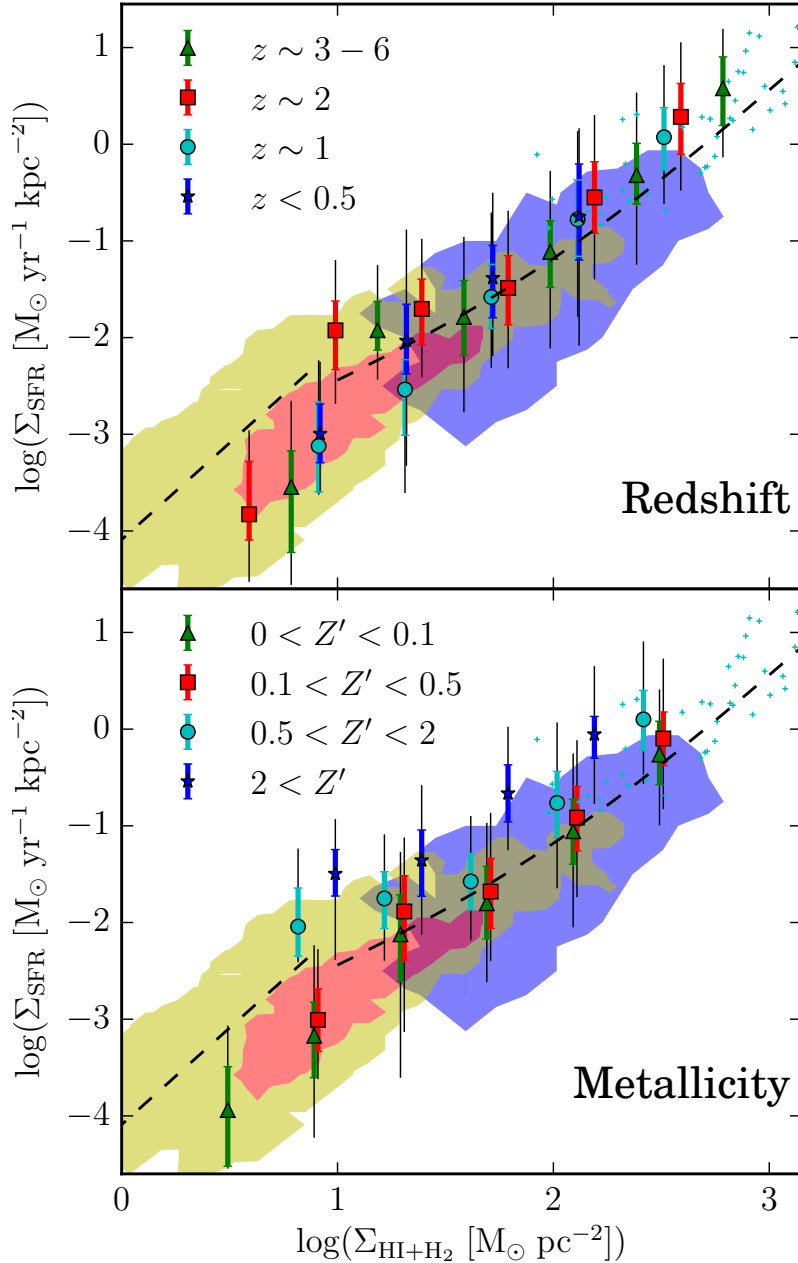
Figure 2.7: KS relation binned in redshift and metallicity at 1 kpc² pixel size. In both panels, within their respective redshift and metallicity bins, median values of the 10 Myr average Σ_{SFR} are plotted in bins of Σ_{HI+H_2}, in the style of Figure 2.2. Shaded regions and small cyan triangles denote representative observations from Kennicutt, Calzetti, et al. (2007), Bigiel, Leroy, Walter, Brinks, et al. (2008), and Genzel et al. (2010), and dotted lines represent the derived star formation relations, all as described in Figure 2.2. **Top Panel:** Simulation snapshots binned by redshift, with markers denoting different epochs. No significant dependence on redshift is seen–the range of data in each bin is greater than any systematic difference between them. **Bottom Panel:** Pixels from snapshots binned by gas metallicity, with markers indicating intervals in $Z' = Z_{gas}/Z_\odot$. A weak positive correlation between Σ_{SFR} and metallicity is seen at all Σ_{HI+H_2}, though the dependence is weak compared to the scatter in each gas bin. No metallicity-dependent cutoff is evident.
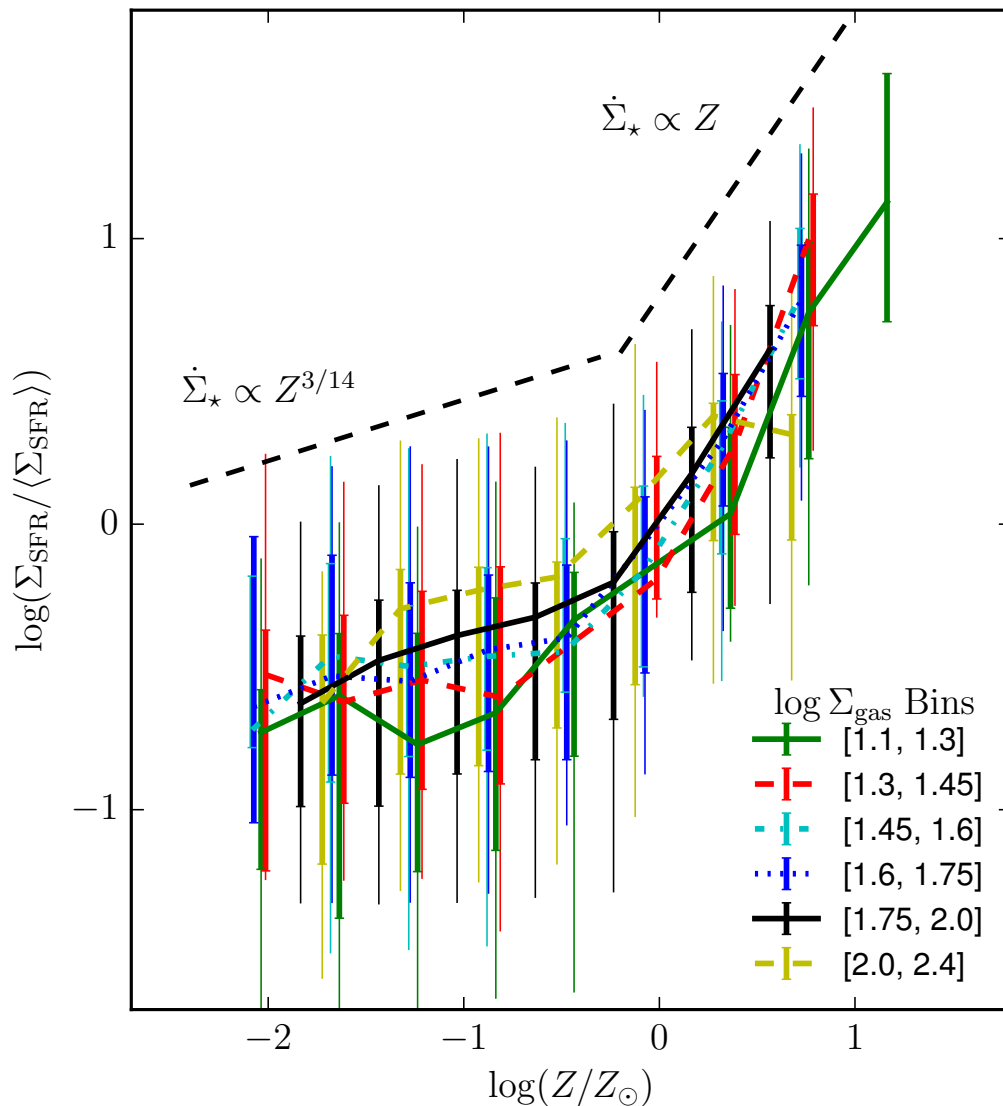
Figure 2.8: Star formation rate dependence on metallicity, binned by Σ_{HI+H_2} at 1 kpc^2 pixel size. Points are median values of the 10 Myr average Σ_{SFR} normalized by the average Σ_{SFR} for a given bin in $Z/Z_\odot$ in each Σ_{HI+H_2} bin. Thick (thin) error bars denote the 25–75% (5–95%) range for resolved star formation in each bin. A weak dependence on metallicity is seen for all gas surface densities for sub-solar metallicities, as demonstrated by the dashed black line of slope $\Sigma_{SFR} \propto Z^{3/14}$. But a stronger, nearly linear, dependence is seen for all gas surface densities above solar-metallicity values, evidenced by the dashed line with slope $\Sigma_{SFR} \propto Z$.
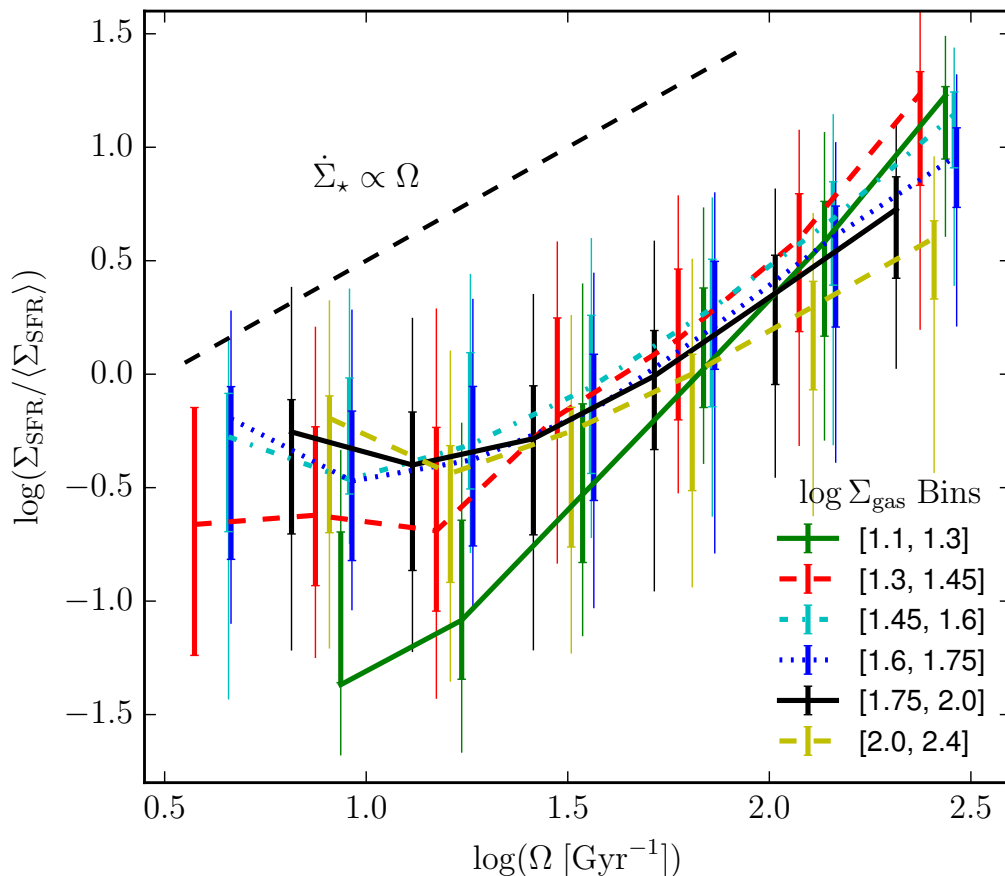
Figure 2.9: SFR surface density versus Ω (1/dynamical time), binned by $\Sigma_{\mathrm{HI+H_2}}$ at 1 kpc^2 pixel size. Points are median values of the 10 Myr average Σ_{SFR} normalized by the average Σ_{SFR} for a given bin in Ω in each $\Sigma_{\mathrm{HI+H_2}}$ bin. Thick (thin) error bars denote the 25–75% (5–95%) range for resolved star formation in each bin. A strong inverse dependence on dynamical time is seen for all gas surface densities despite considerable scatter, as demonstrated by the dashed black line with slope $\Sigma_{\mathrm{SFR}} \propto \Omega = 1/t_{\mathrm{dyn}}$.

Cold & Dense gas mass in each map and then divided these sums by the area circumscribed by the stellar half-mass radius calculated for each snapshot in order to produce analogous global KS results. Our global molecular KS relation is nearly identical in form to that observed, but like other results involving our Cold & Dense gas tracer, our gas surface densities appear to be underestimated by $\sim 0.5 - 0.7$ dex for $\Sigma_{\mathrm{mol}} \gtrsim 1\ \mathrm{M_\odot\ pc^2}$.

At our smallest pixel size (100 pc), however, none of our simulations are able to adequately sample star formation at gas surface densities $\lesssim 10\ \mathrm{M_\odot\ pc^{-2}}$, given our mass resolution; this regime is where observations exhibit the largest scatter. At least three processes cause the correlation of the star-forming gas and young star

particles to break down on scales less than $l \sim 500$ pc. (1) The relative velocities between star-forming gas and the young stars they produce cause them to wander into different pixels, thus they become uncorrelated on a pixel-by-pixel basis, when $v_p \sim l/\Delta t$. For 100 pc pixels and 10 Myr time bins, this is a relative velocity of only ~ 10 km s^{-1} (1 km s^{-1} for $\Delta t \sim 100$ Myr), so we would expect significant scatter to arise from this effect at the smallest pixel sizes. (2) Dynamical processes affecting gas and star particles, like dispersion of GMCs, major mergers, or SNe, over the time bin (i.e., 10–100 Myr) cause greater fluctuations from the power-law average as pixel size decreases. (3) When considering small (< 1 kpc) pixels, scatter is caused by the stochastic nature of the star formation in the simulations. Above ~ 10 M$_\odot$ pc^{-2}, the simulated and observed relations again agree in terms of slope, but the normalization is offset by ~ 1 dex due to the Cold & Dense gas tracer underestimating the molecular gas fraction.

2.3.3 Redshift Independence

We find no significant redshift dependence of either the KS or Elmegreen-Silk relations in the FIRE galaxies. The insensitivity to redshift in the simulations can be seen in Figure 2.6 and the top panel of Figure 2.7, where the snapshots are colored by redshift bin ($z < 0.5$, $0.5 - 1.5$, $1.5 - 2.5$, $3 - 6$) and the 10 Myr-averaged Σ_{SFR} and neutral gas surface density are considered. Similarly, no redshift dependence was seen for the Cold & Dense gas version of either relation; consequently, and due to the extensively discussed issues with the Cold & Dense tracer, these results are not shown. Some scatter is seen in the average values between redshift bins, but any dependence on redshift is much smaller than the range of the data itself. The absence of any redshift dependence persists for all measures of star formation rate. Though the absolute amount of star formation varies with redshift, the correlation between gas column and star formation rate surface density, and star formation efficiency, remains consistent.

2.3.4 Metallicity Dependence

We see in the bottom panel of Figure 2.7 evidence of a weak dependence on metallicity for the KS relation in the FIRE runs. For all neutral gas surface densities, more metal-rich gas exhibits elevated star formation rates, with an admittedly large scatter (there is significant overlap in Σ_{SFR} range for various Z' bins). At low gas surface densities ($\sim 1 - 10$ M$_\odot$ pc^{-2}), the strength of the metallicity dependence appears to be consistent with the predictions of Krumholz et al. (2009b) and Dib

(2011). Interestingly, none of our forms of the KS law exhibit a notable metallicity-dependent cutoff in star formation, as some models predict (Krumholz et al., 2009b). For our 10 and 100 Myr-averaged star formation rates, this may be an issue of adequately sampling star formation rates in the "cutoff" regime of $\dot{\Sigma}_\star \sim 10^{-(3-4)}$ $M_\odot$ yr^{-1} kpc^{-2}. However, for the well-resolved instantaneous star formation rate, the form of the star formation relation does not change at all for any of the metallicity bins in the "cutoff" regime that Krumholz et al. (2009b) find. The instantaneous star formation rate tracer, as with the averaged star formation rate tracers, presents higher star formation rates for metal-enriched gas even at these low gas surface densities, but the change is smooth, rather than a "threshold" effect. The metallicity dependence does not appear to be strongly dependent on gas surface density, and star formation rates remain consistently positively correlated with metallicity above 10 $M_\odot$ pc^{-2}, differing from the model of Dib (2011), which argues for a negative correlation owing to the metallicity dependence of pre-supernova feedback (e.g., momentum coupling in winds).

Figure 2.8 illustrates the strength of the metallicity dependence. Binning pixels by gas surface density Σ_{gas} and normalizing by the average star formation rate in each Σ_{gas} bin, we find that star formation rate surface density increases weakly with metallicity below approximately solar metallicity and considerably stronger above solar metallicity across all Σ_{gas} bins. This presentation of the data normalizes out the Σ_{gas} dependence to highlight the much weaker Z dependence. A by-eye fit of a power law with $\dot{\Sigma}_\star \propto Z'^{3/14}$ for sub-solar metallicities and $\propto Z$ above solar metallicity is plotted as a dashed black line. In the sub-solar regime, this slope is much shallower than the slope derived later in Section 2.4.2 but on the order of the predicted metallicity dependence of SNe feedback's momentum injection (ranging from $\sim 1/10 - 3/14$; Cioffi et al., 1988; Martizzi, Faucher-Giguère, et al., 2015)[8]. A lack of a strong dependence on gas surface density appears to indicate that the metallicity dependence of star formation due to pre-supernova feedback effects are subdominant compared to that of supernova feedback in the FIRE simulations (Dib et al., 2017). Above approximately solar metallicity, a stronger, nearly linear dependence appears. This dependence is more consistent with that derived in Section 2.4.2, but the reasons for its appearance are unclear and warrant future

---

[8]As described in Hopkins, Kereš, Oñorbe, et al. (2014), when SNe explode in regions such that their cooling radii will be unresolved (common in some of the lower-resolution simulations here with particle masses $\gtrsim 10^4$ $M_\odot$), the ejecta are assigned a terminal momentum based on the detailed individual explosion models from Cioffi et al. (1988), which scale as $p_t \propto Z^{3/14}$. However, the metallicity dependence in Figure 2.8 persists if we restrict only to our highest-resolution simulations.

investigation. Though the scatter within bins is quite large, the weak (and stronger) dependence are rather robust across all gas surface densities. A similar dependence on metallicity was found in the Cold & Dense gas version of Figures 2.7 & 2.8, and for brevity, we do not include them.

2.3.5 Dependence on Dynamical Time

In a similar manner to Figure 2.8, we investigate the dependence of SFR surface density on $\Omega (= 1/t_{\text{dyn}})$ in Figure 2.9. Again normalizing the 10 Myr SFR surface density to the average SFR surface density within bins of Σ_{gas}, we see a strong nearly linear dependence of SFR surface density on Ω, as expected both for a turbulently supported ISM, as discussed in Section 2.4.1 (see Eq. 2.6), and the thermally supported regime discussed in Section 2.4.2 (see Eq. 2.13). Interestingly this persists for all gas surface densities, connecting the low- and high-gas-surface-density regimes. The dependence on Ω appears to be weaker at higher gas surface densities, which may point to an increasing prevalence of "turbulent" Toomre stability (see Eq. 2.9, with no explicit Ω dependence).

2.4 Physical Interpretation

On the scales of tens or hundreds of millions of years, it is possible to understand star formation as an equilibrium process (on galactic scales) in which the inputs of either momentum injection from stellar feedback (at high gas surface density) or energy from photoheating (at low gas surface density) balance gravitational collapse.

2.4.1 High Gas Surface Density Regime

In our analysis, there is a marked transition in the star formation rate distribution at gas column densities above $\Sigma_{\text{gas}} \sim 100 \, M_\odot \, \text{pc}^{-2}$. Above this threshold, almost all the gas forms stars on or very near the KS power law. Here, supernova feedback becomes an increasingly important mechanism for injecting momentum into the ISM, as the massive young stars produced are embedded in dense molecular environments to which they can effectively couple.

A star formation relation can be derived in the limit in which the ISM is supported against gravitational collapse by turbulent pressure (Ostriker and Shetty, 2011; Faucher-Giguère et al., 2013; Hayward and Hopkins, 2017; Dib et al., 2017; Torrey et al., 2017). Here, stellar feedback injects momentum into the ISM at a rate per area proportional to $\dot{\Sigma}_\star (P_\star/m_\star)$, where $(P_\star/m_\star)$ is the characteristic momentum injected per mass of young stars formed, and is dissipated in the mass of nearby gas

per area Σ_{gas} on some characteristic timescale related to the coherence time of the turbulent eddies t_{eddy}, where $t_{\text{eddy}} \sim l_{\text{eddy}}/\sigma_{\text{eddy}}$, l_{eddy} being the spatial scale of the eddy and σ_{eddy} the turbulent velocity σ_{T}. As we are considering an approximately disk-like environment for star formation in the high gas surface density regime, the largest eddies will likely have length scales on the order of the disk scale height H (Martizzi, Fielding, et al., 2016), so $l_{\text{eddy}} \sim H \sim \sigma_{\text{T}}/\Omega$, with σ_{T} being the turbulent velocity and Ω being the local orbital dynamical frequency. We are concerned with the largest eddies, which contain most of the turbulent energy. Hence, the timescales of turbulent energy dissipation scale as $t_{\text{eddy}} \approx t_{\text{diss}} \sim H/\sigma_{\text{T}} \sim \Omega^{-1}$. Equating these rates of turbulent momentum injection and momentum dissipation in gas [9] , we find,

$$\dot{\Sigma}_\star (P_\star/m_\star) \approx \sigma_{\text{T}} \Sigma_{\text{gas}}/t_{\text{diss}} \, , \tag{2.5}$$

substituting in our relations, this yields a star formation rate of,

$$\dot{\Sigma}_\star \approx \sigma_{\text{T}} \Omega \Sigma_{\text{gas}} \left(\frac{P_\star}{m_\star} \right)^{-1} \, . \tag{2.6}$$

Relating $\sigma_{\text{T}}\Omega$ back to the disk surface density with a modified Toomre-Q parameter (Toomre, 1964),

$$Q = \frac{\kappa \sqrt{c_s^2 + \sigma_{\text{T}}^2}}{\pi G \Sigma_{\text{disk}}} \, , \tag{2.7}$$

where κ is the epicyclic frequency $\sim \sqrt{2}\Omega$ for galactic potentials, c_s is the sound speed, $\Sigma_{\text{disk}} \approx \Sigma_{\text{gas}} + \Sigma_\star$ is the disk surface density. Here we include the self-gravity contribution from the collision-less stellar component of the disk, which is correct up to some order-unity prefactor. Assuming that we are turbulently rather than thermally supported, $\sqrt{c_s^2 + \sigma_{\text{T}}^2} \approx \sigma_{\text{T}}$. Substituting this in we find,

$$\dot{\Sigma}_\star \approx \frac{\pi}{\sqrt{2}} G Q \left(\frac{P_\star}{m_\star} \right)^{-1} \Sigma_{\text{gas}} (\Sigma_{\text{gas}} + \Sigma_\star) \, . \tag{2.8}$$

Adopting a fiducial value for $(P_\star/m_\star)$ of ~ 3000 km s^{-1} (e.g., Ostriker and Shetty, 2011; Faucher-Giguère et al., 2013; Kim and Ostriker, 2015; Martizzi, Faucher-

---

[9]Here lies a direct connection to the no-feedback isolated disc simulations. If star formation is equated to the mass flux of gas into a "dense" regime times a fixed efficiency, and that dense gas is then prevented from further star formation, we see that we expect a KS relation to arise with the correct slope and normalization, albeit a contrived one.

Giguère, et al., 2015), this yields

$$\dot{\Sigma}_\star \approx 3.3 \times 10^{-2} \left(\frac{P_\star/m_\star}{3000\,\text{km/s}} \right)^{-1} \left(\frac{\Sigma_{\text{gas}}(\Sigma_{\text{gas}} + \Sigma_\star)}{10^4\,\text{M}_\odot^2\,\text{pc}^{-4}} \right) Q$$

$$\text{M}_\odot\,\text{yr}^{-1}\,\text{kpc}^{-2}\,. \quad (2.9)$$

For the gas-dominated regime, where $\Sigma_{\text{gas}} \gg \Sigma_\star$, we recover a quadratic relation for star formation. Similarly, should the stellar component dominate, as may be the case in stellar systems with older populations, a linear law in Σ_{gas} is found; this appears to be in good agreement with the slope of the KS relation seen in the FIRE runs.

The observed weak metallicity dependence seen in Figures 2.7 & 2.8, combined with the result shown in the lower left panel of Figure 2.12, which shows explicitly that the star formation rate varies with the strength of feedback, can be partly explained by a weak dependence of the final momentum injection from SNe feedback on the metallicity of the surrounding gas, e.g., $(P_\star/m_\star)^{-1} \sim Z^{0.114}$ (Martizzi, Faucher-Giguère, et al., 2015).

The KS relation predicted by a turbulence-supported model assuming that the stellar surface density $\Sigma_\star \gg \Sigma_{\text{gas}}$, with its approximately linear power-law slope, agrees remarkably well with the KS relation at moderately high surface density in the FIRE simulations. Remarkably–given the simplicity of the derivation–when Equation 2.9 is used on a pixel-by-pixel basis to predict star formation rates from $\Sigma_{\text{HI+H}_2}$ and $\Sigma_\star$, the predicted rates are nearly identical to the 10 Myr-averaged and instantaneous star formation rates, extending down to $\Sigma_{\text{HI+H}_2} \approx 10^{-1}\,\text{M}_\odot\,\text{pc}^{-2}$.

2.4.2 Low Gas Surface Density Regime

At the other extreme of galactic environments, we consider the low gas surface density regime in which gas is supported by thermal–rather than turbulent–pressure. We expect this transition to occur for $\Sigma_{\text{gas}} \lesssim 10\,\text{M}_\odot\,\text{pc}^{-2}$ (see Schaye, 2004; Ostriker, McKee, et al., 2010; Hayward and Hopkins, 2017, for details). In this regime, a star formation equilibrium rate can be derived by balancing photoheating from young stars with gas cooling. At extremely low gas surface densities, where $\Sigma_{\text{gas}} \ll 1\,\text{M}_\odot\,\text{pc}^{-2}$, the metagalactic UV background itself may become the predominant source of heating, requiring no star formation at all to maintain a thermal pressure equilibrium, providing a physical SFR floor (Schaye, 2004; Ostriker, McKee, et al., 2010).

As derived in Ostriker, McKee, et al. (2010) as an "outer-disk" law, we can balance photoheating with radiative gas cooling. For ionizing and photoelectric photons
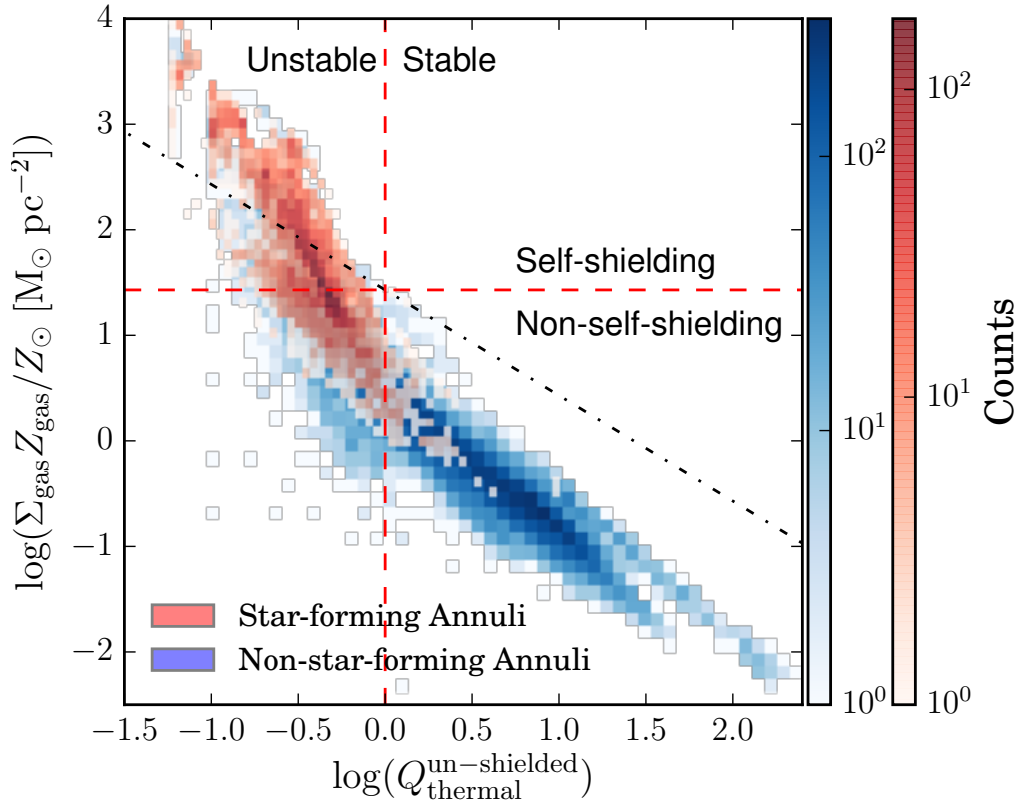
Figure 2.10: Comparison of whether self-shielding or gravitational instability determines the onset of efficient star formation (see Section 2.4.3). For each radial annulus in each galaxy (500 pc wide annuli, at each time from $z = 0.5 - 0$), we measure $\tilde{Q}_{\text{thermal}}^{\text{un-shielded}}$ (Eq. 2.15) and $\Sigma_{\text{gas}} Z_{\text{gas}} / Z_{\odot}$. We plot a heat map of the number of pixels with each value of $\tilde{Q}_{\text{thermal}}^{\text{un-shielded}}$ and $\Sigma_{\text{gas}} Z_{\text{gas}} / Z_{\odot}$, color-coded so star-forming annuli are red (mean $\dot{\Sigma}_{\star} > 10^{-3}$ $M_{\odot}$ kpc^{-2} yr^{-1}) and non-star-forming annuli are blue. $\tilde{Q}_{\text{thermal}}^{\text{un-shielded}}$ is the Toomre-Q parameter if the gas were purely thermally supported with $T = 10^4$ K; this indicates whether the gas could be thermally stabilized against gravitational instabilities if it were not self-shielding. $\Sigma_{\text{gas}} Z_{\text{gas}} / Z_{\odot}$ is a proxy for optical depth, approximating whether or not the gas is self-shielding to ionizing radiation. Vertical and horizontal dotted red lines indicate the $Q = 1$ stability threshold and the self-shielding threshold derived in Krumholz et al. (2009b), respectively. Black dotted line shows the track of varying Σ_{gas} at fixed Z' and Ω. The onset of star formation clearly occurs around $\tilde{Q}_{\text{thermal}}^{\text{un-shielded}} \sim 1$, even though the annuli are not self-shielding–i.e., gravitational instability initiates collapse, which then produces dense self-shielding clumps.
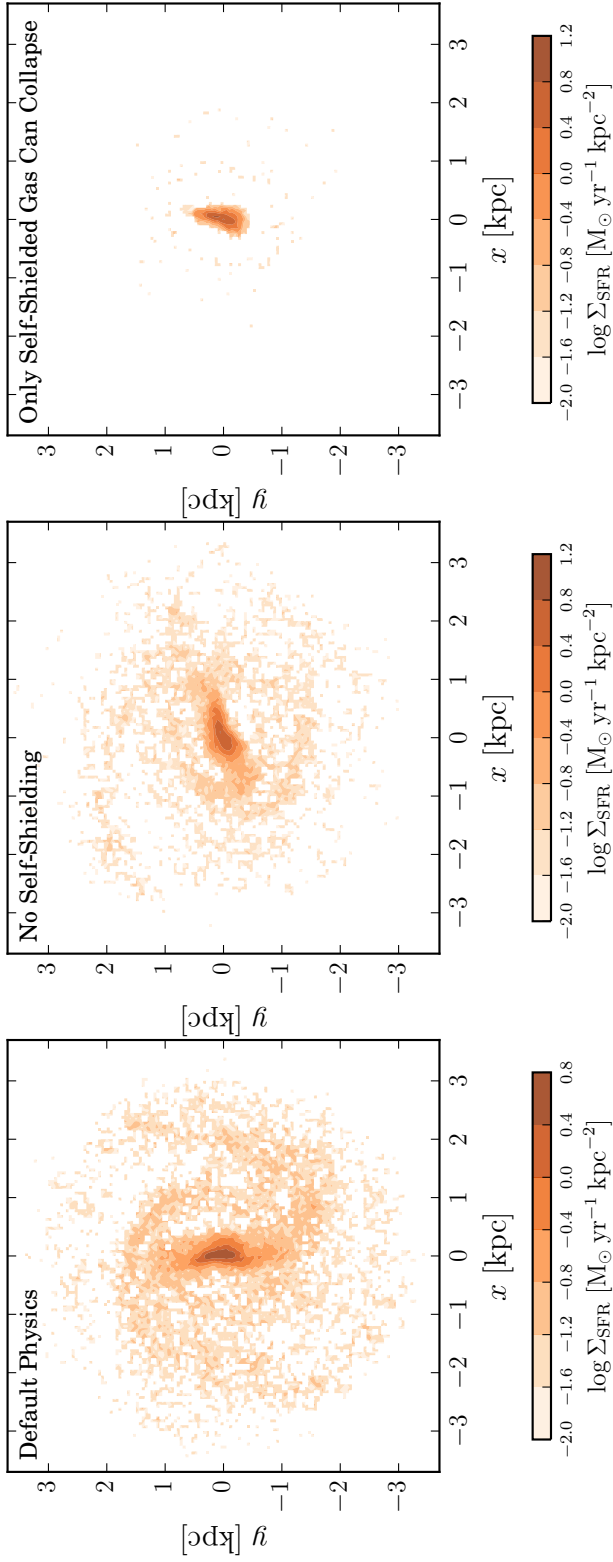
Figure 2.11: Demonstration of the importance of gravitational instability versus self-shielding in star formation. One Milky Way-mass simulation, **m12i** presented in Hopkins, Kereš, Oñorbe, et al. (2014), was restarted from $z \approx 0.07$ and re-run with three sets of physics, the default physics implemented in the FIRE runs (**top**), one with both self-shielding and cooling below 10^4 K disabled (**middle**), and one where shielded gas had normal properties but non-shielded gas had a large artificial pressure floor, effectively disabling gravitational fragmentation until the gas first became self-shielding (**bottom**). Colored pixels indicate the extent and intensity of star formation since the runs were restarted in the form of the 500 Myr-averaged star formation rate surface density. The star formation largely has the same structure with or without self-shielding, as long as fragmentation is allowed (gas can still isothermally collapse and meet the star formation criteria). But when only annuli in a galaxy which are entirely self-shielding can fragment or collapse, only the central $\sim$kpc of the galaxy (where the gas is entirely molecular) efficiently forms stars.

dominating the gas heating, the heating rate per area is

$$\frac{\dot{E}_{\text{heat}}}{l^2} = \frac{f_{\text{abs}}\beta L_\star}{l^2} = f_{\text{abs}}\beta\epsilon c^2 \dot{\Sigma}_\star\,, \tag{2.10}$$

where $f_{\text{abs}}(\lesssim 1)$ is the fraction of the emitted photoheating photons absorbed by surrounding gas, $\beta \sim 0.1$ is the fraction of ionizing radiation emitted by young stars (Leitherer et al., 1999), and $\epsilon \sim 4 \times 10^{-4}$ is the fraction of rest-mass energy radiated by stars in their lifetimes. On the other hand, the cooling rate per area is

$$\frac{\dot{E}_{\text{cool}}}{l^2} = \frac{\Lambda n_e n_i V}{l^2} \approx \frac{\Lambda Z n_g \Sigma_{\text{gas}}}{\mu}\,, \tag{2.11}$$

with $\Lambda \sim 10^{-22}$ erg s^{-1} cm^{-3} being the net cooling rate (Robertson et al., 2008); n_e, n_i, and n_g being the electron, ion, and gas number densities; and $V \sim l^2 h$ being the volume of gas considered. Equating the heating and cooling rates, we find

$$\dot{\Sigma}_\star \approx \frac{\Lambda Z n_g \Sigma_{\text{gas}}}{f_{\text{abs}}\mu\beta\epsilon c^2}\,. \tag{2.12}$$

Furthermore, we have $n_g = \rho_{\text{gas}}/\mu \approx \Sigma_{\text{gas}}/2h\mu$ and $h \approx c_s/\Omega$ in the thermally supported limit, as $\sqrt{c_s^2 + \sigma_T^2} \approx c_s$. Thus, we have $n_g \approx \Sigma_{\text{gas}}\Omega/2c_s\mu$, and $\dot{\Sigma}_\star$ becomes

$$\dot{\Sigma}_\star \approx \frac{\Lambda Z\Omega\Sigma_{\text{gas}}^2}{2f_{\text{abs}}\mu^2\beta\epsilon c^2 c_s} = \frac{\Sigma_0 Z\Omega}{f_{\text{abs}}}\left(\frac{\Sigma_{\text{gas}}}{\Sigma_0}\right)^2\,, \tag{2.13}$$

where $\Sigma_0 \approx 2\mu^2\beta\epsilon c^2 c_s/\Lambda \approx 4\,M_\odot\,\text{pc}^{-2}$, assuming $T = 10^4$ K, for which $c_s \approx 12$ km s^{-1}. Scaling this to approximately Milky-Way values ($\Omega \approx v_c/R \approx 220$ km s^{-1}/R, $Z \approx Z_\odot$), we have

$$\dot{\Sigma}_\star \approx 1.3 \times 10^{-3}\left(\frac{Z}{Z_\odot}\right)\left(\frac{10\text{ kpc}}{R}\right)\left(\frac{\Sigma_{\text{gas}}}{\Sigma_0}\right)^2\frac{1}{f_{\text{abs}}}$$
$$M_\odot\,\text{yr}^{-1}\,\text{kpc}^{-2}\,. \tag{2.14}$$

The star formation rate relation for a thermally supported ISM has the same $\dot{\Sigma}_\star \propto \Sigma_{\text{gas}}^2$ dependence as the turbulently supported high gas surface density regime when the gas surface density dominates, but with an added dependence on Z and Ω. This is similar to the relations found by Ostriker, McKee, et al. (2010) and Krumholz et al. (2009b) at low surface densities, with their dependence on metallicity. The scaling here is in good agreement with the FIRE runs at low gas surface densities for the $\Sigma_{\text{HI+H}_2}$ tracer but differs from the shallower relations found by some observational studies (Bigiel, Leroy, Walter, Blitz, et al., 2010; Roychowdhury et al., 2015).

For low column densities, where $f_{abs} \ll 1$ (and usually $f_g \ll 1$), the fraction of absorbed photoheating photons may go as the optical depth and thus the gas surface density $f_{abs} \propto (1 - \exp(-\tau)) \approx \tau \propto \Sigma_{gas} Z'$, reducing the low gas surface density relation to $\dot{\Sigma}_\star \propto \Sigma_{gas}$, degenerate in form with the relation derived for the high gas surface density regime when $f_g \ll 1$, which may explain the aforementioned shallower observations and weak Z' dependence seen in Figure 2.8. Similarly to the turbulently supported regime derivation, comparing the predictive ability of Equation 2.14 using pixel-by-pixel values of Z, Ω, and Σ_{HI+H_2} with the measured star formation rates, very close agreement is found for $\Sigma_{HI+H_2} \lesssim 10~M_\odot~pc^{-2}$, the regime in which the relation is expected to apply (Hayward and Hopkins, 2017).

The transition between linear and quadratic dependences of the star formation rates on the gas surface density in the KS relation, for both the low and high gas surface density regimes may explain some of the 'kinks' seen in the relation by various observers (e.g., Bigiel, Leroy, Walter, Brinks, et al., 2008).

2.4.3 Star Formation Thresholds

There remains the question of what, physically, *fires* up star formation in the simulations in the first place. Figures 2.10 and 2.11 address this question.

Consider a radial annulus of a smooth gas disk at some large radius R. At sufficiently large R and low densities, the disk is not self-shielding to UV radiation, and even the metagalactic UV background is sufficient to maintain the disk at warm temperatures $T \sim 10^4$ K. The thermal Toomre-Q parameter at this temperature:

$$\tilde{Q}_{thermal}^{un-shielded} \equiv \frac{\kappa\, c_s (10^4~K)}{\pi\, G\, \Sigma_{disk}} \approx 1.2 \left(\frac{\Omega}{Gyr^{-1}} \right) \left(\frac{M_\odot~pc^{-2}}{\Sigma_{disk}} \right) \tag{2.15}$$

is $\tilde{Q}_{thermal}^{un-shielded} \gg 1$, i.e., the disk is fully stable. In this limit, we do not expect (nor see in our simulations) any significant star formation. In the opposite limit (in e.g., the centers of massive galaxies), the surface densities are high, $\tilde{Q}_{thermal}^{un-shielded} \ll 1$ (i.e., thermal support, even in the warm gas, is insufficient to stabilize the disk, so it is supersonically turbulent, with $Q \sim Q_{turb} \sim 1$) and the gas is self-shielding. In this limit, of course, we see efficient star formation.

What determines the transition between these two limits? It has been suggested that when an annulus reaches a critical column density to become self-shielding, it can suddenly cool to $T \ll 10^4$ K, reducing the thermal pressure support of the gas disk against fragmentation (i.e., lowering the Toomre-Q from $\gg 1$ to $\ll 1$) and so initiating gravitational collapse and star formation (e.g., Schaye, 2004; Krumholz

et al., 2009a). This will occur when the dust optical depth $\tau = \Sigma_{\text{gas}}\kappa$ exceeds unity, or more accurately from Krumholz et al. (2009a), when $\Sigma_{\text{gas}} Z' > 27\,\text{M}_\odot\,\text{pc}^{-2}$ (where $Z' \equiv Z/Z_\odot$ reflects the assumption of a constant dust-to-metals ratio).

Alternatively, an annulus which is *not* self-shielding (hence at a temperature $T \sim 10^4$ K) will still become gravitationally unstable, when $\tilde{Q}_{\text{thermal}}^{\text{un-shielded}} \lesssim 1$, i.e., $\Sigma_{\text{disk}}/\Omega \gtrsim 0.7\,\text{M}_\odot\,\text{pc}^{-2}$ Gyr. The annulus would then rapidly fragment isothermally (at $\sim 10^4\,\text{K}$) at first, until individual overdensities/fragments quickly become internally self-shielding (reaching *local* surface densities $\Sigma_{\text{gas}} Z' > 27\,\text{M}_\odot\,\text{pc}^{-2}$ as they collapse), then cool and fragment further to form stars. During this collapse, supersonic turbulence would be driven by gravitational instabilities and feedback to maintain a turbulent $Q \sim 1$, but the important point is that the *thermal* support ($\tilde{Q}_{\text{thermal}}^{\text{un-shielded}}$) is insufficient.

The question is essentially which of these thresholds is reached "first." Figure 8 examines this in our simulations by plotting all annuli in the space of $\tilde{Q}_{\text{thermal}}^{\text{un-shielded}} \propto \Omega/\Sigma_{\text{disk}}$ versus $\tau_{\text{shielding}} \propto \Sigma_{\text{gas}} Z$, and identifying those which are and are not star-forming. Clearly, robust star formation occurs in annuli which are not, on average, self-shielding (they have $\Sigma_{\text{gas}} Z' \approx 1 - 5\,\text{M}_\odot\,\text{pc}^{-2}$). We stress that the small subregions where star formation is occurring *within* those annuli are of course self-shielding (this is in fact required by our resolution-scale star formation model), and reach $\Sigma_{\text{gas}} Z' \gg 100\,\text{M}_\odot\,\text{pc}^{-2}$ locally. In contrast, the onset of star formation corresponds very closely to where $\tilde{Q}_{\text{thermal}}^{\text{un-shielded}} \approx 1$. This is consistent with observations of star-forming spiral galaxies by Martin et al. (2001) who found that gravitational instability thresholds were sufficient to explain the extent of star-forming disks.

Examining Figure 2.10 further, we see that the annuli all lie on a track which intercepts the instability threshold $\tilde{Q}_{\text{thermal}}^{\text{un-shielded}} \approx 1$ more than a dex below the self-shielding threshold $\Sigma_{\text{gas}} Z' \sim 27\,\text{M}_\odot\,\text{pc}^{-2}$. Star formation (red pixels) is seen as annuli cross the instability line, and the distribution then turns upwards as star formation begins to enrich the annuli in Z' without much affecting Σ_{gas} or $\tilde{Q}_{\text{thermal}}^{\text{un-shielded}}$ instantaneously. As annuli cross into the self-shielding regime, Σ_{gas} quickly crosses into the high-surface-density regime, and vigorous star formation results in short depletion timescales for these annuli, preventing highly shielded, low-$\tilde{Q}_{\text{thermal}}^{\text{un-shielded}}$ annuli from remaining long in that regime. Crossing into the self-shielded regime appears to coincide with the rapid rise in the lower envelope of $\dot{\Sigma}_\star$–these regions are vigorously forming stars throughout and are unable to prevent themselves from cool-

ing rapidly and fragmenting, as in Schaye (2004). Moreover, the high-$\tilde{Q}^{\text{un-shielded}}_{\text{thermal}}$ $\gg 10$ annuli with very low $\Sigma_{\text{gas}}Z'$ appear to come from the galactic outskirts at several times the half-mass radii.

To verify the relative importance of gravitational instability versus self-shielding, we also considered an idealized numerical experiment in Figure 2.11. Specifically, we took one of our Milky Way-mass galaxy simulations (run **m12i** from Hopkins, Kereš, Oñorbe, et al. 2014) and re-ran it for about $\sim 1\,\text{Gyr}$ close to $z = 0$ (from $z = 0.07$ to $z = 0$), modifying the physics in the re-run. We considered two cases.

- **(1)** "No Self-Shielding": In this case we disable self-shielding in our radiative heating routines and do not allow any cooling below $10^4\,\text{K}$.[10] Clearly, Figure 2.11 shows that gas is still able to fragment and form stars–the spatial extent of the star formation is nearly identical to our "default" run, in fact, indicating that cooling to $T \ll 10^4\,\text{K}$ is not what determines the outer cutoff of star formation in the disk (consistent with our argument in Figure 2.10). The total star formation rate is also similar within 15%.

- **(2)** "Only Self-Shielded Gas Can Collapse": If self-shielding always preceded fragmentation and star formation, we should be able to disable Toomre-style fragmentation in gas which is not self-shielding, and obtain the same result. This is non-trivial in practice. We attempt to implement this as follows: for gas which is self-shielding (has cooled to $< 8000\,\text{K}$ and/or meets the Krumholz et al. (2009b) criterion), the physics is "normal," but for gas which is not self-shielding, we add an artificial pressure term to the hydrodynamic equations $(P \rightarrow P_{\text{true}} + P_{\text{floor}})$ where $P_{\text{floor}} = 4 \times 10^{-11}\,(n/\text{cm}^{-3})$ (i.e. the pressure the gas would have at $3 \times 10^5\,\text{K}$). The specific value is chosen to ensure the non-shielded gas has an "effective" Toomre-$Q \sim$ a few (sufficient to prevent fragmentation but not "blow up" the galaxy). When we do this, we see that efficient star formation becomes restricted to the central $\sim \text{kpc}$ only (and the total star formation rate falls by a factor ≈ 3). This central region is basically the location of the molecular disk–i.e., the regime where the gas is *entirely* molecular, since that is where the disk is uniformly self-shielding. Clearly, this is not a good description of star formation in the "default" simulation.

---

[10]In our "no self-shielding" run, we still enforce the Krumholz et al. (2009b) requirement described in § 2 for whether an individual gas particle is allowed to form stars, since this is (strictly speaking) just a metallicity-dependent *local* surface density threshold ($\Sigma_{\text{gas}} Z' > 27\,\text{M}_\odot\,\text{pc}^{-2}$) evaluated at the resolution scale.

Star Formation in the Small Magellanic Cloud

The star formation threshold behavior seen in our simulations is consistent with observations of the SMC, as measured by Bolatto, Leroy, et al. (2011) and Hony et al. (2015). The star formation rates seen by Hony et al. (2015) agree well with the spatially resolved KS relation when considering young star counts as a measure of $\dot{\Sigma}_\star$. Moreover, considering the metallicity and surface density of the SMC, in the SMC body/wing, $\tau \sim \Sigma_{\mathrm{gas}} Z/Z_\odot \sim 10$ $\mathrm{M}_\odot$ pc^{-2}, and in the SMC tail, $\Sigma_{\mathrm{gas}} Z/Z_\odot \sim 2$ $\mathrm{M}_\odot$ pc^{-2} (Oliveira, 2009; Nidever et al., 2008), the SMC body is thus not quite at the self-shielding threshold, and the tail is certainly not. On the other hand, when estimating Q for the SMC wing, one finds $Q \sim 2/3$ and for the body $Q \ll 1$ (assuming a linearly rising rotation curve to $v_{\mathrm{rot}} \sim 50$ km s^{-1} at $R \sim 3.5$ kpc found by Stanimirović et al. (2004)); hence, the SMC appears to be consistent with gravitational instabilities triggering star formation.

2.5 Conclusions

In this chapter, we investigated the spatially resolved KS relation in the cosmological FIRE simulations with $z = 0$ central halo masses ranging from 10^{10} $\mathrm{M}_\odot$ to 10^{13} $\mathrm{M}_\odot$. Our principal conclusions are the following:

- The simulated galaxies exhibit a KS-like relation with slope and scatter consistent with observations. We emphasize that this relation emerges naturally rather than being imposed 'by hand' because we assume an instantaneous local star formation efficiency of 100 per cent per free-fall time, but the predicted global star formation efficiency is low, consistent with observations, due to stellar feedback. This is true across many orders of magnitude in halo mass and at all redshifts studied. The exact slope of the relationship between Σ_{SFR} and Σ_{gas} depends on the gas and star formation tracers used, but the two quantities are tightly correlated in all cases explored.

- For the neutral hydrogen form of the relation, the simulations are observations agree well also in terms of normalization. In contrast, for the molecular hydrogen relation, the simulated and observed relations are systematically offset, likely because our proxy for the molecular gas (the 'Cold & Dense' tracer) underestimates the true molecular gas mass by ~ 0.5 dex for gas surface density $\lesssim 100 M_\odot$ pc^{-2}.

- The time-averaged KS relation does not appear to have a significant depen-

dence on pixel size (i.e. map resolution) for gas surface densities with suf-ficiently resolved star formation rate distributions (i.e. above the Σ_{gas} where the KS relation would yield at least a few young star particles per pixel given our mass resolution; see Section 2.2), with the slope of the power law remain-ing effectively unchanged. However, we are unable to resolve star formation rates at gas surface densities at our smallest pixel size (100 pc), for which observations exhibited large scatter in the KS relation ($\Sigma_{\text{gas}} \lesssim 10 \text{ M}_\odot \text{ pc}^{-2}$).

- The KS relation and star formation efficiency in the FIRE simulations is independent of redshift. The simulations do not exhibit any metallicity-dependent cutoff; however, the star formation rate surface density is weakly dependent on the metallicity, on the order expected from SNe feedback's momentum injection dependence on metallicity (Cioffi et al., 1988; Martizzi, Faucher-Giguère, et al., 2015).

- At the high end of gas surface density, where $\Sigma_{\text{gas}} \gtrsim 100 \text{ M}_\odot \text{ pc}^2$ and gas is predominantly molecular, we find that the KS relation obeyed by the sim-ulated galaxies is consistent with injection of momentum from supernovae balancing momentum dissipation in turbulence, or analogously, turbulent "pressure" maintaining vertical hydrostatic equilibrium (Ostriker and Shetty, 2011; Faucher-Giguère et al., 2013; Hayward and Hopkins, 2017). This ex-planation yields a power law independent of redshift or metallicity at high gas surface densities, where $\dot{\Sigma}_\star \propto \Sigma_{\text{gas}}\Sigma_{\text{disk}}$ (see §4.1). Because the disks in our simulations are not particularly gas rich, we find a slightly steeper than linear KS relation in this regime.

- In regions of low gas surface density ($\Sigma_{\text{gas}} \lesssim 10 \text{ M}_\odot \text{ pc}^{-2}$), characteristically in galaxy outskirts and regions between spiral arms, our spatially resolved KS relation agrees well with that expected from a simple local equilibrium between photoheating from ionizing, or near-ionizing, radiation from young stars and radiative gas cooling. This argument yields a $\dot{\Sigma}_\star \propto Z\Sigma_{\text{gas}}^2$ power law (see §4.2), as discussed in Ostriker, McKee, et al. (2010) and Hayward and Hopkins (2017).

- Vigorous star formation begins as gas self-gravity overcomes the gas thermal pressure gradient, thus making the gas Toomre-unstable. This self-gravity driven collapse occurs around $\Sigma_{\text{gas}} \sim 1 \text{ M}_\odot \text{ pc}^{-2}$, an order of magnitude before the gas becomes self-shielding to UV radiation, at $\Sigma_{\text{gas}} \sim 27 \text{ M}_\odot \text{ pc}^{-2}$. Thus,

we find that in the FIRE simulations, star formation is triggered by gravitational instabilities, which then cause the gas to fragment and collapse, thereby becoming self-shielding to ionizing radiation, cooling rapidly, and forming stars. The threshold for gravitational instability, $Q \sim \Omega/\Sigma_{\mathrm{disk}}$, depends only on the density of gas and stars, i.e. the criterion for warm gas ($T \gtrsim 10^4$ K) to support itself thermally against fragmentation, and subsequently star formation, is independent of both Z and z.

Future observations with high spatial resolution and sensitivity to low surface brightnesses should aid in understanding the outskirts of galactic environments where star formation is on the brink of *firing* up and the surface densities of gas and stars are near the thresholds of gravitational instability and self-shielding. This will help determine if gravitational fragmentation–rather than self-shielding–is indeed the primary triggering mechanism of star formation. Similarly, future work implementing chemical networks and radiative transfer post-processing in cosmological simulations will help bridge the gap between simulated tracers of star formation and molecular gas and resolved observations.

Acknowledgments

Robustness of Star Formation Rates to Variations in Star Formation, Cooling, and Stellar Feedback

Here, we demonstrate the robustness of the star formation rate in the FIRE simulations to reasonable changes in the implemented star formation, cooling, and stellar feedback physics (reviewed in detail in Hopkins, Kereš, Oñorbe, et al., 2014). A number of previous studies have consistently demonstrated the convergence of star formation rates and the KS relation, with resolution and numerical implementations of star formation (Saitoh et al., 2008; Federrath et al., 2012; Hopkins et al., 2012a; Hopkins, Kereš, Murray, et al., 2013; Hopkins, Cox, et al., 2013; Hopkins, Narayanan, et al., 2013; Hopkins, Torrey, et al., 2016; Agertz, Kravtsov, et al., 2013). In Figure 2.12, we illustrate this with a set of simple tests using the newest version of the code (part of a more general numerical study, presented in detail in Hopkins, Wetzel, et al., 2018). In each case, we re-start the same Milky-Way mass simulation (**m12i** from Hopkins, Kereš, Oñorbe, et al., 2014, as in Section 2.4.3 in the text), and re-run it from $z = 0.07 - 0$ with different numerical choices. This ensures the initial conditions are identical; Σ_{gas} for the galaxy, for example, is fixed, so we can simply read off from the star formation rate whether the galaxy's location in the KS law would change.

We compare our default star formation model, using the criteria enumerated in Section 2.2, here with $n_{\mathrm{crit}} = 1000\,\mathrm{cm}^{-3}$ and $\epsilon_{\mathrm{sf}} = 1$, where ϵ_{sf} represents the local efficiency with which gas turns into stars in a free fall time, i.e., $\dot{\rho}_\star = \epsilon_{\mathrm{sf}} \rho_{\mathrm{mol}}/t_{\mathrm{ff}}$, to variations with $\epsilon_{\mathrm{sf}} = 0.01 - 100$, $n_{\mathrm{crit}} = 5 - 1000\,\mathrm{cm}^{-3}$, and turning on/off the additional virial and molecular criteria. We find that the star formation rate (and indeed the entire spatially resolved KS relation) is effectively the same in all cases.

The gas in the restarts responds dynamically to these changes in the star formation prescription, as seen in Figure 2.13. Variations in n_{crit} allow gas to evolve to higher/lower densities before turning into stars rapidly, seen in the rapid fall-off of the densest gas in the various models. Changes in ϵ_{sf} yield similar results, with smaller ϵ_{sf} values allowing gas to continue evolving to higher physical densities. Removing the virial and molecular criteria appears to have the same effect as
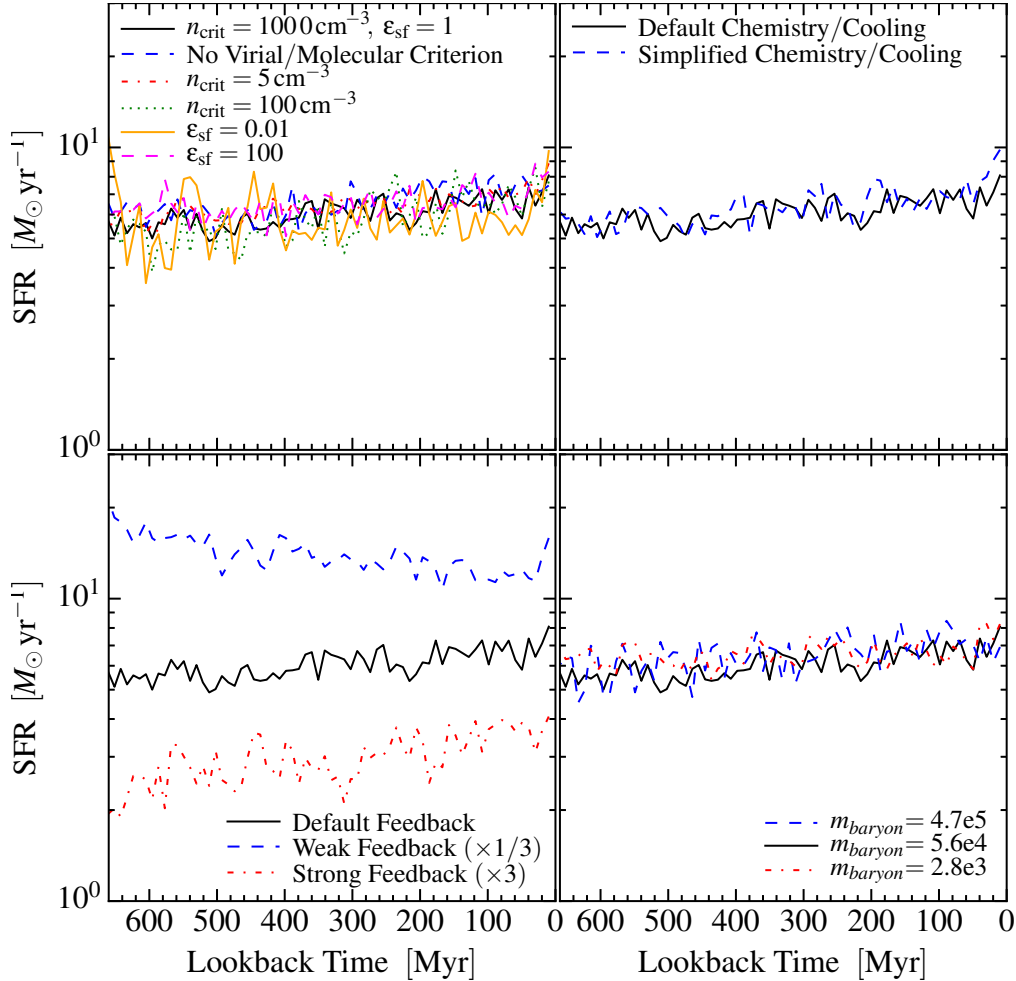
Figure 2.12: Star formation rate versus time in our MW-mass (**m12i**) simulation from redshift $z \approx 0.07 - 0$; the simulation was restarted at $z = 0.07$ and run with varying parameters to study the effect on the star formation rate given the same initial galaxy properties. **Top Left:** Effect of the resolution-scale star formation criteria. In our "default" model, gas that is self-gravitating, molecular, and dense ($n > n_{crit} = 1000\,cm^{-3}$) forms stars at a rate $\dot{\rho} = \epsilon_{sf}\,\rho_{mol}/t_{ff}$, with $\epsilon_{sf} = 1$. We compare (1) removing the self-gravity & molecular restrictions, (2–3) varying n_{crit}, and (4–5) varying ϵ_{sf}. **Bottom Left:** We vary the strength of feedback by multiplying/dividing the rates of all mechanisms per unit stellar mass by three relative to the predictions from the stellar evolution models. **Top Right:** Default physical cooling model compared with a toy model that ignores all low-temperature cooling physics and puts all gas on a single, solar-metallicity cooling curve. **Bottom Right:** Resolution effects, changing the baryonic particle mass. The results of this figure show that only the strength of feedback significantly alters the star formation rate at fixed Σ_{gas}, varying the sub-grid star formation law has essentially no effect.
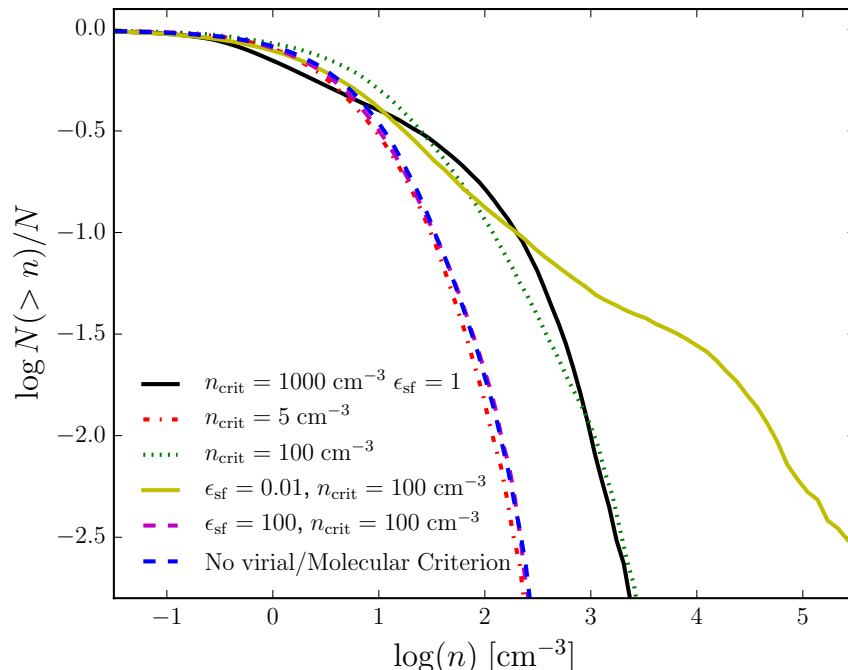
Figure 2.13: Gas number density CDF in our MW-mass (**m12i**) simulation at redshift $z \approx 0$ for the various star formation model test runs in the upper left panel of Figure 2.12. The CDFs evolve dynamically such that the "correct" amount of dense gas forms to support the required SFR to regulate the galaxy. In our (new) "default" model, with the highest $n_{\mathrm{crit}} = 1000\,\mathrm{cm}^{-3}$ more gas evolves to higher densities before turning into stars, compared to the other SF models except for our low-efficiency run. Removing the virial and molecular thresholds is nearly equivalent to drastically reducing n_{crit} (it had $n_{\mathrm{crit}} = 100\ \mathrm{cm}^{-3}$) or increasing ϵ. Intuitively, holding $\dot{\rho}_\star$ constant in Eq. 2.2, i.e., the SFRs converge to the 'necessary' value, we expect that $n \propto \epsilon^{-1/2}$. Indeed, we see that increasing ϵ by a factor of 100 moves the gas density CDF a dex towards lower densities.

lowering the density threshold or raising the local star formation efficiency, likely as more of the gas just above the threshold is converted to stars rapidly that is not necessarily bound. All the while, the star formation rates in the restarts are essentially unchanged; we see that the gas in the galaxies is dynamically evolving to produce the 'correct' star formation rate to regulate itself. Detailed observations of the gas density CDF in the Milky Way and nearby galaxies may thus help constrain sub-grid star formation prescriptions to produce realistic gas density distributions, without altering the overall star formation rates in the simulations.

In Figure 2.12, we also vary our cooling model, replacing all low-temperature cooling physics with a single cooling rate, putting all gas on a single, solar-metallicity cooling curve, and removing the molecular star formation requirement. We see that

there is no effect on the star formation rate; we similarly find no effect on the outflow rate or global morphology. Details of the phase structure, of course, differ, but these have no *large dynamical effect*, consistent with various previous studies that have found that almost all gas in galaxies is supersonically turbulent and has cooling times much shorter than their dynamical times (Hopkins et al., 2011; Hopkins et al., 2012b; Glover et al., 2012).

We also explicitly consider the mass resolution convergence by up- and down-sampling the particle distribution with particle splitting/merging. We find that the star formation rate is nearly identical over ~ 2.5 dex in mass resolution, even a factor of ~ 10 lower resolution compared to our "standard FIRE" resolution. This is consistent with our argument in Section 2.2 that we only need to marginally resolve the Toomre scale to achieve convergence in the star formation rate because the most massive clouds dominate star formation (Williams et al., 1997).

As seen in the bottom left panel of Figure 2.12, variation in the strength of feedback per mass of young stars is the only effective means of changing the star formation rate. As galaxies self-regulate for a given level of feedback, changing the strength of feedback systematically results in higher star formation rates for lower levels of feedback per star and vice versa. This is consistent with our scalings in Section 2.4.

Various Molecular Gas Mass Proxies in the FIRE Simulations

As compared to the neutral gas (atomic *and* molecular) mass, predicting the molecular mass in the FIRE simulations alone is difficult, as cooling and self-shielding are calculated using approximate look-up tables and are not done fully self-consistently with radiative transfer at the particle scale (see Hopkins, Kereš, Oñorbe, et al., 2014, for details of the numerical implementation of cooling and shielding effects in FIRE-1). For reasons presented in Appendix 2.5, getting the cooling and shielding even grossly incorrect in the coolest, densest gas generally has no *dynamical* effect on the simulations but does greatly affect the high-density tail of the gas volumetric-density distribution. Similarly, the gas density threshold for star formation and the instantaneous local star formation efficiency assumed affect the time that gas spends at the highest resolvable densities (see Figure 2.13). What truly constitutes molecular gas in the simulations, or what would be observed as such, requires careful forward modeling of the chemical abundances and molecular line emission. That, coupled with large uncertainties in the gas phase structure at low temperatures and its dependence on the aforementioned grid/particle-scale star formation and cooling prescriptions
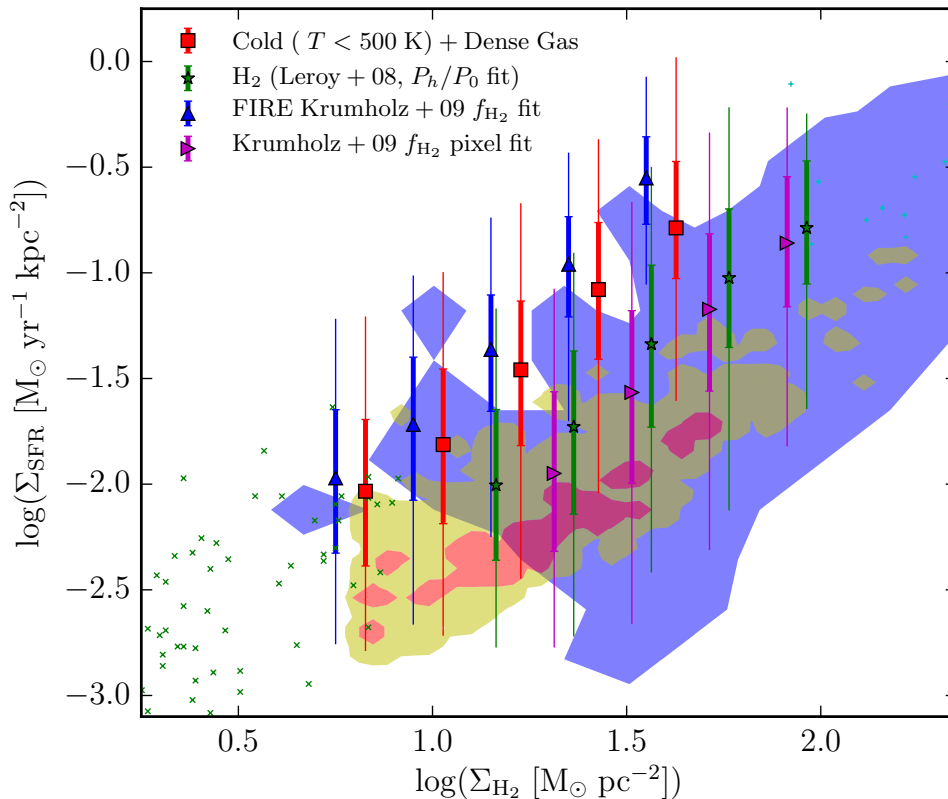
Figure 2.14: Comparison of three of proxies for the molecular gas surface density in the KS relation at 1 kpc^2 from a subset of the galaxy simulations presented in this work from $z \approx 0.2 - 0$. Points, error bars, and shaded regions are in the style of Fig. 2.2. The Cold & Dense (< 300 K and > 10 cm^{-3}) tracer is calculated at the particle level, whereas the H$_2$ masses predicted by the fits from Leroy, Walter, Brinks, et al. (2008) and Krumholz et al. (2009b) are calculated using the kpc-averaged quantities in the mapped pixels. We also apply the Krumholz et al. (2009b) fit directly to the gas particles themselves, as is done in calculating the SFRs in FIRE. The molecular-KS relations obtained when using the Leroy, Walter, Brinks, et al. (2008) and Krumholz et al. (2009b) fits at the pixel scale are more consistent with observations than when the Cold & Dense tracer is used, or when the Krumholz et al. (2009b) fit is applied at the particle scale. At fixed SFR surface density, these particle-level tracers yield molecular gas surface densities ~ 0.5 dex lower than those obtained using kpc-scale fits. This result suggests that the FIRE simulations are producing 'correct' SFRs given the large-scale properties of the ISM (mid-plane pressure and dust opacity), but insufficient gas is able to remain in or reach the highest resolvable densities in the simulations. Other proxies for the molecular gas mass, including a warmer temperature cut (3000 K), yield molecular fractions between the extremal cases presented here. These results suggest a ~ 0.5 dex uncertainty in our estimates of molecular gas surface density, with the Cold & Dense tracer systematically biased low.
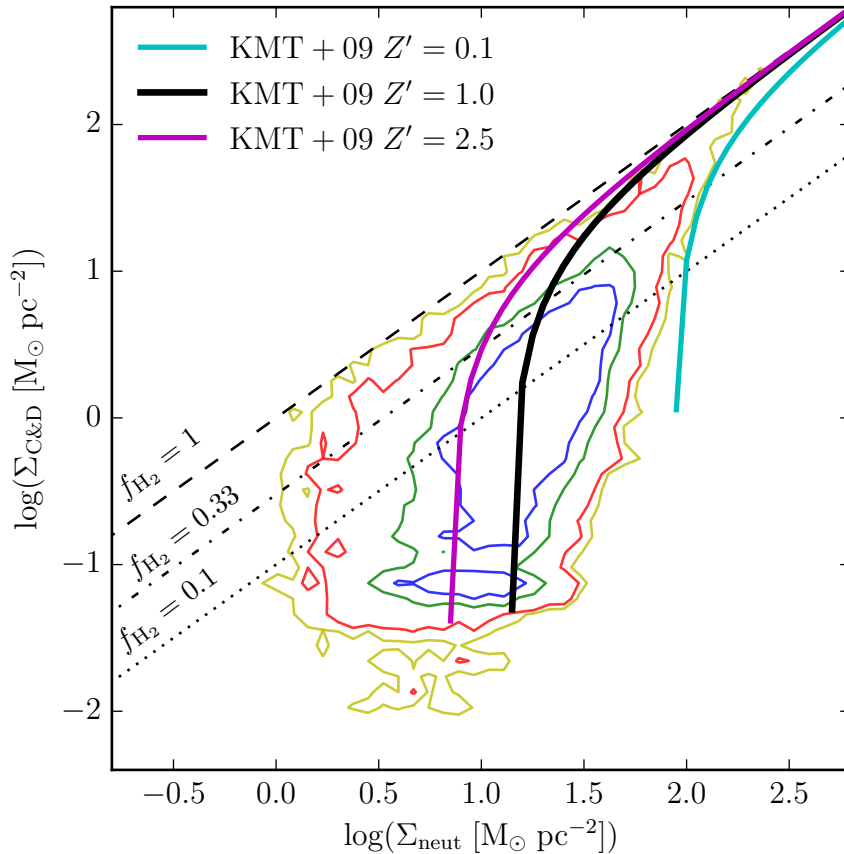
Figure 2.15: Distribution of $\Sigma_{C\&D}$, the Cold & Dense gas surface density, versus Σ_{neut}, the neutral gas surface density, for gas with metallicities $-0.1 < \log Z/Z_\odot < 0.1$ ($Z \approx Z_\odot$) in the FIRE simulations, with pixel sizes of 1 kpc. Colored (yellow, red, green, blue) contours indicate (95-, 90-, 70-, 50-)th-percentile-inclusion contours of the data. Black (dashed, dash-dotted, dotted) lines represents $f_{H_2} = (1, 0.33, 0.1)$. Colored lines (cyan, black, magenta) represent f_{H_2} molecular fraction fits for various metallicities ($Z/Z_\odot = 0.1, 1.0, 2.5$) from Krumholz et al. (2009b). The core of the "molecular fraction" (as represented by $\Sigma_{C\&D}/\Sigma_{neut}$) has a steeply rising slope between $0.5 < \log \Sigma_{neut} < 1.0$. However, the Cold & Dense fraction does not converge to unity as quickly as the fits from Krumholz et al. (2009b) at solar metallicities and has a tail of high fractions to lower gas surface densities, below their metallicity-dependent thresholds.

leaves us with crude, though physically motivated, proxies for molecular gas masses in the simulations. In this work, we have used a conservative estimator for molecular gas, our Cold & Dense (T < 300 K *and* n_H > 10 cm^{-3}) gas tracer. We compare this explicitly with two other empirical estimators for molecular gas at the kpc-scale, and one other local (e.g., few pc) estimate, in Figure 2.14. There, we compare an estimator from Leroy, Walter, Brinks, et al. (2008), for which the molecular fraction is taken to be directly proportional to the mid-plane pressure of the ISM, which is calculated using both the gas and stellar surface densities and dynamical times (see Blitz et al., 2006, from which they adapt their empirical estimator), and fits for the molecular fraction from Krumholz et al. (2009b) relating to local dust opacity applied both at the pixel (kpc) and at the particle (pc) scale.

The two empirical estimators lie roughly 0.5 dex above the Cold & Dense gas tracer at all gas surface densities and are in better concordance with observations, uncertainties in them notwithstanding (see Appendix 2.5). Due to the steepness of the Krumholz et al. (2009b) fitting function at the atomic-to-molecular transition, $\sim 10\,M_\odot\,pc^{-2}$, very few kpc-scale pixels contribute to the data shown (because many kpc-scale pixels have $\log \Sigma_{H_2} \ll -1$), indicating the necessity of assuming clumping factors when applying these fits on scales larger than GMCs themselves in low-gas surface density environments (e.g., disk outskirts). This ~ 0.5 dex discrepancy indicates three things: (1) the FIRE simulations do appear to produce correct SFRs for the large-scale *pressure* of the ISM, (2) the SFRs are in concordance with those expected given the large-scale optical depths of the ISM, and (3) the FIRE-1 simulations appear to either produce insufficient high-density gas or consume high-density gas more quickly than expected. Points (1) and (2) lend credence to trusting the large-scale structure and dynamics of the ISM and the FIRE simulations; however, point (3) indicates that we have not yet converged on producing a realistic phase structure of the ISM *at the highest densities near our resolution limits* (noting that in FIRE-1 the gas density threshold for star formation is ~ 50 cm^{-2}, quite low compared to the densities of PDRs and the critical density of ^{12}CO Hollenbach et al., 1999). We compared several other estimators for the molecular fraction, including a less stringent temperature cut ($T < 3000$ K) and a stellar surface density fit ($\Sigma_{H_2}/\Sigma_{HI} \propto \Sigma_\star$) also explored in Leroy, Walter, Brinks, et al. (2008), but omit them for clarity as they all lay between the extremal values of the Cold & Dense tracer at the low end and the Leroy, Walter, Brinks, et al. (2008)/Blitz et al. (2006) empirical pressure and Krumholz et al. (2009b) opacity fits at the high end. Reconstructing the f_{H_2} fraction of the particles themselves using the fits of Krumholz and Gnedin

(2011) used in GIZMO (also seen in the figure), however agrees more closely (underestimating only by ~ 0.1 dex) with the Cold & Dense gas tracer. The fact that the same estimator applied at the pc- and kpc-scales can produce results with $0.5 - 0.7$ dex differences likely owes to point (3) and the difficulties in estimating the local column depths for shielding. Throughout the main body of this chapter, we use the Cold & Dense tracer as a *lower limit* on the molecular gas column and acknowledge a ~ 0.5 dex uncertainty in our dense gas tracer, dependent on our choice of proxy in order to most fairly show the range of tension between our results and observations given that choice. In Figures 2.2, 2.3 & 2.5, we use arrows to indicate how shifting the molecular gas surface densities based on the Cold & Dense tracer 0.5 dex higher would bring the simulations and observations in closer agreement.

We explicitly compare the approximate molecular fraction versus neutral gas surface density relation obtained using the Cold & Dense gas proxy (T < 300 K *and* $n_H > 10$ cm^{-3}) to fits from Krumholz et al. (2009b), with 1 kpc pixels. A plot of $\Sigma_{C\&D}$, the Cold & Dense gas surface density, versus Σ_{neut}, the total neutral gas (HI + H$_2$) surface density for gas with approximately solar metallicity ($Z_\odot \pm 0.1$ dex), is shown in Figure 2.15. Compared to the steep atomic-to-molecular transition thresholds found by Krumholz et al. (2009b), the ratio $\Sigma_{C\&D}/\Sigma_{neut}$ converges much more slowly to unity (only near ~ 100 M$_\odot$ pc^{-2}). The bulk of pixels ($\sim 70\%$) lie below $f_{H_2} = 0.33$, thus indicating that the Cold & Dense gas tracer is likely consistently underestimating the molecular fraction by $0.5 - 1$ dex for $\Sigma_{gas} > 10$ M$_\odot$ pc^{-2}. For gas surface densities between $1 - 10$ M$_\odot$ pc^{-2}, it is unclear how much of the high values for the molecular fractions at low gas surface densities is due to beam-filling (i.e., cloud-counting) effects, and it is unclear whether the Cold & Dense gas tracer is over- or underestimating the molecular fractions there.

Uncertainty in X_{CO} for Observed Σ_{H_2} and Tension with Simulations

All of the observations to which we compare our results infer molecular hydrogen masses from CO emission using a single- or bimodal-CO-to-H$_2$ conversion factor, X_{CO}, which is used to convert from CO linewidth $W(^{12}C^{16}O\ J = 1 \to 0)$ to H$_2$ column density $N(H_2)$ using the following relation:

$$N(H_2) = X_{CO}W(^{12}C^{16}O\ J = 1 \to 0), \tag{2.16}$$

The value of X_{CO} is on the order of 10^{20} cm^{-2}/(K km s^{-1}) (see Bolatto, Wolfire, et al., 2013, for a review on the X_{CO} conversion factor), but there is tremendous

Disk X_{CO}
Starburst X_{CO}
Narayanan Var. X_{CO}
$H_I + H_2$
H_2
$\log(\Sigma_{SFR}\ [M_\odot\ yr^{-1}\ kpc^{-2}])$
$\log(\dot{\Sigma}_\star\ [M_\odot\ yr^{-1}\ kpc^{-2}])$
$\log(\Sigma_{gas}\ [M_\odot\ pc^{-2}])$
1
0
−1
−2
−3
−4
−5
−1
0
1
2
3
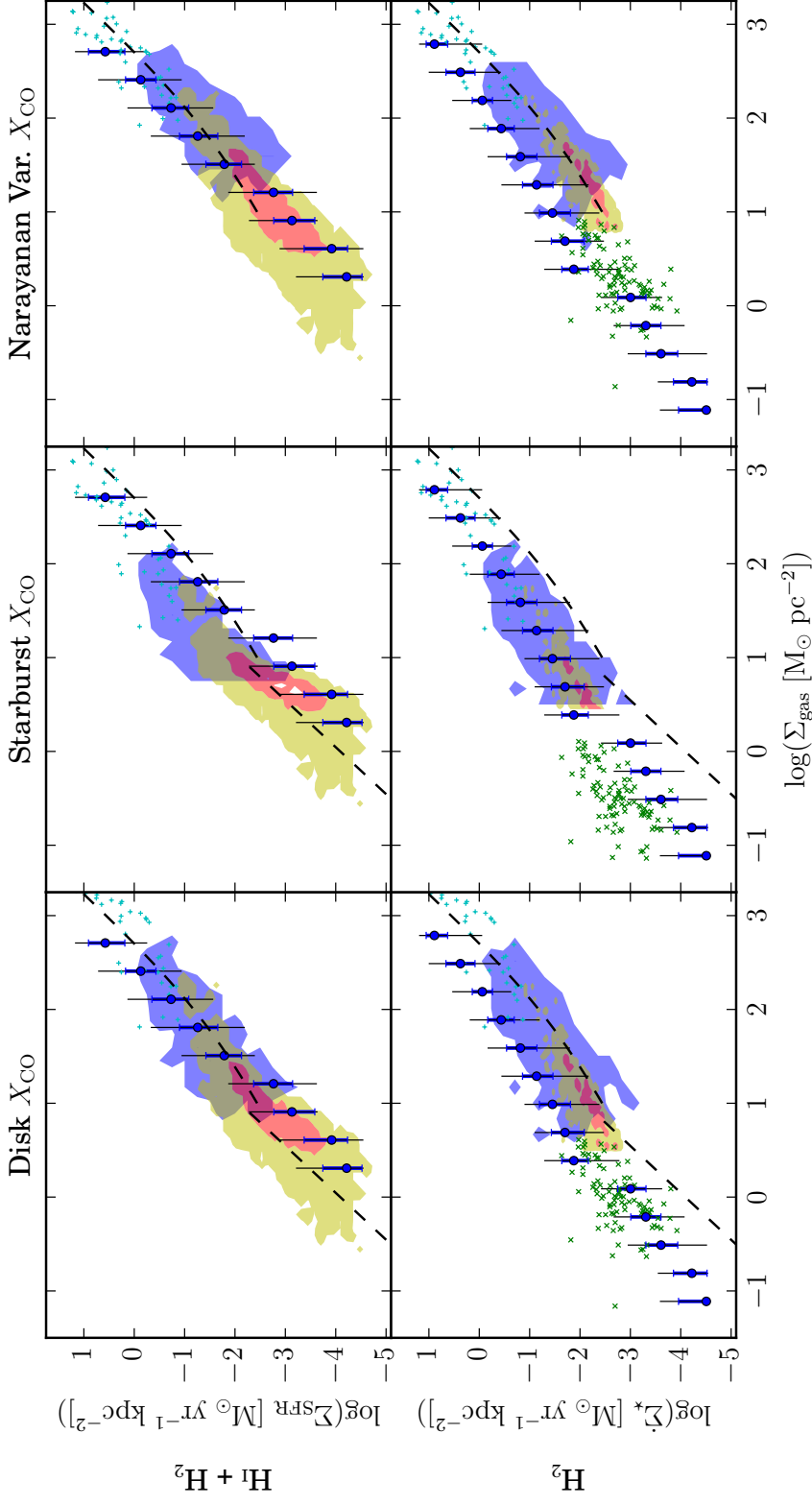
Figure 2.16: KS relation in the FIRE runs in 1 kpc^2 pixels for neutral and “molecular" gas tracers (rows) and the 10 Myr-averaged SFR, with three different X_{CO} conversion factors applied to observations for comparison (columns). Atomic + molecular hydrogen is $\sim \Sigma_{HI+H_2}$ (*top row*), and Cold & Dense gas includes particles with $T < 300$ K *and* $n_H > 10$ cm^{-3} ($\sim \Sigma_{H_2}$, *bottom row*). All observations have been re-calibrated with either a standard “star-forming disk” $X_{CO} = 2\times10^{20}$ cm^{-2}/(K km s^{-1}) (*left column*, as adopted by Bigiel, Leroy, Walter, Brinks, et al. 2008), a “starburst" $X_{CO} = X_{CO,\,disk}/3.2$ (*middle column*, adopted by Genzel et al. 2010), and a variable X_{CO} fit interpolating between the “star-forming disk” and “starburst” X_{CO} values (*right column*, normalized by a factor of 2 higher than either of the other X_{CO}’s) found by Narayanan et al. (2012), as described in §2.2.1. The neutral gas observations have been decomposed into constituent Σ_{HI} and Σ_{H_2} columns, with the latter being corrected. Uncertainty in values of X_{CO}, allowing for ~ 0.5 dex variations in observationally inferred molecular gas masses can affect the (dis)agreement between FIRE and observations, on the same order as variations in choices of molecular gas proxy in our mapping (see Fig. 2.14). We adopt the Narayanan et al. (2012) variable X_{CO} interpolation function throughout the main text.

disagreement about the exact value it takes and its dependences on surface density, metallicity, and other parameters. As a result, we find it necessary to understand the extent to which the observational data can vary for differing, but reasonable, assumptions about X_{CO}. Figure 2.16 shows how various choices for the value of X_{CO} affect the tension between observations and our "standard" tracers of atomic + molecular (Σ_{HI+H_2}) and Cold & Dense ($\sim \Sigma_{H_2}$) gas surface density. We compare three conversion factors: (*left column*) a "star-forming disk" $X_{CO} = 2 \times 10^{20}$ cm^{-2}/(K km s^{-1}), a value widely adopted for low-redshift observations of Milky-Way like galaxies (Strong et al., 1996; Dame et al., 2001; Bigiel, Leroy, Walter, Brinks, et al., 2008; Genzel et al., 2010; Shapiro et al., 2010; Wei et al., 2010; Tacconi et al., 2013; Amorin et al., 2016); (*middle column*) a "starburst" $X_{CO} = X_{CO, disk}/3.2$ which is a factor of 3.2 smaller than the disk conversion factor, owing to the fact that at high gas surface densities in extreme star-forming systems the disk X_{CO} predicts gas masses in excess of observed dynamical masses, which is a known problem for ULIRG observations (Solomon, Downes, et al., 1997; Downes et al., 1998; Solomon and Vanden Bout, 2005; Bothwell et al., 2010); and (*right column*) a variable X_{CO} interpolation function based on Narayanan et al. (2012). We take the form of the Narayanan et al. (2012) interpolation function to be

$$X_{CO} = min[4, 6.75 \times W_{CO}^{-0.32}] \times 10^{20} \frac{cm^{-2}}{K\,km\,s^{-1}} \,, \tag{2.17}$$

which is identical to that presented in their work[11], assuming a solar gas metallicity (see Ostriker and Shetty, 2011, for a comparable interpolation function). We recalibrate all of the observations enumerated in Section 2.2.1 for the KS relation using the X_{CO} value predicted using Eq. (2.17). To correct the Σ_{HI+H_2} measurements, we decomposed the total column into atomic and molecular components (the latter then being corrected in the manner of the Σ_{H_2} values) using data from the references themselves, where available, or assuming a molecular fraction fit from Leroy, Walter, Brinks, et al. (2008) when necessary.

In Appendix 2.5, we demonstrated that the ratio of Cold & Dense tracer to the neutral hydrogen surface density slowly converges to one above ~ 10 M$_\odot$ pc^{-2} and hovers ~ 0.5 dex below other empirical fits and the neutral gas surface density in the KS plane until $\gtrsim 100$ M$_\odot$ pc^{-2}. Considering this, adopting the disk X_{CO} leads to large disagreement at the highest gas surface densities, which we believe our molecular gas surface density proxy is nearly converged for (and other studies of the

---

[11]It is noted that their normalization/maximum X_{CO} is twice that of the "star-forming disk" X_{CO} factor.

FIRE simulations have shown that the centers of our Milky Way-mass galaxies are not outliers in terms of gas surface density or star formation rate, Hopkins, Kereš, Oñorbe, et al., 2014; Hopkins, Torrey, et al., 2016; Torrey et al., 2017), whereas a purely "starburst" X_{CO} seems to suggest our simulations are over-predicting neutral gas surface densities by ~ 0.5 dex everywhere but at the most extreme gas surface densities. Given that there is little support for either of these values of X_{CO} holding for all gas surface densities, it is reasonable to use an interpolation function, such as that of Narayanan et al. (2012), for the range of observations.

Otherwise, between the disk and starburst X_{CO} factors a ~ 0.5 dex uncertainty exists, before even considering reasonable additional factor of a few differences in those values themselves (Bolatto, Wolfire, et al., 2013). This level of variation is on the order of the difference between extremal estimators of our molecular gas masses (see the difference between the Cold & Dense tracer and the Krumholz et al. 2009b relation applied to individual pixels shown in Figure 2.14). Although the Cold & Dense gas tracer is clearly a conservative estimate of the molecular gas mass in the simulations and more careful forward-modeling of CO emission is clearly necessary (motivating a future work), the uncertainty in the observational value of X_{CO} makes it difficult to determine the absolute level of (dis)agreement between observations and simulations (all simulations, not just the FIRE simulations) at the $\sim 0.5 - 1$ dex level. As a result, in order to attempt to compare the results from FIRE on an appropriate footing with the observations throughout this chapter, which both cover a parameter space of star formation rates and gas surface densities in both the "star-forming disk" and "starburst" regimes, we recalibrate the compiled observations with the Narayanan et al. (2012) X_{CO} interpolation function.

References

Agertz, O. & Kravtsov, A. V. (2015) ApJ 804, 18, 18

Agertz, O., Kravtsov, A. V., Leitner, S. N., & Gnedin, N. Y. (2013) ApJ 770, 25, 25

Amorin, R., Muñoz-Tuñón, C., Aguerri, J. A. L., & Planesas, P. (2016) A&A 588, A23, A23

Asplund, M., Grevesse, N., Sauval, A. J., & Scott, P. (2009) ARA&A 47, 481

Becerra, F. & Escala, A. (2014) ApJ 786, 56, 56

Benincasa, S. M., Wadsley, J., Couchman, H. M. P., & Keller, B. W. (2016) MNRAS 462, 3053

Bigiel, F., Leroy, A., Walter, F., Blitz, L., Brinks, E., de Blok, W. J. G., & Madore, B. (2010) AJ 140, 1194

Bigiel, F., Leroy, A., Walter, F., Brinks, E., de Blok, W. J. G., Madore, B., & Thornley, M. D. (2008) AJ 136, 2846

Blanc, G. A., Heiderman, A., Gebhardt, K., Evans II, N. J., & Adams, J. (2009) ApJ 704, 842-862, 842

Blitz, L. & Rosolowsky, E. (2006) ApJ 650, 933

Bolatto, A. D., Leroy, A. K., et al. (2011) ApJ 741, 12, 12

Bolatto, A. D., Wolfire, M., & Leroy, A. K. (2013) ARA&A 51, 207

Bothwell, M. S. et al. (2010) MNRAS 405, 219

Bouché, N. et al. (2007) ApJ 671, 303

Calzetti, D., Liu, G., & Koda, J. (2012) ApJ 752, 98, 98

Chan, T. K., Kereš, D., Oñorbe, J., Hopkins, P. F., Muratov, A. L., Faucher-Giguère, C.-A., & Quataert, E. (2015) MNRAS 454, 2981

Cioffi, D. F., McKee, C. F., & Bertschinger, E. (1988) ApJ 334, 252

Colin, P., Avila-Reese, V., Vázquez-Semadeni, E., Valenzuela, O., & Ceverino, D. (2010) ApJ 713, 535

Daddi, E. et al. (2010) ApJ 714, L118

Dame, T. M., Hartmann, D., & Thaddeus, P. (2001) ApJ 547, 792

Dib, S. (2011) ApJ 737, L20, L20

Dib, S., Hony, S., & Blanc, G. (2017) MNRAS 469, 1521

Dobbs, C. L. (2015) MNRAS 447, 3390

Downes, D. & Solomon, P. M. (1998) ApJ 507, 615

Elmegreen, B. G. (1997) *Revista Mexicana de Astronomia y Astrofisica Conference Series* ed. by J. Franco, R. Terlevich, & A. Serrano vol. 6 Revista Mexicana de Astronomia y Astrofisica, vol. 27, 165

Faucher-Giguère, C.-A., Quataert, E., & Hopkins, P. F. (2013) MNRAS 433, 1970

Federrath, C. & Klessen, R. S. (2012) ApJ 761, 156, 156

Feldmann, R. & Gnedin, N. Y. (2011) ApJ 727, L12, L12

Feldmann, R., Gnedin, N. Y., & Kravtsov, A. V. (2011) ApJ 732, 115, 115

– (2012) ApJ 747, 124, 124

Feldmann, R., Hopkins, P. F., Quataert, E., Faucher-Giguère, C.-A., & Kereš, D. (2016) MNRAS 458, L14

Forbes, J. C., Krumholz, M. R., Goldbaum, N. J., & Dekel, A. (2016) Nature 535, 523

Freundlich, J. et al. (2013) A&A 553, A130, A130

Genzel, R. et al. (2010) MNRAS 407, 2091

Glover, S. C. O. & Clark, P. C. (2012) MNRAS 421, 9

Gnedin, N. Y. & Kravtsov, A. V. (2011) ApJ 728, 88, 88

Gnedin, N. Y., Tasker, E. J., & Fujimoto, Y. (2014) ApJ 787, L7, L7

Grudić, M. Y., Hopkins, P. F., Faucher-Giguère, C.-A., Quataert, E., Murray, N., & Kereš, D. (2018) MNRAS 475, 3511

Hayward, C. C. & Hopkins, P. F. (2017) MNRAS 465, 1682

Hayward, C. C., Lanz, L., et al. (2014) MNRAS 445, 1598

Hollenbach, D. J. & Tielens, A. G. G. M. (1999) Reviews of Modern Physics 71, 173

Hony, S. et al. (2015) MNRAS 448, 1847

Hopkins, P. F. (2013) MNRAS 428, 2840

Hopkins, P. F., Cox, T. J., Hernquist, L., Narayanan, D., Hayward, C. C., & Murray, N. (2013) MNRAS 430, 1901

Hopkins, P. F., Kereš, D., Murray, N., Hernquist, L., Narayanan, D., & Hayward, C. C. (2013) MNRAS 433, 78

Hopkins, P. F., Kereš, D., Oñorbe, J., Faucher-Giguère, C.-A., Quataert, E., Murray, N., & Bullock, J. S. (2014) MNRAS 445, 581

Hopkins, P. F., Narayanan, D., & Murray, N. (2013) MNRAS 432, 2647

Hopkins, P. F., Quataert, E., & Murray, N. (2011) MNRAS 417, 950

– (2012a) MNRAS 421, 3522

– (2012b) MNRAS 421, 3488

Hopkins, P. F., Torrey, P., Faucher-Giguère, C.-A., Quataert, E., & Murray, N. (2016) MNRAS 458, 816

Hopkins, P. F., Wetzel, A., et al. (2018) MNRAS 480, 800

Hu, C.-Y., Naab, T., Glover, S. C. O., Walch, S., & Clark, P. C. (2017) MNRAS 471, 2151

Iffrig, O. & Hennebelle, P. (2017) A&A 604, A70, A70

Kennicutt Jr., R. C. (1998) ApJ 498, 541

Kennicutt Jr., R. C., Calzetti, D., et al. (2007) ApJ 671, 333

Kennicutt, R. C. & Evans, N. J. (2012) ARA&A 50, 531

Kim, C.-G., Kim, W.-T., & Ostriker, E. C. (2011) ApJ 743, 25, 25

Kim, C.-G. & Ostriker, E. C. (2015) ApJ 815, 67, 67

Kim, C.-G., Ostriker, E. C., & Kim, W.-T. (2013) ApJ 776, 1, 1

Kraljic, K., Renaud, F., Bournaud, F., Combes, F., Elmegreen, B., Emsellem, E., & Teyssier, R. (2014) ApJ 784, 112, 112

Kroupa, P. (2002) Science 295, 82

Kruijssen, J. M. D. & Longmore, S. N. (2014) MNRAS 439, 3239

Krumholz, M. R. & Gnedin, N. Y. (2011) ApJ 729, 36, 36

Krumholz, M. R., McKee, C. F., & Tumlinson, J. (2009a) ApJ 693, 216

– (2009b) ApJ 699, 850

Krumholz, M. R. & Tan, J. C. (2007) ApJ 654, 304

Krumholz, M. R. & Thompson, T. A. (2007) ApJ 669, 289

Kuhlen, M., Krumholz, M. R., Madau, P., Smith, B. D., & Wise, J. (2012) ApJ 749, 36, 36

Lee, E. J., Miville-Deschênes, M.-A., & Murray, N. W. (2016) ApJ 833, 229, 229

Leitherer, C. et al. (1999) ApJS 123, 3

Leroy, A. K., Walter, F., Brinks, E., Bigiel, F., de Blok, W. J. G., Madore, B., & Thornley, M. D. (2008) AJ 136, 2782

Leroy, A. K., Walter, F., Sandstrom, K., et al. (2013) AJ 146, 19, 19

Li, Y., Mac Low, M.-M., & Klessen, R. S. (2005) ApJ 620, L19

– (2006) ApJ 639, 879

Liu, G., Koda, J., Calzetti, D., Fukuhara, M., & Momose, R. (2011) ApJ 735, 63, 63

Ma, X., Hopkins, P. F., Feldmann, R., Torrey, P., Faucher-Giguère, C.-A., & Kereš, D. (2017) MNRAS 466, 4780

Martin, C. L. & Kennicutt Jr., R. C. (2001) ApJ 555, 301

Martizzi, D., Faucher-Giguère, C.-A., & Quataert, E. (2015) MNRAS 450, 504

Martizzi, D., Fielding, D., Faucher-Giguère, C.-A., & Quataert, E. (2016) MNRAS 459, 2311

Mihos, J. C. & Hernquist, L. (1994) ApJ 437, 611

Murray, N. (2011) ApJ 729, 133, 133

Murray, N., Quataert, E., & Thompson, T. A. (2010) ApJ 709, 191

Narayanan, D., Krumholz, M. R., Ostriker, E. C., & Hernquist, L. (2012) MNRAS 421, 3127

Nidever, D. L., Majewski, S. R., & Butler Burton, W. (2008) ApJ 679, 432-459, 432

Oklopčić, A., Hopkins, P. F., Feldmann, R., Kereš, D., Faucher-Giguère, C.-A., & Murray, N. (2017) MNRAS 465, 952

Oliveira, J. M. (2009) *The Magellanic System: Stars, Gas, and Galaxies* ed. by J. T. Van Loon & J. M. Oliveira vol. 256 IAU Symposium, 191

Onodera, S. et al. (2010) ApJ 722, L127

Ostriker, E. C., McKee, C. F., & Leroy, A. K. (2010) ApJ 721, 975

Ostriker, E. C. & Shetty, R. (2011) ApJ 731, 41, 41

Padoan, P. (1995) MNRAS 277, 377

Papadopoulos, P. P. & Pelupessy, F. I. (2010) ApJ 717, 1037

Rafelski, M. et al. (2016) ApJ 825, 87, 87

Richings, A. J. & Schaye, J. (2016) MNRAS 458, 270

Robertson, B. E. & Kravtsov, A. V. (2008) ApJ 680, 1083

Rownd, B. K. & Young, J. S. (1999) AJ 118, 670

Roychowdhury, S., Huang, M.-L., Kauffmann, G., Wang, J., & Chengalur, J. N. (2015) MNRAS 449, 3700

Saitoh, T. R. et al. (2008) PASJ 60, 667

Schaye, J. (2004) ApJ 609, 667

Schaye, J. & Dalla Vecchia, C. (2008) MNRAS 383, 1210

Schmidt, M. (1959) ApJ 129, 243

Schruba, A., Leroy, A. K., Walter, F., Sandstrom, K., & Rosolowsky, E. (2010) ApJ 722, 1699

Scoville, N. et al. (2016) ApJ 820, 83, 83

Semenov, V. A., Kravtsov, A. V., & Gnedin, N. Y. (2016) ApJ 826, 200, 200

Shapiro, K. L. et al. (2010) MNRAS 402, 2140

Shetty, R., Clark, P. C., & Klessen, R. S. (2014) MNRAS 442, 2208

Shetty, R., Kelly, B. C., & Bigiel, F. (2013) MNRAS 430, 288

Shetty, R., Kelly, B. C., Rahman, N., et al. (2014) MNRAS 437, L61

Shetty, R. & Ostriker, E. C. (2012) ApJ 754, 2, 2

Silk, J. (1997) ApJ 481, 703

Solomon, P. M., Downes, D., Radford, S. J. E., & Barrett, J. W. (1997) ApJ 478, 144

Solomon, P. M. & Vanden Bout, P. A. (2005) ARA&A 43, 677

Sparre, M. et al. (2015) MNRAS 447, 3548

Springel, V. & Hernquist, L. (2003) MNRAS 339, 289

Stanimirović, S., Staveley-Smith, L., & Jones, P. A. (2004) ApJ 604, 176

Strong, A. W. & Mattox, J. R. (1996) A&A 308, L21

Su, K.-Y., Hopkins, P. F., Hayward, C. C., Faucher-Giguère, C.-A., Kereš, D., Ma, X., & Robles, V. H. (2017) MNRAS 471, 144

Tacconi, L. J. et al. (2013) ApJ 768, 74, 74

Thompson, T. A., Quataert, E., & Murray, N. (2005) ApJ 630, 167

Toomre, A. (1964) ApJ 139, 1217

Torrey, P., Hopkins, P. F., Faucher-Giguère, C.-A., Vogelsberger, M., Quataert, E., Kereš, D., & Murray, N. (2017) MNRAS 467, 2301

Verley, S., Corbelli, E., Giovanardi, C., & Hunt, L. K. (2010) A&A 510, A64, A64

Wada, K. & Norman, C. A. (2007) ApJ 660, 276

Wei, L. H., Vogel, S. N., Kannappan, S. J., Baker, A. J., Stark, D. V., & Laine, S. (2010) ApJ 725, L62

Williams, J. P. & McKee, C. F. (1997) ApJ 476, 166

Wong, T. & Blitz, L. (2002) ApJ 569, 157

Chapter 3

STACKED STAR FORMATION RATE PROFILES OF BURSTY GALAXIES EXHIBIT 'COHERENT' STAR FORMATION

"Stacking is Hacking" – Dr. Christopher C. Hayward

Orr, M. E. et al. (2017) ApJ 849, L2

ABSTRACT

In a recent work based on 3200 stacked Hα maps of galaxies at $z \sim 1$, Nelson et al. find evidence for 'coherent star formation': the stacked SFR profiles of galaxies above (below) the 'star formation main sequence' (MS) are above (below) that of galaxies on the MS at all radii. One might interpret this result as inconsistent with highly bursty star formation and evidence that galaxies evolve smoothly along the MS rather than crossing it many times. We analyze six simulated galaxies at $z \sim 1$ from the Feedback in Realistic Environments (FIRE) project in a manner analogous to the observations to test whether the above interpretations are correct. The trends in stacked SFR profiles are qualitatively consistent with those observed. However, SFR profiles of individual galaxies are much more complex than the stacked profiles: the former can be flat or even peak at large radii because of the highly clustered nature of star formation in the simulations. Moreover, the SFR profiles of individual galaxies above (below) the MS are not systematically above (below) those of MS galaxies at all radii. We conclude that the time-averaged coherent star formation evident in stacks of observed galaxies is consistent with highly bursty, clumpy star formation of individual galaxies and is not evidence that galaxies evolve smoothly along the MS.

3.1 Introduction

Given that star formation is one of the fundamental processes driving galaxy formation, it is crucial to understand what governs star formation, both on local and galactic scales. One of the open questions regarding star formation on galactic scales is whether it is coherent in space and/or time because of, e.g., gas accretion or environmental effects or highly stochastic because of, e.g., violent stellar feedback. The relatively tight correlation found between the star formation rate (SFR) and stellar mass (M_*) of actively star-forming galaxies at a range of redshifts (Brinchmann et al., 2004; Noeske et al., 2007; Peng et al., 2010; Wuyts et al., 2011), commonly referred to as the star formation main sequence (MS), is sometimes taken as evidence of the former. In particular, some authors argue that galaxies evolve smoothly along the sequence (rather than cross it), as is typically the case in large-volume cosmological simulations (such as those of the *Illustris* and EAGLE projects; Vogelsberger et al. 2014; Schaye et al. 2015) that rely on sub-grid ISM models. In such simulations, galaxies maintain their positions relative to the locus of the MS for $\gg$ 100-Myr timescales (Sparre, Hayward, Springel, et al., 2015; Schaye et al., 2015). However, high-resolution cosmological zoom-in simulations that include explicit multi-channel stellar feedback suggest that star formation is very bursty in some regimes (due to the clustered nature of star formation, violent stellar feedback, galactic fountains, and stochastic gas inflow), including at high redshift. This burstiness causes galaxy-scale star formation to be a chaotic process in which galaxies cross the MS many times rather than evolve smoothly along it (Hopkins et al., 2014; Muratov et al., 2015; Sparre, Hayward, Feldmann, et al., 2017; Faucher-Giguère, 2018).

Recent works (e.g., Nelson, van Dokkum, Förster Schreiber, et al., 2016; González Delgado et al., 2016) have investigated the average radial SFR profile of galaxies at a given mass and redshift by stacking Hα maps of hundreds to thousands of galaxies. In particular, this work is motivated by the work of Nelson, van Dokkum, Förster Schreiber, et al. (2016), who, based on a stacking analysis of 3200 galaxies, found evidence for what they term 'coherent star formation': at a given mass and redshift, galaxies above (below) the MS have stacked SFR profiles above (below) those of MS galaxies at all radii; in contrast, their stellar mass profiles are nearly identical. This might be interpreted as evidence for smooth evolution of galaxies along and parallel to the MS, with coherent elevation (suppression) of star formation at all radii for galaxies above (below) the MS. In other words, galaxies above (below) the main sequence remain above (below) the main sequence for long periods of time.

This scenario is seemingly inconsistent with very bursty star formation, i.e., SFR variations of an order of magnitude or more on timescales $\lesssim 100$ Myr.

To determine whether highly bursty star formation is consistent with the observations of Nelson, van Dokkum, Förster Schreiber, et al. (2016), we investigate the radial SFR, stellar mass, and specific SFR (sSFR) surface density profiles of simulated galaxies from the Feedback in Realistic Environments (FIRE) project[1]. We analyze the simulated galaxies in a manner analogous to the observations to understand the differences amongst the profiles of galaxies that lie above, on, and below the MS, and we compare individual galaxy profiles with the stacked profiles. We show that despite the star formation in the FIRE galaxies being highly bursty at the redshifts of interest,[2] which causes them to cross the MS many times rather than evolve parallel to it, the stacked profiles exhibit trends similar to those observed. Consequently, we conclude that the time-averaged coherent star formation evident in stacks of observed galaxies is consistent with highly bursty, clumpy star formation of individual galaxies and is not (necessarily) evidence that galaxies evolve smoothly along the MS.

3.2 Methods

We investigate the radial star formation profiles of a selection of the FIRE-1 galaxy simulations originally presented in Hopkins et al. (2014) and Chan et al. (2015), which were run using GIZMO (Hopkins, 2015) in its pressure-energy smoothed particle hydrodynamics (P-SPH) mode (Hopkins, 2013). The physics, source code, and all numerical parameters are identical to those in all other FIRE-1 simulations. The simulations incorporate cooling from $10 - 10^{10}$ K, including atomic, molecular, and metal-line cooling processes and accounting for photo-heating by a UV background (Faucher-Giguère et al., 2009), in addition to self-shielding. Stars form only in dense ($n \gtrsim 50 \, \mathrm{cm}^{-3}$), self-gravitating, self-shielding, molecular gas. Multi-channel stellar feedback from supernovae, radiation pressure from massive stars, stellar winds, and photo-ionization/heating is treated explicitly based on the outputs of the STARBURST99 (Leitherer et al., 1999) stellar evolution models, assuming a Kroupa (2002) IMF. The stellar and gas masses and stellar half-mass radii of the simulations analyzed here at $z \approx 1$ are presented in Table 3.1.

---

[1] http://fire.northwestern.edu

[2] In the FIRE simulations, galaxies with $M_* \gtrsim 10^{10} \, M_\odot$ exhibit highly bursty star formation at high redshift and transition to steady star formation at $z \lesssim 1$; lower mass galaxies always exhibit bursty star formation (Sparre, Hayward, Feldmann, et al., 2017).
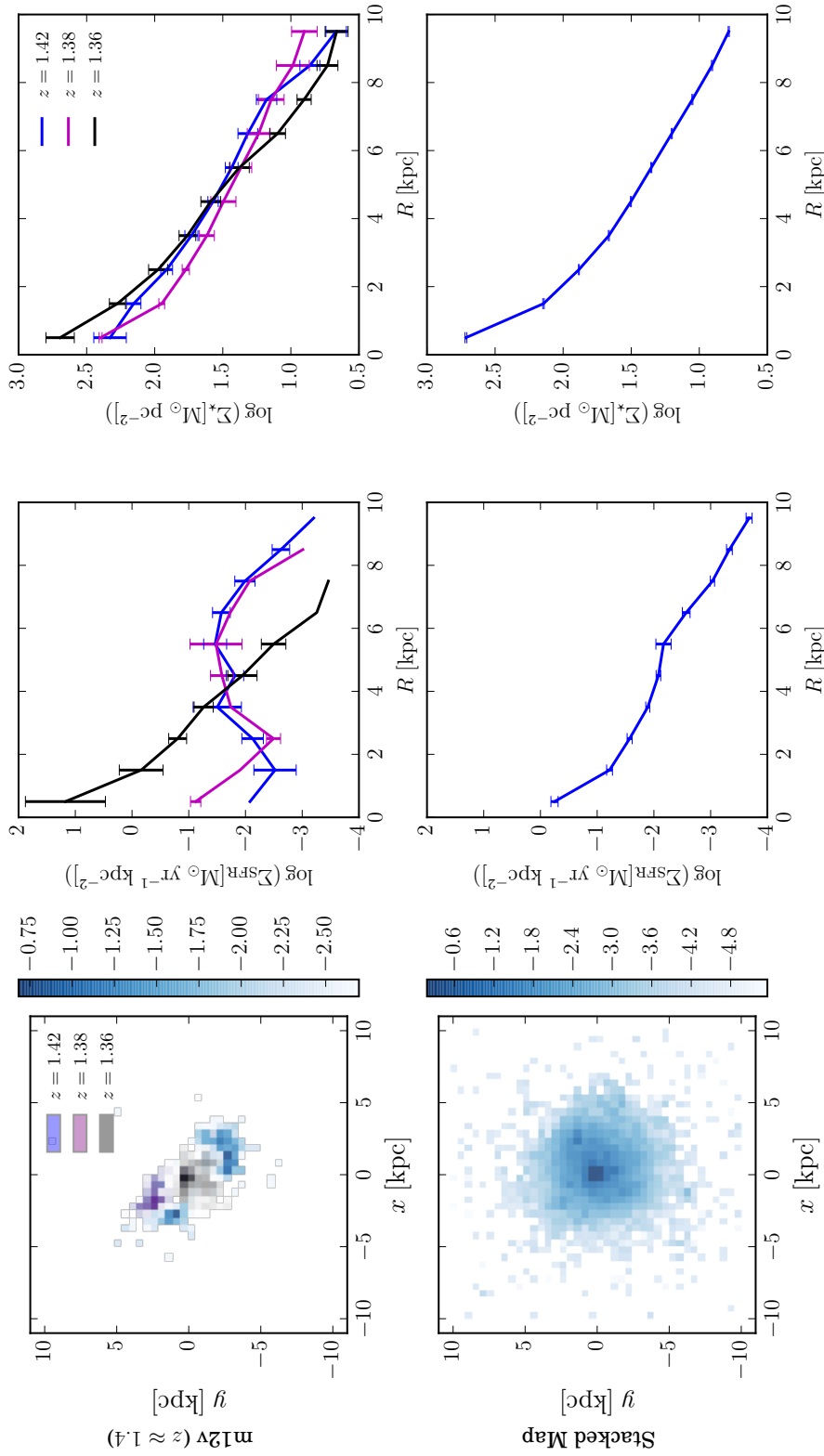
Figure 3.1: *Top row:* three SFR surface density maps (*left column*) and radial SFR (*middle column*) and mass (*right column*) profiles from different time slices of the **m12v** simulation around $z \approx 1.4$. *Bottom row:* the results of stacking 205 snapshots in total from three different central galaxies with $M_* \sim 10^{10}$ $M_\odot$ at redshifts $0.7 < z < 1.5$. The individual galaxy's SFR maps reveal irregular, asymmetric, and highly time-variable SFR spatial distributions, and individual maps are often dominated by off-center star-forming clumps. In two cases, the radial SFR profiles have central peaks, but in one of those cases, the bulk of the star formation corresponds to the local maximum at $R \sim 5$ kpc. The stacked map exhibits a clear central peak in SFR and has a monotonically radially decreasing SFR profile; it thus does not capture the diversity of SFR maps and profiles of single galaxy snapshots. In contrast, the individual galaxies' stellar mass profiles are all similar to the stacked stellar mass profile.
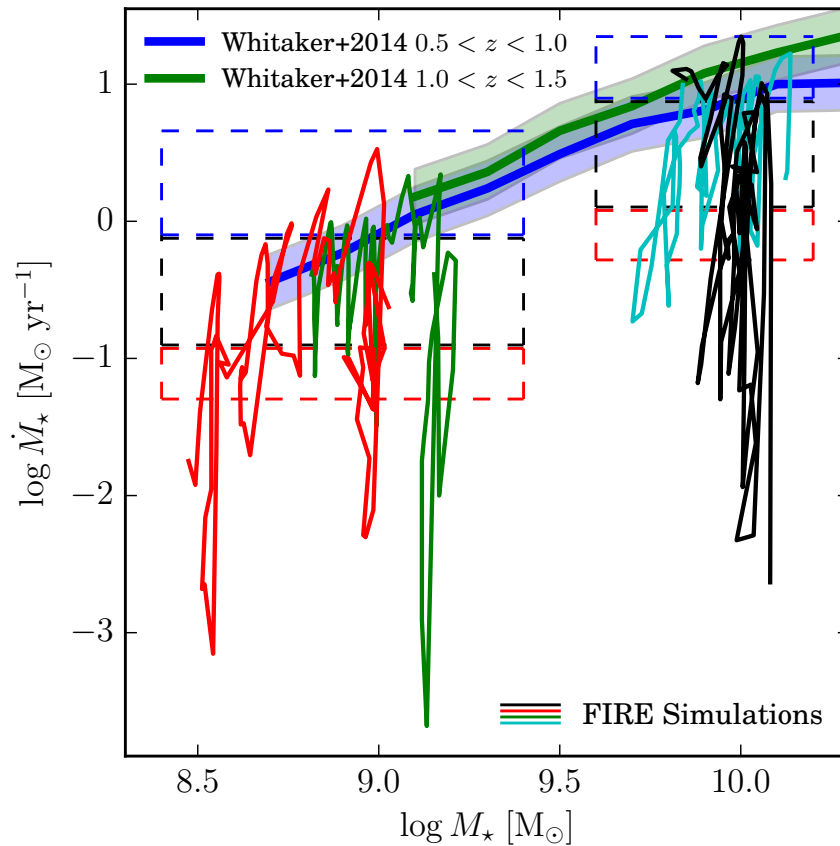
Figure 3.2: Tracks of two individual galaxy runs from each $M_\star$ bin (individually colored) in the SFR-$M_\star$ plane for $0.7 < z < 1.5$. $\dot{M}_\star$ is the 100 Myr-averaged SFR within the central 20 kpc of each main halo; $M_\star$ is calculated within the same aperture. Solid blue (green) lines indicate the star formation main sequence (MS) in the redshift interval $0.5 < z < 1.0$ ($1.0 < z < 1.5$) found by Whitaker et al. (2014); the shaded regions represent the intrinsic scatter of 0.2 dex found by Speagle et al. (2014). The dashed colored boxes indicate the cuts used in this work to classify galaxies as above (blue), on (black), or below (red) the MS. At these redshifts, FIRE galaxies have rapidly changing SFRs and do not evolve parallel to the MS but rather cross it many times.
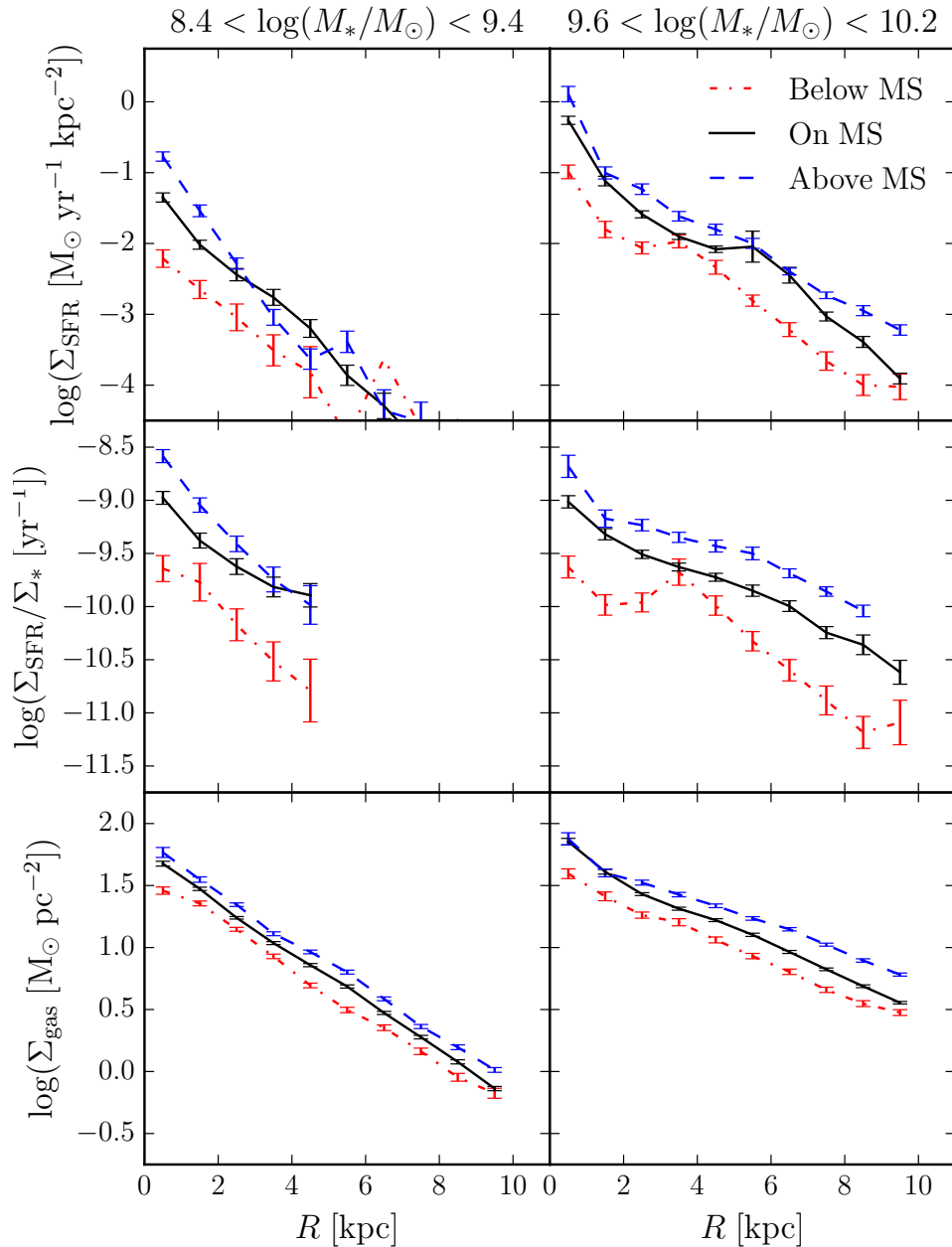
Figure 3.3: Stacked SFR (*top row*), sSFR (*middle row*), and neutral gas (*bottom row*) surface density profiles (binned into 1 kpc annuli) for two stellar mass bins, $8.4 < \log(M_\star/M_\odot) < 9.4$ (*left column*) and $9.6 < \log(M_\star/M_\odot) < 10.2$ (*right column*), for $0.7 < z < 1.5$. Prior to stacking, in each mass bin, the galaxies have been separated according to their position relative to the MS: above (*blue dashed line*), on (*black solid*), or below (*red dash-dotted*). The SFR, sSFR, and Σ_{gas} profiles generally decrease monotonically with radius. Moreover, the stacked profiles of galaxies above (below) the MS are above (below) those of MS galaxies at nearly all radii.
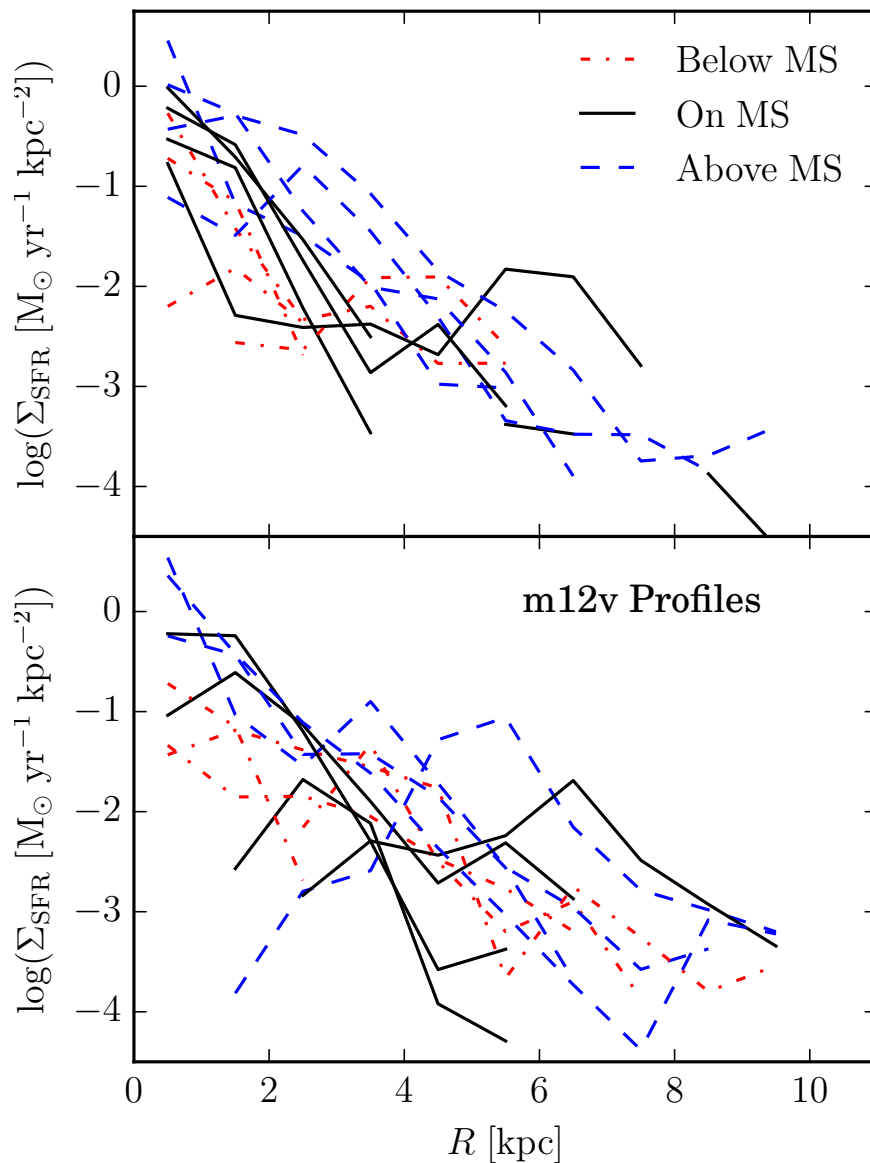
Figure 3.4: *Top*: SFR surface density profiles of randomly selected individual snapshots (at $0.7 < z < 1.5$) with $9.6 < \log(M_\star/\mathrm{M_\odot}) < 10.2$, including those above (*blue dashed*), on (*black solid*), and below (*red dash-dotted*) the MS (four of each type). Error bars have been omitted for clarity. The (10 Myr-averaged) SFR profiles of galaxies above (below) the MS are not systematically above (below) those of MS galaxies. Moreover, in some cases, the profiles peak at large radii. *Bottom*: Consistent results are seen for randomly selected snapshots of a single galaxy run, **m12v**, in the same redshift and mass bins. Stacking reflects the fact that star formation in the simulated galaxies is coherent in a time-averaged sense even though individual galaxies evolve in a bursty manner and not parallel to the MS.

Table 3.1: Simulation Properties at $z = 1$

Name	$M_\star$ $(10^9\,\mathrm{M}_\odot)$	M_{gas} $(10^9\,\mathrm{M}_\odot)$	R_{half} (kpc)
m11h383[†]	1.1	2.3	2.9
m11	0.81	2.3	5.4
m11v	1.7	1.2	5.9
m12q	13	2.3	3.3
m12i	12	6.8	5.4
m12v	13	2.7	6.4

(1) Name: simulation designation.
(2–3) $M_\star$, M_{gas}: Stellar & gas masses in maps.
(4) R_{half}: Stellar half-mass radius.
[†] Except for m11h383 (Chan et al., 2015),
all simulations are from Hopkins et al. (2014).

To probe the radial SFR profiles in the simulations, we use spatially resolved face-on projected maps of SFR and stellar mass surface density from simulated galaxies spanning redshifts $z = 0.7 - 1.5$ produced by Orr et al. (2017). To compare the snapshots with the observations of Nelson, van Dokkum, Förster Schreiber, et al. (2016), we use maps with 1 kpc^2 pixels centered on the centers of the stellar mass distributions in the snapshots. 10 Myr-averaged SFR maps are computed by summing the stellar mass in young ($< 10\,\mathrm{Myr}$) star particles in each pixel, correcting for the mass lost due to stellar evolution effects using STARBURST99 (Leitherer et al., 1999), and dividing by 10 Myr. This time interval approximately corresponds to the timescale traced by recombination lines such as Hα (Kennicutt et al., 2012).

3.3 Results

Fig. 3.1 shows several individual SFR surface density maps and the result of stacking many maps from the same $M_\star$ bin, in addition to their respective radially averaged SFR and stellar mass surface density profiles. The top row shows three of the 10 Myr-averaged SFR maps of the **m12v** central galaxy from Hopkins et al. (2014) at $z \approx 1.4$, with $M_* \sim 10^{10}\,M_\odot$, with 1 kpc pixel sizes, and their associated radially averaged SFR and stellar mass surface density profiles. The SFR profiles of the galaxy vary considerably from $z = 1.42 - 1.36$ and are not always centrally peaked. The bottom row shows the result of stacking the SFR maps of 205 snapshots in total, from three distinct galaxies (~ 70 from each, with $\Delta z = 0.01$ spacing[3]) in the $9.6 < \log(M_\star/\mathrm{M}_\odot) < 10.2$ stellar mass bin. For all radial profiles shown in this

---

[3]For $0.7 < z < 1.5$, the snapshot spacing of $\Delta z = 0.01$ corresponds to time spacing of $25 - 56$ Myr.

work, we compute the error bars by bootstrap resampling the pixels in the annuli following Nelson, van Dokkum, Förster Schreiber, et al. (2016). In the stacked map, we see a much smoother and more azimuthally symmetric spatial distribution, and the corresponding radially averaged profiles are smoother, monotonically decreasing functions of radius. Here, by averaging hundreds of snapshots of galaxies of similar mass, we recover the fact that the simulated galaxies have higher gas densities in their centers, and thus form more stars there on average. However, the SFR profiles of individual galaxies at a given time can differ dramatically from the stacked profile. In contrast, the stacked stellar mass profile is fairly representative of the individual profiles.

Fig. 3.2 shows tracks of four simulated galaxies in the SFR-$M_\star$ plane for $0.7 < z < 1.5$; the 100 Myr-averaged SFR is employed. The observed MS (Whitaker et al., 2014) and scatter (Speagle et al., 2014) in two redshift bins intersecting this interval are shown. In this redshift and mass range, the individual simulated galaxies experience significant (sometimes order of magnitude or more), rapid (timescales $\lesssim$ 100 Myr) SFR variations (see Sparre, Hayward, Feldmann, et al. 2017 for a detailed study) and clearly do not evolve parallel to the MS.[4]

Following Nelson, van Dokkum, Förster Schreiber, et al. (2016), we label individual snapshots as being above, below, or on an MS determined by the distribution of the galaxy-integrated 100 Myr-averaged SFRs in a given $M_\star$ bin (because Nelson, van Dokkum, Förster Schreiber, et al. 2016 classify galaxies relative to the MS according to their UV+IR SFRs, and for actively star-forming galaxies, this indicator traces the SFR over the past $\sim$ 100 Myr; Kennicutt et al. 2012; Hayward, Lanz, et al. 2014). For a given $M_\star$ bin, we rank the galaxies by SFR and consider the median value to be the locus of the MS. We then employ the same SFR cuts as Nelson, van Dokkum, Förster Schreiber, et al. (2016), defining galaxy snapshots within ±0.4 dex of the median SFR to be on the MS and those $+0.4 - 1.2$ dex and $-(0.4 - 0.8)$ dex away to be above and below the MS, respectively. These cuts are represented by the dashed colored boxes in Fig. 3.2.

We then stack individual galaxy maps according to their position with respect to the MS in two bins of M_*, producing average SFR, specific SFR, and neutral gas (atomic + molecular) surface density profiles, which are presented in Fig. 3.3. We see that for both $M_\star$ bins, the stacked SFR profile of galaxies above (below) the MS is above

---

[4]The galaxies' stellar masses do not increase monotonically in time because the stellar mass is computed within a radius of 20 kpc from the halo center; when satellites leave the aperture, the total stellar mass can decrease.

(below) the SFR profile of galaxies on the MS at nearly all radii, i.e., star formation appears to be coherently enhanced (suppressed) at nearly all radii in galaxies above (below) the MS. Moreover, the stacked SFR profiles exhibit a similar approximately exponential shape, peaking in the center and declining with radius, regardless of position with respect to the MS. The stacked stellar mass surface density profiles are nearly identical in each $M_\star$ bin for all classes of galaxies, so we do not show them. The sSFR surface density profiles in Fig. 3.3 also exhibit a clear separation by class. The neutral gas surface density profiles also vary systematically across the MS, but the difference between above- and below-MS galaxies is considerably less than for the sSFR profiles. We note that the results of Fig. 3.3 do not qualitatively change when the maps are re-normalized by their half-mass radii before stacking, indicating that these results are somewhat robust to evolution within the redshift interval and to the particular manner of stacking. We conclude that coherent star formation is apparent in the stacked SFR profiles despite the underlying galaxies exhibiting very bursty star formation and often having their total SFRs dominated by individual off-center clumps.

One apparent tension between the observations and simulations is that in the simulations, the sSFR profiles are generally centrally peaked, whereas the stacked Hα equivalent width profiles of observed galaxies are flat (Nelson, van Dokkum, Förster Schreiber, et al., 2016; Tacchella et al., 2017). This tension may be partially due to dust attenuation (see Nelson, van Dokkum, Momcheva, et al. 2016), especially for above-MS galaxies, which may have significant central dust-obscured star formation (Wuyts et al., 2011; Hemmati et al., 2015). However, it is not clear that correcting for dust would resolve the discrepancy, especially for lower mass galaxies, and this issue deserves further attention. Another possible reason is that in low-mass galaxies, our centering on the stellar center of mass likely differs from the centering in the observations (based on light), which is likely affected by lumpy/irregular morphologies and local variations in mass-to-light ratio; this effect may cause the observed stacked profiles to be artificially flat.

To connect the stacked SFR profiles with those of individual galaxies at a given time, we examine a randomly chosen sub-sample of the individual radial SFR profiles in the $9.6 < \log(M_\star/\mathrm{M_\odot}) < 10.2$ stellar mass bin in the top panel of Fig. 3.4.[5] Although galaxies classified as above the MS have greater 100 Myr-averaged SFR values than those on or below the MS, there is significant crossing of the (10 Myr-

---

[5]Not all of the profiles reach the centers of the galaxies because some have identically zero SFR at their centers.

averaged) SFR profiles at modest galactocentric radii, i.e., the SFR profiles of individual galaxies above (below) the MS are typically not systematically above (below) those of MS galaxies. There does not appear to be significant differences in the *forms* of SFR profiles amongst these classes of galaxies in the FIRE simulations; only their relative normalization differs, a feature that Nelson, van Dokkum, Förster Schreiber, et al. (2016) describe as 'coherent star formation'. By selecting galaxies above (or below) the MS, we tend to select galaxies just as they are forming many stars in a burst (are in a relatively quiescent period). The bottom panel of Fig. 3.4, which shows radial SFR profiles of a single galaxy (**m12v** from Hopkins et al., 2014) at different randomly drawn times within the redshift interval $0.7 < z < 1.5$ (four each above, on and below the MS), reinforces this conclusion. The galaxy's SFR profile varies rapidly with time, and there is no clear dependence on the total SFR (i.e., position relative to the MS).

3.4 Summary and discussion

We have analyzed the individual and stacked SFR maps and profiles of a sample of simulated galaxies from the FIRE project in a manner analogous to the observational analysis of Nelson, van Dokkum, Förster Schreiber, et al. (2016). Despite the FIRE galaxies exhibiting large variations in SFR on $\sim 10 - 100$ Myr timescales and often having their SFRs concentrated in a few massive off-center clumps, their stacked SFR profiles exhibit spatial coherent star formation in a time- and azimuthally averaged sense. Moreover, individual SFR profiles in the FIRE simulations often look nothing like the stacked profiles. A similar effect has been seen in observations: Fig. 4 of Nelson, van Dokkum, Förster Schreiber, et al. (2016), for example, shows that the individual Hα maps combined into stacks exhibit a variety of different morphologies. Moreover, the stacked SFR profiles of simulated galaxies above (below) the MS are above (below) those of the MS galaxies at all radii. This is consistent with the observations of Nelson, van Dokkum, Förster Schreiber, et al. (2016), indicating that in simulations with resolved ISM and bursty stellar feedback, star formation can still be coherent in a time-averaged sense. We stress that in the mass and redshift ranges considered, the FIRE galaxies cross the MS many times throughout their evolution due to their highly bursty star formation histories; thus, one should not interpret the appearance of coherent star formation in stacked SFR profiles as evidence that galaxies maintain their positions relative to the MS for long periods of time.

There are two main lessons from this analysis. First, although stacking recovers

the time-averaged spatial coherence of star formation in the simulations, it hides the chaotic, incoherent nature of star formation on kiloparsec-scales. In the simulations, the SFR is on average higher in the centers of galaxies, owing to galaxies typically having centrally peaked gas surface density profiles; the stacked profiles recover this average behavior. However, the bursty nature of star formation in the FIRE galaxies, in which the SFR at a given time can be dominated by a few short-lived ($\sim$ 20 Myr; Oklopčić et al., 2017; Sparre, Hayward, Feldmann, et al., 2017; Faucher-Giguère, 2018) massive clumps of star formation at various galactocentric radii, is obscured by the stacking procedure. We indeed find that the stacking analysis makes stochastic enhancements in the SFR from massive clumps, which are often located significantly off-center, indistinguishable from global enhancements in the SFR across the disc; this possibility was noted in Nelson, van Dokkum, Förster Schreiber, et al. (2016).

Second, the simulations discussed here provide insight into what causes galaxies to be above or below the MS. In Fig. 3.4, we see that galaxies selected to be above the MS have preferentially recently formed several massive clumps of stars; this is true whether the SFR is averaged over 10 or 100 Myr (i.e., whether Hα- or UV+IR-based SFRs are used). Conversely, galaxies below the MS are unlikely to have formed many massive clumps within the past $\sim$ 100 Myr and rather are likely to be in a low-sSFR period, which can last for a few 100s of Myr in the simulations (Muratov et al., 2015; Sparre, Hayward, Feldmann, et al., 2017); if they have formed a few clumps, the associated SFRs are not as high as in the above-MS galaxies. Moreover, on average, the below-MS galaxies tend to have lower SFRs at all radii than above-MS galaxies (but this is not true of the individual profiles) because these galaxies have, on average, lower gas surface densities (Fig. 3.3) than the above-MS galaxies (owing to stochasticity in gas accretion from both the IGM and galactic fountains and/or recent strong outflows driven by stellar feedback; Muratov et al. 2015; Anglés-Alcázar et al. 2017; Hayward and Hopkins 2017). However, in the simulations, these differences are stochastic rather than long-lived, as evident from the bottom panel of Fig. 3.4, and the FIRE galaxies can cross the MS multiple times within 100 Myr (Fig. 3.2; see also Sparre, Hayward, Feldmann, et al., 2017). Note, however, that the galaxies considered here are of relatively low stellar mass ($M_\star \lesssim 10^{10}$ $M_\odot$), and more massive simulated galaxies tend to exhibit less bursty star formation and smoother mass, metallicity, and SFR profiles, especially at low redshift (Sparre, Hayward, Feldmann, et al., 2017; Ma et al., 2017).

We find that very bursty star formation is consistent with spatially coherent star for-

mation in stacked images. We thus caution against interpreting such time-averaged coherent star formation as evidence that galaxies maintain their positions relative to the MS owing to, e.g., systematic differences in gas accretion rates and thus gas fractions. A crucial next step is to place observational constraints on the timescale over which galaxies oscillate across the main sequence, perhaps via measurement of SFR tracers that probe different timescales (e.g., Guo et al., 2016). Although our analysis does not rule out the possibility that galaxies maintain their positions relative to the MS for long periods of time, it demonstrates that simulations in which this is not the case yield stacked SFR profiles consistent with those observed, including spatially coherent star formation in a time-averaged sense. More generally, our analysis demonstrates that simulations are a valuable tool that can help understand behaviors of individual galaxies that may be masked in stacked observations.

Acknowledgements

References

Anglés-Alcázar, D., Faucher-Giguère, C.-A., Kereš, D., Hopkins, P. F., Quataert, E., & Murray, N. (2017) MNRAS 470, 4698

Brinchmann, J., Charlot, S., White, S. D. M., Tremonti, C., Kauffmann, G., Heckman, T., & Brinkmann, J. (2004) MNRAS 351, 1151

Chan, T. K., Kereš, D., Oñorbe, J., Hopkins, P. F., Muratov, A. L., Faucher-Giguère, C.-A., & Quataert, E. (2015) MNRAS 454, 2981

Faucher-Giguère, C.-A., Lidz, A., Zaldarriaga, M., & Hernquist, L. (2009) ApJ 703, 1416

Faucher-Giguère, C.-A. (2018) MNRAS 473, 3717

González Delgado, R. M. et al. (2016) A&A 590, A44, A44

Guo, Y. et al. (2016) ApJ 833, 37, 37

Hayward, C. C. & Hopkins, P. F. (2017) MNRAS 465, 1682

Hayward, C. C., Lanz, L., et al. (2014) MNRAS 445, 1598

Hemmati, S., Mobasher, B., Darvish, B., Nayyeri, H., Sobral, D., & Miller, S. (2015) ApJ 814, 46, 46

Hopkins, P. F. (2013) MNRAS 428, 2840

– (2015) MNRAS 450, 53

Hopkins, P. F., Kereš, D., Oñorbe, J., Faucher-Giguère, C.-A., Quataert, E., Murray, N., & Bullock, J. S. (2014) MNRAS 445, 581

Kennicutt, R. C. & Evans, N. J. (2012) ARA&A 50, 531

Kroupa, P. (2002) Science 295, 82

Leitherer, C. et al. (1999) ApJS 123, 3

Ma, X., Hopkins, P. F., Feldmann, R., Torrey, P., Faucher-Giguère, C.-A., & Kereš, D. (2017) MNRAS 466, 4780

Muratov, A. L., Kereš, D., Faucher-Giguère, C.-A., Hopkins, P. F., Quataert, E., & Murray, N. (2015) MNRAS 454, 2691

Nelson, E. J., van Dokkum, P. G., Förster Schreiber, N. M., et al. (2016) ApJ 828, 27, 27

Nelson, E. J., van Dokkum, P. G., Momcheva, I. G., et al. (2016) ApJ 817, L9, L9

Noeske, K. G. et al. (2007) ApJ 660, L47

Oklopčić, A., Hopkins, P. F., Feldmann, R., Kereš, D., Faucher-Giguère, C.-A., & Murray, N. (2017) MNRAS 465, 952

Orr, M. E. et al. (2017) ApJ 849, L2

Peng, Y.-j. et al. (2010) ApJ 721, 193

Schaye, J. et al. (2015) MNRAS 446, 521

Sparre, M., Hayward, C. C., Feldmann, R., Faucher-Giguère, C.-A., Muratov, A. L., Kereš, D., & Hopkins, P. F. (2017) MNRAS 466, 88

Sparre, M., Hayward, C. C., Springel, V., et al. (2015) MNRAS 447, 3548

Speagle, J. S., Steinhardt, C. L., Capak, P. L., & Silverman, J. D. (2014) ApJS 214, 15, 15

Tacchella, S. et al. (2017) ApJ 844, L1, L1

Vogelsberger, M. et al. (2014) MNRAS 444, 1518

Whitaker, K. E. et al. (2014) ApJ 795, 104, 104

Wuyts, S. et al. (2011) ApJ 742, 96, 96

Chapter 4

A SIMPLE NON-EQUILIBRIUM FEEDBACK MODEL FOR GALAXY-SCALE STAR FORMATION: DELAYED FEEDBACK AND SFR SCATTER

Orr, M. E., Hayward, C. C., & Hopkins, P. F. (2019) MNRAS 486, 4724

ABSTRACT

We explore a class of simple non-equilibrium star formation models within the framework of a feedback-regulated model of the ISM, applicable to kiloparsec-scale resolved star formation relations (e.g., Kennicutt-Schmidt). Combining a Toomre-Q-dependent local star formation efficiency per free-fall time with a model for delayed feedback, we are able to match the normalization and scatter of resolved star formation scaling relations. In particular, this simple model suggests that large (~dex) variations in star formation rates (SFRs) on kiloparsec-scales may be due to the fact that supernova feedback is not instantaneous following star formation. The scatter in SFRs at constant gas surface density in a galaxy then depends on the properties of feedback and when we observe its star-forming regions at various points throughout their collapse/star formation "cycles". This has the following important observational consequences: (1) the scatter and normalization of the Kennicutt-Schmidt relation are relatively insensitive to the local (small-scale) star formation efficiency, (2) but depletion times and velocity dispersions in the gas are; (3) the scatter in and normalization of the Kennicutt-Schmidt relation is a sensitive probe of the feedback timescale and strength; (4) even in a model where $\tilde{Q}_{\mathrm{gas}}$ deterministically dictates star formation locally, time evolution, variation in local conditions (e.g., gas fractions and dynamical times), and variations between galaxies can destroy much of the observable correlation between SFR and $\tilde{Q}_{\mathrm{gas}}$ in resolved galaxy surveys. Additionally, this model exhibits large scatter in SFRs at low gas surface densities, in agreement with observations of flat outer HI disk velocity dispersion profiles.

4.1 Introduction

One of the fundamental characteristics of star formation is that it is globally inefficient: galaxies convert only a few per cent of their cold gas reservoirs into stars per dynamical time (Kennicutt, Calzetti, et al., 2007). As to why this is the case, there are two broad frameworks for regulating star formation in galaxies: dynamics and feedback. Dynamical regulation argues that stars form as rapidly as they are able, but that dynamical processes such as turbulent shear, differential rotation, or gas expansion behind spiral arms govern the fraction of gas with conditions favorable to star formation (Saitoh et al., 2008; Robertson et al., 2012; Elmegreen and Hunter, 2015; Semenov et al., 2017). In this regime, star formation efficiency (SFE) is low locally, in complement with its global value. Feedback regulation argues instead that star formation could be locally highly efficient in regions which are actually collapsing without local feedback present, but that stellar feedback (usually in addition to dynamical processes), in the form of ionizing radiation or supernova explosions, heat and stir the interstellar medium (ISM), preventing further star formation in most regions and times (Thompson et al., 2005; Murray et al., 2010; Ostriker, McKee, et al., 2010; Shetty et al., 2012; Hopkins, Kereš, et al., 2014; Kim et al., 2015b; Hopkins, Wetzel, et al., 2018, among others).

Within the framework of feedback regulation there have been several related models describing various star formation 'laws', including the "outer disk" model of Ostriker and Shetty (2011), the "two-zone" theory of Faucher-Giguère et al. (2013), and radiation pressure supported models like Thompson et al. (2005), to name a few. Particular focus has been laid on models involving turbulent support of the ISM, as thermal heating processes become relatively ineffective at regulating star formation for gas surface densities above $\sim 10\,\mathrm{M_\odot\,pc^{-2}}$, where a self-shielded component of the ISM necessarily develops (Schaye, 2004; Krumholz et al., 2009a; Krumholz et al., 2009b; Hayward et al., 2017). Broadly, turbulently regulated models incorporate some metallicity dependence (often having to do with the metallicity dependence of the efficiency of SNe momentum coupling, Martizzi et al. 2015), local gas fraction (or stellar surface density, Ostriker and Shetty 2011), or local gas scale height dependence (Faucher-Giguère et al., 2013), in setting the equilibrium star formation rate.

These models have found general agreement with the *mean* observed star formation rates (either galaxy-integrated or as a function of radius) in nearby galaxies. However, observational studies of the spatially resolved (at ~kpc-scales) Kennicutt-

Schmidt relation have apparently characteristic $\pm 2\sigma$ scatters of $\sim 1-2$ dex in star formation rates at constant gas surface densities (Bigiel, Leroy, Walter, Brinks, et al., 2008; Leroy, Walter, Brinks, et al., 2008; Bigiel, Leroy, Walter, Blitz, et al., 2010; Leroy, Walter, Sandstrom, et al., 2013; Leroy, Schinnerer, et al., 2017), with a similar scatter having been seen in cosmological simulations (Orr et al., 2018). Generally, these variations in star formation rates (SFRs) within individual galaxies at constant gas surface density are not readily explained by local variations in metallicity. For instance, at fixed galactocentric radii in discs, gas metallicity is seen to vary at $\lesssim 0.1$ dex levels (Ho et al., 2017), whereas gas surface densities can vary by more than 2 dex, requiring SFE $\propto Z^{20}$ (not seen observationally, or having a theoretical basis for being the case) to explain SFR variations independent of gas surface densities. Nor are metallicity gradients large enough to explain the scatter, as generally gas surface densities fall far more quickly than metallicities (Ma et al., 2017). Gas fractions, too, appear lacking in their ability to drive large scatter in SFRs at constant gas surface density *within* galaxies (Leroy, Walter, Sandstrom, et al., 2013).

This large scatter could suggest that we are still missing some critical physics in our models, or observationally our inferred star formation rates and gas surface densities are introducing much larger errors than usually appreciated. From the side of theory, that we are roughly matching star formation rate distributions, and their scatter in particular, in cosmological simulations is heartening (Orr et al., 2018) and suggests the feedback physics included in simulations like those of Hopkins, Kereš, et al. (2014) and Hopkins, Wetzel, et al. (2018) or Agertz and Kravtsov (2015) are close to sufficient. On the side of observations, there remains work to be done in converging on conversion factors between luminosities or line widths, and star formation rates and gas masses but it is unlikely that these factors randomly vary by ~ 2 dex in neighboring kpc patches of ISM (Kennicutt and Evans, 2012; Narayanan et al., 2012; Bolatto et al., 2013).

Another possible resolution is that rather than star formation being locked to a 'law' dependent on gas surface density, there is some intrinsic uncertainty to it (Schruba et al., 2010; Calzetti et al., 2012; Kruijssen and Longmore, 2014; Kruijssen, Schruba, et al., 2018). Kruijssen and Longmore (2014) argue that star formation relations like that of the Kennicutt-Schmidt relation must necessarily break down on some scale due to the overlap (or lack thereof) both temporally and spatially between tracers of dense gas and star formation, and that scatter in these relations is a necessary

consequence. But to what extent does the framework of feedback regulation itself provide an intrinsic scatter to the predicted equilibrium star formation rates? After all, feedback is not instantaneous with star formation, as ionizing radiation is injected for upwards of 10 Myr (Leitherer et al., 1999), supernova feedback is not felt for the first $\sim$ 5 Myr, and then continues stochastically for $\sim$ 30 Myr (Agertz, Kravtsov, et al., 2013). The timescales for feedback injection are not coincidentally on the order of the lifetimes of star-forming regions themselves in the feedback-regulated model (Oklopčić et al., 2017; Semenov et al., 2018; Grudić et al., 2018). Star formation *equilibrium* need not be expected, even at the 10^6 M$_\odot$ giant molecular cloud (GMC) scale.

Indeed others (Benincasa et al., 2016; Torrey et al., 2017; Semenov et al., 2018) have argued that while star formation might be in static equilibrium (i.e., steady state) in some averaged sense, that it is locally in some *dynamical* equilibrium where the ISM is in a constant cycle of collapse, star formation, and cloud destruction/feedback. It is thus never instantaneously in local equilibrium, and is constantly oscillating between those phases (Benincasa et al., 2016; Semenov et al., 2017; Semenov et al., 2018).

In this chapter, within the framework of feedback regulation, we explore a simple non-equilibrium star formation model, which expands upon these previous works. Critically, we explore models wherein there is a non-trivial delay time, with respect to the local dynamical time, between the formation of young stars and the injection of the bulk of their feedback into the ISM. We investigate the results of including a time dependence between the criteria for star formation being met, and its effects being felt- in particular, the ability to explain significant ($\sim$dex) scatter in star formation rates in resolved galaxy scaling relations. We explore how this ultimately leads to scatter in the Kennicutt-Schmidt relation, but also a number of non-intuitive effects for observed galaxy scalings of quantities that enter the model.

4.2 Model

In a previous work (Orr et al., 2018), we explored the ability of turbulent energy injection, in the form of the effects of Type II SNe, to explain the equilibrium value of the Kennicutt-Schmidt relation in the FIRE simulations at gas surface densities $\gtrsim$ 10 M$_\odot$ pc^{-2} (similar in derivation to Ostriker and Shetty, 2011; Faucher-Giguère et al., 2013; Hayward et al., 2017). The predicted equilibrium was in good agreement with the median values seen in the simulations, which were themselves in good agreement

Table 4.1: Summary of variables used in this chapter

Symbol	Definition
$\dot{\Sigma}_\star$	Star formation rate surface density
Σ_g	Total gas surface density
$f_{\rm sf}$	Gas mass fraction in star-forming phase
f_g	Fraction of disk mass in gas
ρ_0	Disk mid-plane volume mass density
t_d	Delay timescale for the injection of feedback
δt_d	Period of feedback injection
α	Slope of power law for delay-time distribution of Type II SNe
H	Gas scale height
G	Newtonian gravitational constant
$P/m_\star$	Characteristic feedback momentum per mass of stars formed
$t_{\rm eddy}$	Eddy (disk scale height) crossing time
$\langle \epsilon_{\rm sf} \rangle$	Average star formation efficiency per eddy time (here, GMC-scale average value)
$\bar{\epsilon}_{\rm sf}$	Star formation efficiency per orbital dynamical time
$\tilde{Q}_{\rm gas}$	Modified Toomre-Q gas stability parameter
Ω	Local orbital dynamical time
σ	Turbulent gas velocity dispersion (3-D)

with the observed atomic+molecular formulation of the Kennicutt-Schmidt relation. However, the $\pm 2\sigma$ scatter seen, on the order of $\sim 1.5 - 2$ dex, was not fully explained by local environmental variations, e.g., metallicity, dynamical time, or stellar surface density. There appeared to be an intrinsic scatter of $\gtrsim$dex to the star formation rate distribution seen at any given gas surface density.

To explore the physical processes that cause scatter in resolved star formation scaling relations in disk environments within individual galaxies, let us consider a patch of the ISM where the turbulent velocity dispersion is taken to be roughly isotropic, where we assume

$$\sigma^2 = \sigma_R^2 + \sigma_z^2 + \sigma_\phi^2 \approx 3\sigma_R^2 \,, \tag{4.1}$$

or $\sigma \approx \sqrt{3}\sigma_R$ where σ is the overall gas velocity dispersion, and the subscripted σ's denote the velocity dispersions in the radial, vertical (i.e., line-of-sight in face-on galaxies), and tangential directions, respectively.

In the framework of a supersonic turbulent cascade, the largest eddies carry the bulk of the energy and momentum to first order, and we can take the momentum per area

in the turbulent/random motion of the gas to be the velocity dispersion at the largest scale (here, the gas disk scale height H) times the gas mass surface density Σ_g, that is $P_{turb} = \Sigma_g \sigma$. The timescale for the dissipation t_{diss} of this turbulent momentum[1] is roughly the (twice) eddy turnover time t_{eddy}, which is $t_{\text{eddy}} \approx H/\sigma_z$. If we assume that the gas disk is embedded in the potential of stellar disk with a larger scale height, as is seen in the Milky Way with the thin gas disk having a characteristic height of ~ 100 pc embedded within the larger ~ 300 pc stellar scale height (Gilmore et al., 1983; Scoville et al., 1987), and that the gravitational acceleration near the mid-plane due to the local disk mass itself is of the form $4\pi G \rho_0 z$, where ρ_0 is the mid-plane density (gas + stars), and the external potential[2] introduces a vertical acceleration component of $v_c^2 z/R^2 = \Omega^2 z$ (where $\Omega \equiv v_c/R$), then the vertical (z) density profile is a Gaussian with a characteristic scale height of

$$H = \frac{\sigma_z}{\Omega + \sqrt{4\pi G \rho_0}} \ . \tag{4.2}$$

So, $t_{diss} \approx 2t_{\text{eddy}} \approx 2H/\sigma_z \approx 2/(\Omega + \sqrt{4\pi G \rho_0})$. In the absence of stellar feedback, the turbulent momentum of this patch of the ISM would be expected to exponentially decay as

$$\dot{P}_{turb} = -\Sigma_g \sigma/t_{diss} = -P_{turb}(\Omega + \sqrt{4\pi G \rho_0})/2 \ , \tag{4.3}$$

which admits a solution for gas velocity dispersions of

$$\sigma(t) = \sigma_0 \exp\left(-t(\Omega + \sqrt{4\pi G \rho_0})/2\right) \ . \tag{4.4}$$

4.2.1 Equilibrium Model of Instantaneous Feedback Injection in Disk Environments

However, feedback from massive stars acts to inject momentum back into the ISM at the largest scales (i.e., disk scale heights, Padoan et al., 2016). Taking the characteristic momentum injected per mass of young stars formed to be $P/m_\star$, we can establish an equilibrium for σ if we balance the rate of momentum injection

---

[1] In Faucher-Giguère et al. (2013), they assume that turbulent *energy* dissipates in an eddy-crossing time. However, if $E_{turb} \sim P_{turb}^2/2\Sigma_g$ and Σ_g is constant, then $\dot{E}_{turb} \sim P_{turb}\dot{P}_{turb}/\Sigma_g$. The exponential turbulent energy dissipation rate $\dot{E}_{turb} \sim -E_{turb}/t_{\text{eddy}}$ becomes $P_{turb}\dot{P}_{turb}/\Sigma_g \sim -P_{turb}^2/2\Sigma_g t_{\text{eddy}}$, reducing to $\dot{P}_{turb} \sim -P_{turb}/2t_{\text{eddy}}$, i.e., that the turbulent *momentum* decays approximately in twice an eddy crossing time. For consistency, and since SNe are momentum-conserving, we adopt a momentum-centric focus throughout the chapter.

[2] Here, the local dark matter contribution is implicitly included, whereas it is ignored for simplicity in the disk self-gravity acceleration term as the baryonic component dominates the thin disk mass in galaxies. Our model could be extended to gas-rich dwarfs or high-redshift galaxies with poorly defined disks, but would require a different formulation of gas scale-lengths/heights.

from feedback, $\dot{\Sigma}_\star P/m_\star$, with the turbulence dissipation rate in Eq. 4.3, that is,

$$\left(\frac{P}{m_\star}\right)\dot{\Sigma}_\star = \Sigma_g \sigma (\Omega + \sqrt{4\pi G \rho_0})/2 \ . \tag{4.5}$$

Arguing that star-forming disks are marginally stable against gravitational instabilities, we invoke a modified[3] Toomre-Q criterion dictating instantaneous gas stability (Toomre, 1964),

$$\tilde{Q}_{\text{gas}} = \frac{\sqrt{2}\sigma_R \Omega}{\pi G \Sigma_{disk}} \ , \tag{4.6}$$

where $\Sigma_{\text{disk}} = \Sigma_g + \gamma \Sigma_\star$ is the mid-plane surface density, including the stellar component (with the factor γ accounting for the effective fraction of stellar mass within a gas scale height, $\gamma = 1 - \exp(-H/H_\star)$). We substitute this Toomre-Q into Eq. 4.5 for σ, recovering the Kennicutt-Schmidt relation for a turbulently supported ISM,

$$\dot{\Sigma}_\star = \pi G \tilde{Q}_{\text{gas}} \sqrt{\frac{3}{8}} \frac{\Sigma_g \Sigma_{disk}}{P/m_\star} \left(1 + \frac{\sqrt{4\pi G \rho_0}}{\Omega}\right) \ . \tag{4.7}$$

Further, we can calculate the "global star formation efficiency", i.e., the fraction of the gas mass converted to stars per orbital dynamical time, $\bar{\epsilon}_{\text{sf}} \equiv \dot{\Sigma}_\star/\Sigma_g \Omega$, to be

$$\bar{\epsilon}_{\text{sf}} = \pi G \tilde{Q}_{\text{gas}} \sqrt{\frac{3}{8}} \frac{\Sigma_{disk}(\Omega + \sqrt{4\pi G \rho_0})}{(P/m_\star)\Omega^2} \ . \tag{4.8}$$

If we take $\tilde{Q}_{\text{gas}}$ to be a constant, assuming a value near or slightly below one, and consider the case in which the disk is not strongly self-gravitating (likely, with the marginal stability of $\tilde{Q}_{\text{gas}} \approx 1$), such that $\Omega >> \sqrt{4\pi G \rho_0}$; these two relations boil down to a description of gas surface density and mass fraction and a representation of the ratio of disk surface density to inverse dynamical time, respectively:

$$\dot{\Sigma}_\star = \pi G \sqrt{\frac{3}{8}} \frac{\Sigma_g \Sigma_{disk}}{P/m_\star} \quad \& \quad \bar{\epsilon}_{\text{sf}} = \pi G \sqrt{\frac{3}{8}} \frac{\Sigma_{disk}}{\Omega P/m_\star}. \tag{4.9}$$

One deficiency of this model of feedback regulation lies in the calibration of the strength of feedback to isolated Type II SNe simulations (e.g., Kim et al., 2015a; Martizzi et al., 2015). Generally, this overlooks the variation in effective feedback coupling due to the local environment. Especially for predictions regarding the line-of-sight velocity dispersions, the potential saturation or "venting" of feedback after

---

[3]This is not the "real" two component Toomre-Q (Rafikov, 2001), but is a much-simplified version that is sufficiently accurate for our purposes (using the full two-component Q makes little difference to our numerical calculations but prevents us from writing simple analytic expressions).

SNe remnants (super-bubbles or otherwise) break out of the disk plane (Fielding, Quataert, McCourt, et al., 2017), or the enhanced momentum injection efficiency of spatially clustered SNe (Gentry et al., 2019), are possible concerns. We do not explore the effects of feedback saturation or SNe (spatial) clustering here, but they warrant further exploration within the framework of simple analytic models (these effects are self-consistently handled in galaxy simulations that resolve gas disks and supernova remnants in the snowplow phase).

4.2.2 Non-equilibrium Model of Feedback Injection in Disk Environments

The model derived in §4.2.1 is an equilibrium model, which assumes that feedback injection is statically balanced with the dynamical/dissipation rate. However, we might consider here that the departures from equilibrium occurring on the feedback delay timescale are important for setting the scatter seen in $\dot{\Sigma}_\star$ at constant Σ_g in the Kennicutt-Schmidt relation, and at constant $\Sigma_g \Omega$ for the Elmegreen-Silk relation, as well as in σ_z–$\dot{\Sigma}_\star$ space. We will explicitly consider only delayed feedback (i.e., Type II SNe) in this model.[4]

Rather than holding the turbulent velocity dispersion σ constant in time, we allow it to vary, defining the behavior of its derivative $\dot{\sigma}$ as,

$$\dot{\sigma} = \dot{\sigma}_{\mathrm{SNe}} - \sigma/t_{\mathrm{eddy}} \, , \tag{4.10}$$

where $\dot{\sigma}_{\mathrm{SNe}}$ is the term explicitly following the current injection of SNe feedback momentum due to past star formation (see Eq. 4.11, below), and the σ/t_{eddy} term accounts for the exponential decay of supersonic turbulence on roughly an eddy-crossing time (Eq. 4.3). We ignore the fraction of turbulent momentum "locked away" into stars (equivalent to a $\sigma \dot{\Sigma}_g$ term) as the term is negligible with the depletion time of gas typically on the order of ~Gyr in galaxies (Leroy, Walter, Brinks, et al., 2008; Leroy, Walter, Sandstrom, et al., 2013).

Developing a form for $\dot{\sigma}_{\mathrm{SNe}}$, we consider that Type II SNe feedback from a given star formation event is injected after a delay time t_d, and over a period δt_d, corresponding to the lifetime of the most massive star formed, and the time until the

---

[4]Although prompt feedback (e.g., radiation pressure and stellar winds) injects a similar amount of momentum per mass of young stars over their lifetimes (Agertz, Kravtsov, et al., 2013), the 'characteristic' velocity at which this momentum couples to the ISM on large scales is lower by a factor of 20 or so, compared to SNe feedback (Murray et al., 2010; Faucher-Giguère et al., 2013). As we consider here the ability of feedback to regulate the disk scale properties that regulate star formation from the top down, we neglect explicitly treating the prompt feedback effects in our model. Instead, we implicitly incorporate its effects regulating the efficiencies of cloud-scale, < 100 pc, star formation in our "GMC-scale" star formation efficiency model (Grudić et al., 2018).

least massive star to undergo core-collapse does so thereafter. Furthermore, convolving the number of stars of a given mass with their lifetimes produces a shallow power-law distribution in time over which SNe occur after a star formation event, such that $dN_{SNII}/dt \propto t^{-\alpha}$ (see Appendix 4.5 for a more detailed derivation). These quantities, t_d, δt_d, and α, are reasonably known (see Appendix 4.5), and we adopt fiducial values in this chapter of 5 Myr, 30 Myr, and 0.46, respectively. As such, the governing equation for $\dot{\sigma}_{\rm SNe}$ takes the form

$$\Sigma_{\rm g}\dot{\sigma}_{\rm SNe} = (P/m_\star)\chi \int_{t_d}^{t_d+\delta t_d} \frac{\dot{\Sigma}_\star(t-t')}{t'^\alpha} dt' \, , \qquad (4.11)$$

where $P/m_\star$ here is the momentum injected by Type II SNe event per mass of young stars (as opposed to from all sources of feedback as in § 4.2.1), and χ is a normalization factor such that for a constant star formation rate $\dot{\Sigma}_\star$ the equation reduces to $\Sigma_{\rm g}\dot{\sigma}_{\rm SNe} = (P/m_\star)\dot{\Sigma}_\star$. We adopt a fiducial value of $P/m_\star = 3000$ km/s (the same value adopted by the FIRE simulations of Hopkins, Kereš, et al., 2014; Hopkins, Wetzel, et al., 2018), and explore the effects of varying the strength of SNe feedback in § 4.3.1.

It is then necessary to formulate a model for the rate at which star formation proceeds, as a function of the current state of the ISM, as we now consider $\dot{\Sigma}_\star$ to drive $\dot{\sigma}$, rather than being purely in a static equilibrium with the turbulent dissipation.

Taking the large-scale marginal gas stability as a key parameter in setting the current rate of star formation, we invoke a simple "two-phase" model of the ISM, which is instantaneously dependent on the Toomre-Q parameter of the gas disk. Let us assume that some fraction of the gas is in a star-forming phase $f_{\rm sf}$ (i.e., marginally gravitationally bound gas), with the remaining mass in a non-star-forming phase. As explored analytically by Hopkins (2013), supersonic turbulence drives parcels of gas to randomly walk in log-density space such that a fraction (here, $f_{\rm sf}$) are driven to sufficient densities such that local collapse (i.e., leakage) occurs even if the global value of $\tilde{Q}_{\rm gas}$ exceeds the critical threshold for gravitational instabilities Q_0[5]. Following the rationale of Faucher-Giguère et al. (2013, see their Appendix C), adapting the calculations of Hopkins (2013), we argue that the mass fraction of gas susceptible to gravitational collapse ($f_{\rm sf}$), which subsequently would be considered in some stage of star-forming, is functionally dependent on Toomre-Q, with an

---

[5]This is just a formal calculation of the log-normal density distribution of gas in supersonic turbulence. It is to say: turbulence is able to dynamically replenish the fraction of gas in a log-normal density distribution that is above some critical threshold for self-gravity and collapse.

adopted power-law form of,

$$f_{\rm sf}(\tilde{Q}_{\rm gas}) = f_{\rm sf}^0 \left(\frac{Q_0}{\tilde{Q}_{\rm gas}} \right)^\beta , \tag{4.12}$$

for values $\tilde{Q}_{\rm gas} > Q_0$, and is a constant $f_{\rm sf}^0$ for $\tilde{Q}_{\rm gas} < Q_0$, where $f_{\rm sf}^0$ is the maximal fraction of gas in the star-forming phase, Q_0 represents the Toomre-Q stability threshold, and β accounts for the "stiffness" of that threshold. Further, as $\tilde{Q}_{\rm gas}$ evolves (in this model, through evolution purely in σ) smoothly in time, the roll-on (or off, if $\dot{\sigma} > 0$) can also be thought to implicitly parameterize our ignorance in how and at what rate GMCs assemble (for $\dot{\sigma} > 0$, this can approximate ionizing radiation and winds dispersing dense material). In Hopkins (2013), the stiffness of the instability threshold ($\sim \beta$, here) was inversely dependent on the Mach number $\mathcal{M}$ of the turbulence–intuitive, as larger Mach numbers yield a broader log-normal density distribution, increasing the amount of gas above a given density relative to the mean gas density, hence softening the effective gravitational instability threshold. Here, taking $\mathcal{M} \sim \sigma/c_s$, where c_s is the speed of sound for ~ 300 K molecular gas, and $\tilde{Q}_{\rm gas} \sim$ constant, we thus have $\mathcal{M} \propto \sigma \propto \Sigma_g$. And so, in our model at a given gas surface density we adopt a stiffness $\beta = -2 \log(\Sigma_g/{\rm M}_\odot {\rm pc}^{-2}) + 6$, proportional to the Mach number-dependent stiffness fit by (Faucher-Giguère et al., 2013), and substantiated by the observational findings relating Σ_g and $\mathcal{M}$ of Federrath et al. (2017).

Arguing that a ~kpc-sized patch of the ISM likely incorporates a large enough number of $\lesssim 100$ pc clouds so as to approach an average behavior in terms of their individual evolutionary states (Schruba et al., 2010; Calzetti et al., 2012; Kruijssen and Longmore, 2014), we then adopt a ~kpc-scale star formation rate of

$$\dot{\Sigma}_\star(t) = \langle \epsilon_{\rm sf} \rangle \, f_{\rm sf}(\tilde{Q}_{\rm gas}(t)) \Sigma_g / t_{\rm eddy} \tag{4.13}$$

where $f_{\rm sf}(\tilde{Q}_{\rm gas}(t))\Sigma_g$ is the mass of gas in the star-forming state (per area), $\langle \epsilon_{\rm sf} \rangle$ is the average star formation efficiency per eddy-crossing time (fiducially, 0.025, in line with cloud-scale efficiencies discussed in Elmegreen, 2018), and $t_{\rm eddy}$ is the eddy-crossing time. As the quickest instabilities to grow are at the largest scales, the largest being that of the disk scale height itself, the effective free-fall time of gas at the mid-plane density is equivalent to the eddy crossing time $t_{\rm eddy}$ up to an order-unity factor (since $t_{ff} \sim 1/\sqrt{G\rho_0} \sim t_{\rm eddy}$). Again, emphasizing that we defined our efficiency $\langle \epsilon_{\rm sf} \rangle$ (taken to be a constant) as a kpc-scale average quantity,

Table 4.2: Fiducial Model Parameters and Disk Conditions

Parameter	Quantity	Fiducial Value
Toomre-Q Threshold	Q_0	1.0
Max. star-forming fraction	f_{sf}^0	0.3
Average SF efficiency	$\langle \epsilon_{sf} \rangle$	0.025
Feedback Strength	$P/m_\star$	3000 km/s
Feedback Delay Time	t_d	5 Myr
Feedback Duration	δt_d	30 Myr
Power law slope of Type II SNe delay time distribution	α	0.46
Orbital Dynamical Time	Ω	35 Gyr^{-1}
Disk Gas Fraction	f_g	0.33
Stellar Thick Disk Fraction	f_{thick}	0.33
Stellar Disk height (thin)	$H_{thin,\star}$	350 pc
Stellar Disk height (thick)	$H_{thick,\star}$	1000 pc

$\langle \epsilon_{sf} \rangle \equiv \left\langle \dot{M}_\star t_{eddy}/M_{GMC} \right\rangle$ where $M_{GMC} = f_{sf}(\tilde{Q}_{gas}(t))M_g$. It is analogous to a GMC-scale average star formation efficiency, and as such is unable to distinguish between high- or low-efficiency star formation modes on smaller scales (e.g., efficiencies calculated on the basis of higher density gas tracers like HCN Kauffmann et al., 2017; Onus et al., 2018).

The fiducial values of the physical quantities and common initial conditions included in the evolution of our model–essentially the behavior of the PDE for σ, Eq. 4.10, are enumerated in Table 4.2. The initial condition of the gas in the model, in all cases presented here, is taken to be $\tilde{Q}_{gas}(t = 0) = Q_0 + 1$ (and its corresponding velocity dispersion σ) for the given Σ_g, embedded within static stellar disk with thin and thick components having scale heights of 350 and 1000 pc, respectively, and a relative mass fraction $f_{thick} \equiv \Sigma_{thick,\star}/(\Sigma_{thick,\star} + \Sigma_{thin,\star}) = 0.33$.

Connecting $\dot{\Sigma}_\star$, Σ_g with Observables

Except for the nearest star-forming regions, (where young star counts or protostellar cores can be used as proxies), observers rarely have true estimates for the 'instantaneous' star formation rate of a star-forming region. As such, we must connect our 'instantaneous' star formation rate with observables like Hα or IR flux, which are used as average measures of star formation over a recent period of time $\sim 2 - 4$ Myr. For this reason, when we make attempts to compare with observational star formation relations, we average the instantaneous star formation rate $\dot{\Sigma}_\star$ over the last 3 Myr (see Appendix 4.5 for how our results vary with the averaging window). To

compare our gas surface densities with observations, we take our gas mass surface density Σ_g to be the atomic+molecular hydrogen gas, correcting them for Helium mass with a factor of 0.75.

In panels where we plot the Kennicutt-Schmidt relation, we compare results of our simple model with resolved Kennicutt-Schmidt observations from Bigiel, Leroy, Walter, Brinks, et al. (2008) (light and dark grey shaded regions in background). We correct the gas surface densities in their data with a variable X_{CO} fit from Narayanan et al. (2012). Where we plot depletion time against gas stability (Toomre-Q), we compare with the results of Leroy, Walter, Brinks, et al. (2008) (light and dark grey shaded regions in background). For the gas velocity dispersion–star formation rate panels, we present data from the SAMI IFU survey of kpc-scale resolved observations of star forming disks of Zhou et al. (2017). As well, we include HI velocity dispersion data of spiral disks from Ianjamasimanana, de Blok, Walter, Heald, et al. (2015) from the THINGS survey. These data correspond to velocity dispersion–gas surface density observations, lacking direct SFR data. However, given that they are at low gas surface density ($\Sigma_g < 10$ M$_\odot$ pc^{-2}), we take their results to correspond to a range of SFRs for the low gas surface density region in the Bigiel, Leroy, Walter, Brinks, et al. (2008) dataset. They are thus presented as a $5 - 12$ km/s band ranging in $\log(\dot{\Sigma}_\star/\text{M}_\odot \text{ yr}^{-1} \text{ kpc}^{-2})$ from -2 to -5, constraining the low velocity dispersion, low-SFR region for our models.

4.3   Results

The simple model produces relatively stable cycles of star formation, inflation and decay of gas velocity dispersions, and variation in the values of the Toomre-Q parameter, as seen in Figure 4.1 for our set of fiducial values of physical parameters, with disk surface densities and conditions chosen to match the solar circle ($\Sigma_g = 15$ M$_\odot$ pc^{-2}, $\Sigma_\star = 35$ M$_\odot$ pc^{-2}, and $\Omega = 35$ Gyr^{-1} McKee et al., 2015). As star formation is slow and inefficient (gas depletion times are $\gtrsim$ Gyr here), and given the fact that we do not include some gas outflow term, we do not allow Σ_g or $\Sigma_\star$ to vary in the model. And so, $\tilde{Q}_{\text{gas}}$ and σ_z are in phase throughout their cycles, by definition since $\tilde{Q}_{\text{gas}} \propto \sigma_z$ here, ignoring the relatively weak sigma-dependent γ term in front of $\Sigma_\star$ in Σ_{disk}. Moreover, given the relative stiffness of the star formation threshold in Toomre-Q (for $\Sigma_g = 15$ M$_\odot$ pc^{-2}, the 'stiffness' of $f_{\text{sf}}(\tilde{Q}_{\text{gas}})$ is $\beta \sim 4.6$), star formation commences and is arrested by feedback before $\tilde{Q}_{\text{gas}}$ reaches $Q_0(= 1)$, after which the delayed effects of feedback play out, driving $\tilde{Q}_{\text{gas}}$ and the velocity dispersions to their maximal values before the cycle starts anew. The instantaneous
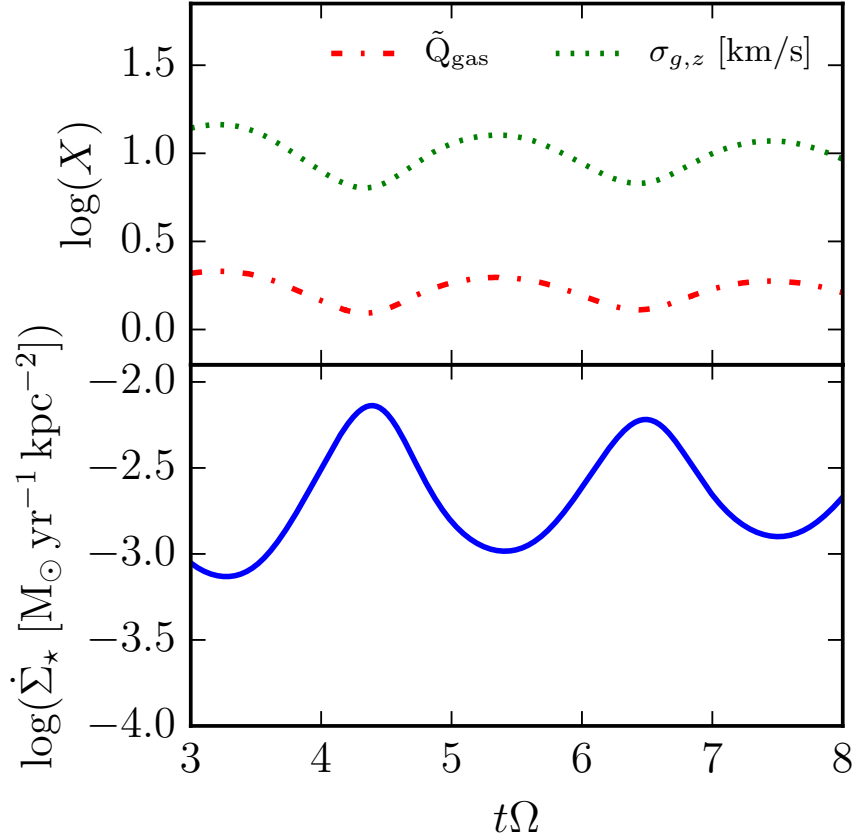
Figure 4.1: Logarithmic values of star formation rate surface density (solid blue line; 3-Myr-averaged rate), local $\tilde{Q}_{gas}$ (dash-dotted red line), and gas velocity dispersion (dotted green line, units: km/s) for a period of five dynamical times in our fiducial model gas patch (for fiducial model parameters, see Table 4.2) with $\Sigma_g = 15$ M$_\odot$ pc^{-2} and $\Sigma_\star = 35$ M$_\odot$ pc^{-2}. The SFR and velocity dispersion maintain stable, albeit slowly decaying, cycles after approximately one dynamical time $\tau_{dyn} \sim \Omega^{-1} \sim$ 30 Myr.

star formation rate (not shown) is nearly completely out of phase with the velocity dispersions and Toomre-Q, rising sharply as $\tilde{Q}_{gas}$ falls and falls nearly as quickly as it rises. The "observable" quantity, the 3 Myr-averaged star formation rate (cf. the Hα SFR tracer), shows how the "observed" star formation rates rise by $\sim$dex as $\tilde{Q}_{gas}$ approaches its minimal value, before falling as the effects of SNe feedback are felt later in the star formation episode.

Variations in the overall strength of feedback, the timing of feedback, and star formation prescription all affect the shape and magnitudes of the star formation cycles in the model, but largely the aforementioned picture holds so long as the timescale of feedback relative to the dynamical time of the system is short but not effectively instantaneous, and that the magnitude of feedback is insufficient to
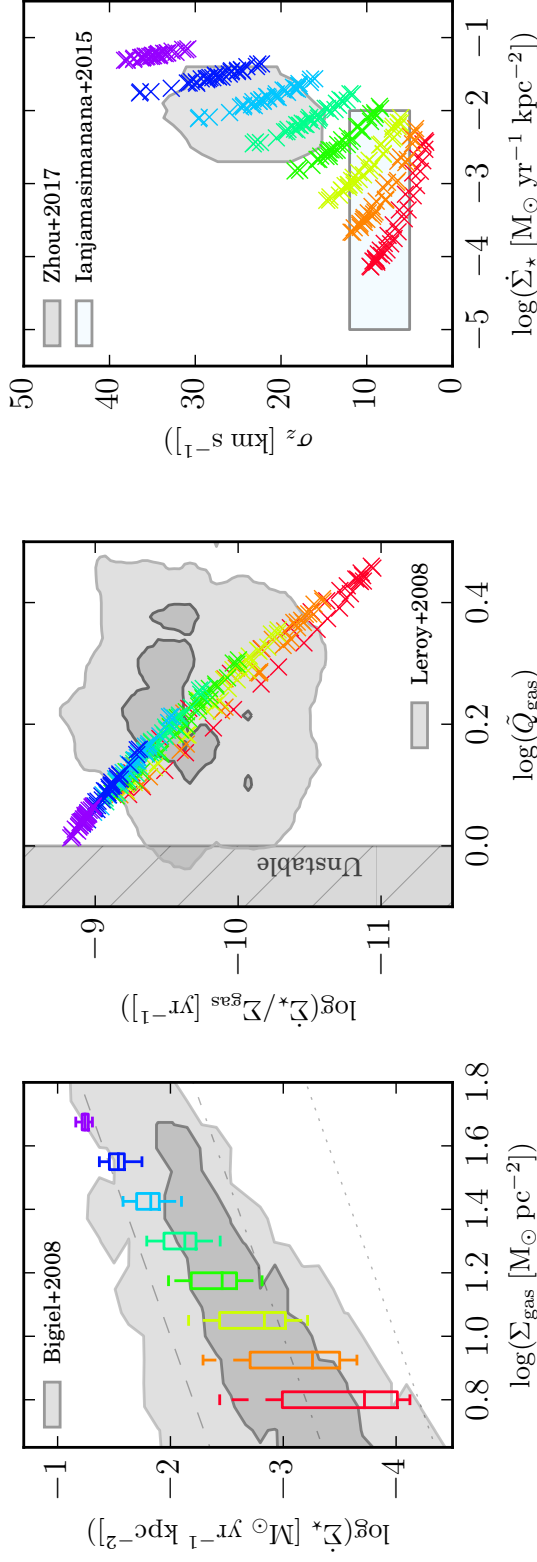
Figure 4.2: Fiducial model Kennicutt-Schmidt (**left**), gas depletion time—Toomre-Q (**middle**), and gas velocity dispersion—SFR (**right**) relations for the fiducial parameters listed in Table 4.2. The shaded regions in the background represent observational data ranges (cf. § 4.2.2) from Bigiel, Leroy, Walter, Brinks, et al. 2008 (left panel), Leroy, Walter, Brinks, et al. 2008 (center panel), and Ianjamasimanana, de Blok, Walter, Heald, et al. 2015 and Zhou et al. 2017 (light blue and grey, respectively, right panel). The dashed, dot-dashed, and dotted lines in the KS panel indicate constant depletion times of 10^9, 10^{10}, and 10^{11} yr, respectively. The hatched grey shaded region to the left in the middle panel denotes the Toomre-unstable region. The fiducial model exhibits good agreement with observations of Kennicutt-Schmidt and gas velocity dispersions. The Q-threshold is sufficiently soft with its $f_{\rm sf}(\tilde{Q}_{\rm gas})$ 'leakage' to allow star formation to reverse collapse before reaching Q_0/disk instability itself. The upturn in σ_z–SFR above $\dot{\Sigma}_\star \approx 10^{-2}$ $M_\odot$ yr^{-1} kpc^{-2} reflects the fact that feedback from individual star formation events injects a smaller fraction of the overall ISM turbulent momentum and thus is less effective at changing the gravitationally unstable fraction of the ISM (especially true, given that the model lacks outflows to remove gas).

totally disrupt the system. This therefore applies to both galactic centers and in the outskirts of disks, even where the dynamical time is quite long compared to feedback timescales, so long as the ISM is turbulently regulated.

Figure 4.2 shows the extent of the star formation cycles in the fiducial model across ∼dex in Σ_g in the Kennicutt-Schmidt, depletion time—stability, and star formation rate—gas velocity dispersion relations. Results in this figure, and throughout the chapter, are plotted as box-and-whiskers in the KS panel represent the median, interquartile region, and 5–95% data range of individual models run at a given Σ_g. Figure 4.2 was run for a range in $\log \Sigma_g = 0.8 - 1.675$ with $\log \Sigma_g$ steps of 0.125 dex, all other figures use a range of $\log \Sigma_g = 0.8 - 1.55$ with 0.25 dex $\log \Sigma_g$ steps, where Σ_g is expressed in units of $M_\odot$ pc^{-2}. Points in other panels (gas velocity dispersion and depletion time–stability relations) are sampled time-steps from those models (seen as clearly separated families of colored points in right panel of Figure 4.2).

At low Σ_g, the model exhibits increasingly large scatter[6] as the effects of feedback from peak star formation rates contribute significantly to the overall momentum budget of the disk (cf. § 4.4.2), producing a larger scatter to in SFRs for KS, and a spur to long depletion times and 'high' Toomre-Qs. In σ–$\dot{\Sigma}_\star$ space, this is seen as a flattening of the relation, covering broad ranges in $\dot{\Sigma}_\star$ with little change in σ. This is broadly in agreement with observations of HI disks in galaxy outskirts having flat velocity dispersion profiles (Ianjamasimanana, de Blok, Walter, and Heald, 2012; Ianjamasimanana, de Blok, Walter, Heald, et al., 2015). The large velocity dispersions in gas seen above $\dot{\Sigma}_\star \approx 10^{-2}\,M_\odot\,\mathrm{yr}^{-1}\,\mathrm{kpc}^{-2}$ reflect the fact that feedback is simultaneously able to drive outflows and turbulence in the cold ISM at these SFRs (Hayward et al., 2017). However, in a multiphase ISM, these high dispersions σ_z would not appear in the cold ISM turbulence as this feedback would instead drive outflows (and thus dispersions in the warm neutral and ionized gas components).

Counter-intuitively–but of central importance to observers–when this model is applied to galaxies as a whole (i.e., many $\lesssim$ kpc-patches), the relatively tight correlation between Toomre-Q (or gas σ_z) and resolved star formation rates within individually evolving patches may be smoothed out by variations in, e.g., local gas fractions, dynamical times, star formation efficiencies, or strength of feedback (i.e., the amount of momentum *coupled* into the cold phase of the ISM per mass of young stars), which may shift subsets of the distribution (cf., later sections of this chapter), effec-

---

[6]Regions in an "off"/low-SFR mode of the cycle may likely be counted as entirely non-star forming in observations, dependent on flux thresholds, given their very low SFRs.

tively widening it on galaxy scales to the relatively broad distribution observed by Leroy, Walter, Brinks, et al. (2008). This argument holding for $\dot{\Sigma}_\star \lesssim 10^{-2}$ M$_\odot$ yr^{-1} kpc^{-2}, above which outflows would be possible, the presence of which may affect interpretations of distributions in depletion time–Toomre-Q (and σ_z here would no longer strictly encapsulate turbulence in the cold ISM, Hayward et al., 2017).

4.3.1   Variations in the Strength and Timing of Feedback

Figure 4.3 explores the effects on this model due to variations in the strength, delay time, and duration of feedback.

Feedback Strength $P/m_\star$

The left column of Figure 4.3 shows the effects of varying the overall strength of feedback, $P/m_\star$, in our fiducial model: we plot both the Kennicutt-Schmidt relation (relating gas mass and star formation rate surface densities) and the gas velocity dispersion–SFR relation. As demonstrated extensively in previous works exploring the feedback-regulated regime, variation in the overall strength of feedback primarily effects the equilibrium star formation rates where gas self-regulates: stronger (weaker) feedback yields lower (higher) overall star formation rates (Hopkins et al., 2011; Hopkins et al., 2012; Shetty et al., 2012; Agertz, Kravtsov, et al., 2013; Hopkins, Kereš, et al., 2014; Orr et al., 2018). By construction, this model follows this paradigm. Interestingly, stronger feedback (per mass of young stars) appears to result in smaller scatter in star formation rates. As the star formation timescales, and the absolute magnitude of momentum injected by feedback, are held roughly constant between models, this can be explained as keeping the relative variance in turbulence constant across the star formation cycles. Hence, if $\Delta\sigma \propto P/m_\star \Delta\dot{\Sigma}_\star$, stronger feedback produces smaller variance in turbulence for smaller variance in $\dot{\Sigma}_\star$.

At low star formation rates, the model is not strongly constrained to high or low feedback strengths by the spiral galaxy HI velocity dispersion dataset of the THINGS survey (Ianjamasimanana, de Blok, Walter, Heald, et al., 2015). However, the higher-SFR, higher-velocity dispersion data from Zhou et al. (2017) do constrain this model in the $P/m_\star \sim 3000 - 6000$ km/s range.
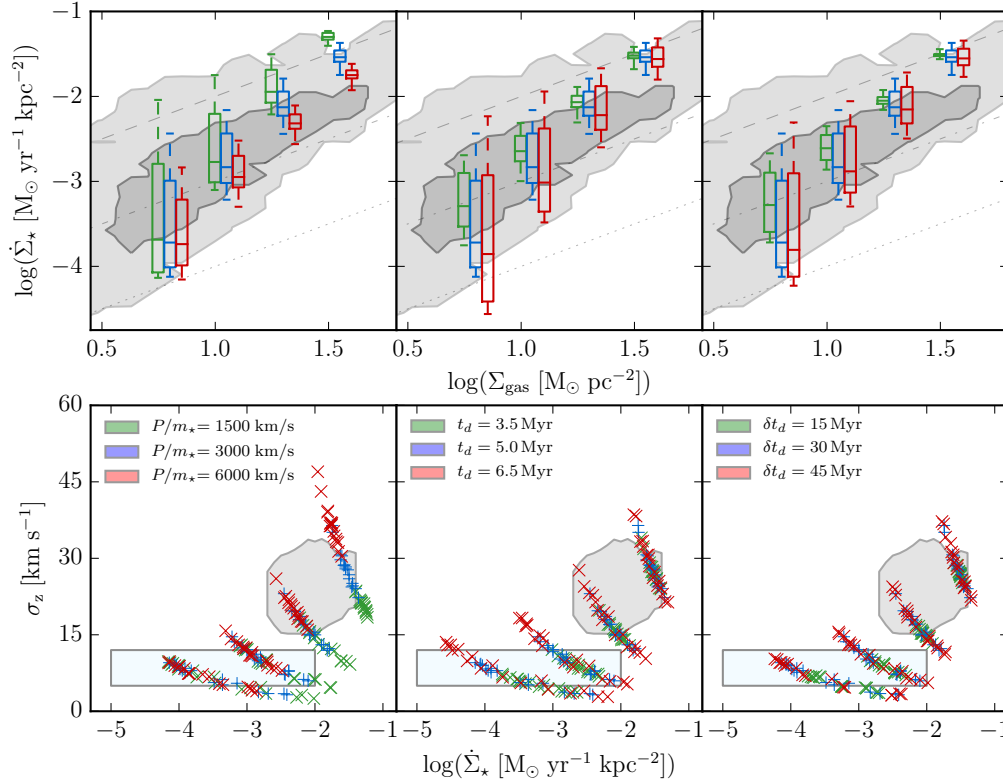
Figure 4.3: Effects on the Kennicutt-Schmidt **(top row)** and gas velocity dispersion–SFR **(bottom row)** relations due to variations **(columns)** in the overall strength $(P/m_\star)$, delay time (t_d) and duration (δt_d) of SNe feedback in the fiducial model for $3 < t\Omega < 8$. Background shaded regions (observations) and dashed lines (constant depletion times) are in the style of Figure 4.2. **(Top row)** Box-and-whiskers for the model at a given Σ_g are offset from the central value to show differences between model parameters; **(bottom row)** colored points are sampled time-points from models at a given Σ_g, but no offsets are introduced. **(Left)** Raising (lowering) the overall strength of feedback per mass of stars formed, $P/m_\star$, systematically lowers (raises) the peak/integrated star formation rates in the KS relation and raises (lowers) the gas velocity dispersion distribution at a given $\dot{\Sigma}_\star$. Scatter in SFRs are also inversely affected. **(Middle)** The delay timescale before the first SNe feedback is injected, t_d, is a strong factor in determining the departures from SF equilibrium and their magnitudes. Longer delays produce larger departures from equilibrium. **(Right)** Varying the period over which SNe momentum is injected by a single stellar population, δt_d, affects the responsiveness of feedback to local ISM conditions. Longer durations weaken the ability of feedback to respond quickly to the ISM conditions, resulting in more scatter in SFRs at constant Σ_g.
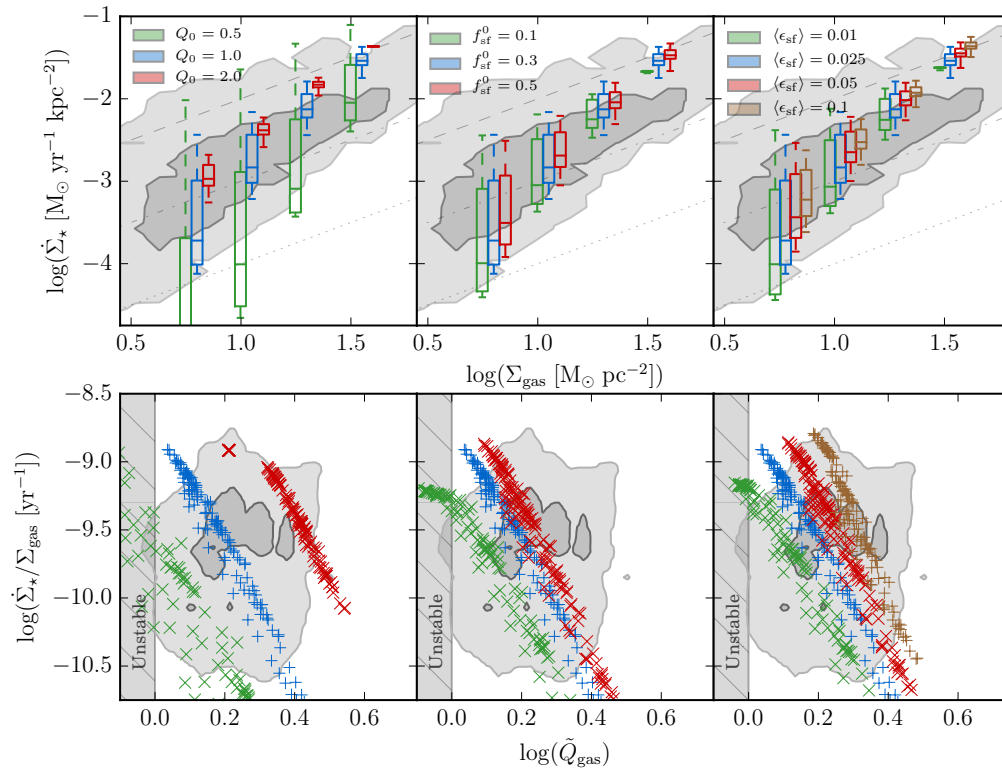
Figure 4.4: Effects on the Kennicutt-Schmidt **(top row)** and depletion time–stability **(bottom row)** relations due to variations **(columns)** in the Toomre-Q threshold (Q_0), maximal star-forming phase fraction ($f_{\rm sf}^0$), and average local star formation efficiency ($\langle \epsilon_{\rm sf} \rangle$). Plotted quantities and observational data regions are in the style of Figure 4.3. **(Left)** Shifting $Q_0 = 1 \rightarrow 2$ moves the distributions in depletion time—stability space by ~ 0.3 dex, effectively renormalizing the velocity dispersions for an otherwise-constant KS relations. The scatter in SFR grows with smaller Q_0; as feedback injection accounts for a larger fraction of the ISM momentum budget (normalized by Q_0), and star formation episodes are less stable cycles than explosive events (see §4.4.2). **(Middle)** Varying the maximum fraction of gas in the star-forming phase $f_{\rm sf}^0$ is largely unimportant to the KS relation, as long as it does not "choke" the amount of gas that would otherwise enter the star-forming phase, but shifts distributions in depletion time—stability space: lower maximum star-forming fractions require lower values of $\tilde{Q}_{\rm gas}$ (i.e., higher gas densities) to achieve the same SFR. **(Right)** Higher local star formation efficiencies $\langle \epsilon_{\rm sf} \rangle$ steepen the peak SFRs in the KS relation and shift the distributions in depletion time–stability space (higher efficiencies mean smaller quantities of unstable gas yield the same SFR), and appear to reduce scatter in KS.

Feedback Delay Time t_d and Duration δt_d

The middle and right columns of Figure 4.3 show the effects of varying the delay timescale t_d for the first SN feedback (i.e., the lifetime of the most massive star formed in a star formation event, plus the time required to propagate the SNe remnant into the ISM and drive turbulence), and the duration of SN feedback δt_d (i.e., the difference in stellar lifetimes between the least and most massive stars to undergo a Type II SN in a star formation event). The scatter in star formation rates is directly affected by the delay time t_d, with shorter delays producing less scatter in star formation rates. Longer delay times allow for gas to over-produce stars to a greater extent before feedback is felt, hence larger departures from star formation equilibrium. Physically reasonable values of $t_d \sim 4-6$ Myr, with a $t^{-0.46}$ weighting, are generally capable of driving $\gtrsim$dex variations in star formation rates.

In a similar vein, shorter feedback durations, δt_d, cause effectively burstier overall feedback and, as such, drive larger scatters in star formation rates. For reasonable feedback durations of $\sim$30 Myr (roughly the difference between the lifetimes of an 8 $M_\odot$ and 40 $M_\odot$ star) the model converges on $\sim$dex scatter in star formation rates. Longer durations smooth out feedback to the extent that it is equivalent in effect to lowering the overall strength of feedback $P/m_\star$.

4.3.2   Variations in Star Formation Rate Model

To bake a strüdel, one must first cook the filling. Analogously, in order to generate stellar feedback in a model, one must first produce stars. The local star formation rate implemented in this model, Eq. 4.13, has two principle components that we investigate. Namely, the gas fraction in the star-forming phase $f_{\rm sf}(\tilde{Q}_{\rm gas}; Q_0, f_{\rm sf}^0, \beta)$ (Eq. 4.12), and the average local star formation efficiency per free-fall time $\langle \epsilon_{\rm sf} \rangle$.

Varying the star formation model (i.e., the local efficiency of star formation and the Toomre-Q threshold for the onset of gravitational fragmentation/star formation) has larger systematic effects on the results of our model in depletion time–stability space compared to the effects of reasonable variations in the feedback implemented demonstrated in the previous subsection.

Toomre-Q Threshold for Star Formation Q_0

The left column of Figure 4.4 demonstrates the effects of the particular choice of the Toomre-Q threshold Q_0 on the Kennicutt-Schmidt and depletion time–Toomre-Q relations. For physically reasonable values, the threshold sets the values of

the equilibrium velocity dispersions that the models oscillate about and thus the average magnitude of turbulent momentum in ISM. Along with the overall strength of feedback, the value of the gravitational instabilities threshold is the parameter that most strongly affects the normalization of the Kennicutt-Schmidt relation in our model.

Larger values of Q_0 produce less scatter in the Kennicutt-Schmidt relation, as Q_0 sets the overall amount of turbulent momentum in the ISM ($P_{turb,0} \sim \Sigma_g \sigma(\tilde{Q}_{gas} = Q_0)$) where star formation occurs and thus dictates the extent to which star formation events can perturb the ISM at a given Σ_g (see § 4.4.2 for more rationale). When $Q_0 = 0.5$, the model breaks down, as feedback is able to at least double the momentum in the ISM after every star formation episode. For values of Q_0 where the model holds reasonably well ($Q_0 \gtrsim 1$), doubling $Q_0 = 1 \rightarrow 2$ produces an expected ~ 0.3 dex shift in the Toomre-Q distribution without greatly affecting depletion times (beyond a slight tightening of the SFR distribution): gas is still able to self-regulate (cf. the predictions of Krumholz and Burkhart, 2016).

As $Q_0 \approx 1$ is a physically motivated value for the local gravitational stability threshold of the ISM (Toomre, 1964), and that other similar formulations of stability parameters differ only by an order-unity factor in their thresholds for gravitational fragmentation (Rafikov, 2001; Kim et al., 2007), we explore only a range in Q_0 of $0.5 - 2$. Generally speaking, this is not a new constraint on Q_0, but rather shows the physical effect of varying the equilibrium level of turbulence on this non-equilibrium model (a "robustness check" of sorts).

Variations in the Maximum Star-forming Fraction $f_{\rm sf}^0$

In this model, we consider that at the onset of disk scale height gravitational instabilities ($\tilde{Q}_{gas} = Q_0$), there is a maximum mass fraction $f_{\rm sf}^0$ of the ISM participating in star formation. Such a constant has been adopted before in analytic models of feedback regulation in disks (Faucher-Giguère et al., 2013). As seen in the middle column of Figure 4.4, we see that so long as this factor $f_{\rm sf}^0$ does not 'choke' the fraction of material in the star-forming phase, variations have rather small effects qualitatively. This 'choking' appears to occur at high gas surface densities where choices of small maximal fractions ~ 0.1 clip the maximum SFRs achieved, whereas larger values of $f_{\rm sf}$ do not appear to be the limiting factor on setting maximal SFRs (see the abrupt flattening of $f_{\rm sf}^0 = 0.1$ points in Figure 4.4 at short depletion times). Larger values of $f_{\rm sf}^0$ move the distributions in depletion time–stability space to shorter depletion

times and higher Toomre-Q values; this is the result of renormalizing the "leakage" curve the model follows as $\tilde{Q}_{\mathrm{gas}}$ evolves (Eq. 4.12).

Variations in Instantaneous Star Formation Efficiency $\langle \epsilon_{\mathrm{sf}} \rangle$

The right column of Figure 4.4 shows how variations from $\langle \epsilon_{\mathrm{sf}} \rangle = 0.01$ to $\langle \epsilon_{\mathrm{sf}} \rangle = 0.1$, motivated by observational bounds (Lee et al., 2016), affect the Kennicutt-Schmidt relation, and gas depletion times and stability (Toomre-Q). Interestingly, variations in the local efficiency over a dex change the maximal star formation rates by $\lesssim 0.5$ dex. In the feedback regulated regime[7], so long as the local efficiency factor is above that required to produce *enough* stars to inject the appropriate amount of feedback in the ISM to achieve equilibrium, $\langle \epsilon_{\mathrm{sf}} \rangle$ should not affect the large-scale, time-averaged star formation rates. However, lower star formation efficiencies do mean that gas must collapse to higher surface densities (i.e., reduced free-fall times) to counteract smaller local efficiencies in order to maintain the momentum balance. More, as the gas collapses further, but does not produce more momentum in feedback overall (to first order), the distributions in depletion time–stability space shift, requiring a less stable ISM generally to support the same SFRs with lower star formation efficiencies (moving by ~ 0.3 dex in $\tilde{Q}_{\mathrm{gas}}$ for a dex change in $\langle \epsilon_{\mathrm{sf}} \rangle$).

Though the effect appears less pronounced at high Σ_g, for $\Sigma_g \lesssim 10 \; \mathrm{M_\odot \; pc^{-2}}$, lower local star formation efficiencies produce larger scatter in star formation rates. This is in part due to the increasing steepness of the unstable gas fraction $f_{\mathrm{sf}}(\tilde{Q}_{\mathrm{gas}})$, and the ability of gas to overshoot equilibrium star formation rates as the arresting effects of feedback are not felt in sufficient amounts at higher velocity dispersions (i.e., larger $\tilde{Q}_{\mathrm{gas}}$'s).

Given the degeneracy of the effects of variations in local star formation efficiency and the strength, delay and duration of feedback, on the Kennicutt-Schmidt relation, that relation may not be a sensitive probe of smaller scale star formation efficiency. Instead, observations in depletion time–stability (Toomre-Q) space have a greater ability to distinguish between low and high local star formation efficiencies in the framework of feedback regulation. Given the definitional difficulties of a star formation efficiency in this model (i.e., that f_{sf} and $\langle \epsilon_{\mathrm{sf}} \rangle$ could be defined together), measurements of the depletion time–stability relation *in similar patches* of the ISM may be useful in quantifying "the maximally participating fraction" of the ISM in

---

[7]See Semenov et al. (2018) for a recent discussion of the relative differences between feedback-regulated and dynamics-regulated star formation.

Table 4.3: Properties of Mock Galaxies for Figure 4.5

Mock Galaxy	$\Sigma_{g,0}$ ($M_\odot/pc^2$)	$\Sigma_{\star,0}$ ($M_\odot/pc^2$)	R_g (kpc)	v_c (km/s)	$\langle \epsilon_{sf} \rangle$
Blue	100	1000	6	300	0.01
Green	50	500	6	300	0.025
Red	125	800	10	275	0.025
Purple	125	1000	6	290	0.075

Notes: $\Sigma_{g,0}$ & $\Sigma_{\star,0}$ are central gas and stellar surface densities for exponential disks, with scale lengths R_g & $R_\star$. $R_\star$ = 3 kpc for all mock galaxies. v_c is the (flat) circular velocity, used for $\Omega = v_c/R$. $\langle \epsilon_{sf} \rangle$ is varied within observational bounds $\sim 0.01 - 0.1$ (Lee et al., 2016).

star formation events. To that end, given our fiducial assumption of $f_{sf} = 0.3$, our model favors low cloud-scale average star formation efficiencies $\langle \epsilon_{sf} \rangle \sim 0.01 - 0.1$, as the depletion time–stability constraints otherwise exclude $\langle \epsilon_{sf} \rangle \gtrsim 0.1$ for our fiducial model.

4.3.3 Reproducing Resolved Galaxy Relations

So far we have considered the star formation cycles of only individual patches of gas. Given that local galaxies ($z \lesssim 0.1$), unlike their high-z progenitors, cannot be modeled as a single star-forming HII region, we build a snapshot of a star-forming galaxy with our model by sampling many patches of a gas disk to understand the global distribution of star formation rates and velocity dispersions. We consider here a few exponential disks of gas and stars. Table 4.3 summarizes the properties of these toy galaxies. We then discretize these disks into cartesian grids of 750 pc-sized pixels, extending 24 kpc on a side, sampling their surface densities at their centers. For each of these points, we run our model with our fiducial parameters (see Table 4.2), except for the cases where we have varied the small-scale star formation efficiency $\langle \epsilon_{sf} \rangle$, and randomly sample one time-step to find our star formation rates, gas surface densities and velocity dispersions. In two cases here, to highlight galaxy to galaxy variation in GMC properties, we have chosen to vary the small-scale star formation efficiency within the bounds of observations (Lee et al., 2016). Ignored here, too, is the variance in Σ_g at constant radius (e.g., spiral arm features) that may contribute to variance in SFE (Gallagher et al., 2018). The results of this are seen in Figure 4.5, where we plot the resulting Kennicutt-Schmidt, gas velocity dispersion–SFR, and depletion time–Toomre-Q relations. We compare our model mock galaxy distributions (light & dark colored shaded regions) with resolved
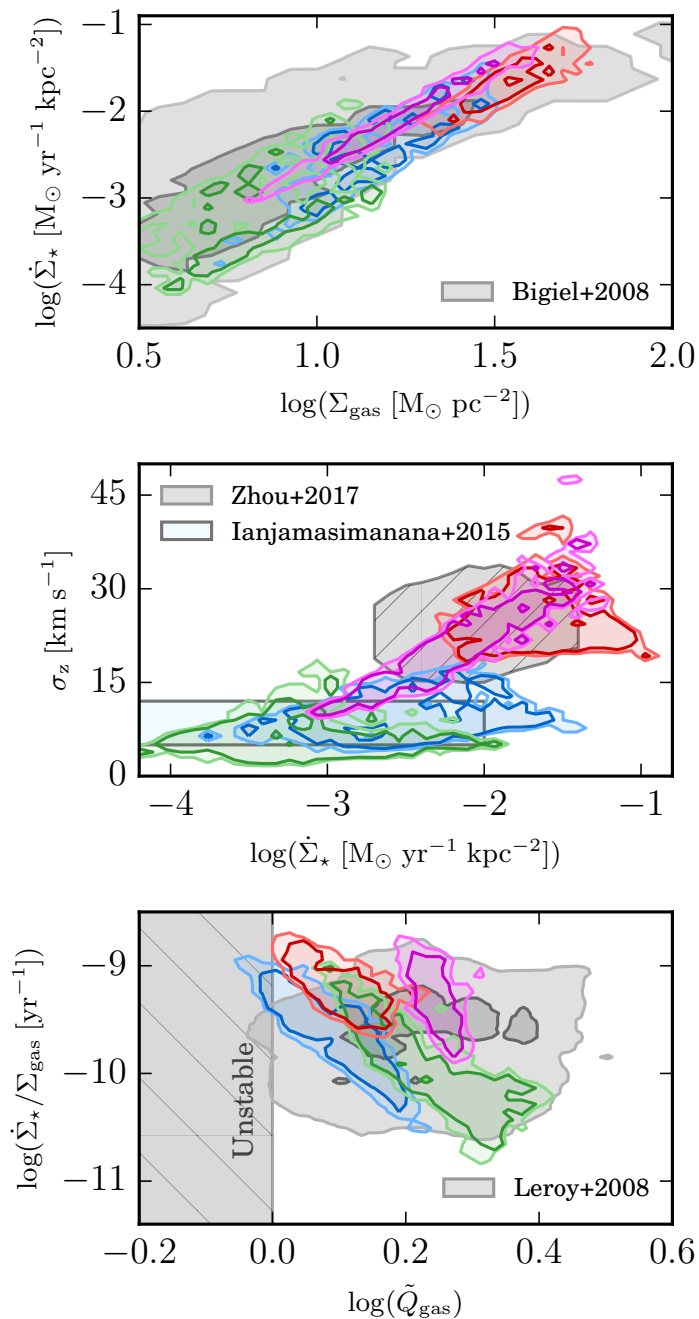
Figure 4.5: Comparison of the KS, gas velocity and Toomre-Q distributions of the non-equilibrium model (brightly colored shaded regions) drawn from mock galaxies. Plotted quantities and observational data contours are in the style of Figure 4.2. Mock galaxies are exponential profiles of gas and stars, whose properties are summarized in Table 4.3. The galaxies are sampled at 750 pc resolution for radii $5 < R < 17$ kpc, and a random time-point is chosen in the $3 < \Omega t < 8$ range for the non-equilibrium model with those local conditions. Dark and light shaded regions indicate 50 and 90 % inclusion regions for the model pixel distributions. Mock distributions have significant overlap with observations in each panel, and together tile a significant portion of the observational data with modest changes in galaxy properties and star formation efficiencies.

galaxy observations like previous figures, and find good agreement between this simple model and data. To enable comparison, the central surface densities, scale-lengths, and orbital velocities used in our mock galaxy model were chosen to be comparable with Milky Way-mass spiral star-forming galaxies. We do not plot pixels in our model with $R < 5$ kpc, as these regions are unlikely to be modeled correctly as independent patches following cycles in star formation rate–gas velocity dispersion space (cf., the central molecular zone of the Milky Way), given the omission of various dynamical effects like gas migration and cloud-cloud collisions (Semenov et al., 2017; Semenov et al., 2018).

The Kennicutt-Schmidt relation produced by our models in this way find good agreement with the 'regulated disk' regime of Bigiel, Leroy, Walter, Brinks, et al. (2008). These models produce a floor in velocity dispersions as a function of star formation rate that is somewhat lower at higher star formation rates ($\gtrsim 10^{-2}$ $M_\odot$ pc^{-2}) that is somewhat below Zhou et al. (2017). However, given the simple structure of our mock galaxies, it is unclear if this a matter of the dynamical times or ratio of thin to thick stellar disk components being unrealistic, or a problem with the model. Moreover, the general scatter in velocity dispersions agrees with that of the observations, using reasonably inferred parameter values. Lacking outflows, or some sub-grid model for local ISM heating, this model may not correctly capture the leading-edge (in SFR for a given σ_z) of the velocity dispersion relation, where the ISM can be disrupted by outflow events.

Observing the depletion time–stability relation of the mock galaxies in the bottom panel of Figure 4.5, the variations (radially) across and between the galaxies affect the normalization of the star formation-turbulence cycles of the individual patches. This results in a widening of the relation within each galaxy, as observed on ~kpc-scales. Galaxy to galaxy variations in gas and stellar properties, and variations in the star formation efficiencies of GMCs, cause the pixel distributions from the mock galaxies to tile the observational space. Though there is still a correlation between the quantities as observed in a single mock galaxy, the correlation is much weaker taken on the whole. Observationally, this may present difficulties in producing a depletion time–stability relation, given that galaxy to galaxy variations in dynamical time and ratios of gaseous and stellar disk scale lengths will result in each galaxy distribution having slightly different normalizations in the depletion time–stability plane, smearing out the signal further through stacking.

Spatially resolved observations of an individual galaxy may indeed see fairly tight

correlation between depletion time and Toomre-Q, the exact slope and normalization of which will depend on the disk structure and GMC properties (here, assumed to be related to the 'small-scale' star formation efficiency $\langle \epsilon_{\mathrm{sf}} \rangle$). However, this is assuming that the star formation parameters are not changing significantly across individual galaxies, e.g., small-scale star formation efficiencies having gas surface density dependencies (Grudić et al., 2018), and again that there are not significant variations in Σ_g between independently evolving ISM patches at constant galactocentric radius.

Non-equilibrium star formation rates, therefore, appear to produce an avenue for explaining ~1-dex scatter in star formation rates in the Kennicutt-Schmidt relation, and scatter in the spatially resolved gas velocity dispersion–SFR relation. And although dynamical evolution of star-forming patches may obscure the relation between depletion time and stability somewhat, the variations in the disk properties across and between galaxies are more likely the reason for difficulties observing a tight correlation between Toomre-Q and SFRs (Leroy, Walter, Brinks, et al., 2008).

4.4 Discussion

4.4.1 The "Instantaneous" Feedback Timescales Limit

Much of this work focuses on the case where the feedback delay timescales t_d and $t_d + \delta t_d$ are within an order of magnitude of the local dynamical time of the galaxy $1/\Omega$ (or for strongly self-gravitating disks, $1/\sqrt{4\pi G \rho_0}$). In the case where t_d and $\delta t_d \ll 1/\Omega$, however, star formation and feedback can be treated as occurring "instantaneously" after a delay time t_d, compressing all SNe and prompt feedback into a spike at t_d. We too can consider the case when the star formation threshold is very sharp, i.e., $\beta \to \infty$ such that Eq. 4.12 becomes

$$f_{\mathrm{sf}}(\tilde{Q}_{\mathrm{gas}}) = \theta(Q_0 - \tilde{Q}_{\mathrm{gas}}) f_{\mathrm{sf}}^0 \,, \tag{4.14}$$

where $\theta(Q_0 - \tilde{Q}_{\mathrm{gas}})$ is the Heaviside step function at the star formation threshold of $\tilde{Q}_{\mathrm{gas}} = Q_0$. In this setting, the turbulent velocity dispersion σ is not allowed to fall much below the threshold value at Q_0, since feedback acts effectively instantaneously once star formation begins to occur.

Thus, the amount of star formation that occurs in a star formation episode is just the amount that can form in one feedback timescale. So, we form a surface density of stars per event

$$\Delta\Sigma_\star = \langle \epsilon_{\mathrm{sf}} \rangle f_{\mathrm{sf}}^0 \Sigma_g t_d / t_{\mathrm{eddy}} \,. \tag{4.15}$$

Interestingly, the amount of stars formed has no (direct) relation to the absolute strength of feedback, so long as the amount of momentum eventually injected back

into the ISM from this mass of stars is enough to at least momentarily halt additional star formation. The time between star formation events is dependent on the fact that each event will pump up the turbulent velocity dispersion by $\Delta\sigma = (P/m_\star)\Delta\Sigma_\star/\Sigma_g$. This extra momentum, above that required strictly to maintain stability, takes a time t_{cycle} to decay back down to the star formation threshold $\sigma(\tilde{Q}_{\text{gas}} = Q_0)$ of

$$t_{cycle} = \ln(1 + \Delta\sigma/\sigma(\tilde{Q}_{\text{gas}} = Q_0))/\Omega . \tag{4.16}$$

It is worth noting, that for the outskirts of galaxies, where the quantity $t_d\Omega$ is likely to be small as we assumed ($1/\Omega$ being the dominant component of the local dynamical time, thanks to exponentially falling disk surface densities), galaxy disks are seen to have relatively constant H$\textsc{i}$ disk velocity dispersions (Tamburro et al., 2009), and so we expect the ratio of $\Delta\sigma/\sigma(\tilde{Q}_{\text{gas}} = Q_0)$ to be small. Thus, we can approximate t_{cycle} as $t_{cycle} \approx \Delta\sigma/\sigma(\tilde{Q}_{\text{gas}} = Q_0)\Omega$.

And so the average star formation rate over a star formation cycle[8] is $\bar{\tilde{\Sigma}}_\star = \Delta\Sigma_\star/t_{cycle}$. Explicitly,

$$\bar{\tilde{\Sigma}}_\star \approx \frac{\Sigma_g\Omega\sigma(\tilde{Q}_{\text{gas}} = Q_0)}{P/m_\star} . \tag{4.17}$$

The average efficiency of star formation per dynamical time is then

$$\bar{\epsilon}_{\text{sf}} = \frac{\bar{\tilde{\Sigma}}_\star}{\Sigma_g\Omega} \approx \frac{\sigma(\tilde{Q}_{\text{gas}} = Q_0)}{P/m_\star} . \tag{4.18}$$

Neither the average star formation rate nor the average star formation efficiency have an explicit dependence on the "small-scale" (GMC-scale) star formation efficiency (here, $\langle\epsilon_{\text{sf}}\rangle$) or eddy-crossing/free-fall time t_{eddy}, or feedback delay timescale t_d (provided $t_d\Omega \ll 1$), so long as the amount of stars formed in a star formation episode injects enough momentum to regulate the ISM but not enough to fully disrupt it (i.e., drive $\tilde{Q}_{\text{gas}}$ to $\gg 1$). Unsurprisingly, this is identical to the result of § 4.2.1, though we are considering a case of extreme dis-equilibrium. This is complementary to the picture of feedback regulation in Semenov et al. (2018), where low star formation efficiencies produce high duty cycles of star formation- after all, less stars formed means $\Delta\sigma/\sigma(\tilde{Q}_{\text{gas}} = Q_0)$ will be smaller. Plugging in 'typical' values for $\sigma(\tilde{Q}_{\text{gas}} = Q_0) \approx 15 - 45$ km/s and $P/m_\star \approx 3000$ km/s yields a global, averaged star formation efficiency of $\bar{\epsilon}_{\text{sf}} \approx 0.005 - 0.015$. These are not altogether unreasonable values for the star formation efficiency in the outskirts of galaxies (Bigiel, Leroy,

---

[8]This is identical to averaging it over a dynamical time, as then we have a star formation rate of $\Delta\Sigma_\star\Omega/\Omega t_{cycle} = \Delta\Sigma_\star/t_{cycle}$.

Walter, Blitz, et al., 2010), and in agreement with the median values of star formation efficiencies of our fiducial model. This provides a reasonable mechanism, reliant on averaging non-equilibrium star formation episodes, for regulating *local* star formation (of any efficiency) to global inefficiency on galactic dynamical timescales.

4.4.2 Low Gas Surface Density Regime/Limit

Seen clearly across the Kennicutt-Schmidt panels of Figures 4.3 and 4.4, the delayed feedback model drives large ~ 2 dex scatter in SFRs for gas surface densities $\lesssim 10$ $M_\odot$ pc^{-2}. As the gas surface density falls below 10 $M_\odot$ pc^{-2}, two processes dovetail to make our feedback-regulated turbulent disk model break down.

Below ~ 10 $M_\odot$ pc^{-2}, the gas disk transitions from a supersonic(turbulently supported) molecular disk, to a transonic atomic disk (with non-negligible thermal support), as the sound speed of 6000 K gas is almost but not quite sufficient with $c_s \sim 6$ km/s to maintain $\tilde{Q}_{\rm gas} \sim 1$ (i.e., providing nearly half of the required support). In these circumstances, stirring due to supernovae no longer dominates as the sole process stabilizing the ISM on kpc-scales, and the maintenance of thermal support in a two-phase medium becomes necessary to include. The thermal support component, and its connection to stellar feedback, is not included in the model, as it would require modeling the molecular gas fraction $f_{\rm H_2}$ and gas cooling, which is beyond the scope of this work. Further, given the increasingly two-phase nature of the ISM at low Σ_g, the treatment of the star-forming fraction $f_{\rm sf}(\tilde{Q}_{\rm gas})$ as a simple power law may break down, contributing to a change in kpc-scale star formation efficiencies (Schaye, 2004; Krumholz et al., 2009b; Krumholz, Burkhart, et al., 2018). Additional considerations at low gas surface densities include the ability of gas self-gravity (not included) to drive sufficient turbulence in the outer H I disks (Agertz, Lake, et al., 2009).

On the other hand, for the "lightest" cold, turbulently supported disks with surface densities ~ 10 $M_\odot$ pc^{-2}, SNe feedback from star formation events can inject significant fractions of the turbulent momentum in the disk. Take a star formation event at a gas surface density of 10 $M_\odot$ pc^{-2}, where our fiducial model reaches peaks star formation rates of $\dot{\Sigma}_\star \sim 10^{-2.5}$ $M_\odot$ kpc^{-2} yr^{-1} for $\sim 10^7$ yr (cf., plausible GMC lifetimes) producing $\sim 10^{4.5}$ $M_\odot$ kpc^{-2} of stars. These young stars then result in a SNe density of $\sim 10^{2.5}$ kpc^{-2} in the proceeding ~ 40 Myr (given a rate of a single SNe per 100 $M_\odot$ of stars formed; Ostriker, McKee, et al., 2010). At a momentum per Type II SNe of $\sim 3 \times 10^5$ $M_\odot$ km/s (Martizzi et al., 2015),

this is a turbulent momentum injection of $\sim 10^8$ M$_\odot$ km/s kpc^{-2}. For a ~ 10 M$_\odot$ pc^{-2} gas disk, with $\tilde{Q}_{\text{gas}} \sim 1$ ($\sigma \sim 10$ km/s), the total turbulent gas momentum is $\sim \Sigma_g \sigma (\tilde{Q}_{\text{gas}} \sim 1) \sim 10^8$ M$_\odot$ km/s kpc^{-2}. As the momentum injected is a non-negligible (tens of percent approaching unity, with uncertainty regarding the feedback budget per SNe Fielding, Quataert, and Martizzi 2018, Gentry et al. 2019) fraction of the momentum contained in the turbulence field of the whole disk patch, feedback is increasingly disruptive to the disk structure. This is more or less the difference between SNe clusters blowing holes in the ISM (dominating), versus churning or stirring it (perturbations).

And so, given that our model does not capture the feedback, star formation and gas physics of the transition from a predominantly atomic ISM with non-negligible thermal support to a turbulently supported, molecularly dominated one, this model exhibits increasingly disruptive star formation events at low gas surface densities. It is not clear, on the basis of this model alone, the extent to which growing scatter ($\gtrsim 2$ dex) in star formation rates due to the time-lag of feedback injection are to be expected for low ($\lesssim 10$ M$_\odot$ pc^{-2}) gas surface density regions. Broadly, this is exemplary of the difficulties in modeling the variety of star formation environments within galaxies with a single, simple model.

4.5 Conclusions

In this chapter, we developed a simple, non-equilibrium model of star formation in the context of sub-kpc patches of disk galaxies (cf. local disk scale heights) and explored its ability to explain the scalings and scatter in galaxy star formation relations. Our principal conclusions are as follows:

- The local strength of feedback $P/m_\star$, in addition to setting the normalization of the KS relation, itself may contribute to setting the scatter in observed SFRs. If the variance in turbulent momentum is roughly constant through star formation events, then the variance in SFRs is inversely proportional to $P/m_\star$ through $\Delta\sigma \propto P/m_\star \Delta\dot{\Sigma}_\star$.

- Longer delay times between star formation and the injection of feedback t_d and overall injection intervals δt_d are able to drive larger departures from star formation equilibrium. This occurs because the ISM is able to "overshoot" and over-produce stars to a greater extent, and the subsequent feedback events drive larger velocity dispersions (Toomre-Qs). Delay times on the order of 4-6 Myr produce ~dex scatter in SFRs.

- The relative steepness of the gravitational instabilities threshold and the timescale of feedback injection may together explain the large range of SFRs seen at low Σ_g with little variance in velocity dispersions in outer HI disk velocity dispersion profiles (e.g., spiral galaxy HI disks in the THINGS survey, Ianjamasimanana, de Blok, Walter, and Heald, 2012; Ianjamasimanana, de Blok, Walter, Heald, et al., 2015).

- This model predicts a correlated depletion time–Toomre-Q relation for individual galaxies (cf., bottom panel of Figure 4.5). However, within individual galaxies a degree of scatter is introduced as the normalization and slope of the locally tightly evolving relation varies across disks with the changing disk properties. Further smearing of this relation is introduced in galaxy surveys by stacking different galaxies with altogether different disk and GMC properties (with their attendant differing slopes and normalizations of the depletion time–stability relation).

The proposed non-equilibrium star formation model can explain the observed ~ 1 dex scatter in resolved star formation scaling relations. More so than the effects of metallicity or variations in gas fraction, non-equilibrium states of star formation can explain large variations in average star formation rates (e.g., Hα-inferred SFRs). This arises due to the fact that the interplay of bursty feedback, injected over some finite timescale, and the roughly smooth dissipation of turbulence (on ~kpc-scales) struggles to find a stable balance on timescales of tens of Myrs.

Careful spatially resolved observations of *individual* star-forming galaxies may be able to identify a depletion time–Toomre-Q relation, provided that the effects of variations in gas fraction at constant radius and changes in star formation efficiency within GMC across the disks can be accounted for. Indeed, the slope and normalization of this relation may even inform on the small-scale star formation efficiency within those specific galaxies.

Future work using resolved galaxy surveys, like the MaNGA and SAMI surveys, at the sub-kpc-scale may help to elucidate the extent to which the scatter in resolved star formation rates correlates with dynamical conditions at the disk scale. The ability to marshal statistically significant samples of star-forming regions with similar physical conditions may make it possible to disentangle potentially confounding local quantities such as metallicity or gas fraction.

Acknowledgments

Parameters of Supernova Feedback

The lifetimes of massive (8–40 $M_\odot$) stars that are the progenitors of Type II SNe events are fairly well constrained for our purposes. Furthermore, the slope of the massive end of the stellar initial mass function (IMF) is also well known (see Krumholz, 2014; Offner et al., 2014, and references therein). Together, these constraints put a strong prior on the parameter space to be explored by this model, in terms of the delay time to the first effects of SNe feedback being felt, how long feedback events last, and the relative distribution of feedback injection in time after a star formation event.

From stellar evolution theory, the main sequence lifetimes of the most massive stars in the local universe range from approximately 4.5 to 38 Myr for 40 to 8 $M_\odot$ stars (Raiteri et al., 1996). We take the lifetime of a 40 $M_\odot$ star as a bound for the minimum delay time to the first SNe feedback effects in our model t_d. Admittedly, longer delay times by perhaps a factor of two are not unreasonable given the (un)likelihood of forming the most massive star first in a local star formation episode, in addition to the various effects of rotation and binarity. On the other hand, there is a broader absolute range in the time for the last Type II SNe to go off of 30–49 Myr (approximately factor of two uncertainty), given the uncertainty in the lower mass limit for Type II SNe progenitors of $8 \pm 1\ M_\odot$ (Smartt, 2009).

To constrain the distribution in time of Type II SNe events from a star formation episode (between the most and least massive progenitor's endpoints), i.e., dN_{SN}/dt, we combine the IMF slope $dN/dM_\star$ and the mass dependence of main sequence lifetimes (specifically $dt/dM_\star$). Taking the lifetimes of massive stars to be proportional to their mass-to-light ratios $t(M_\star) \propto M_\star/L_\star$ and with $L_\star \propto M_\star^{3.5}$, we have

$t(M_\star) \propto M_\star^{-2.5}$ (or $M_\star \propto t^{-2/5}$) and thus $dM_\star/dt \propto t^{-7/5}$ (Böhm-Vitense, 1992). From the slope of the high-mass end of the IMF, we take the canonical Salpeter IMF slope of -2.35, i.e., $dN/dM_\star \propto M_\star^{-2.35}$, and in terms of their stellar lifetimes $dN/dM_\star$ is then $\propto t^{4.7/5}$. Combining these arguments, we yield a power-law distribution of,

$$\frac{dN_{\text{SN}}}{dt} = \frac{dN}{dM_\star}\frac{dM_\star}{dt} \propto t^{-0.46} , \tag{4.19}$$

which is fairly weak (though not flat) in time, as the shorter lifetimes of the most massive stars nearly balance out with their relative rarity.

For the purposes of this study, we thus adopt an initial delay time of $t_d = 5$ Myr, a feedback episode period of $\delta t_d = 30$ Myr, and a time-weighting of $dN_{\text{SN}}/dt \propto t^{-0.46}$.

What About SFR Averaging Timescales?

Observationally, the "instantaneous" star formation rate of a region is ill-defined. YSO counts are perhaps the closest proxy to an true instantaneous star formation rate, but even they have a spread in their lifetimes (hence the averaging timescale of SFRs inferred) of as little as 0.5 Myr for 0/I YSOs to being a Myr or more removed from the star formation event itself in the case of Class II YSOs (Evans et al., 2014; Heyer et al., 2016). As such, any model of non-equilibrium star formation must be convolved with an averaging timescale for the observable tracer. In the case of Hα or IR flux, we are averaging over a $\sim 2 - 4$ Myr timescale, for tracers like the FUV flux, that timescale is significantly longer (~ 30 Myr). Hence, variability in star formation rates on timescales shorter than the averaging timescale of the particular tracer investigated will be smoothed out. We investigate the effects of particular choices of averaging period ΔT_{SFR} in Figure 4.6, wherein we convolve the instantaneous star formation rates produced by our model (Eq. 4.13) with a 2–10 Myr wide time-averaging window ΔT_{SFR}. Specifically choosing this timescale to be a proxy for the Hα and IR flux-inferred star formation rates, to show how the variations in SFR over the cycle are smoothed out. Increasing the averaging window blunts the star formation rate maxima achieved, as the peak in the star formation cycle is smoothed to some degree. The particular choice of averaging window does not alter the predictions of the model with respect to Σ_{gas} or σ_z. The averaging effects on $\dot{\Sigma}_\star$ are relatively small as $\Delta T_{\text{SFR}}\Omega \sim 0.1$ in our fiducial model, and so the averaging window constitutes only a fraction of a star formation cycle. Throughout the main body of the text, we adopt a canonical 3 Myr averaging window for our star formation tracer for simplicity.
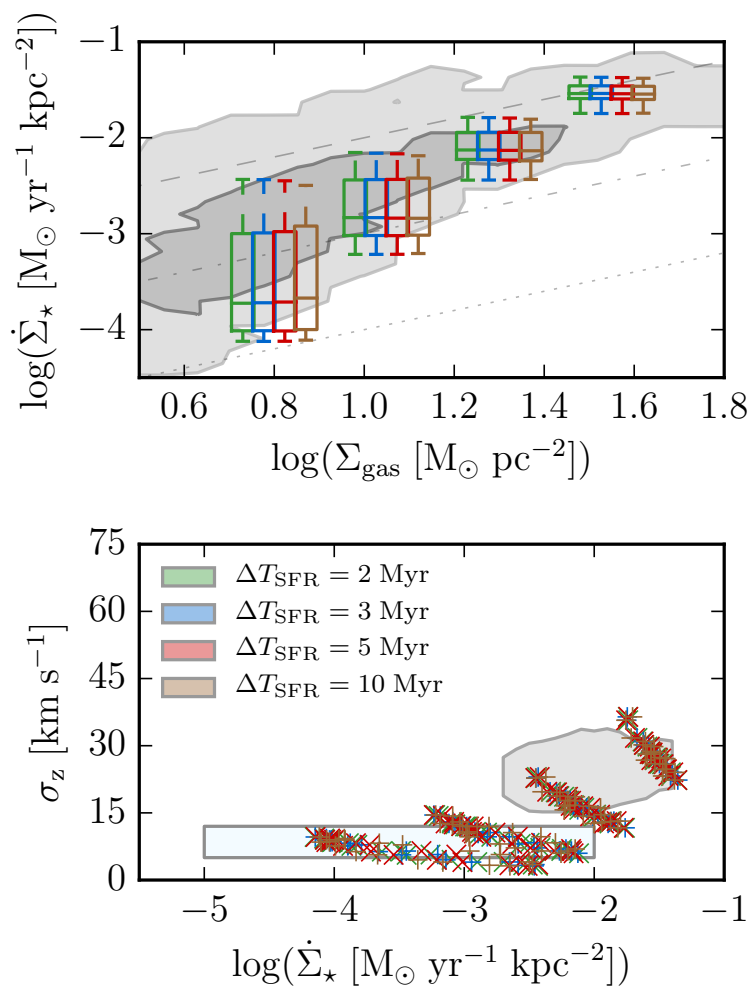
Figure 4.6: Effects of variation in the star formation averaging period on the model KS and gas velocity dispersions for fiducial model parameters. Observational (KS) data and plotted quantities are in the style of Figure 4.3. For reasonable choices of averaging period between 2–10 Myr (cf., the Hα tracer timescale and timescales thereabouts), little to no effect is seen on the average star formation rate distributions.

References

Agertz, O. & Kravtsov, A. V. (2015) ApJ 804, 18, 18

Agertz, O., Kravtsov, A. V., Leitner, S. N., & Gnedin, N. Y. (2013) ApJ 770, 25, 25

Agertz, O., Lake, G., Teyssier, R., Moore, B., Mayer, L., & Romeo, A. B. (2009) MNRAS 392, 294

Benincasa, S. M., Wadsley, J., Couchman, H. M. P., & Keller, B. W. (2016) MNRAS 462, 3053

Bigiel, F., Leroy, A., Walter, F., Blitz, L., Brinks, E., de Blok, W. J. G., & Madore, B. (2010) AJ 140, 1194

Bigiel, F., Leroy, A., Walter, F., Brinks, E., de Blok, W. J. G., Madore, B., & Thornley, M. D. (2008) AJ 136, 2846

Böhm-Vitense, E. (1992)

Bolatto, A. D., Wolfire, M., & Leroy, A. K. (2013) ARA&A 51, 207

Calzetti, D., Liu, G., & Koda, J. (2012) ApJ 752, 98, 98

Elmegreen, B. G. (2018) ApJ 854, 16, 16

Elmegreen, B. G. & Hunter, D. A. (2015) ApJ 805, 145, 145

Evans II, N. J., Heiderman, A., & Vutisalchavakul, N. (2014) ApJ 782, 114, 114

Faucher-Giguère, C.-A., Quataert, E., & Hopkins, P. F. (2013) MNRAS 433, 1970

Federrath, C. et al. (2017) MNRAS 468, 3965

Fielding, D., Quataert, E., & Martizzi, D. (2018) MNRAS 481, 3325

Fielding, D., Quataert, E., McCourt, M., & Thompson, T. A. (2017) MNRAS 466, 3810

Gallagher, M. J. et al. (2018) ApJ 858, 90, 90

Gentry, E. S., Krumholz, M. R., Madau, P., & Lupi, A. (2019) MNRAS 483, 3647

Gilmore, G. & Reid, N. (1983) MNRAS 202, 1025

Grudić, M. Y., Hopkins, P. F., Faucher-Giguère, C.-A., Quataert, E., Murray, N., & Kereš, D. (2018) MNRAS 475, 3511

Hayward, C. C. & Hopkins, P. F. (2017) MNRAS 465, 1682

Heyer, M. et al. (2016) A&A 588, A29, A29

Ho, I.-T. et al. (2017) ApJ 846, 39, 39

Hopkins, P. F. (2013) MNRAS 430, 1653

Hopkins, P. F., Kereš, D., Oñorbe, J., Faucher-Giguère, C.-A., Quataert, E., Murray, N., & Bullock, J. S. (2014) MNRAS 445, 581

Hopkins, P. F., Quataert, E., & Murray, N. (2011) MNRAS 417, 950

– (2012) MNRAS 421, 3488

Hopkins, P. F., Wetzel, A., et al. (2018) MNRAS 480, 800

Ianjamasimanana, R., de Blok, W. J. G., Walter, F., & Heald, G. H. (2012) AJ 144, 96, 96

Ianjamasimanana, R., de Blok, W. J. G., Walter, F., Heald, G. H., Caldú-Primo, A., & Jarrett, T. H. (2015) AJ 150, 47, 47

Kauffmann, J., Goldsmith, P. F., Melnick, G., Tolls, V., Guzman, A., & Menten, K. M. (2017) A&A 605, L5, L5

Kennicutt Jr., R. C., Calzetti, D., et al. (2007) ApJ 671, 333

Kennicutt, R. C. & Evans, N. J. (2012) ARA&A 50, 531

Kim, C.-G. & Ostriker, E. C. (2015a) ApJ 802, 99, 99

– (2015b) ApJ 815, 67, 67

Kim, W.-T. & Ostriker, E. C. (2007) ApJ 660, 1232

Kruijssen, J. M. D. & Longmore, S. N. (2014) MNRAS 439, 3239

Kruijssen, J. M. D., Schruba, A., Hygate, A. P. S., Hu, C.-Y., Haydon, D. T., & Longmore, S. N. (2018) MNRAS 479, 1866

Krumholz, M. R. (2014) Physics Reports 539, 49

Krumholz, M. R. & Burkhart, B. (2016) MNRAS 458, 1671

Krumholz, M. R., Burkhart, B., Forbes, J. C., & Crocker, R. M. (2018) MNRAS 477, 2716

Krumholz, M. R., McKee, C. F., & Tumlinson, J. (2009a) ApJ 693, 216

– (2009b) ApJ 699, 850

Lee, E. J., Miville-Deschênes, M.-A., & Murray, N. W. (2016) ApJ 833, 229, 229

Leitherer, C. et al. (1999) ApJS 123, 3

Leroy, A. K., Schinnerer, E., et al. (2017) ApJ 846, 71, 71

Leroy, A. K., Walter, F., Brinks, E., Bigiel, F., de Blok, W. J. G., Madore, B., & Thornley, M. D. (2008) AJ 136, 2782

Leroy, A. K., Walter, F., Sandstrom, K., et al. (2013) AJ 146, 19, 19

Ma, X., Hopkins, P. F., Feldmann, R., Torrey, P., Faucher-Giguère, C.-A., & Kereš, D. (2017) MNRAS 466, 4780

Martizzi, D., Faucher-Giguère, C.-A., & Quataert, E. (2015) MNRAS 450, 504

McKee, C. F., Parravano, A., & Hollenbach, D. J. (2015) ApJ 814, 13, 13

Murray, N., Quataert, E., & Thompson, T. A. (2010) ApJ 709, 191

Narayanan, D., Krumholz, M. R., Ostriker, E. C., & Hernquist, L. (2012) MNRAS 421, 3127

Offner, S. S. R. et al. (2014) Protostars and Planets VI, 53

Oklopčić, A., Hopkins, P. F., Feldmann, R., Kereš, D., Faucher-Giguère, C.-A., & Murray, N. (2017) MNRAS 465, 952

Onus, A., Krumholz, M. R., & Federrath, C. (2018) MNRAS 479, 1702

Orr, M. E. et al. (2018) MNRAS 478, 3653

Ostriker, E. C., McKee, C. F., & Leroy, A. K. (2010) ApJ 721, 975

Ostriker, E. C. & Shetty, R. (2011) ApJ 731, 41, 41

Padoan, P., Pan, L., Haugbølle, T., & Nordlund, Å. (2016) ApJ 822, 11, 11

Rafikov, R. R. (2001) MNRAS 323, 445

Raiteri, C. M., Villata, M., & Navarro, J. F. (1996) A&A 315, 105

Robertson, B. & Goldreich, P. (2012) ApJ 750, L31, L31

Saitoh, T. R. et al. (2008) PASJ 60, 667

Schaye, J. (2004) ApJ 609, 667

Schruba, A., Leroy, A. K., Walter, F., Sandstrom, K., & Rosolowsky, E. (2010) ApJ 722, 1699

Scoville, N. Z. & Sanders, D. B. (1987) *Interstellar Processes* ed. by D. J. Hollenbach & H. A. Thronson Jr. vol. 134 Astrophysics and Space Science Library, 21

Semenov, V. A., Kravtsov, A. V., & Gnedin, N. Y. (2017) ApJ 845, 133, 133

– (2018) ApJ 861, 4, 4

Shetty, R. & Ostriker, E. C. (2012) ApJ 754, 2, 2

Smartt, S. J. (2009) ARA&A 47, 63

Tamburro, D. et al. (2009) AJ 137, 4424

Thompson, T. A., Quataert, E., & Murray, N. (2005) ApJ 630, 167

Toomre, A. (1964) ApJ 139, 1217

Torrey, P., Hopkins, P. F., Faucher-Giguère, C.-A., Vogelsberger, M., Quataert, E., Kereš, D., & Murray, N. (2017) MNRAS 467, 2301

Zhou, L. et al. (2017) MNRAS 470, 4573

Chapter 5

SPATIALLY RESOLVED GAS VELOCITY DISPERSIONS AND STAR FORMATION RATES IN DISK ENVIRONMENTS OF COSMOLOGICAL SIMULATIONS

ABSTRACT

We present an analysis of the sub-kpc spatially resolved line-of-sight velocity dispersion and star formation rate relation in the FIRE-2 (Feedback in Realistic Environments) suite of cosmological zoom-in simulations. We specifically investigate the relation between gas velocity dispersions (σ) and star formation rates (SFRs) in Milky Way-mass ($10^{10} - 10^{11}$ M$_\odot$ in stellar mass) spiral galaxies at late times ($z < 0.1$). In agreement with observations, we find a relatively flat relationship, with velocity dispersions remaining approximately constant ($\approx 15 - 30$ km/s in neutral gas) across 3 dex in star formation rates. We find that: (1) higher dense gas fractions relate to higher SFRs at constant σ, (2) higher SFRs over 100 Myr timescales correlate with higher σ, but (3) only when recent ($\lesssim 10$ Myr) SFRs are low, (4) dense gas depletion times are short when gas is predominately cold & dense, or when very little of the ISM is, and (5) the outer contours of the σ-$\dot{\Sigma}_\star$ relation appear to correspond with regimes where significant fractions of the ISM can be expelled in outflows. Finally, there is evidence in the simulations for on-off modes of star formation corresponding to feedback injection timescales of 10–100 Myr, where SFRs over and undershoot equilibrium SFR predictions.

Star formation in the local universe (at $z \approx 0$) is dominated by spiral galaxies of approximately Milky Way-mass with stellar masses of $\sim 10^{10} - 10^{11}$ M$_\odot$ (Brinchmann et al., 2004; Behroozi et al., 2013). A hallmark of these disk galaxies at late times is the stability of their disks, and relatively constant global star formation rates over the last several billion years (Ma et al., 2017; Simons et al., 2017). To understand how star-forming galaxies have evolved for half the history of the Universe is thus to understand how star formation and ISM dynamics occur and evolve in disk environments.

As with many endeavors in the study of star formation, the path in understanding star formation in disk environments leads back to early work in our own Milky-Way by Schmidt (1959). In that work, the rate of star formation was first estimated by comparing the local scale heights of the H I disk and the thin stellar disk. This work evolved over the ensuing decades into the well known, and argued over, Kennicutt-Schmidt relation correlating the global neutral gas and star formation rate surface densities (Kennicutt 1989, and see Kennicutt and Evans 2012 for a recent review). This relation is fairly tight ($\lesssim$ a dex) over several decades in galaxy surface densities.

The advent of high-resolution galaxy studies advanced the global Kennicutt-Schmidt relation into the *resolved* Kennicutt-Schmidt relation (Bigiel et al., 2008; Leroy, Walter, Brinks, et al., 2008). Down to scales of individual molecular clouds (~100 pc), the relation has survived in some form or another (Leroy, Walter, Sandstrom, et al., 2013). However, even on kiloparsec-scales, numerous studies have explored the spatial and temporal averaging of star formation and gas tracers upon which the Kennicutt-Schmidt relation, and associated Elmegreen-Silk relation, the "efficiency" counterpart to Kennicutt-Schmidt that compares the star formation rate surface density $\dot{\Sigma}_\star$ to the gas surface density times the local orbital dynamical time $\Sigma_g \Omega$, rely (Schruba et al., 2010; Calzetti et al., 2012; Kruijssen et al., 2014). Much of this has sought to understand the ~dex scatter in Kennicutt-Schmidt at constant gas surface density (or scatter in gas surface density at constant SFR). Theoretical work has explored and treated star formation as an equilibrium process (Thompson et al., 2005; Ostriker et al., 2011; Faucher-Giguère et al., 2013; Hayward et al., 2017). The hierarchy of timescales involved provided motivation: star formation, and the bulk of stellar feedback, occurs on the timescale of a few million years or fewer (tens at most), but the dynamical times of galaxies can be on the order of 100 Myr. If galaxies are to have long-lived coherent structures (e.g., spiral arms), star formation must either be in equilibrium with those structures or be unable to

greatly affect them. The scatter seen in the Kennicutt-Schmidt and Elmegreen-Silk relations has long been viewed as "the weather" of variations in local conditions and differing resulting star formation equilibria.

In particular, the local gas scale height, relating back to the mid-plane density of gas in the galaxy disks, is seen as a particularly important variable in setting the star formation rate locally within galaxies, through both the free-fall time of the gas, where $t_{\rm ff} \sim 1/\sqrt{G\rho} \sim \sqrt{h/G\Sigma}$, and the stability of the gas against gravitational fragmentation and collapse. The stability of neutral gas against gravitational fragmentation and collapse is a key factor, relating to the velocity dispersions in galaxies. Often, a (modified) Toomre-Q parameter (Toomre, 1964) is invoked, with a form similar to:

$$\tilde{Q}_{\rm gas} \equiv \frac{\sqrt{2}\sigma_z\Omega}{\pi G(\Sigma_g + \gamma\Sigma_\star)} \,, \tag{5.1}$$

where σ_z is the vertical (line-of-sight, mass-weighted) velocity dispersion in the gas, Ω the dynamical angular velocity ($\Omega = v_c/R$), G the Newtonian gravitational constant, and ($\Sigma_g + \gamma\Sigma_\star$) being the effective disk surface density, where Σ_g is the neutral (atomic + molecular) gas surface density and the $\gamma\Sigma_\star$ represents the fraction of the stellar component within the gas disk scale height (and thus contributing to the self-gravity of the disk)[1]. It is often assumed that the turbulence field is roughly isotropic on a disk scale height, so the in-plane turbulence in a disk (that used for the 'classical' Toomre-Q parameter) is equivalent to the line-of-sight component, thus $\sigma_R \approx \sigma_z$.

For gas in galaxies with $\tilde{Q}_{\rm gas} \lesssim 1$, there is insufficient (turbulent) support to prevent fragmentation and gravitational collapse. This gas is then collapsing to form stars, removing it from the gas reservoir. Those stars then inject feedback to the remaining gas to stabilize it. On the other hand, gas with large values of $\tilde{Q}_{\rm gas}$ is likely to be dynamically expanding or in the midst of an outflow event. In the event that this gas is not being actively driven to yet larger values of $\tilde{Q}_{\rm gas}$, it is expected that the gas dissipates its turbulence rapidly on a disk-crossing time, driving to $\tilde{Q}_{\rm gas} = 1$. And so, for the purposes of supersonically turbulent disks, we expect that gas ought to converge to a $\tilde{Q}_{\rm gas} \approx 1$.

The rate at which marginally unstable gas (with $\tilde{Q}_{\rm gas} \lesssim 1$) in galaxies ought to form stars is theoretically uncertain. Some feedback-regulation arguments, specifically

---

[1] For all subsequent calculations of $\tilde{Q}_{\rm gas}$ in this work, we calculate the γ factor assuming that the stellar component has an exponential scale height, and thus is $\gamma = 1 - \exp\left(-\sigma_{z,{\rm gas}}/\sigma_{z,\star}\right)$, to simplify direct calculations of this factor in comparisons with observations.

that feedback from young stars balances the gravitational weight of the ISM, are completely agnostic to the velocity dispersions or specific value of Toomre-Q (Ostriker et al., 2011). On the other hand, arguments like those of Faucher-Giguère et al. (2013), reason that feedback injection rates must balance turbulence dissipation (at its decay rate of $\sim \Sigma \sigma \Omega$), and thus $\dot{\Sigma}_\star \propto \tilde{Q}_{\text{gas}}$. When the equilibrium $\tilde{Q}_{\text{gas}} \approx 1$ is true, this identical in scaling to that of (Ostriker et al., 2011). Other theories arguing that star formation occurs with a constant low efficiency per free-fall time in the disk predict a $\dot{\Sigma}_\star \propto \tilde{Q}_{\text{gas}}^{-1}$ scaling (Krumholz and Burkhart, 2016).

Star-forming regions themselves have avoided the large-scale equilibrium framework from the perspective of the "small-scale" star formation and ISM communities. Studies of local star-forming complexes like Orion and Taurus do not see star formation in equilibrium, rather it is seen as a dynamic and often destructive (for the molecular clouds themselves) process (Goldsmith and Li, 2005; Goldsmith, Li, and Krčo, 2007; Pineda, Goldsmith, et al., 2010). Equilibria in molecular clouds reside on a smaller scale in clouds, in the form of the PDR chemistry that traces internal dense structures like cores and filaments from which young stars form (Goldsmith, Heyer, et al., 2008; Orr, Pineda, et al., 2014; Xu et al., 2016), as significant cloud evolution occurs over only a few free-fall times (Grudić et al., 2018).

And so, in spite of the arguments for $\tilde{Q}_{\text{gas}} \rightarrow 1$ convergence on large scales, non-equilibrium star formation on the scale of giant molecular clouds (GMCs, $\gtrsim 100$ pc) has been argued as a source of scatter in star formation rates seen in Kennicutt-Schmidt (Benincasa et al., 2016; Torrey et al., 2017; Sparre et al., 2017; Orr, Hayward, and Hopkins, 2019). Recent work by Torrey et al. (2017) to understand how the outflows and "breathing modes" of central molecular regions are tied to star formation show that non-equilibrium star formation rates, on timescales of tens of millions of years, arise naturally from the competition between the stellar feedback and dynamical timescales involved as. Further work by Benincasa et al. (2016) and Orr, Hayward, and Hopkins (2019) have explored the dynamical and star formation rate responses in the ISM of disk environments to changing velocity dispersions and feedback injection on the timescales of tens of Myr.

Observationally, much of the work understanding the velocity dispersion structure of gas in local galaxies and their relationship with local star formation rates has been focused on the HII regions of those galaxies (Larson, 1981; Gallagher and Hunter, 1983; Rozas, Sabalisck, et al., 1998; Rozas, Richer, et al., 2006; Zhou et al., 2017). This is in part due to the relative difficulty in adequately measuring at high velocity-

space resolution the velocity structure of the colder, fainter dense molecular gas tracers like CO or HCN. Modern IFU surveys are just now beginning to report on the galaxy-wide, spatially resolved velocity structure and surface density distributions in the cold, dense molecular gas (Leroy, Schinnerer, et al., 2017; Gallagher, Leroy, Bigiel, Cormier, Jiménez-Donaire, Ostriker, et al., 2018; Gallagher, Leroy, Bigiel, Cormier, Jiménez-Donaire, Hughes, et al., 2018; Sun et al., 2018; Querejeta et al., 2019). Much of this recent work has focused on how dense gas fractions and the mid-plane pressure of the ISM correlate with star formation efficiencies, and whether or not variations in these quantities can explain the variations seen in star formation rates across the galaxies as a whole.

Cosmological zoom-in simulations have reached the state that they are beginning to resolve the ISM on scales within GMC complexes, with sub-parsec spatial resolution and mass resolutions reaching sub-10^3 M$_\odot$ (Hopkins, Kereš, et al., 2014; Wetzel et al., 2016; Hopkins, Wetzel, et al., 2018). Given the ability to resolve ISM dynamics on the scales within star-forming regions, recent work by Orr, Hayward, Hopkins, et al. (2018) has explored the spatially resolved properties of the Kennicutt-Schmidt relation and its dependences on local gas properties in the FIRE simulations. Another investigation of the FIRE suite by El-Badry et al. (2018) investigated the kinematic and morphological properties of gas within galaxies. However, neither study explicitly explored the connection between the spatially resolved gas kinematics (velocity dispersions) and the local star formation rates, leaving open the question of whether or not scatter in star formation rates within these simulated galaxies can be understood by variations in the instantaneous properties of the gas kinematics on kpc scales.

In this work, we explore the relationship between various spatially resolved (250 and 750 pc pixel sizes) measures of gas velocity dispersion and star formation rates that have direct observational proxies using the FIRE-2 cosmological zoom-in simulations. We explore the dependences of the velocity dispersions and star formation rates in Milky Way-like disk environments on local physical quantities in the simulated galaxies, like gas stability (Toomre-Q, Eq. 5.1), gas fractions, etc., and compare where possible with observational datasets.

Table 5.1: Summary of $z \approx 0$ properties of the FIRE-2 Milky Way-like galaxies used in this work

Name	$\log(\frac{M_\star}{M_\odot})$	$\log(\frac{M_{\text{gas}}}{M_\odot})$	$\frac{R_{\star,1/2}}{\text{kpc}}$	$\frac{R_{\text{gas},1/2}}{\text{kpc}}$	$\frac{v_c}{\text{km/s}}$ *
m12b	10.8	10.3	2.7	9.4	266
m12c	10.7	10.3	3.4	8.6	232
m12f	10.8	10.4	3.9	11.6	248
m12i	10.7	10.3	2.9	9.8	232
m12m	10.9	10.4	5.0	10.2	283
m12r	10.2	10.0	4.7	9.9	156
m12w	10.6	9.8	3.1	3.1	244

Note: all quantities measured within a 30 kpc cubic aperture.

*Circular velocities evaluated at $R_{\text{gas},1/2}$.

5.1 Simulations & Analysis Methods

5.1.1 FIRE-2 Simulations

The simulations used in this chapter were run with the gravity+hydrodynamics code GIZMO (Hopkins, 2015), and comprise the core FIRE-2 Milky Way-mass spiral galaxies (Hopkins, Wetzel, et al., 2018). Specifically, the simulations were run with a mesh-free Lagrangian Godunov (meshless finite mass, MFM) method that is second-order accurate and maintains many of the advantages of traditional SPH codes, while avoiding some of the traditional SPH code issues, e.g., struggling to accurately capture shocks, for which grid-based codes have been better in the past.

A brief summary of the $z = 0$ properties of the galaxy simulations used here are included in Table 5.1. These simulations all have a minimum baryonic particle mass of $m_{b,min} = 7100$ M$_\odot$, and minimum adaptive force softening lengths of 0.27 pc (**m12m**, **m12r**, **m12w**), 0.5 pc (**m12c**) and 0.7 pc (**m12b**, **m12f**, **m12i**). As these softening lengths are adaptive, it is useful to note that the typical/median softening length within the disk in one of the runs at $z = 0$, **m12i**, is $h \sim 20 - 40$ pc. The minimum length-scales considered in this work are on the order of hundreds of parsecs, and so are about three orders of magnitude above the minimum resolvable scales in the simulations. All of the simulations employ a standard flat ΛCDM cosmology with $h \approx 0.7$, $\Omega_M = 1 - \Omega_\Lambda \approx 0.27$, and $\Omega_b \approx 0.046$.

Star Formation Prescription in FIRE-2

As in FIRE-1 (Hopkins, Kereš, et al., 2014), star formation is allowed to proceed in the gas that is dense, molecular, and gravitationally bound in the simulations. However, a newly imposed (since FIRE-1) requirement that the gas is also Jeans

unstable is included. Formally, these requirements for star formation are:

- Density threshold: gas particles must have densities $n > 10^3$ cm^{-3}. Generally this is not a terribly stringent requirement. Its value does, however, affect the shape of the gas density PDF.

- Molecular/self-shielded: adopting the fitting functions of Krumholz and Gnedin (2011) for the molecular fraction of a given column of gas, assuming a local Sobolev approximation and accounting for the metallicity of the gas we calculate a molecular fraction f_{mol}. The gas that is forming stars must be molecular/self-shielded, and so $\rho_{\mathrm{mol}} = f_{\mathrm{mol}}\rho_{\mathrm{gas}}$ is the mass reservoir of star-forming gas on a per-particle basis. Due to the high density threshold ($n = 10^3$ cm^{-3}), this requirement is almost always superseded by the density and gravitationally bound requirements as dense, bound gas is almost completely molecular in nature.

- Jeans unstable: gas is required to have a particle mass below the maximum thermal Jeans mass, to ensure that any resolved, massive self-gravitating objects which should collapse coherently are followed self-consistently and not simply turned into stars. In practice, this criterion is almost always met when the others are.

- Gravitationally bound: locally, the gas must have a virial parameter $\alpha_{vir} \equiv (\delta v^2 + c_s^2)\delta r/Gm_{\mathrm{gas}}(< \delta r) = [||\nabla \otimes v||_i^2 + (c_{s,i}/h_i)^2]/(8\pi G\rho_i) < 1$, where $\delta v = ||\nabla \otimes v||_i h_i$ and c_s are the kinetic and thermal energy, respectively, within the smoothing scale $\delta r \to h_i$ around the particle ($\otimes$ is the outer product). This is the most stringent of the criteria, disallowing unbound gas from forming stars.

In the event that all of these criteria are met for a gas particle, the particle is turned into stars probabilistically at a rate $\dot{\rho}_\star = \rho_{\mathrm{mol}}/t_{\mathrm{ff}}$ where t_{ff} is the local free-fall time. It is stressed that this is the rate that *locally self-gravitating clumps* form stars, which is generally a small fraction of the overall dense gas mass in the simulations. The efficiency of dense gas in converting to stars per free-fall time in GMCs ($\sim 1 - -10\%$) and per galactic dynamical time in the FIRE simulations has been explored extensively (Hopkins, Kereš, et al., 2014; Orr, Hayward, Hopkins, et al., 2018), and found to be in agreement with observed efficiencies (Bigiel et al., 2008; Leroy, Walter, Brinks, et al., 2008; Lee et al., 2016).

Feedback Physics Implemented FIRE-2

The stellar feedback physics implemented in FIRE-2 are identical to those of FIRE-1, with updates only to accuracy and improved algorithmic implementations. Once a star particle is formed, it is treated as a single stellar population with known age, metallicity, and mass. The physics include: supernovae (Type Ia and II), stellar mass loss (OB/AGB-star winds), photoionization and photoelectric heating, and radiation pressure. Detailed descriptions of these physics and their implementation can be found in (Hopkins, Wetzel, et al., 2018). All feedback quantities are taken from standard stellar population models (STARBURST99, Leitherer et al. 1999), assuming a Kroupa 2002 IMF.

5.1.2 Mapping out FIRE-2: Resolved 'Observations' of the Simulations

In order to investigate line-of-sight velocity dispersions in the FIRE-2 simulations (hereafter, simply FIRE), and their relation to local star formation rates, we generate mock observational maps from a set of snapshots with $z \lesssim 0.1$ of a number of Milky Way-mass simulations from Hopkins, Wetzel, et al. (2018). We produce these maps in the manner of Orr, Hayward, Hopkins, et al. (2018), by centering on the stellar centers of mass and projecting the galaxies face-on with respect to the angular momentum of their stellar components. The particles in these projected snapshots are then binned into square pixels, varying from 100 pc to 750 pc on a side. The maps themselves are 30 kpc on a side, and integrate particle properties only 30 kpc along the line-of-sight. By integrating only 30 kpc along the line-of-sight, we include the relevant components of the ISM and stellar populations in our maps, and exclude distant galaxies which might lie along the line-of-sight by chance in the cosmological box.

We generate star formation rate tracers analogous to observational measures of star formation by calculating the average star formation rates over the past 10 and 100 Myr using the star particle ages, with,

$$\Sigma_{\text{SFR}} = \frac{M_\star(\text{age} < \Delta t)}{\eta l^2 \Delta t} \, , \tag{5.2}$$

where $M_\star$(age is the summed mass of all star particles in the pixel with ages less than the averaging window Δt, l^2 being the pixel size (in kpc), and η is a factor correcting for mass loss from stellar winds and evolutionary effects using predictions from STARBURST99 (Leitherer et al., 1999), with values of 0.85 and 0.70 for the $\Delta t = 10$ Myr and 100 Myr timescales, respectively. The 10 and 100 Myr intervals were chosen for

their approximate correspondence with the timescales traced by recombination lines like Hα, and emission in the UV and FIR, respectively (Kennicutt and Evans, 2012)[2]. The instantaneous star formation rate of the gas particles, as described above, is also considered as a tracer of *in situ* star formation rates. The instantaneous star formation rate of the gas particles is distinct from the time-averaged star formation rates, as it is a continuous quantity intrinsic to the gas particles themselves, which is sampled at each time-step per the star formation prescription described in § 5.1.1 to determine if the gas particles form stars. This allows us to interrogate the conditions under which star formation is proceeding in our simulations *in situ*, and investigate how feedback is called upon to regulate the dense ISM. This quantity demonstrates both how the stage is set initially for star formation, and the direct consequences of feedback from recent star formation on the gas by locally indicating whether star formation continues to proceed, whereas the other two SFR tracers are more analogous to observables.

To understand the structure and source of the turbulent support in the ISM of these galaxy simulations, we calculate the mass-averaged line-of-sight velocity dispersions σ_z for various components of the ISM. In this work, we focus on two components, the total neutral gas column Σ_{gas}, which is a combination of atomic and molecular gas, and the "cold & dense" gas with $T < 500$ K and $n_{\mathrm{H}} > 1$ cm^{-3}. The latter gas reservoir taken as a proxy for the cold molecular gas in the simulations following the methodology of Orr, Hayward, Hopkins, et al. (2018) but with a more liberal higher temperature cut for what constitutes "cold" in the ISM. The intention with these two proxies are to match (ignoring a Helium mass-correction of ≈ 0.76) the velocity dispersions in the combined H$\textsc{i}$ + H$_2$ and H$_2$ gas, respectively.

In addition to calculating the star formation rates in each pixel and the velocity dispersions of the various components of the ISM in the FIRE snapshots, we also calculate the mass surface densities of these gas components as well as the stellar surface density to understand the resolved galactic structure. We also calculate the dynamical angular velocity Ω in each pixel, defined here as

$$\Omega = \frac{v_c}{R} = \frac{(GM(< R))^{1/2}}{R^{3/2}} \, , \tag{5.3}$$

where R is the galactocentric radius of the pixel and M($< R$) is the total mass enclosed within that radius (and G is the gravitational constant).

---

[2]Post-processing the snapshots to model Hα or UV fluxes would make for a more direct comparison to observations, but accounting for the complexities involved, that is beyond the scope of this work.

These quantities allow us to investigate the dependence of star formation on the local gas properties, and relate galactic dynamical times and structure to star-forming regions. In our analysis we treat pixels from all simulations and all times equally, unless otherwise stated. Fiducially, we present our data at 750 pc pixel sizes for comparison with large-scale IFU surveys.

5.1.3 Comparison to Observations

While exploring the relationship between gas line-of-sight velocity dispersions and star formation rates, we compare our simulations with studies with resolved observations of HII region and resolved HCN-traced gas line-of-sight velocity dispersions in star-forming galaxies. Zhou et al. (2017) provide a comparison dataset at ~kpc-scales from the SAMI IFU survey (Cortese et al., 2014), relating HII region velocity dispersions to Hα-inferred SFRs. We compare this data to our neutral gas velocity dispersion and 10 Myr-averaged SFR tracers. With our higher-resolution pixel at 250 pc, we take data from Rozas, Richer, et al. (2006, HII region velocity dispersions) for comparison with neutral gas velocity dispersions in FIRE, and from Querejeta et al. (2019, HCN-traced gas velocity dispersions and dense gas depletion times) for comparison with our cold & dense gas dataset.

5.2 Spatially Resolved Velocity Structure and SFRs in FIRE

Broadly speaking, the velocity dispersions and star formation rates seen in the FIRE Milky Way-massed spirals agree well with similar resolved observations of local disk galaxies (Rozas, Richer, et al., 2006; Zhou et al., 2017; Querejeta et al., 2019). Across all seven of our **m12** galaxies, 95% of the pixels (that also have had recent star formation according to either the 10 Myr or 100 Myr average star formation rate tracer) have velocity dispersions in the neutral gas of 10–50 km/s. **m12w** is distinct in this sample, both morphologically, and having higher velocity dispersions (it is discussed in more detail in § 5.2.1).

Figures 5.1 and 5.2 show the $z = 0$ snapshots of the seven **m12** galaxies (by row), for a number of resolved physical quantities (by column) at a pixel size scale of 250 pc. By and large, we see that the galaxies are dominated by regions with low (< 40 km/s, blue shades, first column) velocity dispersions, with pockets of high-dispersion gas. And although correlated by formulation, it is not easy to see structures traced by the low or high values of Toomre-Q (gravitational stability, Eq. 5.1, second column) in velocity dispersions. However, it *is* easily seen in several cases that regions with the shortest depletion times (as calculated with the 100 Myr SFR tracer, third column)
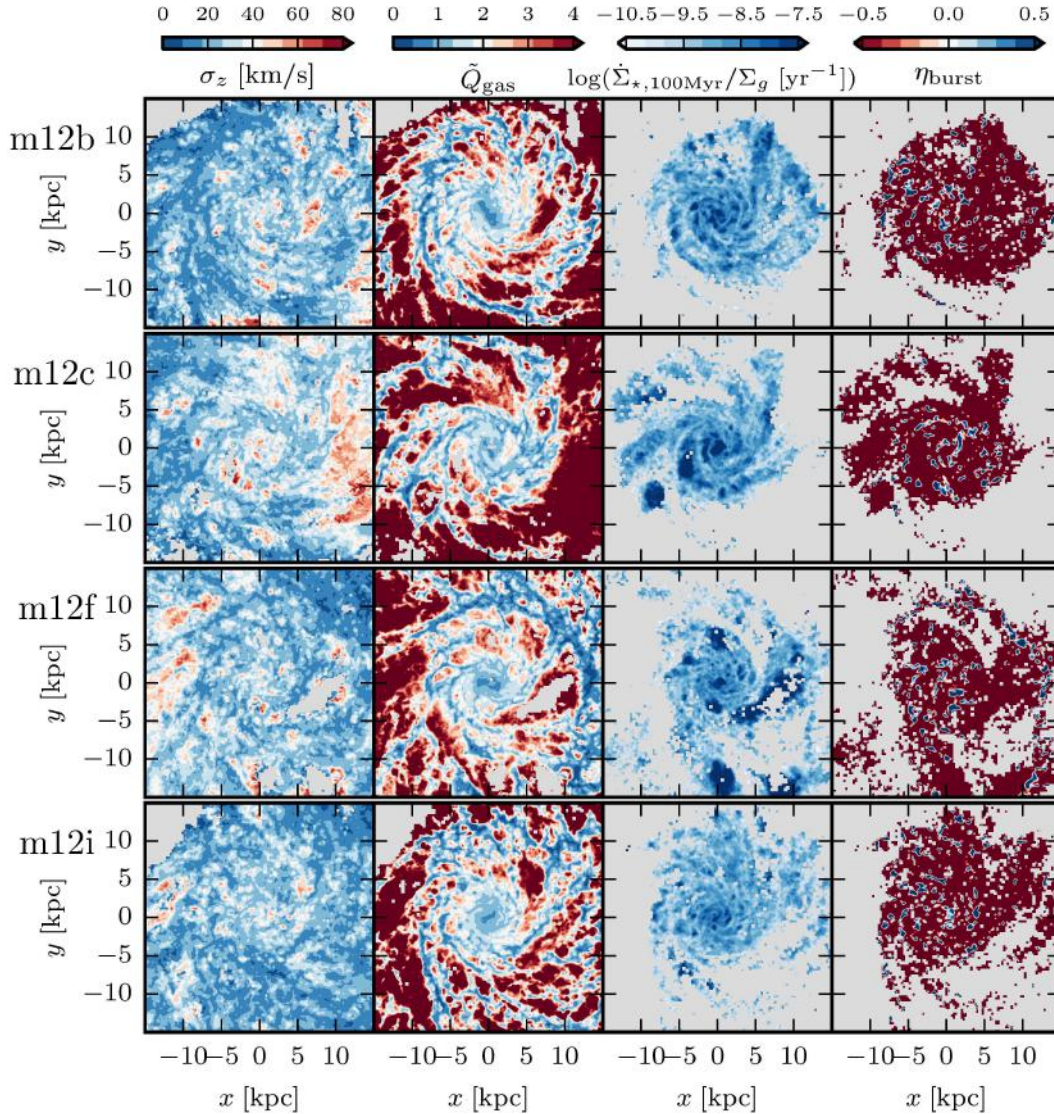
Figure 5.1: Maps of star formation and gas quantities in the FIRE galaxies (**m12b-m12i**, **rows**) at $z = 0$ with 250 pc pixel size. Maps depict the central 30 kpc on a side of the galaxies, face-on. Regions with no data are colored light grey. **Left column:** shaded by neutral (atomic + molecular) gas velocity dispersions. Majority of spiral structures correspond to low $\sigma_z \lesssim 40$ km/s dispersions, with interspersed high-dispersion structure. **Center left column:** shaded by turbulent gas stability, $\tilde{Q}_{\mathrm{gas}}$. Bluer regions ($\tilde{Q}_{\mathrm{gas}} < 2$) are at least marginally unstable. Spiral structure clearly visible as marginally stable and unstable regions. **Center right column:** pixels shaded by gas depletion time, calculated with the 100 Myr-averaged SFR. Several large (~kpc) regions with short depletion times correspond with large bubbles of high-$\tilde{Q}_{\mathrm{gas}}$, indicative of SNe super-bubbles. **Right column:** shaded by $\eta_{\mathrm{burst}} \equiv (\dot{\Sigma}_{\star,\mathrm{10Myr}} - \dot{\Sigma}_{\star,\mathrm{100Myr}})/(\dot{\Sigma}_{\star,\mathrm{10Myr}} + \dot{\Sigma}_{\star,\mathrm{100Myr}})$, cf. Figs. 5.11 & 5.12. Redder (bluer) regions indicate more past (current) star formation relative to current (past) star formation. Much of the area of the galaxies are covered by regions with past star formation, indicating that feedback momentum injection is relatively smoothly spread across the galaxies on ~ 100 Myr timescales. Bluer regions of high 10 Myr SFR correlate with current GMC structures in the galaxies.
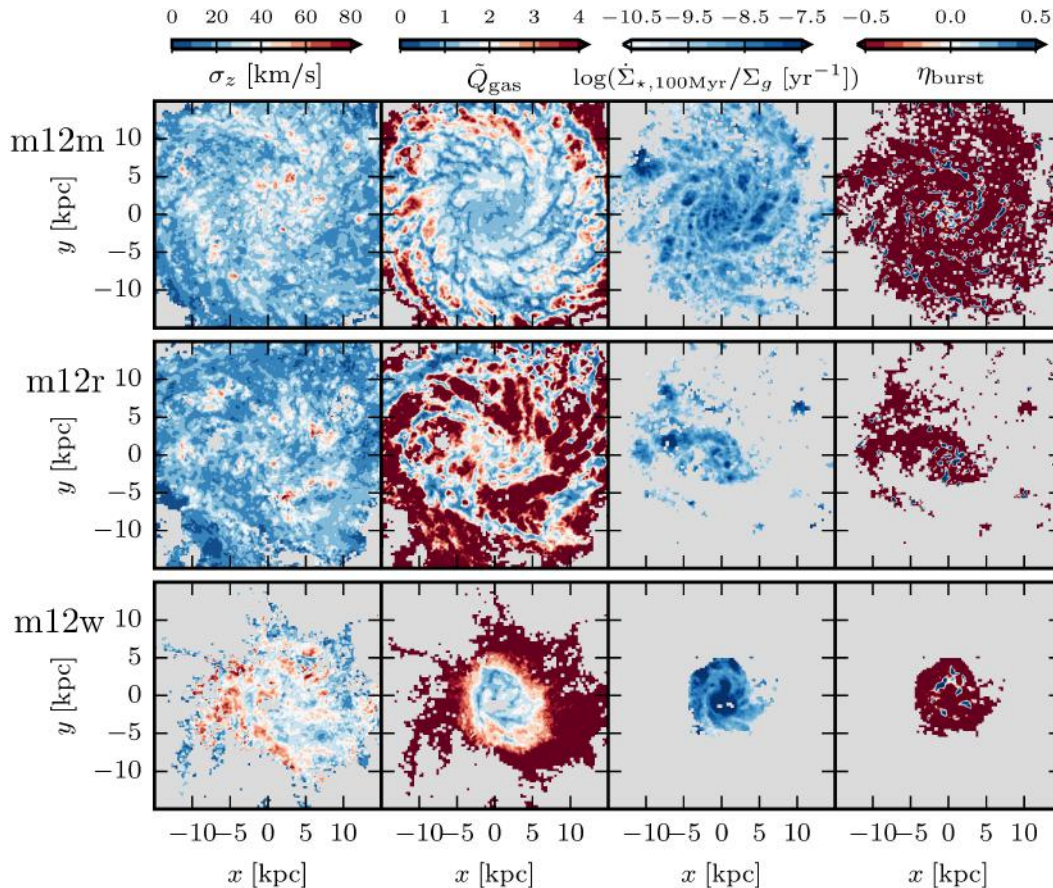
Figure 5.2: Identical in style and plotted quantities to Fig. 5.1, but for FIRE simulations: **m12m**, **m12r**, and **m12w** at $z = 0$. Galaxy **m12w** is the least gas rich and most compact in its gas disk of the sample. Unlike the other more extended disks in the sample, **m12w** consists entirely (in gas) of a ~ 3 kpc in radius dense, gravitationally unstable, nuclear gas disk.

do correspond to regions of high Toomre-Q. Lastly (fourth column), a measure of the "burstiness" of star formation $\eta_{\text{burst}} = (\dot{\Sigma}_{\star,10\text{Myr}} - \dot{\Sigma}_{\star,100\text{Myr}})/(\dot{\Sigma}_{\star,10\text{Myr}} + \dot{\Sigma}_{\star,100\text{Myr}})$, shows that the galaxies are dominated in area by regions that have formed stars in the past 100 Myr (and thus, for the most part, those stars have injected all their feedback already) but have had little or no star formation in the past 10 Myr. Given the small size of the regions with significant 10 Myr star formation rates, this result is somewhat smoothed on 750 pc scales, which we fiducially present in this study.

5.2.1 Line of Sight Velocity Dispersions and Star Formation Rates

Figure 5.3 shows the line-of-sight velocity dispersion structure as a function of the 10 Myr-averaged star formation rate at low redshift, $z \lesssim 0.1$, on 750 pc scales in the individual galaxy simulations (including two dwarf galaxies, **m11h** and **m11q**,
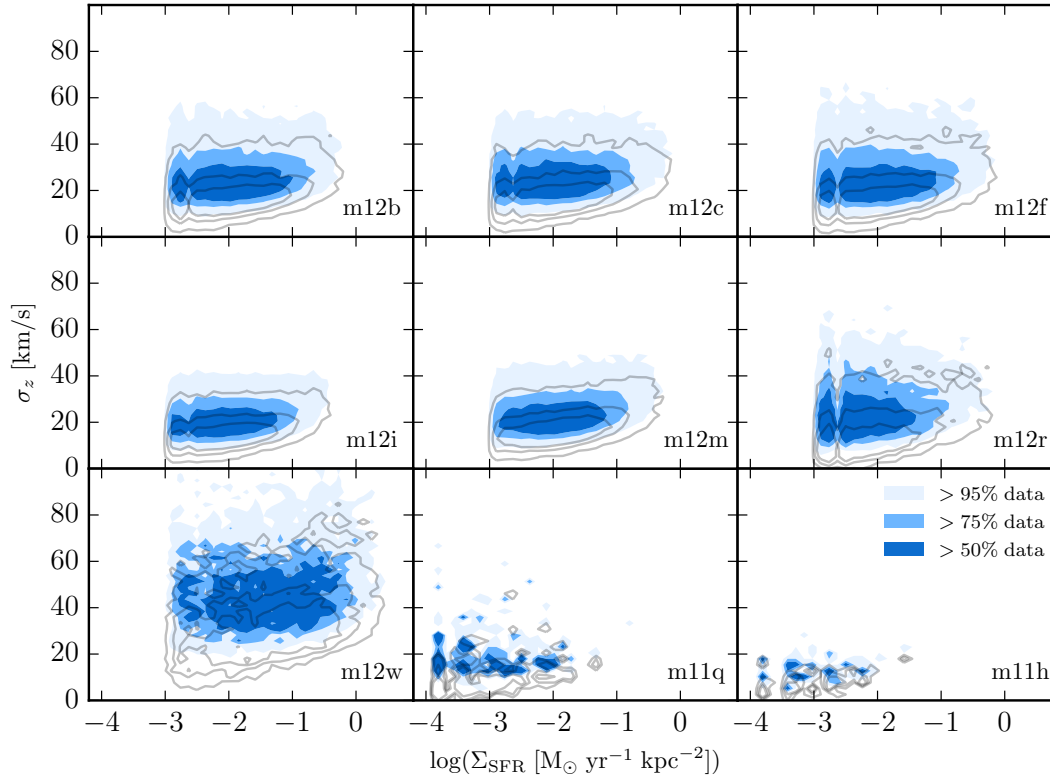
Figure 5.3: Spatially resolved (750 pc pixel size) gas velocity dispersions and star formation rate surface densities in individual FIRE galaxies for $z \lesssim 0.1$. Gas velocity dispersions are the standard deviation of the line-of-sight velocities in gas. Shaded regions depict neutral gas (atomic + molecular), with 'cold & dense' $T < 500$ K and $n > 1$ cm^{-3} gas in unfilled contours. Star formation rates are the 10 Myr-averaged rates. Across ~3 dex in star formation rates, the gas velocity dispersions are nearly constant, with a rising lower envelope for dispersions at a given star formation rate. The two dwarf galaxies (**m11q** and **m11h**), not having strong disks or large extents, do not show the same characteristic relation. Their data are not included in subsequent figures.

that are otherwise excluded from the analysis of the Milky Way-massed spirals). Two differently weighted velocity dispersions are plotted: the neutral (atomic + molecular) gas mass-weighted dispersions in (blue) colored contours, and the "cold & dense" ($T < 500$ K, $n_H > 1$ cm^{-3}) gas mass-weighted dispersions in unfilled contours. The cold and dense gas dispersions have a very similar structure in σ_z-SFR space, albeit with a lower overall normalization indicative of its dynamically colder state.

By and large, all of the Milky Way mass spirals (those with the **m12** signifier) have similar structures in their dispersions-SFRs phase space. There is little variation in

the structure of the dispersions across ~ 3 dex in SFRs, with the exception of a rising lower envelope in velocity dispersions with SFR. **m12w** stands out with regards to the other simulations in its velocity dispersion structure. However, visually (bottom row, Fig. 5.2), this galaxy appears morphologically distinct in its gas disk with a ~ 3 kpc radius gravitationally fragmenting nuclear gas disk, lacking the ~ 10 kpc radial extent of the other simulations at $z = 0$. To a lesser extent, **m12r** also stands out: visually, it has an irregularly structured gas disk at $z = 0$ compared to the other spirals, but does not have as compact a gas distribution as **m12w**.

Stacking together the data from all the snapshots of the Milky Way-massed FIRE spirals, we can see the velocity dispersion–SFR relation in the simulations for variously weighted tracers of gas velocity dispersion and star formation rate in Figure 5.4. The extent of the data to low star formation rates in each panel is mass resolution limited, with lower limits of $\Sigma_{SFR} \approx 10^{-2.8}$, $10^{-3.75}$ $M_\odot$ yr^{-1} kpc^{-2} for the $(750$ pc$)^2$ pixels, with minimum baryonic masses of 7100 $M_\odot$ at 10 Myr and 100 Myr (with their associated evolutionally mass correction factors), respectively. For the gas instantaneous star formation rate, the minimum star formation rate for a pixel with one gas 7100 $M_\odot$ particle at the density threshold is $\Sigma_{SFR} = M_{min}/(l^2 t_{ff,1000}) = 10^{-2.04}$ $M_\odot$ yr^{-1} kpc^{-2} for 750 pc pixels, where $t_{ff,1000}$ is the free-fall time for gas with a density of 10^3 cm^{-3}.

Generally, the core of the distributions for the neutral (atomic + molecular) gas and cold & dense gas velocity dispersions are all between 15–40 km/s and 10–30 km/s, respectively. There is a tail in the distributions to ≈ 60 km/s and ≈ 45 km/s for the 95% data inclusion regions for their respective ISM components. For the Milky Way-like rotational velocities $v_c \approx 240$ km/s of these simulations, the dispersion ratios are $\sigma_z/v_c \approx 0.06 - 0.25$ and $0.04 - 0.19$ in the gas (respective to $\sim 95\%$ of the two ISM components). That is to say broadly, the disks are thin in the FIRE **m12** simulations.

We compare directly with the SAMI IFU data of Zhou et al. (2017) in the top center panel of Figure 5.4, for our 10 Myr averaged star formation rate and neutral gas velocity dispersion data. Their data has complete overlap with our 75% inclusion region (and nearly total overlap with our 50% region). Our inclusion of **m12w**, with its fairly 'hot' disk is a large part of the spray to higher velocity dispersions in the FIRE data. As well, given the fact that we have no difficulty in orienting our galaxies face-on, and thus that beam-smearing and inclination effects in the line-of-sight velocity dispersions are negligible, we do not throw out pixels with
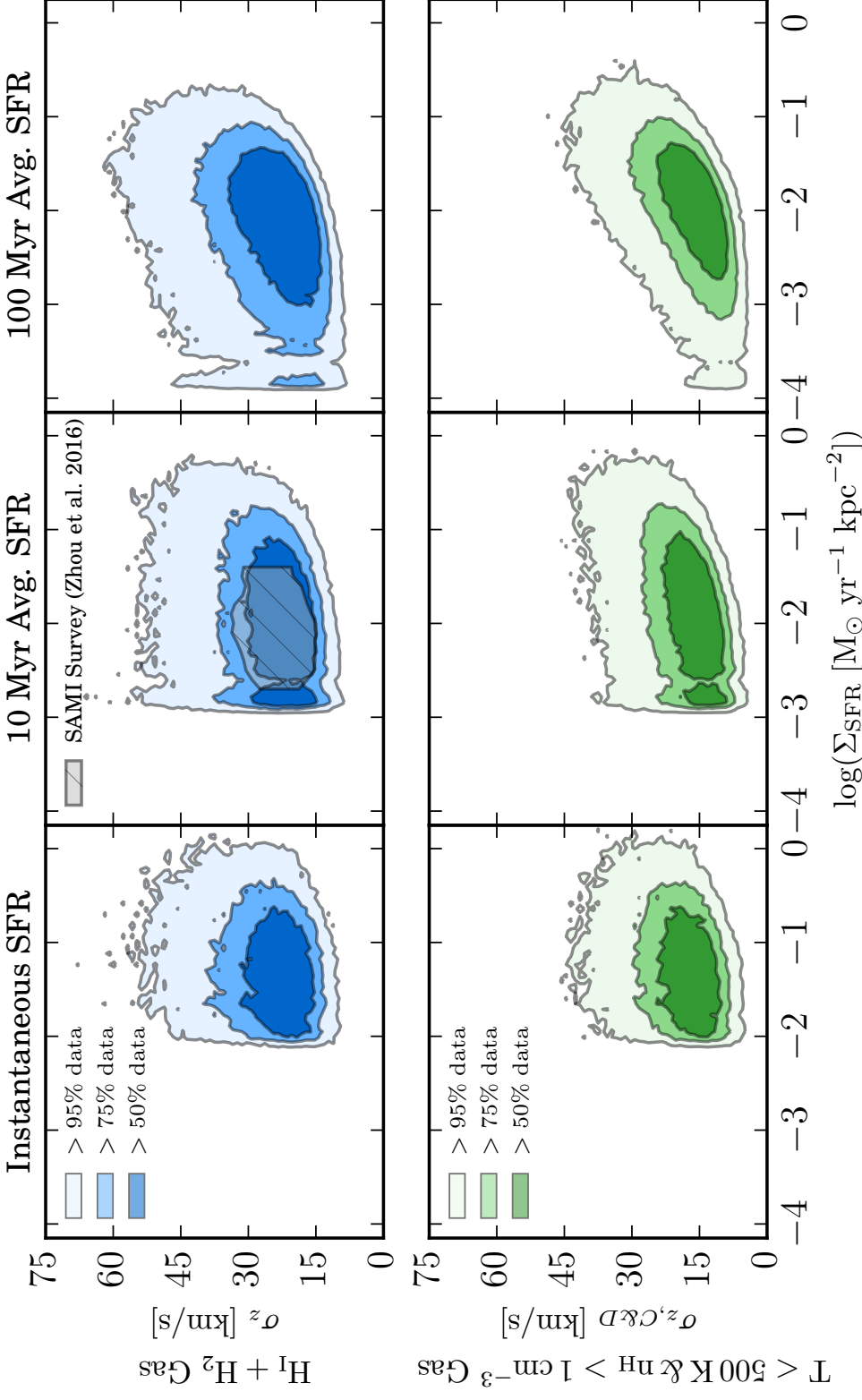
Figure 5.4: Gas line-of-sight velocity dispersions as a function of star formation rate, for various tracers, in the FIRE simulations near $z \approx 0$. All data from individual m12 galaxies (Fig. 5.3) stacked together. Filled contours indicate 95, 70, 50-percentile inclusion regions for the simulation data. The velocity dispersions for the cold and dense gas are lower than for all gas, indicating the dynamically colder state of the dense molecular component of the ISM. Tracers with longer averaging timescales (10 Myr vs. instantaneous, 100 Myr vs. 10 Myr) are able to trace the relation to lower star formation rates and gas velocity dispersions.

velocity gradients as done in Zhou et al. (2017).

The distributions all have increasing velocity dispersions as a function of star formation rates. However, the effect is fairly weak, with the most visible case being with the 100 Myr star formation rate tracer. Universal, however, is the rising lower envelope of velocity dispersions as a function of star formation rate. The nature of this lower envelope is explored in § 5.2.6.

5.2.2 Velocity Dispersions and Mass Surface Densities

Figure 5.5 shows how the line-of-sight velocity dispersions relate to the various (gas, stellar, gas + stellar) mass surface densities in the galaxies. Like in Figure 5.3, the neutral (atomic + molecular) velocity dispersions are plotted in (blue) shaded contours, and the "cold & dense" gas velocity dispersions are plotted in unfilled, grey contours. Generally, the neutral gas velocity dispersions exhibit less scatter at higher gas surface densities. This may be explained by the fact that high surface density gas disks are more self-bound gravitationally, resulting in shorter gas scale heights and thus eddy turnover times for a given σ_z. If supersonic turbulence typically runs down on an eddy turnover time, then high velocity dispersions would be quickly dissipated in the ISM. For surface densities including the stellar component (center and right panels) the velocity dispersions peak in the range of $\Sigma = 10 - 10^2$ M$_\odot$ pc^{-2}. This may be an inflection point between velocity dispersions driving large scale heights and the self-gravity of the disks increasing the rate of turbulence dissipation in the ISM.

Like the velocity dispersion–SFR relations in Figure 5.4, the velocity dispersions have a lower envelope of dispersions for a given surface density. This lower limit can be rationalized as a stability limit. For dispersions below a certain value, the ISM would be gravitationally unstable to fragmentation, and thus collapse, turning into stars, both removing that gas from the dispersion relation and also causing feedback that will drive turbulence in the remaining at least marginally stable gas.

For all mass surface densities, the "cold & dense" gas velocity dispersions generally rise with surface density, though always have a lower overall normalization compared to the neutral gas velocity dispersions. This is in line with the fact that the mass fraction of "cold & dense" gas is rising, and that it is a dynamically colder component of the ISM. The rapid increase in velocity dispersions in the cold & dense gas between $\Sigma_{\mathrm{gas}} \approx$ 1–10 M$_\odot$ pc^{-2} overlaps with the H$\textsc{i}$ to H$_2$ transition threshold generally discussed in the literature (Krumholz, McKee, et al., 2008; Sternberg
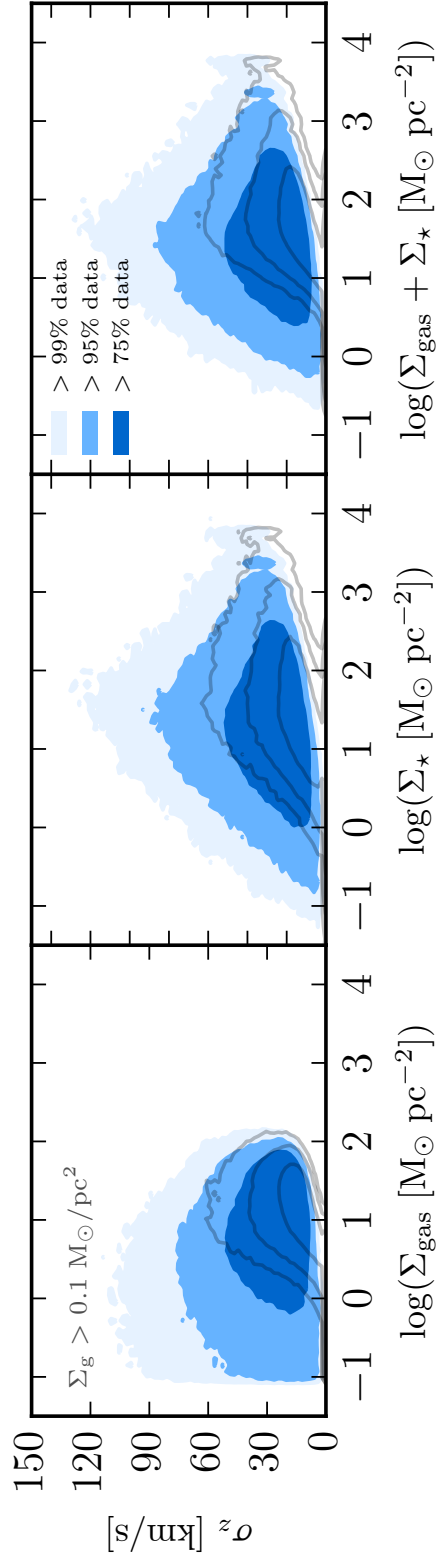
Figure 5.5: Neutral gas line-of-sight velocity dispersions as a function of gas and stellar surface densities, in the FIRE simulations for $z \lesssim 0.1$ (unfilled contours depict cold & dense gas velocity dispersions). Gas surface densities are cut off below $\Sigma_g = 0.1\ M_\odot\ pc^{-2}$ to ensure at least ~ 10 gas particles per pixel for calculating σ_z. Filled contours indicate 99, 95, 75-percentile inclusion regions for the FIRE data. Largest scatter in velocity dispersions occurs for $\log \Sigma_\star \sim 1.5$. Generally higher neutral gas surface densities have a lower scatter to high dispersions, whereas the cold & dense gas velocity dispersion consistently rise with increasing gas and stellar surface densities.

et al., 2014; Pineda, Langer, et al., 2017).

5.2.3   Gas Fractions and Dense Gas Fractions

The top panel of Figure 5.6 depicts the dependence of the σ_z–SFR relation on the mass fraction of cold & dense gas in the neutral (atomic + molecular) ISM. This is a rough proxy for the molecular gas fraction on ~kpc scales. Here we clearly see that for a given amount of turbulence (velocity dispersion) more molecularly rich gas has higher star formation rates on average. This is not surprising, considering that star formation occurs predominantly in cold and dense gas in molecular clouds.

However, this may appear as a bias in observations that correlate star formation rates with velocity dispersions that are pegged to the dynamics of dense gas regions. Observations may be more correlated with the dense gas tracers, e.g., CO line-widths, given the difficulty in measuring Hɪ on small (~ 100) scales to combine with dense gas measurements to get a full accounting of the turbulent momentum in the ISM on kpc-scales. For example, this may arise when combining datasets of low-star formation rate spirals with higher redshift starburst systems (Lehnert et al., 2009; Zhou et al., 2017), where each dataset may comprise of the most dense gas rich systems and thus a steep upturn in velocity dispersions appears for $\dot{\Sigma}_\star \sim 10^{-1}$ $M_\odot$ yr^{-1} kpc^{-2}.

The overall gas fraction, $f_g = \Sigma_g/(\Sigma_g + \Sigma_\star)$, is another factor that clearly affects the normalization of the velocity dispersion for a given star formation rate. Here, in the middle panel of Figure 5.6, we see there is little variation in average gas fractions for a given amount of turbulence (velocity dispersion). Instead, at a given star formation rate, lower gas fractions yield larger turbulence velocity dispersions across 3 dex in SFRs. At lower gas fractions, for a given amount of gas (presumably, here SFRs still correlate with gas surface densities), a larger stellar component in the disk produces a deeper potential well for the gas to stabilize itself in. Just as larger Σ_g require higher σ_z in Eq. 5.1, so does larger $\Sigma_\star$.

As neutral (atomic + molecular) gas fractions approach zero at the highest velocity dispersions ($\sigma_z > 100$ km/s), it is evident in these galaxies that an appreciable fraction of the gas is becoming ionized and is in a hot, usually outflowing state, and thus no longer either neutral in nature, nor in any equilibrium state.
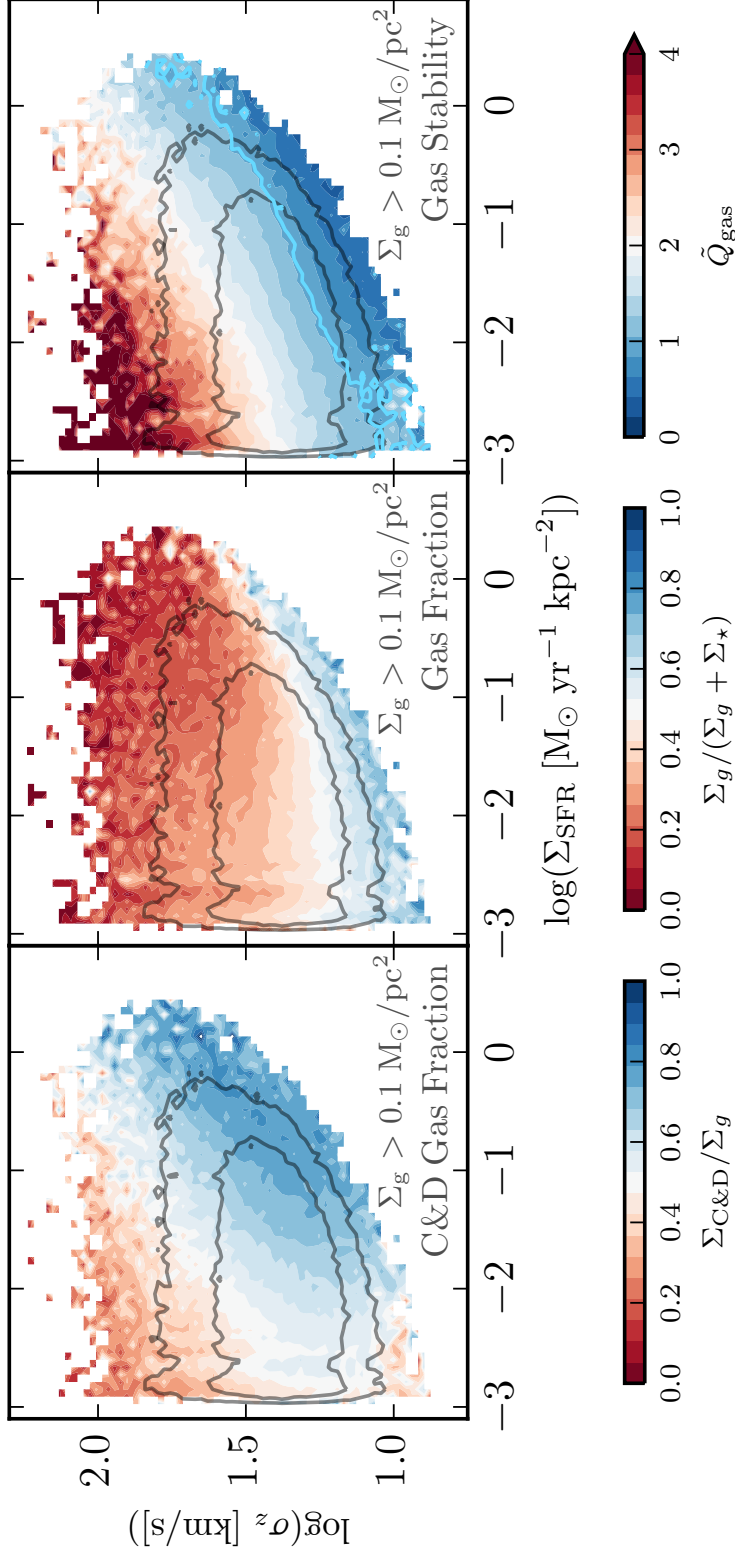
Figure 5.6: Velocity dispersions in neutral (atomic + molecular) gas and 10 Myr average SFRs with 750 pc pixel size, in gas with surface densities $> 0.1\,M_\odot\,pc^{-2}$, colored by various gas properties. Grey outlines indicate extent of 95% and 75% of data. **Top:** shaded by average cold & dense (C&D, $T < 500$ K and $n > 1\,cm^{-3}$) gas fraction. C&D gas fraction approaches unity as SFR increases for constant velocity dispersion. **Middle:** colored by average gas fraction. Gas-rich regions have the lowest velocity dispersions for their SFRs. For a constant amount of gas/star formation, gas in a deeper potential (higher stellar surface densities) must have larger velocity dispersions to maintain stability. **Bottom:** shaded by average gas stability against gravitational fragmentation ($\tilde{Q}_{gas}$, Eq. 5.1). Cyan line denotes $\tilde{Q}_{gas} = 1$ threshold for instabilities (i.e., pixels in this region of $\Sigma_{SFR} - \sigma_z$ space are on-average unstable). Less stable gas (for a given velocity dispersion) produces higher 10 Myr average star formation rates.

5.2.4 Velocity Dispersions and Gas Stability

The bottom panel of Figure 5.6 shows the velocity dispersion–SFR relation colored by the average gas stability (our modified Toomre-Q, Eq. 5.1). The average trend is similar to the trend in cold and dense gas fraction and star formation rates: less stable gas is both more predominantly cold and dense in nature, and has higher star formation rates for a given amount of turbulence (velocity dispersion). Interestingly, the trend follows a $\sigma \propto \dot{\tilde{\Sigma}}_{\star}^{-1/6}$ relation for constant $\tilde{Q}_{\mathrm{gas}}$ (see the cyan line for $\tilde{Q}_{\mathrm{gas}} = 1$, with its ∼1/6 slope). This power-law slope is shallower than expected for a feedback-regulated, turbulent star formation environment, as derived in Eq. 5.5, suggesting that a simple turbulently regulated feedback framework alone is insufficient to describe the σ-$\dot{\Sigma}_{\star}$ relation, and processes that raise σ at low SFR (e.g., non-negligible thermal support) or depress it at high SFR (e.g., momentum going into outflows or a hot ISM phase instead of σ) are required at a minimum.

As well, all of the velocity dispersions calculated for the neutral gas are in excess of ∼ 10 km/s, above the sound speed for 8000 K atomic gas $c_s \approx 6$ km/s. This is in line with many observations of the star-forming ISM, where few, if any, star-forming regions are purely thermally supported even at the lowest star formation rate surface densities (Stilp, Dalcanton, Warren, et al., 2013; Stilp, Dalcanton, Skillman, et al., 2013).

5.2.5 Velocity Dispersions and SFR Timescales

Figure 5.7 investigates the dependence of the velocity dispersion–SFR relation, when considering the 10 Myr average star formation rate, on alternative star formation tracers. Here we see that all gas that has had star formation in the past 10 Myr, has by construction a non-zero 100 Myr averaged star formation rate, but not all gas has a non-zero instantaneous (current) star formation rate.

The instantaneous star formation rate (top panel) has a high degree of correlation with the 10 Myr-averaged star formation rate, unsurprising given that the 10 Myr timescale is fairly short compared to the dynamical times of the gas disks. However, there is a corner of σ_z–$\dot{\Sigma}_{\star}$ space cut out of the data set for instantaneous star formation rates, corresponding to the region with $\tilde{Q}_{\mathrm{gas}} \gtrsim 3$ in the bottom panel of Figure 5.6. The lack of regions with current (instantaneously) star formation for high (very stable) values of $\tilde{Q}_{\mathrm{gas}}$ is expected, after all, the regions are currently stabilized against fragmentation. The fact that this disappears from the 10 Myr star formation rate dataset is suggestive that star-forming regions in some cases

are able to regulate and inject sufficient stabilizing feedback momentum on sub-10 Myr timescales, which correlates with both the timescale for the bulk of ionizing radiation from massive stars, and the first (few) SNe in a GMC.

Probing star formation rates on 100 Myr vs. 10 Myr timescales provide an interesting test of the feedback-regulation picture, where longer star formation rate tracers are sensitive to regions that have already injected all, or a significant fraction, of their feedback budget. Thus, shorter timescale tracers are indicative of the current demands of the ISM, feedback-wise, whereas longer tracers should trace the more-averaged history of the momentum balance in the ISM. The bottom panel shows this, where at low recent (10 Myr) star formation rates, the amount of star formation that has occurred in the past 100 Myr is strongly correlated with the amount of turbulence (velocity dispersions) seen in the ISM. However, at high recent star formation rates, both the dynamical times of the regions become shorter (thus leaving little room temporally for on-off star formation modes) and the velocity dispersions are compressed into a smaller range for a given 10 Myr star formation rate. Given this, the 100 Myr tracer has little correlation with very high recent star formation rates, the ISM 'forgets' its feedback history when there are high recent/current rates of star formation.

5.2.6 Velocity Dispersions and Outflow-prone Fractions

In previous sections, we explored how the velocity dispersion–SFR relation depends on properties of the gas and star formation. However, only two quantities clearly correlated with 'edges' in the relation: the (neutral) gas fractions and gas stability ($\tilde{Q}_{\rm gas}$). Naturally, regions that approach having no neutral gas ($f_g \to 0$) will no longer be able to support star formation. As well, patches of the galaxy can only be so unstable ($\tilde{Q}_{\rm gas} \to 0$). The third edge in the relation here, that of a minimum star formation rate, is resolution limited, and not indicative of a physical cutoff in star formation rates. However, there was not a clear reason physically for either the $f_g \to 0$ or the $\tilde{Q}_g \to 0$ edge to occur where they did, in terms of the normalization of σ_z. Figure 5.8 explores the role of an outflow threshold in setting the limits of the turbulence in the ISM for a given star formation rate and recent history. Rescaling the velocity dispersions by their ratios to the local circular velocity in the galaxy, as is often discussed when considering galactic outflows, we see first that the vast majority (> 75 % by area) of the galaxies have disk aspect ratios v_c/σ_z between $\sim 4 - 20$. They have, by and large, thin disks over most of their areas.
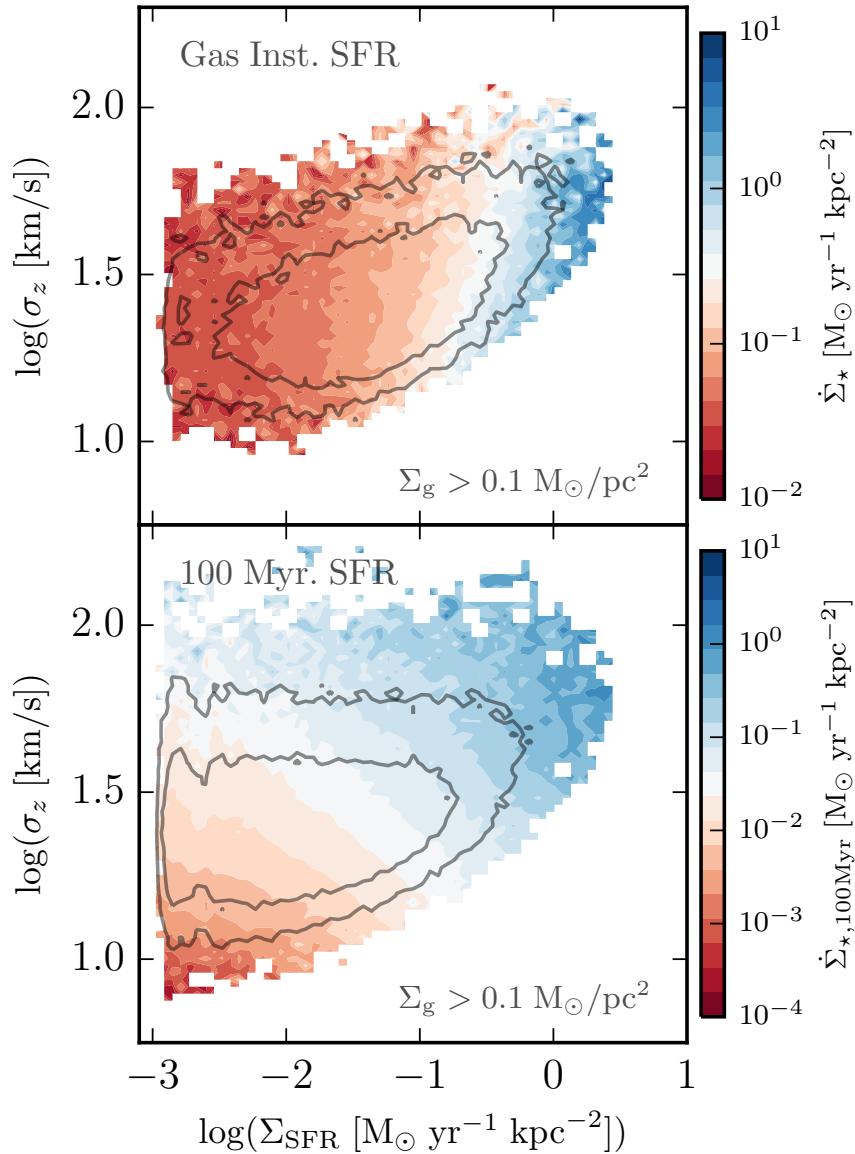
Figure 5.7: Spatially resolved (750 pc pixel size) velocity dispersions in neutral (atomic + molecular) gas and 10 Myr average SFRs with 750 pc pixel size, in gas with surface densities > 0.1 M$_\odot$ pc^{-2}, colored by alternative timescale SFR tracers. Grey outlines indicate extent of 95% and 75% of data. **Top:** shaded by instantaneous star formation rate of the gas particles (average of all pixels at that point in $\Sigma_{\rm SFR} - \sigma_z$ space). By nature of both having short effective averaging timescales, the gas' instantaneous and 10 Myr-averaged SFRs are highly correlated on 750 pc scales, turning over slightly as high 10 Myr-averaged SFRs are approached for a given velocity dispersion. **Bottom:** shaded by (average in $\Sigma_{\rm SFR} - \sigma_z$ space) 100 Myr averaged SFR. For low-10 Myr-averaged SFRs, 100 Myr-averaged SFRs correlate strongly with velocity dispersions, the gas retains an imprint of past (perhaps cyclic) star formation. But for high-10 Myr average SFRs the two SFR tracers are correlated more strongly with each other.

We consider the threshold for outflows to occur to be that of Hayward et al. (2017) , where there is a surface density threshold in the gas for which a given amount of feedback per area in time $(P/m_\star)\dot{\Sigma}_\star$ can accelerate that patch of gas to the local escape velocity in a coherence time (roughly equivalent to an eddy-crossing time). This threshold, Eq. 5 in Hayward et al. (2017), is $\Sigma_g < (P/m_\star)\dot{\Sigma}_\star/\sqrt{2}R\Omega^2$. In Figure 5.8, we shade the (σ_z/v_c)-$\dot{\Sigma}_\star$ relation by the fraction of pixels that have gas surface densities below this threshold and thus find themselves 'outflow-prone' at that position in (σ_z/v_c)-$\dot{\Sigma}_\star$ space. Interestingly, the different edges of the (σ_z/v_c)-$\dot{\Sigma}_\star$ relation for neutral gas velocity dispersions and the 10 Myr star formation rate tracer, excluding the mass resolution limit, map to the regimes where significant fractions of gas become outflow-prone depending on the different timescale star formation tracers. As the coherence time is on the order of the eddy-crossing time, all of the star formation tracer timescales are equal or less than this ($\sim$ 100 Myr), so they each are integrating in parts the feedback events that end up driving outflows.

Focusing on the material that is outflow-prone when considering the instantaneous SFR, it appears that the hard-limit in the velocity dispersion–SFR relation at constant σ is set by the amount of momentum that the ISM can absorb before appreciable fractions of it are blown out efficiently. On short ($<$ 10 Myr) timescales, as per the discussion in § 5.3.1, it is reasonable to consider σ constant or only very slowly varying as star formation *fires* up. On the other extreme of our star formation tracer timescales, when we consider the outflow fractions as calculated by the 100 Myr tracer, we see that the outflow-prone material traces the most extreme σ_z/v_c, above $\log(\sigma_z/v_c) \geq -0.5$. this is understandable, as on 100 Myr timescales, feedback is able to pump velocity dispersions on disk scales, and regions that are marginally outflow-prone and still have any gas left will have the highest velocity dispersions. The outflow fraction approaching unity for 100 Myr timescale star formation rates in disk environments thus provides a physical reason for the top edge of the (σ_z/v_c)-$\dot{\Sigma}_\star$ relation.

The 10 Myr SFR tracer prediction, lying between these two natural extreme timescales, connects the two limits, rounding the corner from the state where feedback has not yet been felt to that where most of it has been deposited.

5.2.7 Velocity Dispersions and Depletions Times

Figure 5.9 explores how gas depletion times vary across the velocity dispersion–SFR relation for both 250 pc and 750 pc pixel sizes. We explore both how the depletion
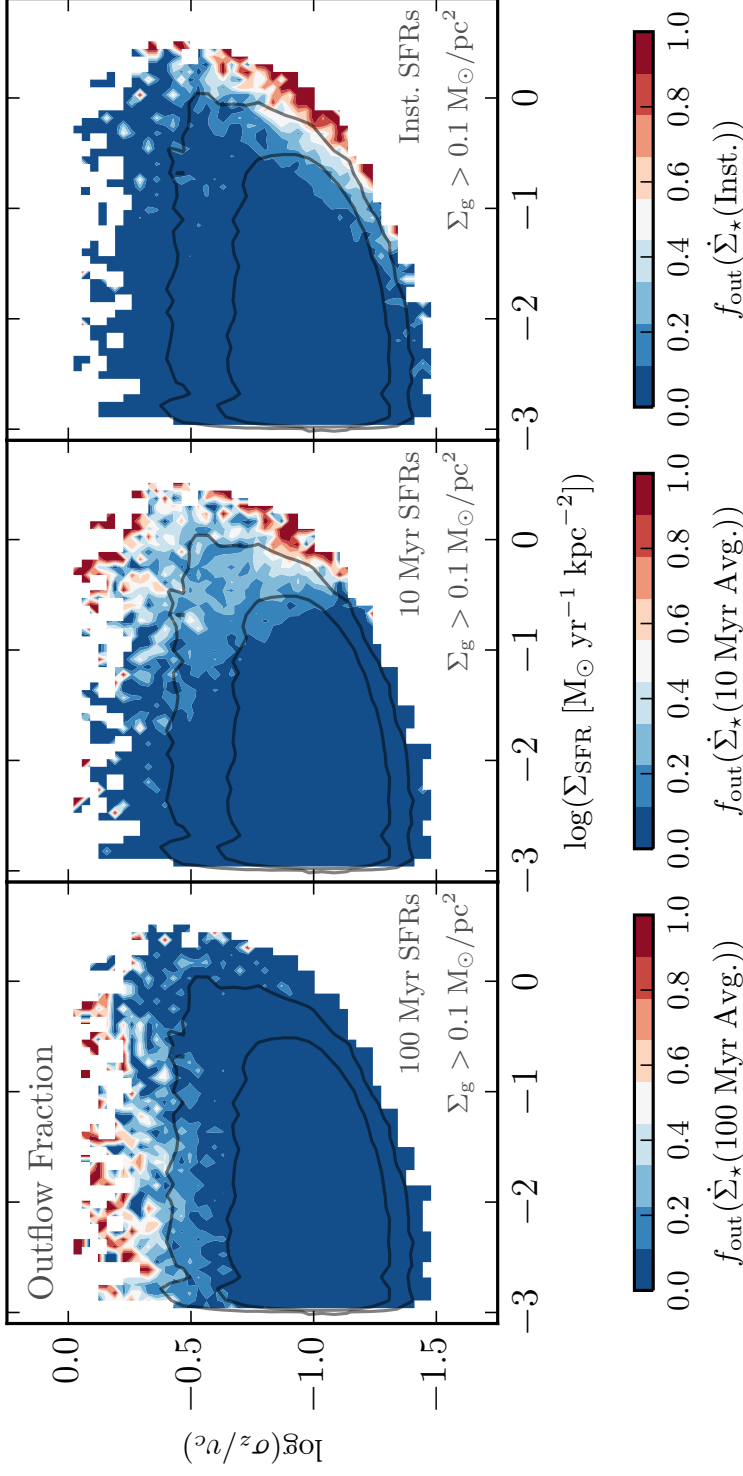
Figure 5.8: Velocity dispersions to orbital velocity ratios in neutral (atomic + molecular) gas and 10 Myr average SFRs with 750 pc pixel size, in gas with $\Sigma_g > 0.1$ M$_\odot$ pc^{-2}, colored by the fraction of pixels with gas surface densities that can be blown out as outflows by feedback in a coherence time (i.e., $\Sigma_g < (P/m_\star)\dot{\Sigma}_\star/\sqrt{2}R\Omega^2$, Eq. 5 from Hayward et al. 2017, calculated with various SFR tracers/timescales). Grey outlines indicate extent of 95% and 75% of data. **Top/Middle/Bottom:** Outflow fraction for 100 Myr, 10 Myr, and instantaneous SFRs, respectively. Dispersion support-SFR relation is bounded on three sides (left side is simulation-resolution limited) by the transition from turbulence driving to outflow driving in the ISM by feedback over various timescales. Longer timescale star formation events (consistently high SFRs for long timescales) are correlated with larger ratios of dispersion to orbital velocities, having the ability to affect the turbulent velocity structure of the ISM.

time of the cold & dense gas and of all neutral gas vary with their respective velocity dispersions for the 10 Myr averaged tracer of star formation. Here we directly compare with three observational datasets: two H$\textsc{ii}$ velocity dispersions and Hα SFR studies (Rozas, Richer, et al., 2006; Zhou et al., 2017), and one of the velocity dispersions and depletion times in HCN (tracing very cold and dense gas, Querejeta et al. 2019). Neither the Rozas, Richer, et al. (2006) nor the Zhou et al. (2017) datasets include gas depletion time estimates, and so only constrain the extent of our σ-SFR relation. With these, we find good agreement.

The Querejeta et al. (2019) data, however, did include measurements of the depletion time of the dense gas. We compare our cold & dense depletion time data directly against the $\Sigma_{\text{SFR}}/\Sigma_{\text{HCN}}$ with the same colorbar, and find very good qualitative agreement[3]. Particularly interesting for comparison with the Querejeta et al. (2019) data, there are two distinct regions (bluer) with shorter dense gas depletion times on 250 pc scales: (1) low velocity dispersions for a given 10 Myr-averaged SFR, which is the scaling that their observational dataset covers, and (2) high 10 Myr-averaged SFRs *and* high $\gtrsim$ 30 km/s dense gas velocity dispersions, which their dataset did not trace. This is not seen as strongly in the 750 pc dataset, but does exist to a weaker extent with $\tau_{\text{dep}} = \Sigma_g/\Sigma_{\text{SFR}}$ falling to $\sim 10^{8.5}$ yr at low velocity dispersions.

5.2.8 ISM Component Momenta and Depletion Times

Previous works have explored the connection between the dynamical state of the dense gas in galaxies, and its star formation efficiency (Leroy, Walter, Brinks, et al., 2008; Faucher-Giguère et al., 2013; Gallagher, Leroy, Bigiel, Cormier, Jiménez-Donaire, Ostriker, et al., 2018; Orr, Hayward, Hopkins, et al., 2018; Orr, Hayward, and Hopkins, 2019). In particular, the stability of the molecular gas against gravitational fragmentation has been zeroed in on as a key driver of the star formation rates in dense gas. Figure 5.10 explores the relation between the magnitude of the turbulent momentum in the "cold & dense" gas phase and various measures of depletion time. Here we estimate the amount of turbulent momentum carried by the less dense atomic component of the ISM as simply the difference between the momentum (per unit area) carried in the whole neutral gas phase, $P_{\text{gas}} \approx \Sigma_g \sigma_z$, and that of the cold and dense phase, $P_{\text{C\&D}} \approx \Sigma_{C\&D}\sigma_{z,C\&D}$. For the neutral (atomic + molecular) gas depletion time, calculated by the 10 Myr average

---

[3]The reader may be forgiven for believing the Querejeta et al. (2019) data to be presented as unfilled circles on top of the FIRE dataset, instead of being colored by their local $\Sigma_{\text{SFR}}/\Sigma_{\text{HCN}}$, as the depletion times agree closely with the FIRE dataset.
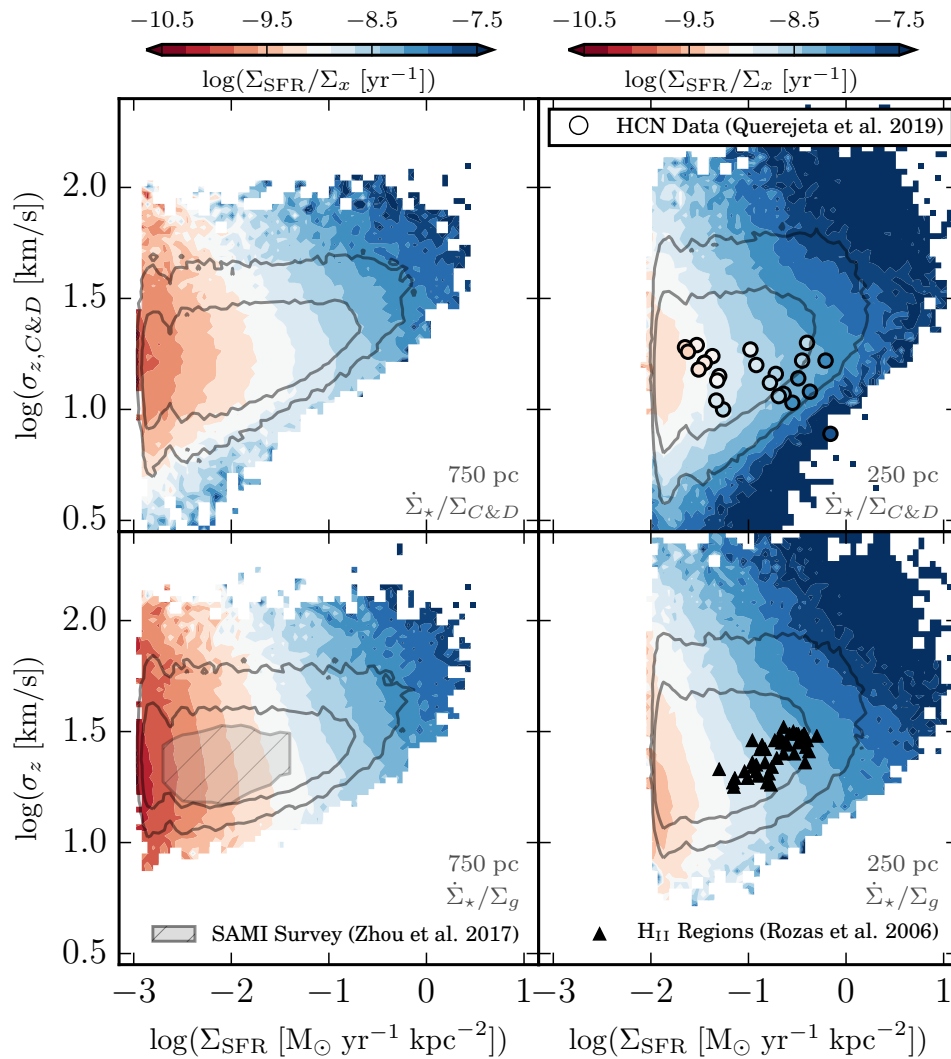
Figure 5.9: Spatially resolved (750 pc pixel size) velocity dispersions in Cold & Dense gas **(top)** and neutral (atomic + molecular) gas **(bottom)** and 10 Myr average SFRs with 750 pc pixel size, in gas with surface densities > 0.1 M$_\odot$ pc^{-2}, colored by respective gas depletion timescale using the 10 Myr SFR tracer. Grey outlines indicate extent of 95% and 75% of data. **Top:** shaded by depletion time of the Cold & Dense gas (average of all pixels at that point in $\Sigma_{\mathrm{SFR}} - \sigma_{z,\mathrm{C\&D}}$ space). Cold & Dense gas velocity dispersions are weakly correlated with cold and dense gas depletion times, only near the lower envelope of velocity dispersions for a given 10 Myr SFR are lower dispersions correlated with shorter depletion times. **Bottom:** shaded by (average in $\Sigma_{\mathrm{SFR}} - \sigma_z$ space) neutral gas depletion time. Velocity dispersions in the neutral gas are weakly correlated with gas depletion times, with a slight dependence only at higher SFRs.
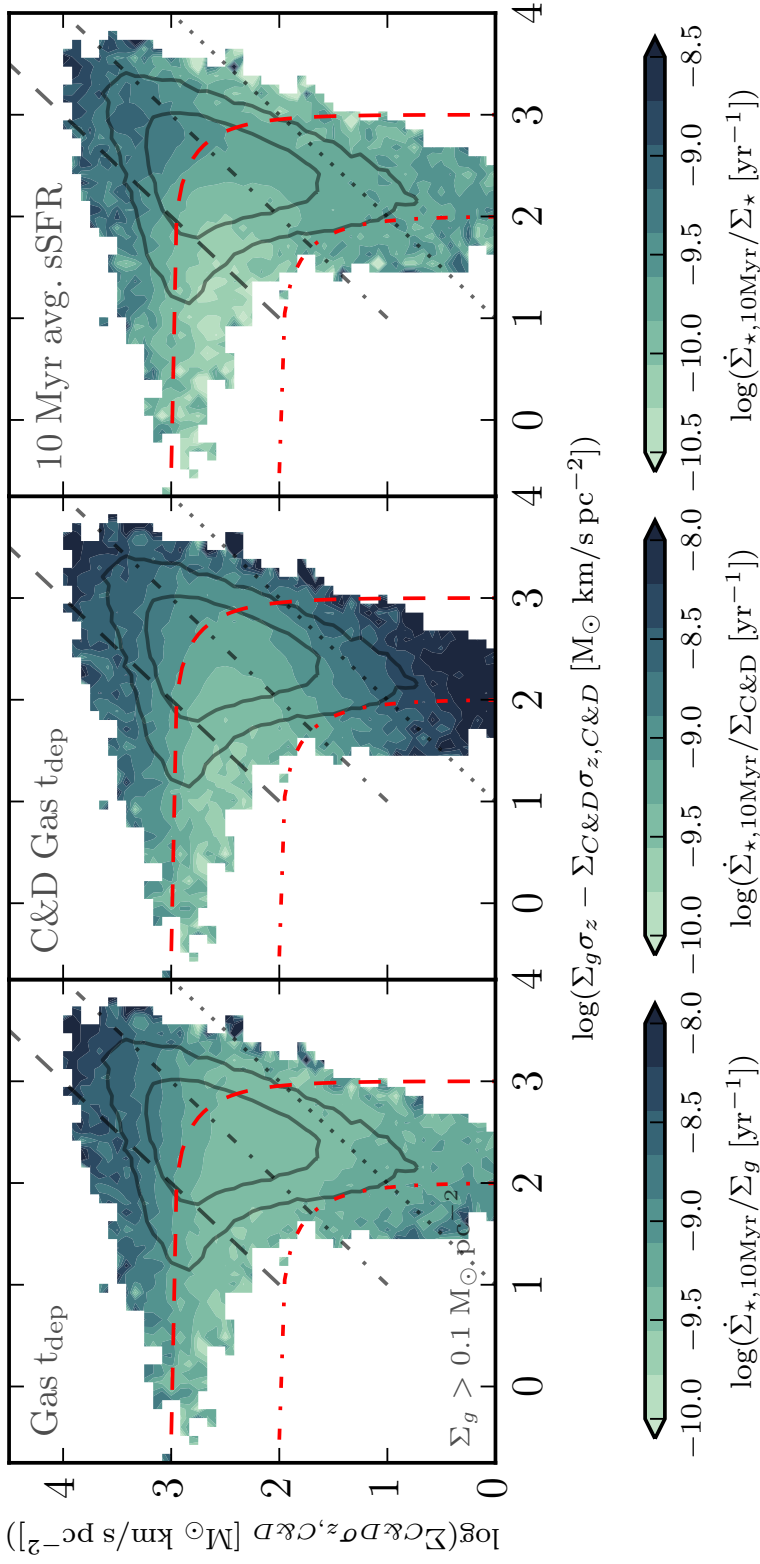
Figure 5.10: Dependence of neutral and cold & dense gas depletion times, and specific star formation rate (using 10 Myr-averaged SFR tracer) on turbulent momentum in the ISM in the FIRE simulations on 750 pc scales. Vertical axis for all panels depicts the momentum in the cold & dense gas component of the ISM, and the horizontal axis depicts the gas momentum *not* contained in the cold & dense component (cf. atomic/H I gas). Gas surface densities are cut off below $\Sigma_g = 0.1$ $M_\odot$ pc^{-2} to ensure at least ~ 10 gas particles per pixel for calculating σ_z. Contours are the 95 and 75% data inclusion regions. Black dashed, dash-dotted, and dotted lines denote 10x, 1x, 0.1x momentum in the cold & dense vs. "atomic" phase. Red lines are lines of constant neutral gas momentum (e.g., $\Sigma_g \sigma_z = 10^2$, 10^3 $M_\odot$ km/s pc^{-2}). **Left:** Shaded by total gas depletion time. Shorter depletion times depend only on momentum in cold & dense phase. **Center:** Shaded by cold & dense gas depletion time. Two regions of short depletion times: high cold & dense gas phase momentum, regions with relatively little cold & dense gas (hence high "atomic" phase momentum fractions). **Right:** Shaded by specific star formation rates. Mirrors neutral gas depletion times. Regions with high "atomic" phase momentum fractions have long (approaching a Hubble time) stellar mass doubling times.

SFR tracer, larger amounts of dense gas momentum correlate with shorter depletion times. Considering the depletion time of the cold and dense gas alone (center panel), $\Sigma_{\text{SFR}}/\Sigma_{\text{C\&D}}$, there are two phases with short depletion time (cf., top right panel of Figure 5.9). In one case, it follows the overall neutral component, when large quantities of turbulent momentum are carried in the cold and dense phase, overlapping with the regions where the ISM is predominantly molecular in nature.

On the other hand, the dense gas depletion times also become short in regions where only a small fraction of the ISM is cold and dense (and its contribution to the overall turbulent momentum is low). This latter case occurs further out in galactic outskirts where the ISM is considerably more diffuse, but requires some stabilizing feedback. There, the ISM evolves to produce just enough dense gas to form stars, but it is relatively rapidly consumed in the process.

Interestingly, regions with the longest cold and dense gas depletion times overlap significantly with the regions of lowest specific star formation rate (sSFR, right panel). In these regions, the turbulent momentum is predominantly (a factor of ~ 10 or so greater) carried by the cold and dense phase of the ISM.

In all the panels, there is a spray to low 'atomic' phase gas momentum as the momentum in the cold and dense phase reaches $\approx 10^{2.5}$ $M_\odot$ km/s pc^{-2}. This corresponds to the HI-to-H$_2$ phase transition in the ISM, as the median $\sigma_z \approx 10^{1.3}$ km/s, where the atomic component becomes volume filling and does not necessarily contain a large fraction of the mass or momentum. And so, as the ISM becomes predominantly molecular in a surface density sense, that molecular component also becomes the primary carrier of momentum in the ISM.

5.2.9 Gas Stability, Star Formation Timescales, and Depletion Times

Figure 5.11 plots the predicted velocity dispersions in each pixel, assuming $\tilde{Q}_{\text{gas}} = 1$ versus the measured σ_z, and colors the relation by average gas fractions, outflow-prone fractions (calculated with the 100 Myr tracer) and $\eta_{\text{burst}} = (\dot{\Sigma}_{\star,\text{10Myr}} - \dot{\Sigma}_{\star,\text{100Myr}})/(\dot{\Sigma}_{\star,\text{10Myr}} + \dot{\Sigma}_{\star,\text{100Myr}})$, a measure of the star formation bursty-ness. If all the patches of the galaxies had $\tilde{Q}_{\text{gas}} = 1$, then the whole dataset would fall on the dotted $\tilde{Q}_{\text{gas}} = 1$ line, so the plots show how these quantities vary with how far from equilibrium the regions are. A much smaller fraction of gas finds itself with $\tilde{Q}_{\text{gas}} < 1$, than between 1–10. The data is bounded nicely on the $\sigma_z \lesssim 8$ km/s end, where we expect the atomic phase of the ISM to provide non-negligible thermal support with $c_s \approx 8$ km/s, thus providing a floor to σ_z. Whereas the predicted
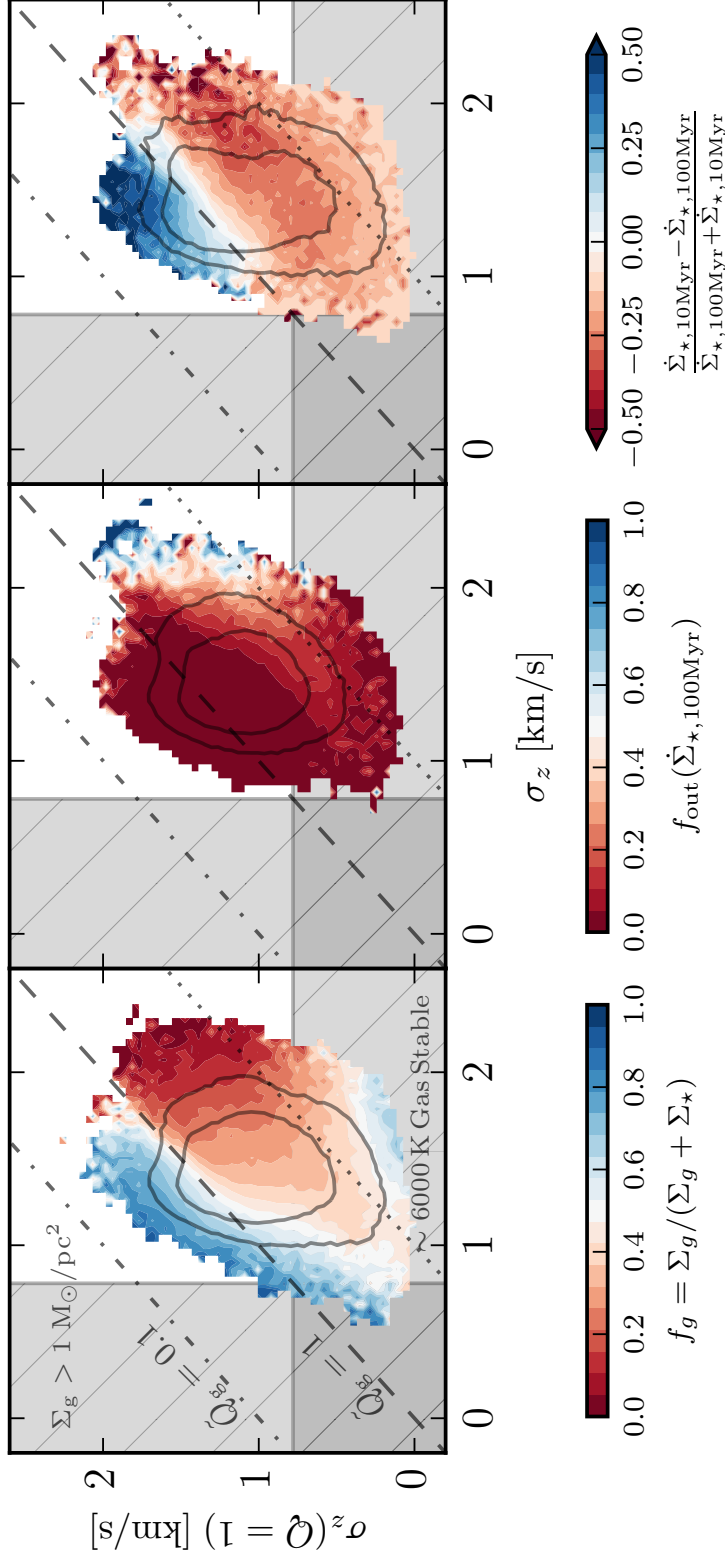
Figure 5.11: Neutral gas velocity dispersions and velocity dispersion required to maintain gas stability ($\tilde{Q}_{\rm gas} = 1$) in the FIRE simulations, at 750 pc pixel size, colored for varying gas- and star formation-related properties. Predicted gas velocity dispersions are those required to maintain $\tilde{Q}_{\rm gas} = 1$ on a pixel-by-pixel basis, as per Eq. 5.1. Grey contours indicate 95% and 75% data inclusion regions (by pixel number). Shading is by the average value of the gas/star formation quantity at that position, for pixels with $\Sigma_g > 1\,{\rm M}_\odot\,{\rm pc}^{-2}$ (lower density gas will have a significant non-turbulent support component, requiring little additional turbulent support to maintain stability). Hatched shaded region denotes patches that would be stabilized thermally by ~ 6000 K gas (6 km/s), essentially the upper limit of non-turbulent support. Dash-dotted and dashed lines show lines of constant $\tilde{Q}_{\rm gas} = 0.1, 1, 10$. **Left:** Shaded by average pixel gas fraction. **Center:** Shaded by fraction of gas that can be expelled in outflows by feedback in a coherence time (calculated with the 100 Myr-averaged SFR). High (actual) velocity dispersion ($> 100 km/s$), unstable gas is predictive of the outflow-prone fraction. **Right:.** Shaded by a measure of relative current star formation to past star formation (difference in 10 Myr and 100 Myr SFRs normalized by their sum). Bluer regions indicate more vigorous current star formation, and that young stars in those regions have yet to inject the bulk of their (stabilizing) feedback momentum. Regions with significant past relative to current star formation are on-average stable against fragmentation.
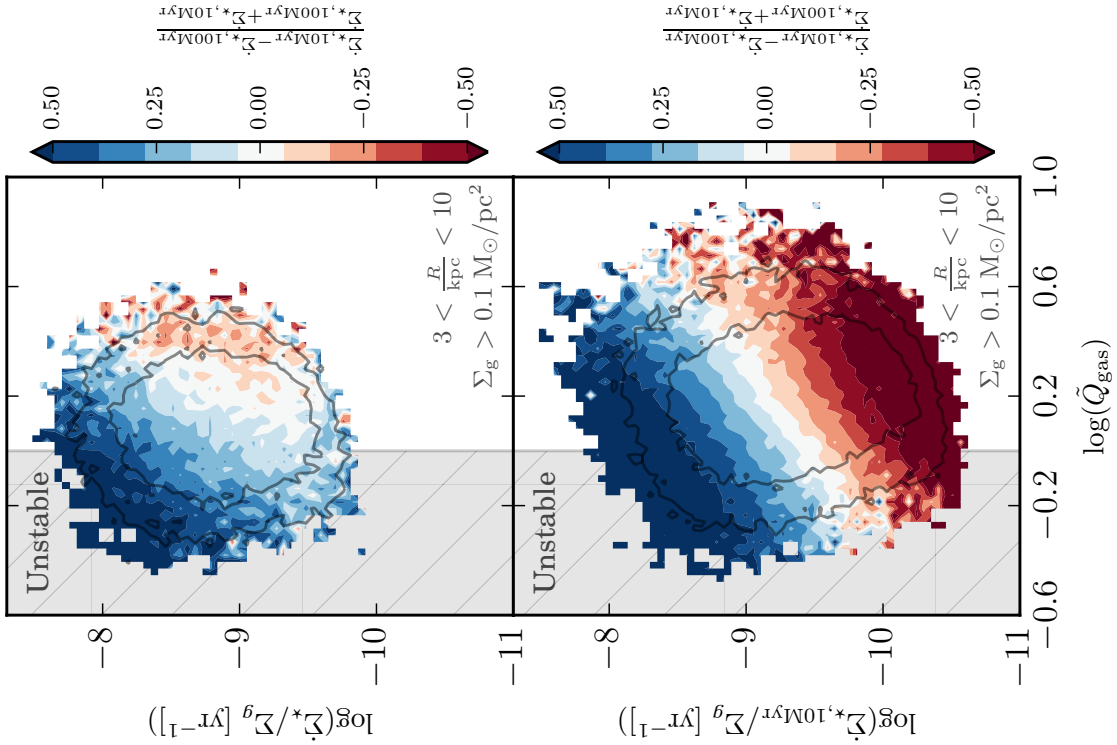
Figure 5.12: Gas stability against gravitational fragmentation $\tilde{Q}_{\rm gas}$ (Eq. 5.1) and gas depletion time in the FIRE simulations, with 750 pc pixel size and colored by a measure of the relative current *vs.* past star formation rate. Hatched gray shaded region to the left indicates $\tilde{Q}_{\rm gas} < 1$ gravitationally unstable region. Gray contours indicate 95% and 75% data inclusion regions (by pixel number). Pixel are cut for $\Sigma_g < 0.1\,{\rm M}_\odot\,{\rm pc}^{-2}$ and outside of $3 < R/{\rm kpc} < 10$. Bluer regions indicate that 750 pc patches have on-average more recent star formation (in the last 10 Myr), and redder regions more star formation occurring on longer timescales (> 10 Myr) in the past. **Top:** Depletion time calculated with the instantaneous star formation rate in the gas particles. Less stable regions have more recent star formation relative to the past, and is more pronounced for shorter depletion times (higher instantaneous SFRs). **Bottom:** Depletion time calculated with the 10 Myr average star formation rate. The most intensely recently bursty (bluest) star-forming regions are on-average more gravitationally unstable and have shorter depletion times for unstable gas. Regions with longer depletion times and more gravitationally stable having had more star formation in the past (reddest regions). Past star formation has occurred on timescales such that the vast majority of their feedback momentum has already been injected into the nearby ISM, indicative of cyclic star formation.

$\tilde{Q}_{gas}$ can fall to arbitrarily low values, and any amount of thermal support may be sufficient to stabilize the gas.

In the simulations, regions with $\tilde{Q}_{gas} < 1$ are on-average gas rich with $f_g > 0.5$. The most stable regions, with required support $\sigma_z(\tilde{Q}_{gas} = 1) > c_s \approx 8$ km/s are the least gas rich with higher values of σ_z having $f_g \rightarrow 0$ on-average.

Related to this, the middle panel shows the outflow-prone fraction when considering the 100 Myr average star formation rate. These high velocity dispersion, low gas fraction regions are by and large the only areas with significant outflow-prone fractions. This suggests that significant feedback events over 100 Myr timescales have had a chance to drive these dispersions to high values, i.e., $\tilde{Q}_{gas} \gg 1$. Evidently, these regions do not just have high velocity dispersions because they have deep disk potentials with high $\Sigma_\star$, though these quantities are correlated to some extent.

Finally, looking at an indicator of how bursty star formation is, i.e., the relative amount of star formation occurring now versus the recent past, η_{burst}, we see that the $\tilde{Q}_{gas} = 1$ threshold is a demarcating line between an abundance of current star formation as compared to the past (bluer shades representing more recent star formation) and vice versa. This falls squarely in line with the idea that vigorous star formation occurs in the ISM when the gas is gravitationally unstable against fragmentation, and collapses on the Toomre scale (here, the disk scale height).

Exploring this last aspect further, Figure 5.12 shows how the gas depletion time (calculated by the time for neutral gas consumption with two different star formation tracers, the gas instantaneous and 10 Myr average star formation rate) correlates with gas stability using $\tilde{Q}_{gas}$. The relation is shaded by the star formation burst indicator η_{burst}. Importantly, we exclude gas outside 3 kpc $< R <$ 10 kpc, and with $\Sigma_g < 0.1$ M$_\odot$ pc^{-2}, as it is either not shielded and likely has significant thermal support, or is at radii with a rising rotation curve and has significant shear across the 750 pc pixels, thus $\tilde{Q}_{gas}$ being a poor representation of gas stability.

When considering the instantaneous star formation rate gas depletion time, we see that $\tilde{Q}_{gas}$ alone is a good predictor of η_{burst} with less stable regions having significant present relative to past star formation. Notably, there are few regions with $\eta_{burst} \lesssim -0.5$, i.e., pixels that have significant instantaneous (current) star formation and have recent star formation histories dominated by past (10 Myr$< t_{ago} <$ 100 Myr) star formation.

On the other hand, the 10 Myr average star formation rate gas depletion time panel

shows two clearly separated in depletion time regimes: (1) short depletion times are dominated by regions with more recent versus past star formation ($\eta_{\text{burst}} > 0.5$) and are on-average less stable ($\tilde{Q}_{\text{gas}}$ is ~ 0.3 dex lower), and (2) long-depletion time regions have slightly higher values of $\tilde{Q}_{\text{gas}}$ on-average, and are dominated by past versus recent star formation. This agrees with recent work by Orr, Hayward, and Hopkins (2019), where on-off cycles of star formation can be driven on $1/\Omega$ timescales by feedback from Type II SNe and their ~ 40 Myr delay-time distribution.

5.3 Discussion

5.3.1   A Hierarchy of Timescales: Why is σ_z-$\dot{\Sigma}_\star$ So Flat?

It is notable that for three dex in (10 Myr averaged) star formation rates, σ_z hardly budges, the lower envelope in velocity dispersions notwithstanding. This however, like the discussion regarding scatter in the resolved Kennicutt-Schmidt relation at high spatial resolution (Schruba et al., 2010; Kruijssen et al., 2014; Orr, Hayward, and Hopkins, 2019), may be understood through a discussion of a hierarchy of timescales. Within the framework of supersonic turbulence dominating the velocity dispersions, the turbulent momentum in a patch of the ISM is decaying on an eddy-crossing time $t_{\text{eddy}} \sim 2/\Omega$, and so $\dot{\sigma}_z \sim -2\sigma_z\Omega$. For the Milky Way-like galaxies explored here $\Omega = v_c/R \sim 250$ km/s $/10$ kpc ~ 25 Gyr^{-1}, thus $t_{\text{eddy}} \sim 80$ Myr. This is far longer than the free-fall time for a GMC with a mean density of $n = 100$ cm^{-3}, $t_{\text{ff}} = \sqrt{3\pi/32Gm_p n} \approx 5$ Myr. As a result, while σ_z is only able to slowly evolve as turbulence is dissipating, short timescale tracers of star formation are able to light up from zero and wick back out again before the effects of feedback are felt in the disk scale height scale velocity dispersions (of course, 'prompt' feedback like winds and ionizing radiation are locally felt immediately). Considering that the feedback momentum from supernovae are meted out over a period of $\sim 5 - 40$ Myr (to say, $t_{\text{fb}} = 40$ Myr) since the formation of massive stars, it is understandable that some evolution in σ_z is seen for σ-$\dot{\Sigma}_\star$ when considering the 100 Myr averaged star formation rate tracer, as it incorporates the effects of injecting feedback on the disk scale height scale velocity dispersions. This is picture is especially true when considering the gas instantaneous star formation rate, where there is effectively no evolution in the velocity dispersions as the star formation rate flits on and off. Instantaneous star formation rates do not appear to have any correlation with velocity dispersions in the ISM (barring the slight lower envelope in velocity dispersions for a given instantaneous SFR, seen more strongly for the 10 and 100 Myr SFR relations). The distribution of velocity dispersions is simply smeared out across the range of

star formation rates are they rapidly rise and fall. And so, it is expected that we see a flat distribution in velocity dispersion, and a slightly positive slope in it, for 10 Myr and 100 Myr tracers of star formation, respectively, with a hierarchy of timescales: $t_{\text{ff}} \ll 10\ \text{Myr} < t_{\text{fb}} < 100\ \text{Myr} \sim t_{\text{eddy}} \sim 1/\Omega$.

5.3.2 What Drives Velocity Dispersions (Theoretically)?

There have been a number of attempts at understanding the relationship theoretically between star formation rates locally and the gas structure of the disk (i.e., scale heights, velocity dispersions, etc.). Often, these have been viewed through the lens of star formation as an equilibrium process in galaxies (e.g., Ostriker et al., 2011; Faucher-Giguère et al., 2013; Hayward et al., 2017), given the fact that the most massive stars form and live only for a fraction of a galactic dynamical time. However, some work has sought to understand how non-equilibrium models of star formation might behave in Milky Way-like disk environments, when gas dynamical and stellar feedback timescales are on a comparable footing (Benincasa et al., 2016; Orr, Hayward, and Hopkins, 2019).

Generally, models of star formation in disks invoke feedback as a regulator of either the gravitational weight of disks, or the momentum in the cold turbulent ISM. However, there are classes of models where star formation is the result of disk/galactic structure, and does not appreciably act as a regulator of large-scale (~kpc) ISM structure.

These scalings can be grouped into several categories:

1. **Feedback Balances Gravity:** The feedback from stars balances the weight of the disk (e.g., Ostriker et al., 2011). The weight of a disk being approximately described as $\frac{\pi}{2}G\Sigma_g(\Sigma_g + \gamma\Sigma_\star)$, where the γ term again is the fraction of the stellar surface density within a gas scale height. This is balanced with the feedback momentum $(P/m_\star)\dot{\Sigma}_\star$. Thus,

$$\left(\frac{P}{m_\star}\right)\dot{\Sigma}_\star \approx \frac{\pi}{2}G\Sigma_g(\Sigma_g + \gamma\Sigma_\star)\ . \tag{5.4}$$

   This is agnostic to the actual velocity dispersion or scale height of the gas disk[4]. Often, however, it is connected by invoking $\tilde{Q}_{\text{gas}} \sim \sigma\Omega/\Sigma_{\text{disk}} \sim 1$. In which case, the result is identical to the next feedback-related scaling. Barring

---

[4]Only indirectly, in the relative difference in scale heights between the gaseous and stellar disks does the gas scale height ($\sim \sigma_z/\Omega$) enter in γ.
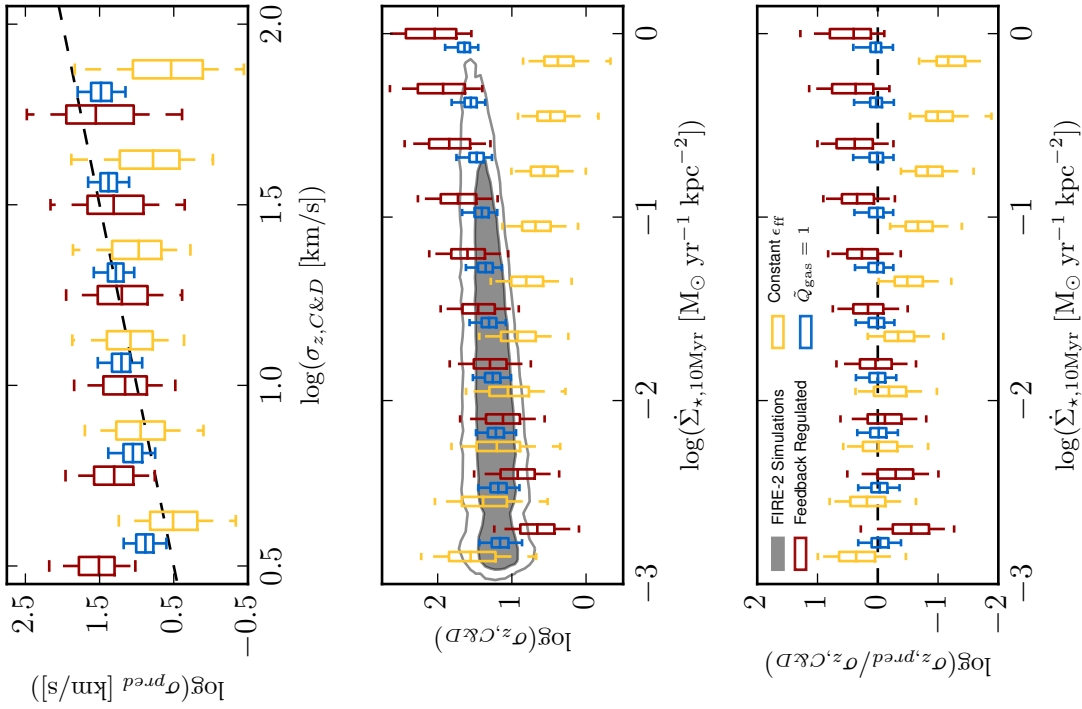
Figure 5.13: Pixel-by-pixel predictions of velocity dispersions by feedback-regulated model (cardinal, § 5.3.2 2), a constant-efficiency model (gold, § 5.3.2 3), and assuming $\tilde{Q}_{\rm gas} = 1$ (blue, Eq. 5.1) compared against actual dispersions in the FIRE simulations (grey). Shaded region denotes 75% data inclusion region, with unfilled contour showing the 95% inclusion region for the FIRE data. Box-and-whiskers denote interquartile region (with median), and whiskers extend to 5–95% of data in bin. All scalings are calculated and presented with the 10 Myr average star formation rate tracer. **Top:** Predicted σ_z for star formation models and $\tilde{Q}_{\rm gas} = 1$ versus measured $\sigma_{z,C\&D}$. Both star formation models produce a similar dispersion around the actual values, albeit diverging from the data at low and high velocity dispersions for the feedback-regulated and constant-efficiency models, respectively. $\tilde{Q}_{\rm gas} = 1$ is a closer predictor than either at all σ_z. Black dashed line is $\sigma_{\rm pred} = \sigma_{z,C\&D}$. **Middle:** Velocity dispersion–SFR relation, showing both model distributions and the FIRE dataset (grey region and contours). Here the reciprocal slope scalings of the star formation models with respect to $\dot{\Sigma}_\star$ are on display: feedback regulation predicts rising σ with $\dot{\Sigma}_\star$, whereas constant-efficiency star formation predicts falling dispersions. $\tilde{Q}_{\rm gas} = 1$ falls on top of the FIRE data at all SFRs. **Bottom:** Comparing the discrepancies between the model predictions and the FIRE dataset as a function of $\dot{\Sigma}_\star$. Both star formation models generally fall within a dex of the FIRE data at all $\dot{\Sigma}_\star$, whereas $\tilde{Q}_{\rm gas} = 1$ is within ±0.3 dex at all SFRs.

that, this feedback-regulated formulation actually makes *no* prediction directly as to the velocity dispersions or turbulence in the disk.

2. **Turbulent Momentum Injection Balances Dissipation:** The rate of feedback momentum injected by massive stars balances the rate of turbulence dissipation in the supersonic ISM (e.g., Faucher-Giguère et al., 2013; Hayward et al., 2017). Here, turbulent momentum is argued to decay on an eddy (disk) crossing time. where $P_{\text{turb}} \sim \Sigma_g \sigma$ and so $\dot{P}_{\text{turb}} \sim -\Sigma_g \sigma \Omega/2$. this balances with feedback injection at a rate of $(P/m_\star)\dot{\Sigma}_\star$. Together, $(P/m_\star)\dot{\Sigma}_\star \approx \sqrt{3}\Sigma_g \sigma_z \Omega/2$. Or,

$$\sigma_{z,FB} \approx \frac{2}{\sqrt{3}} \frac{(P/m_\star)\dot{\Sigma}_\star}{\Omega\Sigma_g} \ . \tag{5.5}$$

This, and often the argument that disks regulate themselves to $\tilde{Q}_{\text{gas}} \approx 1$, does a fairly good job matching observations of the Kennicutt-Schmidt relation, and so this and the previous formulation are often conflated as the feedback-regulated model.

3. **Constant (Low) Efficiency Star Formation:** Star formation proceeds at a constant efficiency per free-fall time in a marginally unstable Toomre disk (e.g., Krumholz, Dekel, et al., 2012; Salim et al., 2015). Here, $\dot{\Sigma}_\star = \epsilon_{\text{ff}}\Sigma_g/t_{\text{ff}}$, where $\epsilon_{\text{ff}} \approx 0.01$, and t_{ff} is derived arguing that vertical hydrostatic equilibrium is maintained in the disk with the mid-plane disk pressure being:

$$P_{\text{midplane}} = \rho\sigma^2 \approx \frac{\pi}{2}G\Sigma_g(\Sigma_g + \gamma\Sigma_\star) \ . \tag{5.6}$$

this results in a scaling for the constant-efficiency star formation rate of:

$$\sigma_{z,\epsilon_{\text{ff}}} \approx \frac{4\epsilon_{\text{ff}}G\Sigma_g\sqrt{\Sigma_g(\Sigma_g + \gamma\Sigma_\star)}}{3\dot{\Sigma}_\star} \ , \tag{5.7}$$

which has a reciprocal slope in $\dot{\Sigma}_\star$ from the feedback-regulated model.

4. **Accretion Driven Turbulence/Star Formation:** The gravitational potential energy of in-falling gas is converted to turbulent motions, i.e., σ, and gas migrates through the disk to the centers of galaxies, all while star formation is occurring (Klessen et al., 2010; Krumholz and Burkert, 2010; Cacciato et al., 2012). Following the work of Krumholz and Burkert (2010), if star formation occurs with fixed low efficiency, and the disk maintains a steady state with

accreted gas moving radially towards the center, then the velocity dispersions in this accretion powered model will scale with star formation as:

$$\sigma_{z,acc} \propto \frac{\epsilon_{\mathrm{ff}}^2 f_g^2 \Omega^4 \dot{M}_{\mathrm{acc}}}{G \dot{\Sigma}_\star^2} \; , \tag{5.8}$$

where $\dot{M}_{\mathrm{acc}}$ is the rate that gas accretes onto the galaxy disk. This scaling has the velocity dispersions fall even more rapidly with rising SFRs than the low-efficiency model **(iii)**.

Figure 5.13 shows the result of using the local surface densities, dynamical times, etc., in the spatially resolved FIRE data to predict the velocity dispersions in the gas using both the feedback-regulated **(ii)** and the constant-efficiency **(iii)** models. This is compared against the actual velocity dispersions calculated in these pixels in the cold and dense gas. We do not compare the accretion powered model **(iv)**, as its predicted velocity dispersions fall off even more rapidly than the (just) constant-efficiency model and so finds significant disagreement with the simulations in a spatially resolved sense.

Although the first panel suggests that both models do equally poorly in agreeing with the actual dispersions on a pixel-by-pixel basis, we see that they each find ~dex disagreement with the data in different star formation regimes (due to their reciprocal slopes in scaling with $\dot{\Sigma}_\star$). The middle panel shows that the feedback-regulated picture over-predicts σ_z at high $\dot{\Sigma}_\star$, by ~0.5 dex, whereas the constant-efficiency model under-predicts by close to a dex there. At high star formation rates, as per § 5.2.6 and the work of Hayward et al. (2017), it is likely unfair to argue that all of the momentum goes into the velocity dispersions of the cold molecular medium. Rather, some outflowing material or heating of the ISM is warranted, and ought to carry away some of the momentum budget, and this framework naturally then overestimates the velocity dispersion in this regime. On the other hand, the constant efficiency model significantly under-predicts σ_z, and would most easily be rectified by arguing that ϵ_{ff} rises with Σ_g (cf., Grudić et al. 2018).

At the other extreme, for low $\dot{\Sigma}_\star$, the feedback-regulated framework under-predicts σ_z by ~ 0.5 dex, with the constant-efficiency model over-predicting it by about the same amount. In this case, the picture of the ISM as a purely turbulently supported medium breaks down, and the ISM begins to have significant (but not sufficient) thermal support from the atomic phase ($T \approx 8000$ K, $c_s \approx 6$ km/s). Including the thermal component c_s in quadrature with the turbulent scaling predictions would

not significantly affect the constant-efficiency model, as it predicts tens of km/s of dispersions at the low end of star formation, but would bring the feedback-regulated model into closer agreement.

In summary, both the feedback-regulated and constant efficiency models appear to produce similar disagreement with the velocity dispersions seen in FIRE (and in turn, due to the good agreement of FIRE with observations, reality). However, there are reasonable physical arguments that may alleviate discrepancies at high and low star formation rates for the feedback-regulated model. These physical effects do not aid the constant-efficiency model (and in fact would only add to its tension).

5.4   Summary & Conclusions

In this chapter, we explored the properties of the various spatially resolved (fiducially, 750 pc) line-of-sight gas velocity dispersions, and their relationships with different star formation rate tracers and gas stability. These properties were investigated in the context of face-on 'observations' of the Milky Way massed disk galaxies ($M_\star \approx 10^{10.2} - 10^{10.9}$ $M_\odot$ at $z \approx 0$) of the FIRE cosmological zoom-in simulations, and found to be in good agreement with resolved observations of local spiral galaxies. Our principal results are as follows:

- Velocity dispersions in neutral (atomic + molecular) gas are nearly constant across 3 dex in 10 Myr average star formation rates, distributed between $\approx 15 - 30$ km/s in our sample of simulated Milky Way-mass spirals (Fig. 5.4). There exists a lower envelope in velocity dispersions for neutral gas, which is especially pronounced in the cold & dense gas, at constant $\dot{\Sigma}_\star$.

- In regions with low recent (≤ 10 Myr) star formation rates, velocity dispersions correlate with past ($\lesssim 100$ Myr) star formation rates (Fig. 5.7). This coincides with the timescale over which past star formation events will have injected all their feedback momentum into the ISM. At high recent star formation rates, the ISM in these galaxies does not appreciably 'remember' past star formation activity.

- The outer contours of the σ_z-$\dot{\Sigma}_\star$ relation corresponds to conditions where the ISM is hosting star formation rates (over different timescales) sufficiency high to expel significant fractions of the ISM as outflows/galactic fountains (Fig. 5.8). In other words, the ISM can only sustain so much feedback

over 10–100 Myr timescales, without being driven out as outflows/galactic fountains.

- Dense gas depletion times ($\Sigma_{g,C\&D}/\dot{\Sigma}_\star$) are shortest in the cases where either a small fraction of the ISM is dense (thus, nearly all the dense gas is involved in star formation) or where gas surface densities are high and nearly all of the ISM is cold and dense (Figs. 5.9 & 5.10).

- There is evidence for on-off cycles of star formation in the disks (Fig. 5.12): less gravitationally stable patches of ISM with little past ($\sim 10 - -100$ Myr ago) star formation have the shortest gas depletion times/most vigorous current ($\lesssim 10$ Myr) star formation rates, and conversely, more gravitationally stable regions with long gas depletion times have had star formation/feedback events in the recent past (10–100 Myr ago).

- The FIRE-2 simulations, and observations, show that regions with higher $\dot{\Sigma}_\star$ tend to have higher σ_z, while models with constant efficiency star formation predict that such regions should have lower σ_z. This is in broad agreement with feedback-regulated models that predict SFRs should scale positively with velocity dispersions.

The velocity dispersion structure of the FIRE Milky Way-massed spirals dovetails with our general understanding of gas disks in the turbulently supported framework of disk structure stability. By and large, the dispersions seen and their attendant star formation rates are consistent with the feedback regulated model of star formation (cf.,§ 5.3.2).

The differing timescales traced by various proxies for star formation rates (e.g., Hα fluxes tracing $\lesssim 10$ Myr vs. UV fluxes tracing $\lesssim 100$ Myr timescales) and the dynamical times involved for the evolution of turbulent gas linewidths (disk/eddy-crossing times) are a frequent difficulty in interpreting studies of velocity dispersions and star formation rates in galaxies. However, they also pose a unique opportunity to study the dynamical evolution of the ISM over those timescales. We have seen evidence in the relative flatness of the σ_z-$\dot{\Sigma}_\star$ relation for star formation rates over 10 Myr timescales that the ISM can respond relatively quickly in terms of *firing* up/turning off star formation compared to the actual driving/decay rate of gas turbulence. Further, between the present dynamical state of gas, and current star formation rates, in regions with high or low past star formation rates in the FIRE

spirals present evidence of the regulation timescales of feedback injection, and vigorous on-off cycles of star formation occurring over $\sim 10 - -100$ Myr timescales and ~kpc length-scales.

Future work, both from the modeling side of simulations, where theorists may explicitly model dense molecular gas line emission and linewidths to allow for more direct comparisons with IFU observations, and on the observational side with more complete censuses of spatially resolved galactic gas structures and star formation rates in on-going IFU surveys, will only help uncover the connections between the local gas dynamics on kpc-scales and star formation in disk environments.

Acknowledgements

References

El-Badry, K. et al. (2018) MNRAS 473, 1930

Behroozi, P. S., Wechsler, R. H., & Conroy, C. (2013) ApJ 770, 57, 57

Benincasa, S. M., Wadsley, J., Couchman, H. M. P., & Keller, B. W. (2016) MNRAS 462, 3053

Bigiel, F., Leroy, A., Walter, F., Brinks, E., de Blok, W. J. G., Madore, B., & Thornley, M. D. (2008) AJ 136, 2846

Brinchmann, J., Charlot, S., White, S. D. M., Tremonti, C., Kauffmann, G., Heckman, T., & Brinkmann, J. (2004) MNRAS 351, 1151

Cacciato, M., Dekel, A., & Genel, S. (2012) MNRAS 421, 818

Calzetti, D., Liu, G., & Koda, J. (2012) ApJ 752, 98, 98

Cortese, L. et al. (2014) ApJ 795, L37, L37

Faucher-Giguère, C.-A., Quataert, E., & Hopkins, P. F. (2013) MNRAS 433, 1970

Gallagher, J. S. & Hunter, D. A. (1983) ApJ 274, 141

Gallagher, M. J., Leroy, A. K., Bigiel, F., Cormier, D., Jiménez-Donaire, M. J., Hughes, A., et al. (2018) ApJ 868, L38, L38

Gallagher, M. J., Leroy, A. K., Bigiel, F., Cormier, D., Jiménez-Donaire, M. J., Ostriker, E., et al. (2018) ApJ 858, 90, 90

Goldsmith, P. F., Heyer, M., Narayanan, G., Snell, R., Li, D., & Brunt, C. (2008) ApJ 680, 428

Goldsmith, P. F. & Li, D. (2005) ApJ 622, 938

Goldsmith, P. F., Li, D., & Krčo, M. (2007) ApJ 654, 273

Grudić, M. Y., Hopkins, P. F., Faucher-Giguère, C.-A., Quataert, E., Murray, N., & Kereš, D. (2018) MNRAS 475, 3511

Hayward, C. C. & Hopkins, P. F. (2017) MNRAS 465, 1682

Hopkins, P. F. (2015) MNRAS 450, 53

Hopkins, P. F., Kereš, D., Oñorbe, J., Faucher-Giguère, C.-A., Quataert, E., Murray, N., & Bullock, J. S. (2014) MNRAS 445, 581

Hopkins, P. F., Wetzel, A., et al. (2018) MNRAS 480, 800

Kennicutt Jr., R. C. (1989) ApJ 344, 685

Kennicutt, R. C. & Evans, N. J. (2012) ARA&A 50, 531

Klessen, R. S. & Hennebelle, P. (2010) A&A 520, A17, A17

Kroupa, P. (2002) Science 295, 82

Kruijssen, J. M. D. & Longmore, S. N. (2014) MNRAS 439, 3239

Krumholz, M. R. & Burkhart, B. (2016) MNRAS 458, 1671

Krumholz, M. R., Dekel, A., & McKee, C. F. (2012) ApJ 745, 69, 69

Krumholz, M. R. & Gnedin, N. Y. (2011) ApJ 729, 36, 36

Krumholz, M. R., McKee, C. F., & Tumlinson, J. (2008) ApJ 689, 865

Krumholz, M. & Burkert, A. (2010) ApJ 724, 895

Larson, R. B. (1981) MNRAS 194, 809

Lee, E. J., Miville-Deschênes, M.-A., & Murray, N. W. (2016) ApJ 833, 229, 229

Lehnert, M. D. et al. (2009) ApJ 699, 1660

Leitherer, C. et al. (1999) ApJS 123, 3

Leroy, A. K., Schinnerer, E., et al. (2017) ApJ 846, 71, 71

Leroy, A. K., Walter, F., Brinks, E., Bigiel, F., de Blok, W. J. G., Madore, B., & Thornley, M. D. (2008) AJ 136, 2782

Leroy, A. K., Walter, F., Sandstrom, K., et al. (2013) AJ 146, 19, 19

Ma, X., Hopkins, P. F., Feldmann, R., Torrey, P., Faucher-Giguère, C.-A., & Kereš, D. (2017) MNRAS 466, 4780

Orr, M. E., Hayward, C. C., & Hopkins, P. F. (2019) MNRAS 486, 4724

Orr, M. E., Hayward, C. C., Hopkins, P. F., et al. (2018) MNRAS 478, 3653

Orr, M. E., Pineda, J. L., & Goldsmith, P. F. (2014) ApJ 795, 26

Ostriker, E. C. & Shetty, R. (2011) ApJ 731, 41, 41

Pineda, J. L., Goldsmith, P. F., Chapman, N., Snell, R. L., Li, D., Cambrésy, L., & Brunt, C. (2010) ApJ 721, 686

Pineda, J. L., Langer, W. D., et al. (2017) ApJ 839, 107, 107

Querejeta, M. et al. (2019) A&A 625, A19, A19

Rozas, M., Richer, M. G., López, J. A., Relaño, M., & Beckman, J. E. (2006) A&A 455, 539

Rozas, M., Sabalisck, N., Beckman, J. E., & Knapen, J. H. (1998) A&A 338, 15

Salim, D. M., Federrath, C., & Kewley, L. J. (2015) ApJ 806, L36, L36

Schmidt, M. (1959) ApJ 129, 243

Schruba, A., Leroy, A. K., Walter, F., Sandstrom, K., & Rosolowsky, E. (2010) ApJ 722, 1699

Simons, R. C. et al. (2017) ApJ 843, 46, 46

Sparre, M., Hayward, C. C., Feldmann, R., Faucher-Giguère, C.-A., Muratov, A. L., Kereš, D., & Hopkins, P. F. (2017) MNRAS 466, 88

Sternberg, A., Le Petit, F., Roueff, E., & Le Bourlot, J. (2014) ApJ 790, 10, 10

Stilp, A. M., Dalcanton, J. J., Skillman, E., Warren, S. R., Ott, J., & Koribalski, B. (2013) ApJ 773, 88, 88

Stilp, A. M., Dalcanton, J. J., Warren, S. R., Skillman, E., Ott, J., & Koribalski, B. (2013) ApJ 765, 136, 136

Sun, J. et al. (2018) ApJ 860, 172, 172

Thompson, T. A., Quataert, E., & Murray, N. (2005) ApJ 630, 167

Toomre, A. (1964) ApJ 139, 1217

Torrey, P., Hopkins, P. F., Faucher-Giguère, C.-A., Vogelsberger, M., Quataert, E., Kereš, D., & Murray, N. (2017) MNRAS 467, 2301

Wetzel, A. R., Hopkins, P. F., Kim, J.-h., Faucher-Giguère, C.-A., Kereš, D., & Quataert, E. (2016) ApJ 827, L23, L23

Xu, D., Li, D., Yue, N., & Goldsmith, P. F. (2016) ApJ 819, 22, 22

Zhou, L. et al. (2017) MNRAS 470, 4573

Chapter 6

SUMMARY & FUTURE WORK

6.1 Synopsis Overview & Past Work

My research has sought to understand how the physics of star formation, stellar feedback from massive stars, and gas cooling physics shape and regulate the interstellar medium within galaxies. Particularly, my focus has lain on the scale of the largest coherent structures in galaxies–the disk scale height in Milky Way-mass galaxies. To explore these physics, I have primarily used cosmological zoom-in simulations, specifically those of the FIRE project (Hopkins, Kereš, et al., 2014; Wetzel et al., 2016; Hopkins, Wetzel, et al., 2018). Cosmological zoom-in simulations, which evolve cosmologically-sized volumes but focus their computational power on a small region of that volume, have reached a point that they can answer questions tied to star formation and the ISM, combining a cosmological context and realistic environments in which entire galaxies form with high-resolution zoom-in regions that allow for detailed, meaningful studies of the gas and stellar populations *within* galaxies at the parsec scale. State-of-the-art simulations are now able to match resolved quantities *within* galaxies, and I have worked to understand what processes work to regulate the internal dynamics of galaxies to produce this concordance.

Many of my first-author projects, turned thesis chapters, have focused on exploring spatially resolved star formation in cosmological zoom-in simulations. My work probes the intersection of cosmological simulations and observed star formation scaling relations and tracers of dense gas. The past several years of research, presented here as thesis chapters, can be seen as connected by a consistent thread of projects:

6.1.1 *Kennicutt-Schmidt* on FIRE

The FIRE simulations (Hopkins, Kereš, et al., 2014) were among the first cosmological simulations to reach the mass resolutions required to study star formation on sub-kiloparsec-scales, and thus follow the fragmentation and collapse of gas, rather than impose a pressure/density floor. As my first independent project, I conducted a study of the spatially resolved Kennicutt-Schmidt relation (Schmidt, 1959; Kennicutt, 1998), which is an empirical relation between gas surface density and star formation rates, in the FIRE simulations (Orr, Hayward, Hopkins, et al., 2018).

The goal was to study and understand the emergent nature of the scaling relation, as the star formation prescription in FIRE at the particle scale does not include it *a priori*. I developed a pipeline to produce spatially resolved maps of simulation snapshots, yielding star formation rates, and properties of the gas in the galaxies at 100 parsec to kiloparsec resolution. Examining the emergent star formation relation in a dozen distinct simulations with several hundred snapshots of each, we were able to explore various formulations of the Kennicutt-Schmidt relation (comparing different tracers of star formation rate and gas surface densities), and their dependencies on metallicity, local dynamical times, and redshift evolution. We found that the Kennicutt-Schmidt relation in FIRE agrees well with both the normalization and scatter found in observations (Bigiel et al., 2008; Leroy, Walter, Brinks, et al., 2008; Leroy, Walter, Sandstrom, et al., 2013). The scatter in star formation rates at constant gas surface density, interestingly, was not fully explained by local variations in quantities like metallicity or dynamical time, suggesting that some intrinsic scatter arises due to the evolutionary state of individual star forming regions (see, e.g., Schruba et al., 2010; Kruijssen and Longmore, 2014)—this was explored further in Orr, Hayward, and Hopkins (2019), and continues to be an area of interest for me.

6.1.2   What *fires* up Star formation?

As part of studying the Kennicutt-Schmidt relation in the FIRE simulations, the question arose: what set the extent of the star-forming disks in the simulations (i.e., what causes star formation to *fire* up in the outskirts)? A number of arguments had existed relating to star formation thresholds in galaxies (Martin et al., 2001; Schaye, 2004; Krumholz et al., 2005; McKee et al., 2007; Shetty and Ostriker, 2008; Semenov et al., 2016). With two main arguments, that either marginal stability in the gas against gravitational fragmentation was key or that gas cooling and opacity were for setting the onset of star formation. In Orr, Hayward, Hopkins, et al. (2018), we explored the relative gravitational stability, quantified with the Toomre-Q parameter (Toomre, 1964), and opacity (as a proxy for the molecular state) of the gas where star formation occurred in the FIRE simulations. We found definitively that star formation occurred where gas was first unable to maintain marginal stability with thermal support alone in galaxies, and that star formation occurred as a matter of course to provide additional required turbulent support. In collaboration with the MaNGA galaxy survey (Bundy et al., 2015), we found this also to be the case in observations, with the onset of gravitational instabilities corresponding to breaks in star formation rate profiles in disk galaxies (Stark et al., 2018).

6.1.3   Stacking is Hacking

Current observations of star formation in the high-redshift ($z \sim 1$) universe are limited by low signal-to-noise and spatial resolutions at 1 kpc or larger (Nelson et al., 2016). Observers have therefore developed a number of observational techniques to address low signal-to-noise and pull out radial profiles in galaxies, including stacking observations of many galaxies (Nelson et al., 2016; González Delgado et al., 2016; Liu et al., 2018). In order to explore the difficulties and pitfalls of analyzing stacks of galaxy observations, I collaborated with Dr. Erica Nelson, whose own work uses the stacking technique, to conduct an identical analysis of $z \sim 1$ spatially resolved star formation maps from my Kennicutt-Schmidt study (Orr, Hayward, Nelson, et al., 2017). Our primary findings indicated that temporal variations in spatially resolved star formation rates *within* individual galaxies were more than enough to bias analysis of stacks of star formation rate profiles chosen to be above or below the star formation rate main sequence, a scaling relation between observed star formation rates $\dot{M}_\star$ and stellar masses $M_\star$ (Brinchmann et al., 2004; Wuyts et al., 2011). The letter (chapter) ended up being a cautionary tale, warning that care need be taken in choosing how to stack galaxy observations and interpreting results from stacking.

6.1.4   Delayed Feedback & SFR Scatter

Understanding why star formation rates exhibited ~dex scatters even at constant gas surface density piqued my interest through my work with the Kennicutt-Schmidt relation. I found it particularly intriguing that comparing the expected star formation rate from turbulent-regulation theories (e.g., Ostriker et al., 2011; Faucher-Giguère et al., 2013) matched the average star formation rates seen in the distributions, considering the local conditions, but failed to explain the scatter consistently. In exploring the velocity dispersions in the gas, as part of an on-going project involving the FIRE-2 simulations, I began to analytically explore the effects of non-negligible delay times between star formation and feedback injection. The comparability of free-fall times in GMCs (few Myr), the lifetimes of massive stars ($\sim 3 - -40$ Myr), and disk-crossing times (~10 Myr) suggested that no process could be considered to be "instantaneous" and that any equilibria reached would be cyclic and not static (cf., a harmonic oscillator in a dynamical equilibrium). This has led to a work in press, Orr, Hayward, and Hopkins (2019), that identifies this feedback delay time as a key parameter in driving local (kpc-scale) *cycles* in star formation and for reasonable values of the delay time, I can reproduce the scatter (~dex variability), an aspect

missed in previous formulations of turbulence regulation (Benincasa et al., 2016).

6.1.5 Spatially Resolved Gas Velocity Dispersion–SFR Scaling Relations

Velocity dispersions (i.e., linewidths) in various gas tracers (e.g., CO or hydrogen recombination lines) have been used as measures of line-of-sight structure, and turbulent or thermal energy in the ISM (Lehnert et al., 2009; Bolatto et al., 2013; Zhou et al., 2017). For this reason, there is the natural question: how is star formation connected with either vertical structure or the turbulent energy in the ISM at any given time? I have explored how gas velocity dispersions and star formation rates relate in snapshots of Milky Way mass disk galaxies in the FIRE-2 simulations (Hopkins, Wetzel, et al., 2018), using the spatially resolved mapping machinery developed for the Kennicutt-Schmidt project. I am especially interested in the extent to which star formation is able to drive kpc-sized patches of disks away from marginal stability (i.e, Toomre's $Q \sim 1$). The FIRE-2 simulations appear to not depart far from stability, and understanding why this occurs and how quickly local patches can regulate themselves, is a focus of that work.

6.2 Future Work: Signatures of Star Formation and Feedback Physics in Spatially Resolved Synthetic Observations

6.2.1 Motivation

The fields of star formation and galaxy evolution are now in the age of highly spatially resolved galaxy studies and surveys that yield the spectra of thousands of galaxies at sub-kiloparsec (kpc) resolution (e.g., Schinnerer et al., 2013; Bundy et al., 2015). With the tremendous throughput of data, we are faced with the quandary of how these observations connect to the underlying ground truths of galaxies, e.g., how well do various gas emission lines trace star formation on kpc-scales, or what are the signatures of different star formation and feedback theories buried in these high-dimensional datasets? Cosmological zoom-in simulations have evolved over the last 25 years to a level of realism where they can begin to tackle these questions (e.g., Katz et al., 1996; Hopkins, Wetzel, et al., 2018). Whereas a decade ago simulations faced difficulty in matching even global properties of observed galaxies (e.g., the ratio of stellar mass to total halo mass), the state of the art is now able to meaningfully recover resolved quantities in galaxies that were not put into the simulations by hand (e.g., the Kennicutt-Schmidt star formation scaling relation, see Figure 6.1 for an example of this in the FIRE simulations, Orr, Hayward, Hopkins, et al., 2018). However, there remains a gap between simulations and observations.

Theorists typically report physical quantities taken directly from their simulations, while observers must derive the underlying properties from, e.g., linewidths and luminosities by making a wide array of assumptions about molecular and atomic processes, and the dynamical state of the gas.

In order to address the gap, I have developed a pipeline for producing spatially resolved spectral maps of cosmological zoom-in simulations, so as to be able to directly compare spatially resolved luminosities and linewidths predicted by simulations with those from observations. In my future work, I will explore the signatures of variations in star formation, feedback (e.g., cosmic rays, supernovae, radiation pressure, photoionization, etc.), and gas physics in resolved galaxy scaling relations, and probe various observables (e.g., CO or C^+ emission) to constrain those physics.

6.2.2 Future Research Directions

Producing sub-kpc-scale line-emission maps of simulated Milky Way-mass galaxies requires accurate chemical abundances, a realistic radiation field, and an accurate accounting of how the radiation propagates. I will therefore post-process the simulations using the CHIMES chemistry solver (Richings et al., 2014b; Richings et al., 2014a) to produce equilibrium chemical abundances, using a modern stellar population model to supply realistic radiation fields for the chemistry and dust temperatures (e.g., FSPS, Conroy, Gunn, et al., 2009; Conroy, White, et al., 2010), and (3) use a 3D Monte Carlo radiative transfer code (RADMC3D, Dullemond et al. in prep.) to follow the photons out of the galaxy to the observer. My pipeline predicts equilibrium chemical abundances from the local gas shielding column, radiation field, and the density and temperature of the nearby gas, and thus tracks the effects of star formation/feedback/gas physics self-consistently. Figure 6.2 shows an example of a spatially resolved CO $J = 1 \rightarrow 0$ line-emission datacube produced by this pipeline. I will leverage this machinery to make resolved submillimeter line emission maps of a variety of commonly observed species (e.g., CO, ^{13}CO, C, C^+, N^+). Because RADMC3D even handles line-transfer (i.e. emission/absorption at specific frequencies), I will also calculate recombination lines such as $H\alpha$ that are commonly used to estimate star formation rates on short timescales.

Ultimately, my pipeline will yield spatially resolved multi-wavelength emission maps from simulations, enabling detailed studies of dense gas and star formation tracers. I will use these maps to validate empirical conversion factors between observed and inferred quantities, investigate in what ways state-of-the-art cosmo-
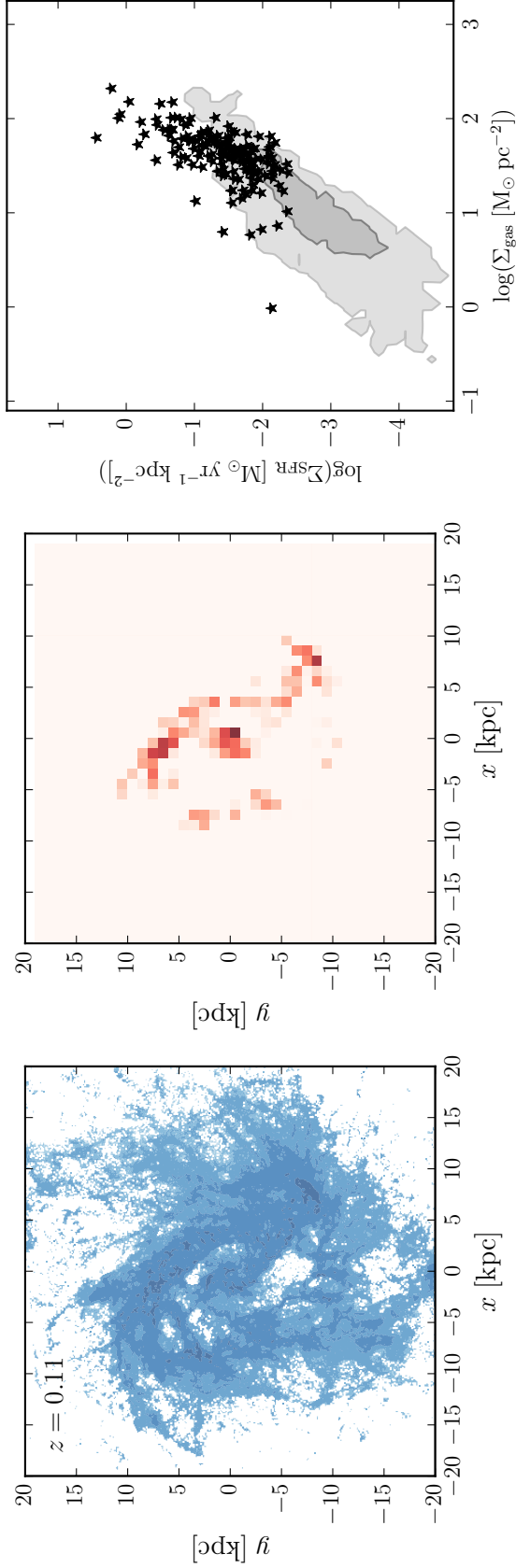
Figure 6.1: Spatially resolved Kennicutt-Schmidt relation in a Milky Way mass spiral galaxy from the FIRE-2 project (Hopkins, Wetzel, et al., 2018). **Left:** Gas surface density, at 100 pc resolution, smoothed to 1 kpc resolution, the star formation rate traces the central molecular zone of the galaxy, and to a lesser extent at this time, the spiral features. **Center:** Star formation rate, smoothed to 1 kpc resolution, extensive spiral structure is evident. **Right:** Resulting spatially resolved Kennicutt-Schmidt relation at 1 kpc resolution, agrees with the gas-rich end of of data from Bigiel et al. 2008 (greyscale region in background), with some scatter to higher star formation rates. Unpublished data from Orr, Hayward, Hopkins, et al. (2018).
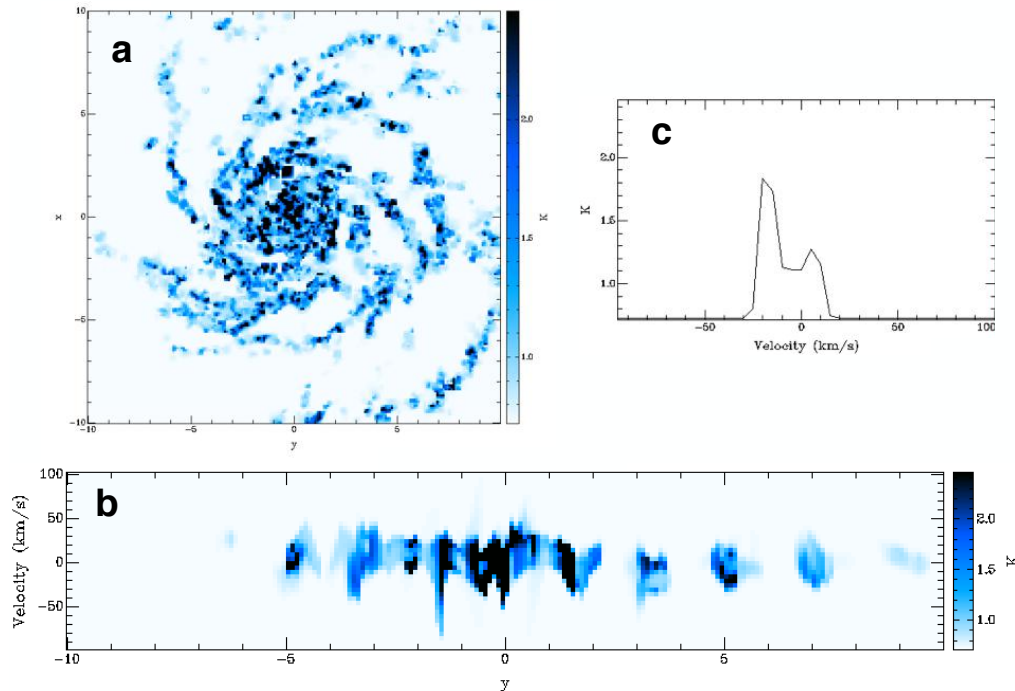
Figure 6.2: Early science result from the synthetic observations pipeline. Example of synthetic CO map from a Milky Way mass spiral galaxy from the FIRE project (Hopkins, Wetzel, et al., 2018). Counter-clockwise from top left, **(a)** Slice of CO line emission in the galaxy (face-on) at 100 pc resolution. Spiral features and central gas region are clearly visible (units, kpc), **(b)** slice in velocity space (units, km/s and kpc), showing velocity structure of CO emission through the center of the galaxy, **(c)** example of a CO line profile taken from a point along one of the spiral arms, with a clear double peaked feature.

logical zoom-in simulations are either able or unable to reproduce current kpc-scale observations, and explore the observational signatures of various physics. For example, by using a low-redshift snapshot from a cosmological zoom-in simulation as initial conditions for runs that vary the prescriptions for star formation and feedback, I will investigate how those variations impact observables from an otherwise identical galaxy, e.g., the ratio between observed CO emission and gas mass (i.e., the observer's X_{CO} factor). *I will leverage my pipeline for observing simulations, together with exploring the parameter space of star formation and feedback physics through simulation restarts, to see how, and to what extent, various resolved galaxy scaling relations constrain theory.* I will directly address questions in star and galaxy formation, e.g.: What is the relative balance between radiative and mechanical feedback in star-forming regions? How do gravity and stellar feedback together regulate star formation rates? My work will focus on identifying clean observational

tests to answer these questions.

Three proposed thrusts using zoom-in simulations and synthetic observations are as follows:

6.2.3 Strand I: X_{CO} and CO-Dark Gas Fractions in Cosmological Simulations

It is extremely difficult to observe H_2 directly, so observers use a litany of molecular gas tracers, e.g. CO and HCN, to infer the gas masses and dynamics in the dense, predominantly molecular ISM (Hollenbach et al., 1999). Among the gas tracers, CO has become a gold standard, due to its brightness, lack of confounding nearby lines, and because it traces 'low' density ($\sim$10–10^3 cm^{-3}) gas (Bolatto et al., 2013). However, given its strength, CO is almost always optically thick, such that we cannot observe emission deep within a galaxy–presenting difficulties in mapping what is essentially emission from a surface into an estimate for the volume (and therefore mass) of dense gas. The conversion factor between the observed emission and the gas mass is the observer's X_{CO} (the basis of which relies on a chain of reasoning regarding virialized clouds and collisionally excited CO), and has a large amount of uncertainty associated with it (Pineda et al., 2010; Bolatto et al., 2013; Clark et al., 2015). Moreover, several authors have pointed out that not all H_2 has associated CO emission (perhaps due to evolutionary effects in star-forming regions owing to the relative ease of CO destruction by ionizing radiation), such that some fraction of the gas may be "CO-dark" (e.g., Liszt et al., 2012; Shetty, Kelly, et al., 2014; Tang et al., 2016). Using cosmological zoom-in simulations and my synthetic observations pipeline, I will produce detailed maps of both the CO emission and of the total dense gas (mapping the HI and H_2 directly), yielding a self-consistent determination of the normalization and scatter in the simulated X_{CO}, and estimates of the CO-dark gas fractions. Further, with simulations varying the low-temperature gas cooling, shielding, and feedback physics, I will explore how sensitive X_{CO} and the CO-dark gas fractions are to different choices in the implemented physics.

6.2.4 Strand II: Spatial and Temporal Correlations Between Star formation & Gas Tracers

In the past decade, observers have begun to explore the spatial correlation between tracers of star formation and dense gas (Schruba et al., 2010; Kruijssen and Longmore, 2014; Kruijssen, Schruba, et al., 2018, Leroy et al. in prep.). Though various scaling relations have canonically been plotting two tracers against each other (e.g. formulations of Kennicutt-Schmidt), the information encoded in the spatial corre-

lation or anti-correlation between tracers has been argued to indicate evidence of *dynamical* evolution of the ISM. For example, regions with dense gas tracers evolve into regions with star formation tracers (with quickly fading dense gas tracers)–so, on some scale there is an expected anti-correlation between the two, the "uncertainty principle for star formation" (Schruba et al., 2010; Kruijssen and Longmore, 2014; Orr, Hayward, and Hopkins, 2019). I will take full advantage of the unique power of simulations to explore both high spatial resolution and temporal evolution by producing maps of dense gas and star formation tracers from individual galaxies that are closely spaced in time. I will disentangle the cross-correlations between spatial and temporal variations in gas and star formation rate tracers, elucidating the ways that variations in ISM conditions *across* a galaxy are related (or not) with how individual star-forming regions *evolve*.

6.2.5 Strand III: Signatures of Star Formation and Feedback Physics on Scaling Relations

How star formation proceeds, and its dependence on conditions at the sub-parsec level (i.e. local virial criterion, Mach number, gas density) remains uncertain (Martin et al., 2001; Krumholz et al., 2005; Hopkins, Narayanan, et al., 2013; Somerville et al., 2015). Surprisingly, simulations indicate that global star formation rates (and the spatially resolved distributions to some not fully explored extent) are not very sensitive to at least some of these local conditions, as the ISM self-regulates its phase structure (Orr, Hayward, Hopkins, et al., 2018; Orr, Hayward, and Hopkins, 2019). However, the exact correlation between how tracers of dense gas and star formation rates evolve with variations in star formation thresholds and physics (e.g., high- or low-star-formation efficiency per free-fall time) has not been studied. Nor is it fully understood how sensitive different scaling relations (observed at ~kpc-scales) are to various parsec-scale physics. I will vary the star formation and feedback physics in the simulations (e.g., the balance between radiative and mechanical feedback, the overall strength of feedback, and the timescales over which it is injected into the ISM), and then employ my synthetic observations pipeline. Comparing the synthetic observations against each other and against observational datasets, I will explore how star formation scaling relations can distinguish between various models of star formation and feedback, and constrain current and future theories of star formation with their predicted observable consequences.

6.2.6 Summary

In order to glean all that we can from sub-kpc resolution observations, we must both understand the signatures of star formation and feedback physics in the observables, and the extent to which those observables are reflective of the ground truth in galaxies. To address these points, I have developed a pipeline to produce spatially resolved synthetic observations of cosmological simulations, allowing me to both validate empirical observational relations and investigate the observational signatures of star formation and feedback physics in resolved galaxy scaling relations. The gap between observations and theory will most easily be closed through careful and diligent work, by observers with an ear for theory and theorists with an eye on the observables.

References

Benincasa, S. M., Wadsley, J., Couchman, H. M. P., & Keller, B. W. (2016) MNRAS 462, 3053

Bigiel, F., Leroy, A., Walter, F., Brinks, E., de Blok, W. J. G., Madore, B., & Thornley, M. D. (2008) AJ 136, 2846

Bolatto, A. D., Wolfire, M., & Leroy, A. K. (2013) ARA&A 51, 207

Brinchmann, J., Charlot, S., White, S. D. M., Tremonti, C., Kauffmann, G., Heckman, T., & Brinkmann, J. (2004) MNRAS 351, 1151

Bundy, K. et al. (2015) ApJ 798, 7, 7

Clark, P. C. & Glover, S. C. O. (2015) MNRAS 452, 2057

Conroy, C., Gunn, J. E., & White, M. (2009) ApJ 699, 486

Conroy, C., White, M., & Gunn, J. E. (2010) ApJ 708, 58

Faucher-Giguère, C.-A., Quataert, E., & Hopkins, P. F. (2013) MNRAS 433, 1970

González Delgado, R. M. et al. (2016) A&A 590, A44, A44

Hollenbach, D. J. & Tielens, A. G. G. M. (1999) Reviews of Modern Physics 71, 173

Hopkins, P. F., Kereš, D., Oñorbe, J., Faucher-Giguère, C.-A., Quataert, E., Murray, N., & Bullock, J. S. (2014) MNRAS 445, 581

Hopkins, P. F., Narayanan, D., & Murray, N. (2013) MNRAS 432, 2647

Hopkins, P. F., Wetzel, A., et al. (2018) MNRAS 480, 800

Katz, N., Weinberg, D. H., & Hernquist, L. (1996) ApJS 105, 19

Kennicutt Jr., R. C. (1998) ApJ 498, 541

Kruijssen, J. M. D. & Longmore, S. N. (2014) MNRAS 439, 3239

Kruijssen, J. M. D., Schruba, A., Hygate, A. P. S., Hu, C.-Y., Haydon, D. T., & Longmore, S. N. (2018) MNRAS 479, 1866

Krumholz, M. R. & McKee, C. F. (2005) ApJ 630, 250

Lehnert, M. D. et al. (2009) ApJ 699, 1660

Leroy, A. K., Walter, F., Brinks, E., Bigiel, F., de Blok, W. J. G., Madore, B., & Thornley, M. D. (2008) AJ 136, 2782

Leroy, A. K., Walter, F., Sandstrom, K., et al. (2013) AJ 146, 19, 19

Liszt, H. S. & Pety, J. (2012) A&A 541, A58, A58

Liu, Q., Wang, E., Lin, Z., Gao, Y., Liu, H., Berhane Teklu, B., & Kong, X. (2018) ApJ 857, 17, 17

Martin, C. L. & Kennicutt Jr., R. C. (2001) ApJ 555, 301

McKee, C. F. & Ostriker, E. C. (2007) ARA&A 45, 565

Nelson, E. J. et al. (2016) ApJ 828, 27, 27

Orr, M. E., Hayward, C. C., & Hopkins, P. F. (2019) MNRAS 486, 4724

Orr, M. E., Hayward, C. C., Hopkins, P. F., et al. (2018) MNRAS 478, 3653

Orr, M. E., Hayward, C. C., Nelson, E. J., et al. (2017) ApJ 849, L2

Ostriker, E. C. & Shetty, R. (2011) ApJ 731, 41, 41

Pineda, J. L., Goldsmith, P. F., Chapman, N., Snell, R. L., Li, D., Cambrésy, L., & Brunt, C. (2010) ApJ 721, 686

Richings, A. J., Schaye, J., & Oppenheimer, B. D. (2014a) MNRAS 440, 3349

– (2014b) MNRAS 442, 2780

Schaye, J. (2004) ApJ 609, 667

Schinnerer, E. et al. (2013) ApJ 779, 42, 42

Schmidt, M. (1959) ApJ 129, 243

Schruba, A., Leroy, A. K., Walter, F., Sandstrom, K., & Rosolowsky, E. (2010) ApJ 722, 1699

Semenov, V. A., Kravtsov, A. V., & Gnedin, N. Y. (2016) ApJ 826, 200, 200

Shetty, R., Kelly, B. C., et al. (2014) MNRAS 437, L61

Shetty, R. & Ostriker, E. C. (2008) ApJ 684, 978

Somerville, R. S. & Davé, R. (2015) ARA&A 53, 51

Stark, D. V. et al. (2018) MNRAS 474, 2323

Tang, N., Li, D., Heiles, C., Wang, S., Pan, Z., & Wang, J.-J. (2016) A&A 593, A42, A42

Toomre, A. (1964) ApJ 139, 1217

Wetzel, A. R., Hopkins, P. F., Kim, J.-h., Faucher-Giguère, C.-A., Kereš, D., & Quataert, E. (2016) ApJ 827, L23, L23

Wuyts, S. et al. (2011) ApJ 742, 96, 96

Zhou, L. et al. (2017) MNRAS 470, 4573